Continental collision and slab break-off: numerical models and surface observables

ANDREW DAVID BOTTRILL

BOTTRILL, ANDREW DAVID (2014) Continental collision and slab break-off: numerical models and surface observables. Doctoral thesis, Durham University.

Continental collision and slab break-off: numerical models and surface observables

Andrew David Bottrill

Earth Science Department

Durham University

A thesis submitted for the degree of

Doctor of Philosophy (PhD)

2014

---

1. Reviewer: Dr Huw Davies

2. Reviewer: Dr Colin Macpherson

Day of the defence: 16^{th} May 2014

Signature from head of PhD committee:

Abstract

Collision zones worldwide show a vast array of complexity that is difficult to relate to simple collision dynamics. Here we address the problem of linking surface observables to collision dynamics through the use of two and three-dimensional numerical models. We will focus on two specific observables, topography and the presence of ultra-high pressure metamorphic terranes. Our model topography predictions are used to explain the uplift and subsidence history for the Arabia-Eurasia collision. This allows us to relate the post-collisional marine deposits, found on the overriding plate, to a steepening of the subduction interface.

Our three-dimensional model is used to explore possible exhumation mechanisms for the Western Gneiss Complex in Norway. From these models we show how an asymmetric collision can help drive exhumation of material that has experienced comparable conditions to the Western Gneiss Complex. The linking of upper mantle and lithosphere dynamics to both topography observation and exhumation patterns allow better understanding of the subduction and collision process.

Acknowledgements

Firstly I would like to acknowledge the funding for this PhD provided by the Charles Waites studentship and the support of the Waites family throughout the project.

I would like to acknowledge my supervisors Jeroen van Hunen and Mark Allen, for all their help and support though out this project. As well as their tolerance for my endless questions and patience with my occasionally creative use of the English language.

I would like to acknowledge the support and input from colleagues from other institution. Particularly Simon Cuthbert from UWS and Hannes Brueckner from Colombia University who have provided specific knowledge on UHP complexes.

I would also like thank all of my colleagues in Durham for making the last 3 years a great experience.

I should also thank my girlfriend Jen Burrows for putting up with living with me throughout the writing up process.

Finally I leave you with a quote

> “Scientists still do not appear to understand that all earth sciences must contribute evidence toward unveiling the state of our planet in earlier times” - Alfred Wegener

Declaration

I, Andrew Bottrill, declare that this thesis, presented for the degree of Doctor of Philosophy at Durham University, is a result of my own original research and has not been previously submitted to Durham University or any other institution. I have clearly indicated, when appropriate, the contributions of colleagues and have made every effort to acknowledge all collaborative work.

The thesis work was conducted from October 2010 to March 2014 under the supervision of Dr Jeroen van Hunen and Dr Mark Allen at Durham University.

Andrew Bottrill
Durham University
April 2014

Contents

List of Figures

LIST OF FIGURES

List of Tables

1

Introduction

1.1 Plate tectonics

The theory of plate tectonics divides the surface of earth into a number of tectonic plates that can move independently over a convecting mantle. Plate tectonics was developed out of the continental drift hypothesis [Wegener, 1912] that was born out of the observation that the major continents seem to fit neatly together. The driving force for the movement of plates was proposed to be heat generated internally in the earth [Holmes, 1931]. The movements of tectonic plates over time show lateral translations and rotations around the earth's surface (Fig. 1.1). The history of these motions over time have been reconstructed [e.g. Torsvik *et al.*, 1996, 2012] (Fig. 1.1), which shows that plates have travelled large distances throughout Earth's history, with velocities of up to 100 mm/year [Davidson *et al.*, 2002].

Plate tectonics is important in allowing heat produced in the earths core, mantle and crust to escape, with recent estimates of the total surface heat flow of 47 ± 2 TW [Davies & Davies, 2010]. It is estimated that $> 60\%$ of total mantle heat loss is through the oceans [Jaupart *et al.*, 2007], with the majority at mid ocean ridges [van Hunen & Moyen, 2012]. The first development of plate tectonics on earth is still an area of active research with disagreement on the exact timing of the initiation of what we currently recognise as plate tectonics. It is, however, accepted that plate tectonics in its current form has operated for at least the last billion years and potentially as far back as 3.2 billion years [Korenaga, 2013]. Proposed higher mantle temperatures, during earth's early history, have been suggested to generate different tectonic regimes [Ernst, 2009; van Hunen *et al.*, 2008; van Hunen & Moyen, 2012] further complicating how we define the initiation of our current tectonic regime.

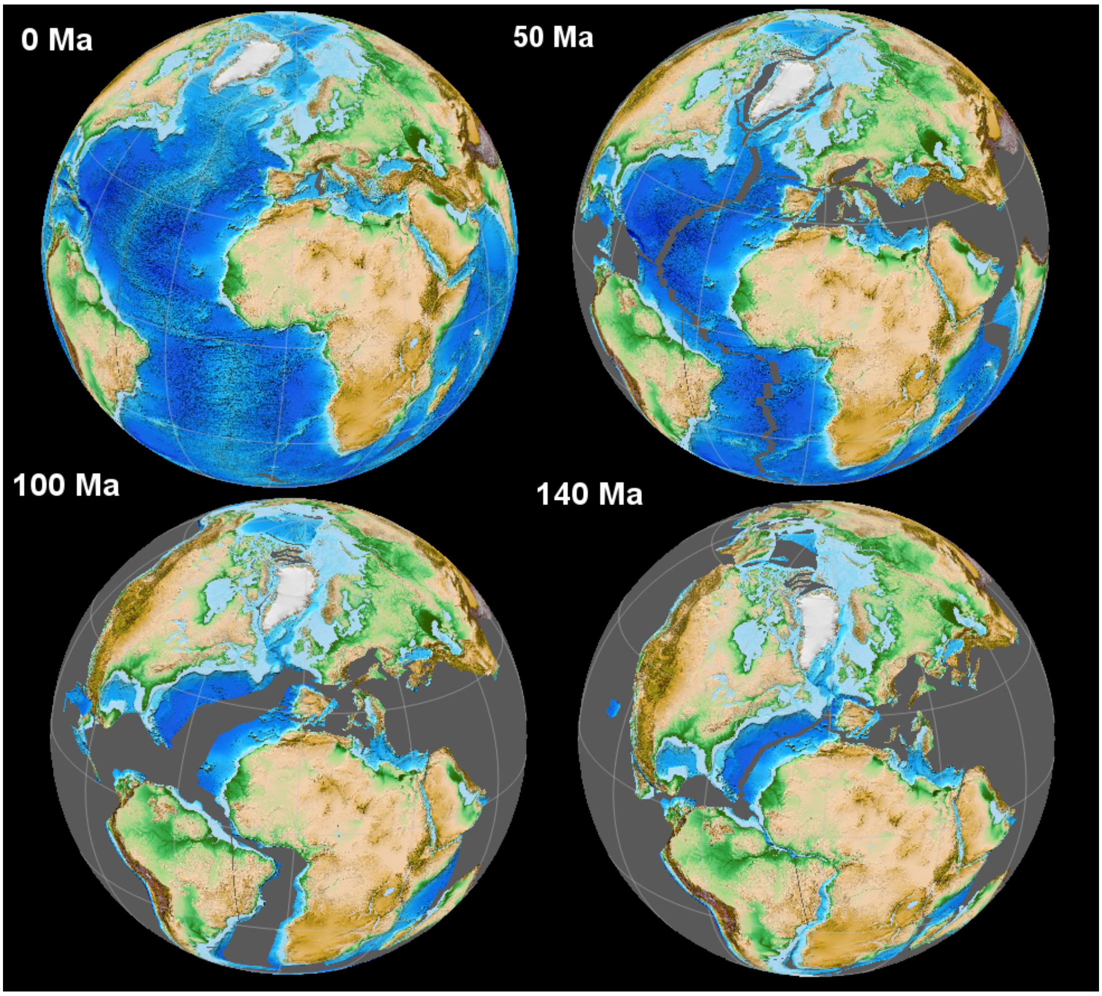

Figure 1.1: Plate reconstruction - Plate motions over the last 140 Myrs showing the opening of the Atlantic and collision of Arabia with Eurasia. [gplates, Williams *et al.*, 2012]

Tectonic plates are made up of a mantle lithosphere topped with crustal material (Fig. 1.2). In oceanic regions, the lithosphere is between 0-150 km thick with its thickness proportional to the square-root of the plate age [Turcotte & Schubert, 2002], although this relationship starts to break down for older oceanic lithosphere. Oceanic crust is generally thin (7 km) and predominantly basaltic in composition. This structure is created due to pressure-controlled partial melting at mid-ocean ridges (MORs) which forms the basaltic crust, while the residue creates the harzburgite layer below. Continental regions have thicker lithosphere (100-200 km) and a thicker crust (10-60 km) with predominately andesitic bulk composition [Rudnick, 1995]. Production of continental crust remains a current area of active research. Presently, continental crust production is thought to mainly occur at subduction zones by arc volcanoes. However, it is not clear if continental crust has always been generated this way [Hawkesworth & Kemp, 2006; Martin & Moyen, 2002]. The production of continental crust has been proposed to be episodic [Condie, 1998], and episodes of high production have been linked to the break-up of supercontinents. However, there is still debate as to whether the current age distribution of continental crust demonstrates episodic production or a preservation bias [Hawkesworth & Kemp, 2006].

The boundary between oceanic and continental material in an intra-plate setting is referred to as a passive margin (Fig. 1.2). Passive margins are usually characterised by an old rift structure with later sedimentation overlaying it. Plates can move as they do due to the strength of the earth's lithosphere compared to the asthenosphere that it overlies.

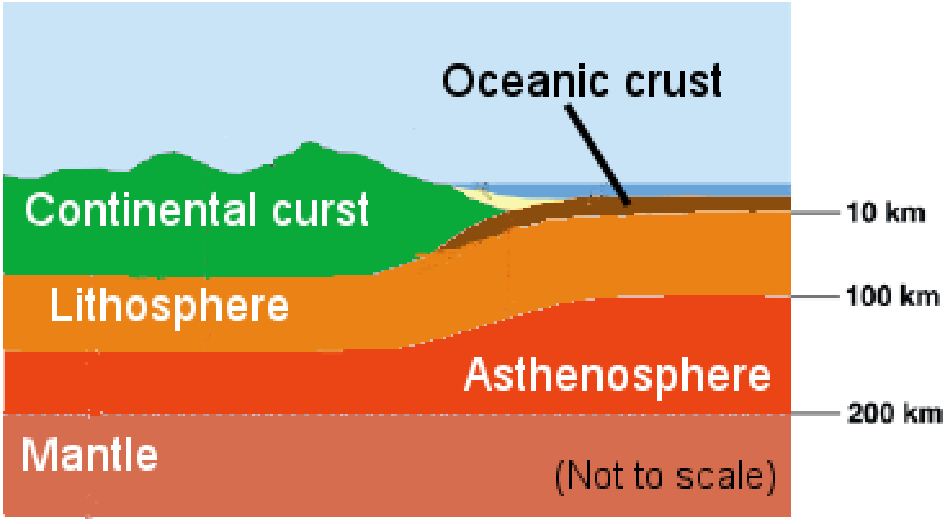

Figure 1.2: Lithosphere structure - Idealised structure of upper mantle in both continental and oceanic regions. After Pidwirny [1999]

The movement between plates is accommodated by plate boundaries. The nature of these boundaries are determined by the two plate's relative motion. Three major plate boundary types exist on earth; divergent boundaries, convergent boundaries and transform zones. Each type of boundary displays different surface expressions and characteristics. Divergent boundaries are where the two plates are pulling apart and are associated with rifting, sea floor spreading and the effusive volcanism such as found all along the mid-Atlantic ridge. This is where new oceanic plates are created. Transform zones are where the two plates are pushing past each other, the world's best studied example of this is the San Andreas Fault in western USA. Transform faults are often associated with relatively large magnitude earthquakes but little volcanism. Convergent margins are where two plates are moving towards each other. These can be subdivided into two distinct types; subduction, where one plate if forced under the other, and collision, where neither plate is pushed under the other and both are deformed by the convergence. Convergent margins are the focus of this study and their structure is further discussed below. The creation of a new oceanic plate at mid ocean ridges and its destruction in subduction zones demonstrates the cyclic nature of plate tectonics [Wilson, 1966] (Fig. 1.3).

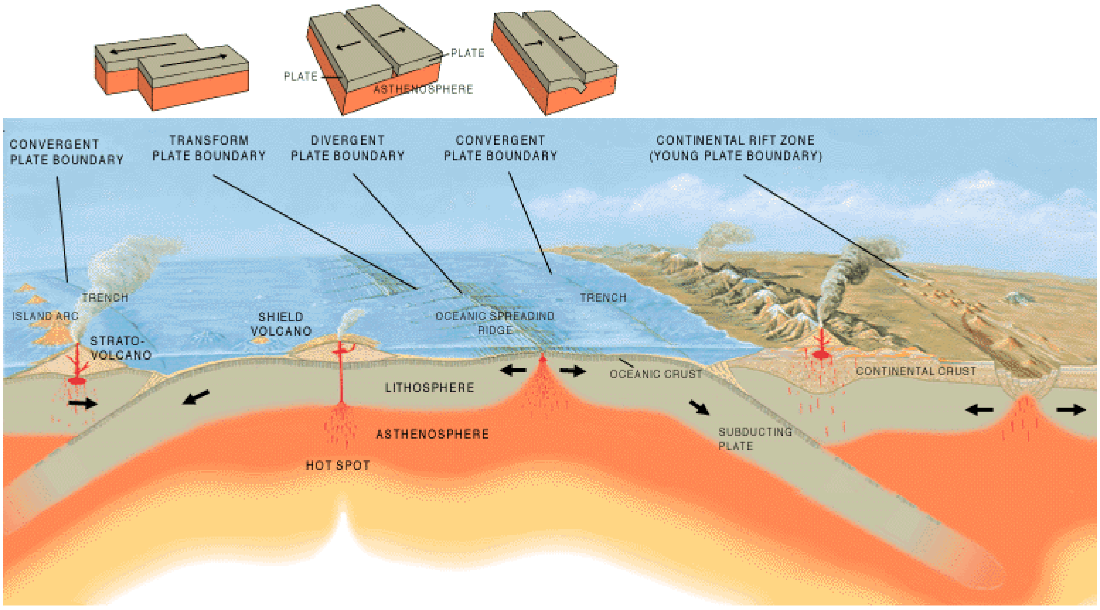

Figure 1.3: Plate boundary styles - A cross section illustrating the main types of plate boundaries. Top left show a transform fault top centre a divergent plate boundary and top right shows a convergent plate boundary. After Vigil [2013] USGS.

The overall driving force for plate tectonics is gravity [Forsyth & Uyeda, 1975] and the loss of heat from the earth. The forces exerted on a tectonic plate can be subdivided into a number of different types. The dominant force for plate tectonics is slab pull [Vlaar & Wortel, 1976] which is the down dip component of the gravitational pull on the dense subducted slab [Mckenzie, 1969]. Slab pull forces are estimated to be at least an order of magnitude larger than any of the other forces that operate on tectonic plates [Turcotte & Schubert, 2002]. There are, however, a number of other forces that influence plate tectonics. These include ridge push, frictional resistance, interaction of subducted slabs with mantle phase transitions and traction exerted on tectonic plates by the convecting mantle. Ridge push is generated by the cooling and contracting of oceanic lithosphere over time. Its magnitude can be calculated by integrating the resultant horizontal pressure gradient. Resistance to motion is provided by mantle drag as well as compositional buoyancy of the subducting plate. A plate will also resist subduction due to friction in the plate interface and internal resistance to bending the plate during subduction. The frictional resistance is evident in the large number of earthquakes produced at subduction zones. The bending of the subducting plate is also thought to release a substantial amount of energy [Conrad & Hager, 1999].

The interaction of slabs with the major mantle phase transitions has been shown to be able to provide an additional force on the slab. The 410 km discontinuity has a positive Clapeyron slope, and provides extra suction to subducting slabs. The discontinuity at 660 km has a negative Clapeyron slope and so is thought to provide resistance to subducting slabs [Christensen, 1995]. The exact nature of the forces exerted on subducting slabs by phase changes is still being actively studied [Tan *et al.*, 2002; Fukao *et al.*, 2009]. Seismology studies image slabs that both collect at the 660 km discontinuity and appear to pass though unimpeded suggesting that the different slabs experience differing amounts of resistance. Mantle traction on the base of tectonic plate such as those exerted by the up-welling of a hot mantle plume is also proposed to influence the movement of plates [Wilson, 1993].

1.2 Structure of tectonic plates

Tectonic plates on earth can be divided into two categories; oceanic and continental. Oceanic plates are formed at mid ocean ridges and recycled back into the mantle at a subduction zone (Fig. 1.3) [Wilson, 1966]. Oceanic plates are made up of a mantle lithosphere and a thin oceanic crust (Fig. 1.2). Oceanic lithosphere thickness increases away from the ridge where it was formed, as the plate cools, with thicknesses up to ~150 km. Oceanic crust is primarily composed of mafic material and is generally less that 10 km thick. The structure of oceanic crust has been studied from emplaced ophiolites which show pillow lavas at the surface fed by sheeted dykes which in turn is underlain by layered gabbro and finally harzburgitic mantle material [Erickson, 1996; Davidson *et al.*, 2002].

Oceanic crust has an average density of about 2900 km/m^3 [Fowler, 2005], though during subduction this crust is thought to be rapidly transformed into denser phases (eclogite) [Anderson, 2007], so it retains little of its compositional buoyancy at depth. For old oceanic regions with thick cold lithosphere and modest crustal thickness the excess density of the plate compared to the mantle becomes negative allowing the plate to sink.

A continental plate, in contrast, has a much thicker mantle lithosphere of around 150 km, and can be up to 250 km in areas of old stable cratons [McKenzie & Priestley, 2008]. Continental upper crust has a felsic or granitic bulk composition [Davidson *et al.*, 2002] and is much thicker than oceanic crust, typically 25 - 60 km [Rudnick, 1995]. Continental crust is generally thought to be formed at arc settings [Hawkesworth & Kemp, 2006], though as discussed above, the nature and timing of continental crust formation is still an active area of research. The structure of continental crust is complex and varies between different regions on earth. Most continental regions also have a layer of sedimentary deposits, at the surface, that overlay a basement of metamorphic material that is considered the top of the continental crust. Continental crust is also less dense with an average value of 2700 km/m^3. This density contrast between the whole continental plate and mantle is important as it means that continental regions resist recycling into the mantle.

1.3 Convergent margins

Convergent margins are where the two plates are moving towards each other. Convergent margins come in three main type; ocean-ocean subduction, continent-ocean subduction and continental collision (Fig. 1.4 A-C). Subduction zones are generally associated with a deep marine trench and arc volcanism. Continental collision builds mountains and it's onset can be considered the final stage of the subduction process.

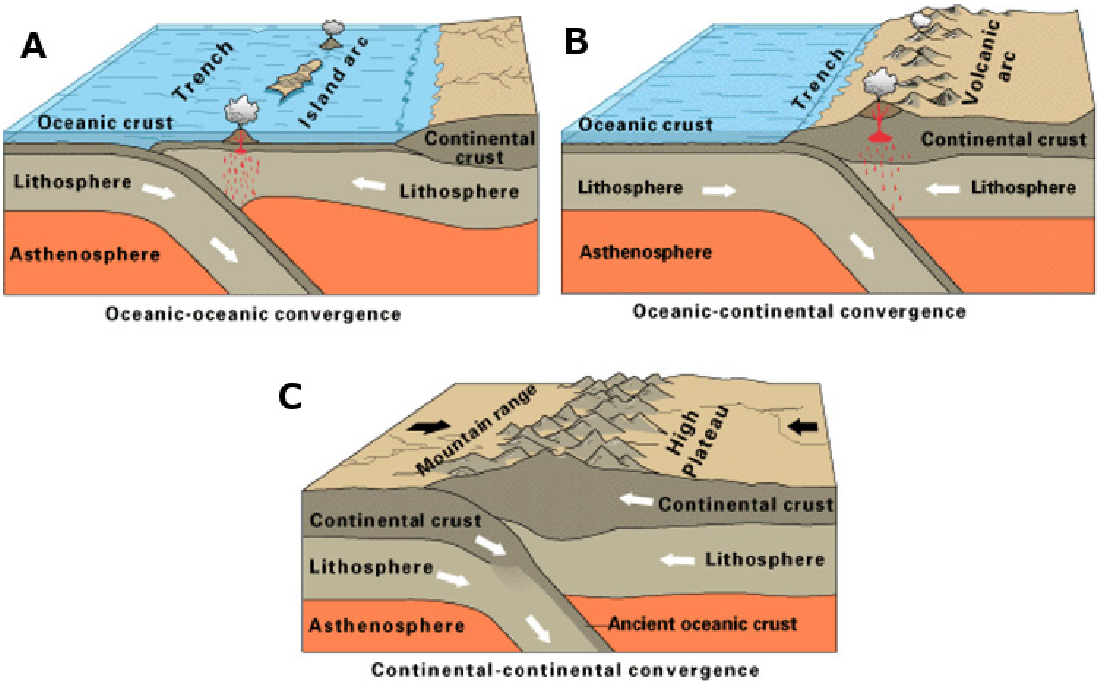

Figure 1.4: Convergent margins - Three types of plate convergence resulting in subduction. [Image Source. US Gelogical Survey].

Subduction is the process by which one tectonic plate is forced below another and sinks into the mantle. This process can occur between two oceanic plates, such as the ongoing subduction at the South Sandwich arc, or between a continental and an oceanic plate, such as Andean subduction zone off the west coast of South America. The frictional resistance between the two plates generates earthquakes along the plate interface and deeper inside the subducted slab. This zone of earthquakes is referred to as the Wadati-Benioff zone [**?**]. The discovery of Wadati-Benioff zones at convergent margins showed the presence and position of the subducted slab at depth. Attenuation studies [Toksöz *et al.*, 1979] and the invention of seismic tomography allowed slabs to be imaged in the mantle [Woodhouse & Dziewonski, 1984]. The frictional resistance to subduction is linked to the internal strength of the slab as strong slab are harder to deform [Heuret *et al.*, 2011]. The majority of subduction zones on earth have slab dips of 25-70°. However, the geometry and dynamics of subduction zones is an area of continuing study [Jarrard, 1986; Lallemand *et al.*, 2005]. A number of world subduction zones demonstrate interesting and atypical behaviour, such as the flat slab subduction under South America.

Slabs also show variety in behaviour when interacting with the main mantle phase transition at 660 km (ringwoodite to perovskite and magnesiowüstite). Some slabs seem to pass virtually unimpeded into the lower mantle, whereas others are stalled, at least temporarily, at the transition zone. This slab-transition zone interaction is imaged in mantle tomography [Fukao *et al.*, 2001; Li *et al.*, 2008]. How slabs interact with this phase transition is important as it will affect the dynamics of the subduction system by changing the slab pull force [Čížková *et al.*, 2002].

Subduction zones are also associated with arc volcanism. In ocean-ocean subduction, island arc volcanoes are produced, such as those present on the Tonga-Kermadec arc. For ocean-continent subduction, large volcanoes that erupt explosively are formed, such as the Cascade Range volcanoes in the USA. The transport of volatiles such as water to depth in the subducting slab is considered important in generating arc melts. The release of these volatiles has been proposed to control the positioning of volcanoes relative to the arc [Iwamori, 1998]. However more recent studies have suggested that there is no simple inverse relationship between slab dip and the position of the volcanic arc [England & Katz, 2010; Syracuse & Abers, 2006]. Arc magmatism is also one method of producing continental crust which is critical in producing our current habitable planet [Rudnick, 1995].

Continental collision occurs when two continental plates come together. This is generally associated with the final phase of subduction where buoyant continental crust starts to enter the subduction zone. Due to the continental crust's compositional buoyancy, it resists subduction, causing the convergence between the plates, to be accommodated mainly by internal deformation of the continental plates, rather than pure subduction. The internal deformation and thrusting of material builds an orogenic belt or mountain ranges such as the Himalayas or Zagros mountain ranges [Davidson *et al.*, 2002]. Convergence at collision zones can continue for tens of millions of years after the initial collision. The cessation of subduction due to continental collision allows the slab to heat up and thermally neck [Gerya *et al.*, 2004] due to the slab hanging in the mantle. Some collision zones display post-collisional magmatism that is chemically different from subduction magmatism. Explanations for this magmatism are wide-ranging and include small scale convection [Kaislaniemi *et al.*, 2014], delamination [Bird, 1978], compressional melting [Allen *et al.*, 2013] and slab break-off [Davies & von Blanckenburg, 1995].

1.4 Slab break-off

The process of slab beak-off or slab detachment is the removing the subducted oceanic plate from the rest of the plate and it sinking into the mantle. Observations to first support the idea that slabs break off into the mantle came from the presence of earthquake gaps in the Wadati-Benioff zone for some subduction zones [Barazangi *et al.*, 1973]. The gap in earthquakes at depth was interpreted as a sign of mechanical decoupling between the slab and plate left at the surface. With the advent of higher resolution mantle tomography the presence of gaps in these oceanic plates at between 100 km and 400 km [Wortel & Spakman, 1992] were observed. Studies have also proposed that other high velocity anomalies around the upper-lower mantle boundary [Faccenna *et al.*, 2011] and even the core mantle boundary could be remnants of detached slabs [Hutko *et al.*, 2006]. The fate of slabs at the base of the mantle is still not completely clear. Seismology has shown a number of LLSVPs (Large Low Shear Velocity Provinces) at the base of the mantle, which some have proposed to be the remains of previously subducted slabs [Spasojevic *et al.*, 2010]. The nature of these LLSVPs is still debated with some researchers favouring a purely thermal formation [Davies & Davies, 2009] where others favouring a compositional heterogeneity [Masters *et al.*, 2000]. Observations suggest that these LLSVPs are the source of deep mantle plumes [Burke *et al.*, 2008].

Slab break-off is thought to occur due to a build-up of stress in the subducted plate and thermal necking of the subducted slab. The depth at which this occurs and the mechanism have been the subject of multiple studies using numerical [for example Zhong & Gurnis, 1994; Gerya *et al.*, 2004] and analogue models [Regard *et al.*, 2008]. This process is proposed to operate due to the stopping of subduction, which allows the slab to start heating up, but also provides a resistance force to slab pull. The resistance to ongoing subduction and the continued pull of the dense subducted slab produce extensional stresses in the slab, which eventually lead to breaks-off of the dense oceanic slab. Most commonly subduction is stopped by incoming buoyant continental crust that can not subduct. Lateral tearing (Fig. 1.5) is proposed as the mechanism by which a slab is removed along a whole collision zone [Wortel & Spakman, 2000]. This lateral tearing has also been reproduced in numerical models [Yoshioka *et al.*, 1995; van Hunen & Allen, 2011] who show that a tear can rapidly propagate laterally along the collision zone with speeds of 1-100 cm/yr. Vertical tearing has also been observed [Obayashi *et al.*, 2009] and proposed to be needed to accommodate a slab lying flat on the mantle phase transition. With a combination of vertical and lateral tears, slab windows can develop such as those proposed under the Apennine collision under Italy [Faccenna & Becker, 2010]. The large variation in proposed dynamics for slab break-off is summarised in Nolet [2009]. Some possible detachment mechanisms that are proposed are; lateral tearing of the slab [Wortel & Spakman, 2000], horizontal tearing [Obayashi *et al.*, 2009] and fragmentation. This variation in slab dynamics highlights the challenges associated with understanding the general slab break-off process.

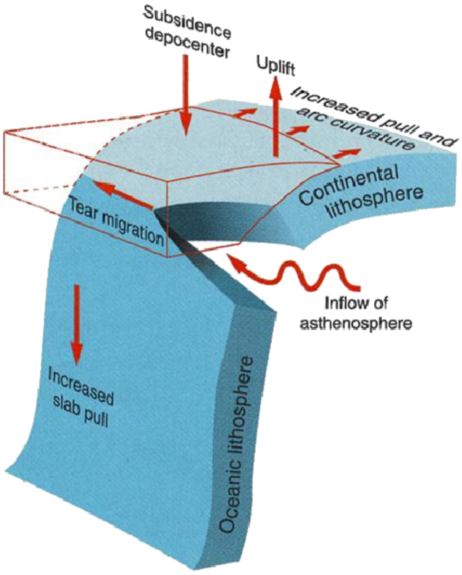

Figure 1.5: Slab Break-off - Schematic diagram of a lateral tear forming in a subducted slab [Wortel & Spakman, 2000].

The slab detachment mechanism and the surface dynamics associated with it have been studied extensively using numerical and analogue simulations in order to gain further insight into the process [Gerya *et al.*, 2004; Regard *et al.*, 2008; Andrews &

Billen, 2009; Baumann *et al.*, 2010; Burkett & Billen, 2010; van Hunen & Allen, 2011]. These studies highlight the range of estimates produced for the topographic expression of slab break-off, with estimates of uplift and subsidence of between 1 and 10 km [Zhong & Gurnis, 1994; Andrews & Billen, 2009; Duretz *et al.*, 2011b; Bottrill *et al.*, 2012]. Estimates of the depth of slab break-off also vary over a range of 10-100 km. Below, we elaborate two key surface observables the topographic change associated with slab break-off and the exhumation of UHPM material.

1.5 Surface topography

The topography of the earth's surface shows evidence of both current and paleo-tectonic processes. The topography at any point on the earth's surface can be thought of as a combination of the isostatic compensation height and any dynamic forces from the mantle. The isostatic compensation height is controlled by the thickness and density of both the crust and lithosphere. It is calculated by assuming that each point at the surface can be represented as a column of material floating in a liquid mantle (Fig. 1.6) and the isostatic compensation height is purely the amount of the column that is above the surface (h).

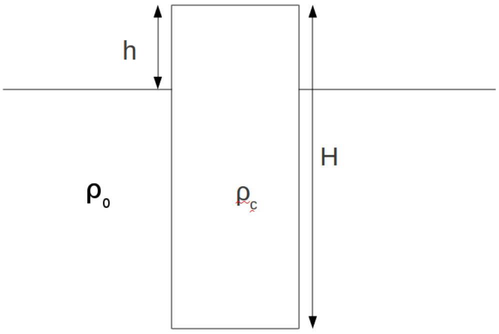

Figure 1.6: Isostatic compensation - The theoretical construct used to calculate Airy isostasy, where h is the height of the topography, H is the total height of the plate block, ρ_c the average density of the plate and ρ_0 the density of mantle.

$$\frac{h}{\delta\rho} = \frac{H}{\rho_0} \qquad \text{where} \qquad \delta\rho = \rho_c - \rho_0$$

Dynamic topography [Hager, 1984] is generated by forces imposed on the base of the lithosphere by the convecting mantle as well as internal plate forces such as plate elasticity. Studying topography, in the framework of plate tectonics, is useful as it can give an insight into deep dynamics as well as the movement of crustal material. Topography also has the advantage that past topography changes are partially recorded in the sedimentary record and so can give a potential record of dynamics over time [Roure, 2008; Ascione *et al.*, 2012].

Subduction zones produce their own unique topography of subduction trench, fore arc bulge and back arc basin [Melosh & Raefsky, 1980]. How this topography is affected by dynamics in the mantle has been explored in a number of studies [Melosh & Raefsky, 1980; Zhong & Gurnis, 1994; Faccenna *et al.*, 2011; Husson, 2012]. These studies show that convection in the mantle can exert significant forces on the base of tectonic plates and so generate topographic signals. How topography changes during the transition from subduction to collision is also of interest as, again, the topography may reflect mantle dynamics [Gerya *et al.*, 2004; Burkett & Billen, 2010; Duretz *et al.*, 2011a]. Topography changes during collision may show a surface expression of the detachment of a slab and its subsequent sinking into the mantle. The topography changes would come from two main effects; unloading the subducted plate of its slab anchor and the mantle flow induced by the movement of the slab. We would also expect there to be a change in topography due to the movement of crustal material during collision.

A number of studies have predicted the topography changes associated with the slab break-off process [Gerya *et al.*, 2004; Andrews & Billen, 2009; Duretz *et al.*, 2011a]. These have shown that the slab break-off is generally associated with uplift of the area of collision. The dynamics and initial state of the plate involved in the collision are important as they have a large effect on the topographic response to slab break-off. Further numerical modelling results [Bottrill *et al.*, 2012] (Chapter 3) demonstrate how changes in the topography on the overriding plate can be used to detect slab break-off.

1.6 High/Ultra-high pressure metamorphism

Ultra-high pressure metamorphism (UHPM) is a term used for crustal material which has been transported to depth within the earth before being returned to the surface. UHPM rocks are classified as crustal material that has experienced pressures in excess of 2.8 GPa, which is equivalent to being transported to a depth of greater than 95 km. At this pressure coesite is stable at 700°C [Chopin, 1984]. The presence of coesite is one of the diagnostic minerals for a rock being categorised as ultra-high pressure (UHP metamorphic).

Globally there are over 20 UHPM exposures on earth, mostly in Phanerozoic continental orogenic belts [Liou *et al.*, 2004]. Some of these sites show multiple episodes of UHPM exhumation over 10 million years. The size of these terranes also vary quite dramatically from $> 30,000km^2$ giant UHP terranes in Norway [Little *et al.*, 2011] and China [Li & Gerya, 2009] to small kilometre-sized bodies found in mélanges such as the European Alps [Federico *et al.*, 2007]. A lot of these bodies are made up of quartzofeldspathic gneiss with a few mafic rocks (eclogite) or ultramafic rocks (garnet-bearing peridotite) included in them [Massonne, 2003; Coleman Robert, 2005]. UHPM rocks can also contain diamonds due to the extreme pressures they have experienced. Some of the larger units also include evidence of sediments and rift volcanic units that can be interpreted as evidence of the exhumation of a previous continental margin. Most UHPM terrains record a history of high pressure (around 3 GPa) but relative low temperatures (800 °C). This history suggests that exhumation of these rocks happens fast before they can thermally equilibrate to the expected lithospheric temperature at that depth. The range of temperatures, some as high as 1200 °C such as Kokchetav Massif [Massonne, 2003] and pressure, some as high as 4.5 GPa [Vrijmoed *et al.*, 2009] demonstrate the need for multiple exhumation mechanisms.

It is generally agreed that the only process capable of transporting crustal material to the depths required to form these UHP metamorphic rocks is subduction [Coleman Robert, 2005]. Crustal material is transported by the subducting plate which in some cases allows material to reach depth of greater than 100 km. The subduction of oceanic crust and sediments is well documented in many arc settings around the world, where crustal signatures can be recognised in arc lavas [Hacker *et al.*, 2005]. These signatures potentially show that crustal material is transported to the depth at which melt is generated (more than enough to form UHPM rocks) by subduction. Although this shows that material is transported to depth during ongoing subduction, it does not give a mechanism to return it to the surface. It has been suggested that large UHPM terranes are associated with the start of collision and the subduction of continental crustal material [Davies & von Blanckenburg, 1995]. This allows enough crustal material to enter the subduction system. If this material is not melted or metamorphosed (producing denser mineral assemblages), it will retain its compositional buoyancy which is proposed to provide the driving force for exhumation in most exposed UHPM terranes [Warren, 2013].

There are a number of different suggested mechanisms for the exhumation of UHPM terranes, all of which offer a good explanation for some of the UHPM terrains on earth. One proposed mechanism for the Western Gneiss Complex in Norway is eduction or the reversal of the subduction process after slab break -off. Here it is proposed that after slab break-off, the removal of the slab pull force causes the subducting plate to move backwards [Andersen *et al.*, 1991], exhuming crustal material that had previously been subducted. This material is then combined into the collision zone as continued convergence of the collision zone occurs. This mechanism has advantages for explaining large areas of UHMP rock as it allows a large section of crustal material that was previously subducted to be returned to the surface coherently. A criticism for this method is that some believe that the 3D nature of a subduction zone would not allow a reversal of subduction after break-off due to continued subduction at other points along the arc.

Another method suggested for the exhumation of mélange style UHPM rock is a return of material back up the subduction channel. The Subduction channel describes the zone of highly deformed material between the subducting and overriding plate [Cloos & Shreve, 1988]. In this method, it is proposed that traction on the base and top of the “subduction channel” causes chaotic flow in this channel region that returns material to the surface [Federico *et al.*, 2007]. These UHPM terranes are categorised by the chaotic nature of the emplaced material in a mélange style UHPM terranes [Ring & Glodny, 2010]. Recent studies have shown how slab roll back and shallowing of the subduction angle aids this exhumation of material through modifying the flow pattern in the mantle wedge [Brun & Faccenna, 2008; Husson *et al.*, 2009]. A difficulty with this explanation is that relatively little is known about the nature of the subduction channel and interface. A few numerical studies have attempted to model exhumation in these settings [Burov *et al.*, 2001] where exhumation was shown to be sensitive to the rheological description. For exhumation to happen in this way the subduction channel would need to be of sufficiently low viscosity to allow flow to transport material to the surface, yet high enough to be able to transport material at all.

Yet another method proposed for the exhumation of UHP terranes is the detachment and buoyant rising of crustal material from the subducted plate and emplacement into the overriding plate. This mechanism is sometimes referred to as a cold plume [Little *et al.*, 2011; Vogt *et al.*, 2012]. The resulting surface expression is often combined into the thrust sheets in the orogenic wedge and is the method proposed for some of the large UHPM terrains observed such as those in China [Li & Gerya, 2009]. Numerical modelling suggest that crustal strength has a strong influence on generating upwellings of crustal material [Gerya & Yuen, 2003]. Field observations suggest that at least some UHP material is entrained in a buoyant melt phase [Wang *et al.*, 2003]. The rheology description will also have to allow crustal material to delaminate at depth but not be so weak that all crustal material is scraped off during on-going subduction.

All three described methods have been the focus of numerical and analogue modelling work [e.g. Burov *et al.* [2001]; Gerya & Stöckhert [2005]; Brun & Faccenna [2008]; Husson *et al.* [2009]; Li & Gerya [2009]; Duretz *et al.* [2011b]. Most of these studies focus on one exhumation mechanism and how it is applicable to a specific UHPM terrain. From field observation we know that there are areas that have experienced a number of phases of exhumation [Gordon *et al.*, 2012]. The presence of multiple exhumation events at a single collision zone highlight the complex dynamics associated with the formation and exhumation of these rock. So far, there are few numerical or analogue models that can successfully simulate all proposed exhumation mechanisms. This will lead to a better understanding of the subduction and collision processes, and potentially explain the variation in subduction and collision styles found on earth.

1.7 Thesis outline

This thesis aims to deal with the question of what surface expression can we expect during the transition of a subduction zone into a collision zone. It contains seven chapters that are briefly summarised below. Chapter 3 and 6 are based on published manuscripts. Any co-authorship in these publications reflects the training, discussion and specialist knowledge provided by these collaborators. I conducted all the numerical experiments, compiled and wrote the manuscript for publication.

Chapter 2 - describes the governing equation of our models and the rheological description used for material in our models. I also introduce the numerical techniques used to solve the governing equations and elaborate on a number of methods used for comparison of our numerical modelling results to surface observations from global collision zones.

Chapter 3 - Two-dimensional numerical models of the closure of an oceanic basin are used to explore the topography change associated with continental collision and slab break-off. Elastic filtering of topography is used so comparisons can be drawn between numerical models and observation, in this case from, the Arabia-Eurasia continental collision. This chapter is published as [Bottrill, A.D., van Hunen, J. & Allen, M.B. (2012). Insight into collision zone dynamics from topography: numerical modelling results and observations. *Solid Earth*, **3**, 387–399, doi:10.5194/se-3-387-2012]

Chapter 4 - Three-dimensional numerical models of an asynchronous collision are used to investigate the along-strike changes in topography. Results from these models are compared to both the Apennine and Carpathian collision zones. We also use these models and further 2D models to investigate how the topography changes link more precisely to collision dynamics.

Chapter 5 - Two-dimensional numerical models are used to investigate how the physical properties of a subduction / collision system affect its ability to exhume UHP metamorphic material. We investigate crust and lithosphere thickness as well as factors that affect the subduction interface between the plates. These results are compared to P-T data from the Western Gneiss Complex in Norway.

Chapter 6 - Three-dimensional numerical models that simulate either asynchronous or orthogonal continental collision are used to investigate if plate rotation can assist in the eduction UHP metamorphic material. Results for both the spatial distribution and the peak P-T conditions experienced by educted matrial are again compared to the Western Gneiss Complex in Norway. This chapter is published as [Bottrill, A.D., van Hunen, J., Cuthbert, S.J., Brueckner, H.K. & Allen, M.B. (2014). Plate rotation during continental collision and its relationship with the exhumation of uhp metamorphic terranes: Application to the norwegian caledonides. *Geochemistry, Geophysics, Geosystems*, doi:10.1002/2014GC005253]

Chapter 7 - Summarises the results from all chapters and general conclusions are presented alongside some suggestions for future work and directions that this research could continue in.

2

Methodology

2.1 Governing equations

Models of mantle dynamics describe the motion of material by buoyancy-driven flow. The sources of these buoyancy variations can be from thermal and compositional sources and from the phase transitions at depth in the mantle. Subduction and continental collision modelling is a specific application of these general convection models where the plate forms a mobile thermal boundary layer at the surface. The lower temperature of the plates compared to the surrounding mantle makes them denser. However crustal regions have a lower density due to the chemical composition of crustal material. The equation of state for this this set-up is:

$$\Delta\rho(T,C) = \rho_0 \left(\frac{-\Delta\rho_c}{\rho_0} - \alpha(T - T_s) \right) \tag{2.1}$$

Symbols are defined in Table 2.1. The thermal density change arises due to the thermal expansion of material, described by the coefficient α which represents the density decrease with increasing temperature for a given material. This makes the cold plates at the surface denser than mantle material. In this study we also employ compositional buoyancy in continental crustal regions. We use a composition density difference of $\Delta\rho_c = -600kgm^{-3}$ between oceanic and continental regions ($\rho_c = 2700kg.m^{-3}$, $\rho_0 = 3300kgm^{-3}$).

The governing equations for such a convecting system are conservation of mass, momentum, energy and composition. In our models we apply the Boussinesq approximation where we negate these density differences, except in the driving force of the momentum equation and assume that the model is incompressible. The conservation of mass in an incompressible fluid is described by a divergence free velocity field:

$$\nabla.\mathbf{u} = 0 \tag{2.2}$$

The Stokes equation (eq 2.3) describes conservation of momentum:

$$\nabla P - \nabla(\eta\dot{\epsilon}_{ij}) = -\Delta\rho g \tag{2.3}$$

This equation includes terms that represent the deviatoric pressure, viscous drag forces and internal body forces. The Stokes equation is a simplification of the full Navier-Stokes equation where the time dependent inertia terms are dropped. This simplification is justifiable for mantle flow simulations as the Prandtl number (Pr) for mantle convection approaches infinity. The Prandtl number defines the ratio of momentum diffusivity to thermal diffusivity; low Prandtl numbers define thermal diffusion dominated systems, whereas high Prandtl numbers define pure convection systems. This means that in the mantle, momentum diffusivity dominates and so it acts in a convective regime with a thin thermal boundary layer. Dropping of the time dependence also allows us to solve for the steady state case which is numerically more efficient.

The temperature field is described through conservation of energy where heat can be moved through both advection and diffusion:

$$\frac{\partial T}{\partial t} + \mathbf{u} \cdot \nabla T = k\nabla^2 T \tag{2.4}$$

The Boussinesq approximation leads to a number of simplifications in the heat equation, including ignoring viscous and adiabatic heating. The adiabatic gradient of 0.5°C$/km$ [Turcotte & Schubert, 2002] is small and so does not greatly affect the thermal structure of our models of the upper mantle. Viscous heating will have most effect in areas of high strain with its full effect an area of continuing study [Gerya & Stöckhert, 2005]. A further simplification for our model is that radiogenic heating is also ignored in this form of the heat equation. This assumption is acceptable in the mantle where radiogenic heating operates over a much longer time scale than our models.

Composition C is also conserved, and is moved through advection of material (eq 2.5):

$$\frac{\partial C}{\partial t} + \mathbf{u} \cdot \nabla C = 0 \tag{2.5}$$

This set of equations is non-dimensionalised using the following scaling relations, where the primes denote the non-dimensional (scaled) version of the parameters. This scaling of the governing equations allows model properties to be expressed as an intrinsic value of the problem. This scaling of equations offers both a simplification in the equations solved as well as a computational advantage of storing smaller numbers.

$\mathbf{x} = \mathbf{x}^{'}h$ $\quad t = t^{'}\frac{h^2}{\kappa}$ $\quad \mathbf{u} = \mathbf{u}^{'}\frac{\kappa}{h}$ $\quad T = \Delta T(T^{'} + T^{'}{}_0)$ $\quad \eta = \eta_0\eta'$

Substitution and dropping of the primes gives us the following set of non-dimensional equations

$$\nabla \cdot \mathbf{u} = 0 \tag{2.6}$$

$$-\nabla P + \nabla \cdot (\eta(\nabla \mathbf{u} + \nabla \mathbf{u}^T)) + (RaT + RbC)e_z = 0 \tag{2.7}$$

$$\frac{\partial T}{\partial t} + \mathbf{u} \cdot \nabla T = \nabla^2 T \tag{2.8}$$

$$\frac{\partial C}{\partial t} + \mathbf{u} \cdot \nabla C = 0 \tag{2.9}$$

Where the Rayleigh numbers Ra and Rb control the vigour of convection and are defined as follows:

$Ra = \frac{\alpha \rho_0 g \Delta T h^3}{\kappa \eta_0}$ $\quad Rb = \frac{\Delta \rho_c g h^3}{\kappa \eta_0}$

Symbol	**Definition**	**Value and units**
C	Compositional Parameter	[-]
C_P	Heat capacity (constant pressure)	1250 $[J.kg^{-1}.K^{-1}]$
e_z	Vertical unit vector	[-]
g	gravitational acceleration	9.81 $[ms^{-1}]$
h	Model dimension	660 [km]
P	Deviatoric pressure	[Pa]
Ra	Thermal Rayleigh number	4.4×10^6 [-]
Rb	Compositional Rayleigh number	1.7×10^7 [-]
ΔT	Temperature range	$0 - 1350$ [°C]
T	Temperature	[°C]
T_0	Surface temperature	0 [°C]
T_m	Mantle temperature	1350 [°C]
t	time	[s]
$\mathbf{u}$	Velocity	[m/s]
α	Thermal expansivity	3.5×10^{-5} [K^{-1}]
κ	Thermal diffusivity	1×10^{-6} [$\mathrm{m}^2\,\mathrm{s}^{-1}$]
η_0	Reference viscosity	10^{20} [Pa·s]
ρ	Density	$[kgm^{-3}]$

Table 2.1: Symbols and definitions used in the governing equations

2.2 Model setup

The models in this study simulate the closure of a small oceanic basin leading to continental collision and subsequent slab detachment. The initial model setups are shown in Fig. 2.1 for the 2D models and Fig. 2.2 for the 3D models. These models have a continental overriding plate with an oceanic lithosphere subducting under it. Embedded in the oceanic lithosphere is a continental block made up of a thicker continental lithosphere and continental crust. For the 3D models (Fig. 2.2) the overriding plate stretches the full width of the model. The subducting plate is oceanic with a continental block embedded in the centre of it. The subducting oceanic plate increases in age away from the mid-ocean ridge defined to be the left model boundary, using a given spreading rate (3 cm/yr for default models). The initial thermal structure of the oceanic lithosphere is calculated using the half space cooling model and the oceanic plate age [Turcotte & Schubert, 2002] for the default model the oceanic plate entering the trench initially is 60 Myrs old. The thermal structure of the overriding continental region is set as a linear geotherm from 0°C at the surface to mantle temperature, for the default model mantle temperature is reached at 150 km. The continental block embedded in the subducting plate has the same linear geotherm as the overriding plate for the default model (Fig. 2.4). This thermal structure of the tectonic plates in the model does not exactly mimic the expected increase of oceanic plate age away from a continental region. Although for high oceanic plate ages, where there is little increase in lithosphere thickness with increasing age, this approximation is adequate.

The modelling domain is 660 km by 2640 km giving a 1:4 aspect ratio for the 2D models, the 3D models are extended along the third axis by 2640 km giving a 1:4:4 aspect ratio. Grid refinement is applied in the top 200 km and between 1700 km and 2200 km along the x-axis which covers the collision zone (Fig. 2.3). This gives a grid resolution, over the collision zone, of 4 km by 5 km, in the x and z directions, respectively for the 2D models and 10 km by 20 km by 10 km in the x, y and z directions respectively for 3D models. The model uses an Eulerian grid with rectangular elements that are non-deformable.

Flow boundary conditions for the model are free slip on the top and sides with no slip on the base. The no slip boundary condition at the base of the model is designed to simulate the interaction of a slab with the higher viscosity lower mantle below the

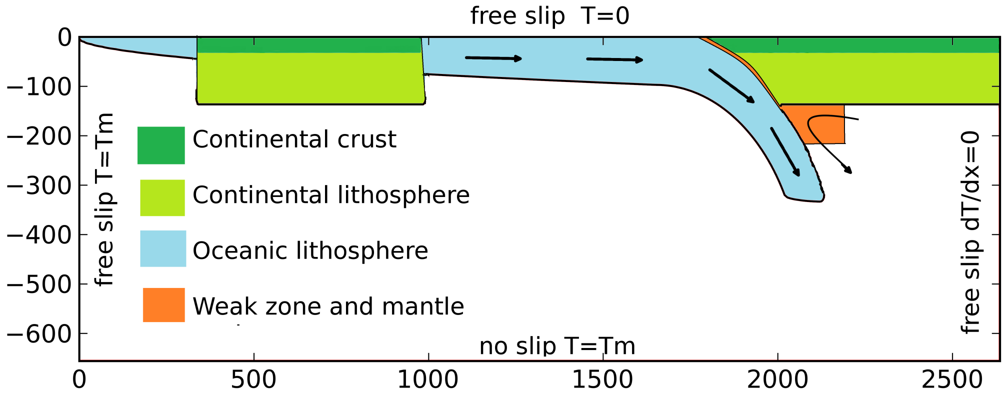

Figure 2.1: Schematic model setup used for 2D models - in this study. The oceanic lithosphere thickness is defined using the half space cooling model; the continental lithosphere has a linear geotherm. Continental regions contain a buoyant crust, whereas, oceanic plates do not contain any crustal material. A weak zone and mantle wedge are used to keep the two plates decoupled.

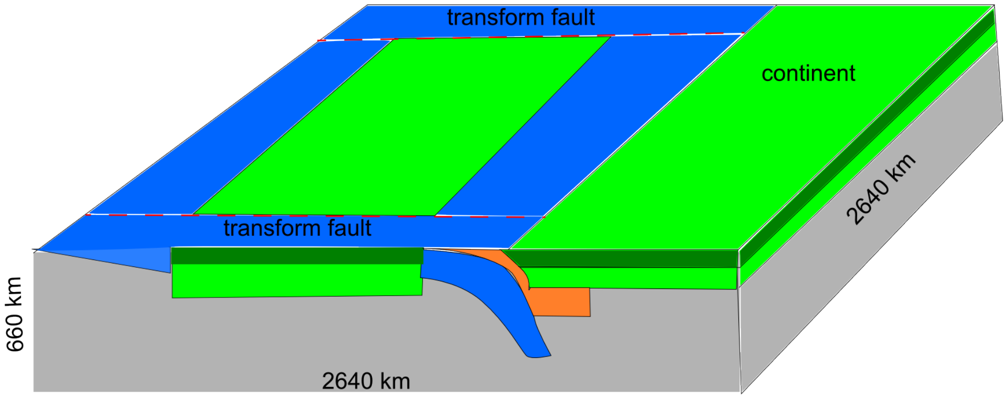

Figure 2.2: Schematic model setup used for 3D models - in this study. This model is similar to the 2D model but has been extended along the y-axis by 2640 km. The subducting plate is decoupled from the overriding plate by a weak zone and mantle wedge that extends the width of the model domain. The subducting plate is decoupled from the model boundaries by two weak zones either side of the model that act as transform faults. This setup is the same as used in [van Hunen & Allen, 2011]

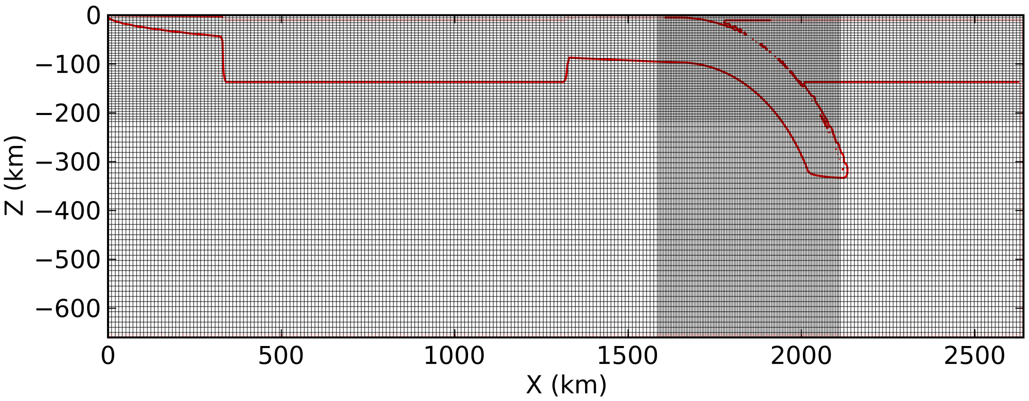

Figure 2.3: Numerical model grid - used for 2D subduction calculations in this study. The red contour shows the 1350 C contour at the start of model run to outline the initial position of the plates. For the 2D models presented here the grid resolution is 4km × 5km in x and z direction, respectively.

proposed phase change at 660 km [Ringwood, 1994]. This no slip boundary is defined such that all points at the base of the model domain have zero horizontal velocity. The free slip boundary is defined such that material at the edge of the modelling domain experiences no friction from the boundary and is free to move parallel to it. At the surface this boundary condition is designed to simulate the lack of friction provided by either air or water to the movement of tectonic plates. At the sides, this boundary condition represents a continuation of the plate in contact with the boundary outside the model domain. The thermal boundary conditions are 0°C at the surface and mantle temperature (1350°C) at the bottom and x = 0 boundary. The other sides of the modelling domain have a zero heat flux boundary condition in both 2D and 3D model setups. A zero heat flux boundary is defined as there being no temperature gradient across the boundary so no inflow or outflow of heat. This boundary condition represents a reflection of the model in the boundary or symmetric boundary condition.

Subduction is initiated by a partially subducted hanging slab (Fig. 2.1 & 2.2). We also include a weak zone of 20 km between the two converging plates that is held at a low viscisity of 10^{20} Pa·s throughout the model calculations. This zone is curved and defined as a section from a circle with a set radius, the default radius used is 528 km which gives an approximate slab dip of 45°. Steeper and shallower subduction dips are investigated such as the range of subduction dips suggested in [Jarrard, 1986;

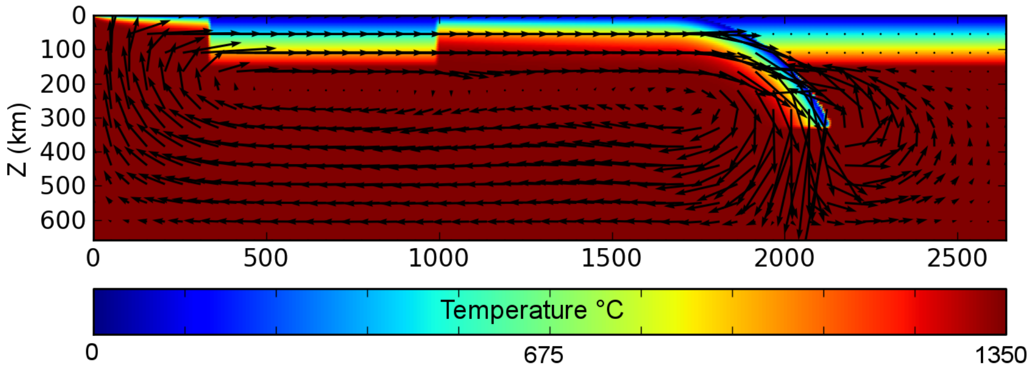

Figure 2.4: The initial thermal setup - used for all 2D models and representative of a slice through the 3D model perpendicular to the y-axis.

Lallemand *et al.*, 2005]. The weak zone is designed to create an interface where large strains are localised between the plates [Barazangi & Isacks, 1976]. The plate interface is thought to be weak partly due to hydration of material as well as the formation of weaker mineral assemblages such as serpentinite [Deschamps *et al.*, 2013] that is found in many subduction settings. We also include a weak mantle wedge that is positioned below the overriding plate's lithosphere (Fig. 2.1 and 2.2) and in our default model is positioned between 130 at 230 km depth. The effect of changing its depth is investigated in Chapter 3 and 5. Such weak mantle wedge is included to simulate the weakening that occurs due to the hydration of the mantle above a subducted slab due to slab dehydration at depth [Hirth & Kohlstedt, 1996; Billen & Gurnis, 2001]. This dehydration is particularly associated with the subduction of oceanic lithosphere due to the high water contents and occurs at depths of 50-250 km. Both the weak zone between the two plates and the weak mantle wedge enable the decoupling between the plates.

In the 3D models, the subducting plate's continental block is placed in the centre of the subducting plate. There are two transform faults that lie on either side of the continental block (Fig. 2.2) that decouple the central portion of the subducting plate from the model boundaries. This consists of a zone 20 km wide that cuts the subducting plates lithosphere perpendicular to the trench. In all 3D and 2D models presented in this work, a low viscosity of 10^{20} Pa·s is used for the strength of the weak zones.

2.2.1 Rheology

The rheology of the mantle is a fundamental control on plate tectonic processes. Most estimates for mantle rheologies come from lab experiments or analysis of post glacial rebound and geoid anomalies [Cathles, 1975; Hager, 1984; Forte & Mitrovica, 1996]. Estimates for the mantle viscosity from post-glacial rebound are 3-4$\times10^{20}$ Pa·s [Lambeck *et al.*, 1998] and from geoid anomalies of 2-6$\times10^{20}$ Pa·s [Ricard & Wuming, 1991]. Strength of material near the surface of earth generally deforms by brittle failure mechanisms [Burov & Watts, 2006], though material in the lower crust is thought to deform in a ductile regime.

The strength of the material in our models is described by temperature and stress dependent rheology. Four different deformation mechanisms are used: diffusion creep, dislocation creep, a stress limiting rheology, and a model maximum viscosity to ensure numerical stability. The effective viscosity is defined as the minimum calculated viscosity from the four deformation mechanisms.

$$\eta_{eff} = min(\eta_{df}, \eta_{ds}, \eta_{sl}, \eta_{mv}) \tag{2.10}$$

The mantle is thought to behave as a non-Newtonian fluid where its strength is both temperature and stress dependent [Karato & Wu, 1993]. This means that in mantle regions diffusion creep and dislocation creep dominate the deformation. Diffusion creep is limited by the diffusion of atoms or vacancies through the rocks grains. This gives a linear stress-strainrate relationship ($n = 1$) and a strong grain size dependence. For dislocation creep, flow is limited by the motion of dislocations through the crystal lattice that makes up the grains. For this mechanism there is no grain size dependence but a strong stress dependence ($n = 3.5$). For both diffusion creep and dislocation creep the viscosity is described by the general solid-state creep process [Karato & Wu, 1993].

$$\eta_{(diff,dis)} = A\dot{\epsilon}^{\frac{1-n}{n}} exp(\frac{E}{nRT_{abs}}) \tag{2.11}$$

Rheological pre-exponents A of 10^{20} Pa$^{-1}s^{-1}$ and 6.5×10^{6} Pa$^{-3.5}s^{-1}$ and rheological power law exponents n of 1 and 3.5 are used for diffusion creep and dislocation creep, respectively [Karato & Wu, 1993; Ranalli, 1995]. For this study a reference mantle viscosity of 10^{20} Pa·s is used, which represents the mantle viscosity in a region that is not deforming.

For the upper lithosphere and crustal portion of the model a brittle rheology is needed. Rocks have limited strength and yield under high-enough stresses, both close to the surface, as described by Byerlee's rule [Byerlee, 1978], and deeper using Peierl's creep [Guyot & Dorn, 1967; Kameyama *et al.*, 1999]. We impose the following stress limiting rheology which approximates both these mechanisms and where the viscosity is defined as follows and symbols defined in Table 2.1.

$$\eta_{sl} = \frac{\tau_y}{2\dot{\epsilon}} \tag{2.12}$$

where the yield stress $\tau_y = min(\tau_0 + \mu p_0, \tau_{\mathrm{max}})$

τ_{max} represents the maximum yield strength for material in the model, which, for all models presented here, has a value of 4×10^8 Pa $\cdot \tau_0 + \mu p_0$ represents Byerlee's law [Byerlee, 1978] and τ_0 is the surface yield strength (cohesion) for which a default value of 1×10^7 Pa is used.

A maximum viscosity is also defined for the models to prevent cold material at the surface of the model becoming unfeasibly strong. For all models in this study a value of 10^{24} Pa·s is used. This gives a viscosity contrast with the average mantle at depth of 4 orders of magnitude. One simplification we make for all models presented in the study is that we use the same rheological description for both mantle and crustal material. This simplification implies that as we deal with a strong-crust endmember, where we don't model a weak lower crust, as suggested in suggested in some studies [Burov & Watts, 2006]. The rheological description used also contains no elasticity, which we compensate for when calculating topography by adding an elastic filter (described below).

Symbol	Definition	Value and units
A	Rheological pre-exponent	10^{20} (df), 6.5×10^{6} (ds) $[Pa^{-n}s^{-1}]$
E^*	Activation energy	360 [kJ/mol]
n	Rheological power law exponent	1 (df), 3.5 (ds)
p_0	Lithostatic pressure	[Pa]
R	Gas constant	8.3 [J/mol]
$\dot{\epsilon}$	Strain rate	$[s^{-1}]$
η	Viscosity	[Pa·s]
μ	Friction coefficient	0.1 [-]
τ_y	Yield stress	[MPa]
τ_0	Surface yield stress	10 [MPa]
τ_{max}	Maximum yield stress	400 [MPa]

Table 2.2: Symbols and definitions used in the rheological description.

2.3 Numerical method

2.3.1 Finite element Method (FEM)

The set of non-dimensional equations is solved using the Cartesian version of the parallel finite element code Citcom [*Moresi and Gurnis*, 1996; *Zhong et al.*, 2000]. The conservation of mass, momentum and energy equations are solved using Eulerian finite element technique. This method employs a fixed grid where velocity and temperature are defined at the nodes of the grid. The grid used in the 2D calculations in this study is shown in Fig. 2.3. Here we can see how the grid is refined over the subduction zone. All 3D model runs and some 2D model runs were done in parallel where computation is split over multiple processors. To achieve this the model domain was decomposed into a number of smaller sub-domains. Each processor then solves the governing equations on their smaller sub-domain. This shortens the time taken to run calculations.

The composition advection equation is solved using the Lagrangian tracer particle method (described fully below). Here, the particles (tracers), initially distributed randomly throughout the model domain and are advected (equation 2.9) in accordance with the calculated velocity field.

The Finite Element Method (FEM) is a method commonly used to solve partial differential equations (PDE). This is done by taking a set of ordinary differential equations that describe the problem and a domain over which to solve the equations. The differential equations are discretized to allow a solution to be approximated at the nodes of the finite element grid.

This discretization allows us to rewrite the conservation of mass (divergence free velocity) and momentum equation (Stokes equation) in a discrete form [Moresi & Solomatov, 1995]

$$Au + Bp = f \tag{2.13}$$

$$B^T u = 0 \tag{2.14}$$

where A is the stiffness matrix; B the discrete gradient operator; f is the vector representing the body forces acting on the fluid; u is the unknown velocity vector; p is the unknown pressure vector. The coefficients A, B and f are obtained using a standard finite element formulation with linear velocity and constant pressure shape function [Hughes, 2012]. Equation 2.13 can be transformed by multiplying by $B^T A^{-1}$ and using equation 2.14 to eliminate the velocity term:

$$B^T A^{-1} Bp = B^T A^{-1} f \tag{2.15}$$

This is a form of the Uzawa algorithm and is solved using an iterative conjugate gradient method. The conjugate gradient method is used, since the matrix A is typically large, ($e \times e \times n$ where e is the number of elements and n is the number of nodes per element e.g. 4 in 2D and 8 in 3D) and which makes equation 2.15 difficult to solve by direct methods. For a typical 2D model run in this study there are approximately 27000 elements in the model domain and a 3D model has approximately 900000 nodes.

A standard Petrov-Galerkin method is used to solve the discretized conservation of energy equation. For the Petrov-Galerkin method, a test function is used to obtain a weak formulation of the function which is then solved using an explicit forward Euler approach.

2.3.2 Tracer Method

Composition properties are advected using a Lagrangian tracer particle method [Di Giuseppe *et al.*, 2008; Schmeling *et al.*, 2008]. This method allows us to solve the conservation of composition equation 2.5, and eliminates problems with numerical diffusion. Initially the tracers are placed randomly throughout the model domain. To ensure all areas have adequate tracer coverage, a large number of tracers are used (> 40 per element). These tracers are advected using the velocity field and a second order Runge-Kutta method. The second order Runge-Kutta method is an adaptation of the midpoint method where a trial step at the midpoint of the interval is used to minimise numerical error. In this particular application of the tracer advection method, the composition function C that we use has values of 1 or 0, where 1 represents purely continental crust material and 0 represents other material. At each time step interpolation is done for all the tracers to each element to determine the bulk composition of each element and node. This composition information is then used to determine the buoyancy of material in the FEM model.

2.4 Surface observables

2.4.1 Topography Calculation

The topography of the earth's surface gives us a useful observable for processes both in the mantle lithosphere and mantle. Many studies have made use of topography measurements over varying wavelengths to infer mantle dynamics [Melosh & Raefsky, 1980; Forte & Mitrovica, 1996]. Topography also has the advantage that sedimentary systems preserve some record of topographic changes over time.

The topography at any point on Earth's surface has three major contributions; the isostatic buoyancy of material, its flexural rigidity and dynamic contributions associated with flow of material in the mantle. Isostasy refers to a column of tectonic plate (crust + lithopshere) being in gravitational equilibrium (floating in the mantle) at a height determined by its thickness and density [Watts, 2001]. Tectonic plates have a flexural rigidity that has the effect of spreading out the effects of a local density anomaly, with the width of the effect being controlled by a plate's elastic thickness [Watts & Burov, 2003]. There can also be dynamic influences on topography where the topography is influenced by movement of material. This movement can be over a range of mantle dynamics scales, from the large-scale flow associated to the proposed African superswell [Lithgow-Bertelloni & Silver, 1998], or to the production of back arc basins [Husson, 2006].

Two different methods are used to calculate the topography produced by the model. Due to the non-deformable grid the simplest method to calculate the model topography is to just convert the normal stress at the surface into an uplift or subsidence. This method does not include any contribution from the elasticity of tectonic plates. The second method applies the normal stress to an elastic beam and then predicts the topography as the deflection of the beam. This method compensates for the elasticity of the lithosphere to produce a more realistic topography prediction. Neither method for calculating topography accounts for the effect of water loading where areas of the model domain would be under an ocean.

2.4.2 Normal stress method

The modelling domain has a fixed boundary at the surface. From the model runs the topography is calculated from the normal stress σ_n at the surface. Equation 17 describes the realtionship between the topography (U) and the normal stresses where symbols are defined in 2.3.

$$U = \frac{\sigma_n}{\rho_0 g} \tag{2.16}$$

Equation 2.16 is derived from the isostasy principle that the buoyancy force experienced by a column of material will be equal to the force exerted by its surface mass m. Here the buoyancy force is assumed to be the normal stress exerted on the top of the box. The height of material (U) required to counteract this buoyancy force is calculated and assumed to be the topography. The calculated topography needs to be calibrated to sea level. This is done by setting mid-ocean ridge depth in the model to $U = -2.7$ km depth, which is the average depth below sea level of the worlds mid-ocean ridges [Stein & Stein, 1992].

2.4.3 Elastic topography

Long term deformation of the lithosphere shows that it deforms (visco-)elastically under applied loads [Watts, 2001]. This elasticity has an effect on the wavelength of topographic features produced by forces applied to the lithosphere. This can be seen from the flexural budges associated with island arc loads [Watts *et al.*, 1980]. To reproduce the increased wave length of topographic features due to elasticity the topography is calculated to include an elastic effect. For this we assume uniform elastic thickness for the whole model and a continuous unbroken elastic beam [Turcotte & Schubert, 2002].

The elastically filtered topography is calculated by solving the elastic beam equation

$$D\frac{d^4w}{dx^4} + \Delta\rho g w = \sigma_n(x) \tag{2.17}$$

for the periodic loading generated by the normal stress exerted at the surface. The parameters used in equation 18 are defined in 2.3. The normal stress is $\sigma(x)$ the loading on the beam.

The flexural parameter D is calculated as

$$D = \frac{Eh^4}{12(1-\nu^2)} \tag{2.18}$$

To solve this equation for the topography (w the deflection of the beam), a finite difference approach is then used to solve this system for the steady state solution. This is done by rewriting the equation in the matrix formation

$$Aw(x) = \sigma_n(x) \tag{2.19}$$

where the matrix A represents the coefficients of w after discretisation.

This equation is then solved for w using a linear algebraic solver. Four boundary conditions are needed to solve this 4^{th} order differential equation. Here we use a fixed topography at both boundaries and that there is no change in topographic gradient $\frac{d^2w}{dx^2} = 0$. At the left edge of the model a depth of -2.7 km is used to represent the average depth of a mid-ocean ridge [Stein & Stein, 1992], at the other boundary the isostatic topography height is used.

This filtering of topography gives us a more realistic response for the model topography by adding back in the expected effect of elasticity that is neglected in our visco-plastic rheology. For our subduction models we use an effective elastic thickness (T_e) of 30 km as a representative value for continental lithosphere. A number of different elastic thicknesses were tested and the results from these test are presented in Appendix 8.2.2

Symbol	Definition	Value and units
D	Flexural rigidity	Equation 2.18
dx	Model Discretisation in x direction	$[m]$
E	Young's modulus	$7 \times 10^{10}[Pa]$
g	Acceleration due to gravity	$9.81[ms^{-2}]$
q_0	Normal stress	2D $[Nm^{-2}]$ 3D $[Nm^{-3}]$
T_e	Elastic thickness	30000 $[m]$
U	Surface topography	$[m]$
w	Deflection of the elastic beam (topography)	$[m]$
ρ	Density contrast between mantle and crust	600 $[kgm^{-3}]$
ν	Poisson's ratio	0.25 $[-]$

Table 2.3: Symbols and definitions used in calculation of topography

2.4.4 Strain rate and tensor

The strain exerted on material at the earth's surface controls the type and pattern of deformation observed. Structures such as slip on faults and deformation fabrics record both the magnitude and direction of the experienced strain. In order to compare model results with surface observation, the code was adapted to allow the output of the information needed to plot the strainrate ellipsoid ($\dot{\epsilon}$) for all points in the model. This is useful as it shows the areas of most deformation in the model as well as giving information on the deformation that occurs in these regions.

To calculate the strainrate ellipsoid in 2D, the first differential of velocity was output from the code at each element. From this the stainrate tensor is:

$$\dot{\epsilon}_{ij} = \begin{pmatrix} \dot{\epsilon}_{xx} & \dot{\epsilon}_{xz} \\ \dot{\epsilon}_{zx} & \dot{\epsilon}_{zz} \end{pmatrix} \tag{2.20}$$

where $\dot{\epsilon}_{xx} = 2\frac{\partial v_x}{\partial x}$, $\quad \dot{\epsilon}_{zz} = 2\frac{\partial v_z}{\partial z}$, $\quad \dot{\epsilon}_{xz} = \frac{\partial v_x}{\partial z} + \frac{\partial v_z}{\partial x}$

The second invariant of the strainrate tensor gives the magnitude of the strain experience in that region of the model and is calculated as:

$$E = (\frac{1}{2}(\dot{\epsilon}_{xx}^2 + \dot{\epsilon}_{xz}^2 + \dot{\epsilon}_{zx}^2 + \dot{\epsilon}_{zz}^2))^{\frac{1}{2}} \tag{2.21}$$

The strainrate is plotted by calculating the maximum axis of extension and compression and the angle that they make with the principal z-axis in the mode. The angle of the axis of greatest extension with the principal z-axis is calculated:

$$\tan 2\theta_s = \frac{\dot{\epsilon}_{zz} - \dot{\epsilon}_{xx}}{2\dot{\epsilon}_{xz}} \tag{2.22}$$

$\theta_s = \theta \pm 45°$

The magnitude of compression and extension are calculated using

$$\dot{\epsilon}_{1,2} = \frac{\dot{\epsilon}_{xx} + \dot{\epsilon}_{zz}}{2} \pm \left(\frac{(\dot{\epsilon}_{xx} + \dot{\epsilon}_{zz})^2}{4} + \dot{\epsilon}_{xz}^2 \right) \tag{2.23}$$

A graphical representation of the strainrate tensor is shown in Fig. 2.5.

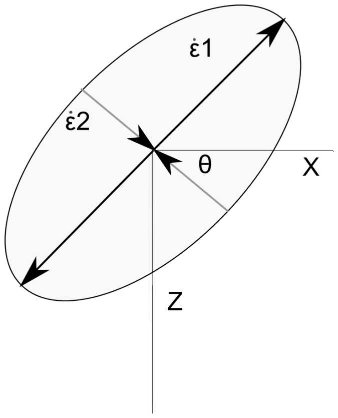

Figure 2.5: Diagram of strainrate tensor - with principal direction and angle marked$\epsilon_1$and ϵ_2 represent the axis of compression and axis of extension

The calculation of strain ellipsoids was tested for a simple Couette flow model (Appendix 8.1) and found to agree with the theoretical expected strain rate tensor.

2.4.5 Pressure-temperature-path calculation

Analysis of the chemical composition of metamorphic rocks allows us to constrain their pressure and temperature history. High and ultra-high pressure rocks are found at a number of collision zones. These rocks are important as they offer an insight into subduction and collision dynamics. In order to compare our models to observations from metamorphic rocks we need to record pressure-temperature histories for crustal material in the model.

The model tracers are used to reconstruct pressure-temperature-time paths for pieces of continental material. For this, a single tracer (called a material marker) is selected and its position reported at every time step. Technically, this was achieved by creating a global list of all tracers so that their position could continue to be reported even when the tracer moved between processors.

Marker temperatures are calculated at each time step by interpolation from the temperature mesh calculated by the model for that time step. We also add a temperature increase of $0.5°\mathrm{C}/km$ [Fowler, 2005] to account for adiabatic heating. The pressure experienced by the tracer is calculated by assuming only lithostatic pressures are present in the model. This allows us to simply convert the depth the tracer achieves to pressure using a lithostatic pressure gradient of approximately 33 MPa/km.

3

Collision zone topography

Insight into collision zone dynamics from topography : numerical modelling results and observations.[1]

Dynamic models of subduction and continental collision are used to predict dynamic topography changes on the overriding plate. The modelling results show a distinct evolution of topography on the overriding plate, during subduction, continental collision and slab break-off. A prominent topographic feature is a temporary (few Myrs) basin on the overriding plate after initial collision. This “collisional dynamic basin” (CDB) is caused by slab steepening, drawing material away from the base of the overriding plate. Also, during this initial collision phase, surface uplift is predicted on the overriding plate between the suture zone and the CDB, due to the subduction of buoyant continental material and its isostatic compensation. After slab detachment, redistribution of stresses and underplating of the overriding plate cause the uplift to spread further into the overriding plate. This topographic evolution fits the stratigraphy found on the overriding plate of the Arabia-Eurasia collision zone in Iran and south east Turkey. The sedimentary record from the overriding plate contains Upper Oligocene-Lower Miocene marine carbonates deposited between terrestrial clastic sedimentary rocks, in units such as the Qom Formation and its lateral equivalents. This stratigraphy shows that during the Late Oligocene–Early Miocene the surface of the overriding plate sank below sea level before rising back above sea level, without major compressional deformation recorded in the same area. Our modelled topography changes fit well with this observed uplift and subsidence.

3.1 Introduction

In this study we aim to look at the evolution through time of topography on the overriding plate at a collision zone. 2-D numerical models of lithosphere-mantle interactions at subduction and continental collision zones are used. These generic modelling results are compared to specific observations from the Arabia-Eurasia collision zone. The study aims to illustrate that topography can be used as an indicator of the dynamics associated with continental collision and slab break-off.

To a first order, the topography of Earth's surface can be explained by isostasy causing regions of variable crustal thickness to equilibrate at different heights. These variation in crustal thickness are caused by a variety of local processes including tectonic thrusting and rifting. However crustal thickness is just one contributor to the Earth's topography and to fully account for topography we need to consider all forces that act on the Earth's surface. The forces that influence topography can be broadly categorised into isostatic forces, from thermal and crustal buoyancy, flexure forces associated with the lithosphere, resistive forces due to crustal / lithospheric strength as well as stresses imposed at the base of lithosphere due to mantle dynamics. Topography driven by flow in the mantle is referred to as dynamic topography [Lithgow-Bertelloni & Silver, 1998]. Many modelling studies have found a change in the dynamics of mantle flow during the transition between subduction, collision, and oceanic slab break-off [Gerya *et al.*, 2004; Andrews & Billen, 2009; Duretz *et al.*, 2011b]. These changes in flow in the mantle would be expected to affect the topography generated due to changes in the stresses at the base of the lithosphere [Faccenda *et al.*, 2009].

Subduction zone topography is characterised by a long linear oceanic trench flanked by an outer rise on the subducting plate side and raised topography on the overriding

---

[1] This chapter is modified from the published manuscript Bottrill, A.D., van Hunen, J. & Allen, M.B. (2012). Insight into collision zone dynamics from topography: numerical modelling results and observations. *Solid Earth*, **3**, 387–399, doi:10.5194/se-3-387-2012. The numerical experiments and production of the manuscript were done by A. D. Bottrill who would like to acknowledge the useful discussions, training, support and geological knowledge provided by his co-authors.

plate [Melosh & Raefsky, 1980; Hager, 1984; Gephart, 1994]. The origin of this topography is the result of the sum of dynamic forces and isostatic forces [Forte *et al.*, 2010; Husson *et al.*, 2012]. Linking of subduction dynamics to topography [Husson, 2006] has shown how features such as the back arc basin depth can be correlated to subduction velocity. Numerical modelling [Husson, 2006] and analogue models [Husson *et al.*, 2012] further show predictions of topography due to mantle dynamics.

Crustal shortening and thickening at collision zones produces topographic signals, via isostasy, in addition to those caused by mantle processes. The transformation of a subduction zone to a fully formed collision zone is thought to be categorised by two important events: initial collision of the continental material and later, break-off of the subducting oceanic slab. Slab break-off has been proposed to occur when the arrival of continental material at the subduction zone slows and eventually stops subduction [Davies & von Blanckenburg, 1995]. This resistance to continued subduction by the buoyant continental crust could then cause a build up of stress where the oceanic material joins the continent. The slowdown of subduction is also thought to allow the subducting slab to heat up, further weakening it. A combination of the build up in stress and thermal weakening is thought to cause the slab to neck and detach. Recent numerical modelling work [Gerya *et al.*, 2004; Andrews & Billen, 2009; van Hunen & Allen, 2011] has shown that both these mechanisms play important roles in the ability of slabs to detach. Estimates for the lag time of break-off after initial collision vary between 5–40 Myrs [Gerya *et al.*, 2004; Andrews & Billen, 2009; van Hunen & Allen, 2011] and have been found to be dependent on the age and associated strength of the subducted lithosphere.

Many studies have produced numerical models of the dynamics of slab break-off [Buiter *et al.*, 2002; De Franco *et al.*, 2008; Faccenda *et al.*, 2009; Andrews & Billen, 2009; van Hunen & Allen, 2011]. Various estimates have been made of the change in topography due to slab break-off, ranging from 1–10 km [Gerya *et al.*, 2004; Andrews & Billen, 2009; Duretz *et al.*, 2011b] of uplift due to the loss of the slab. This large variation in estimates clearly shows the need for further work.

One of the challenges with topography is to separate the contributions to topography from different sources. Collision zones produce elevated topography due to the shortening and thickening of the crust as well as uplift associated with slab break-off, plate flexure and dynamic effects from the mantle. Recent work [Duretz *et al.*, 2011b] has also highlighted that different break-off dynamics would produce different topography changes. Numerical modelling results have also been related to observation for South America [Shephard *et al.*, 2010] showing that the modelled topography changes can be linked to observations. The study by Shephard *et al.* [2010] focuses on the proposed drainage reversal in South America during the opening of the south Atlantic and proposes that the subsidence and uplift patterns required can only be explained by changes in subduction dynamics influencing the topography.

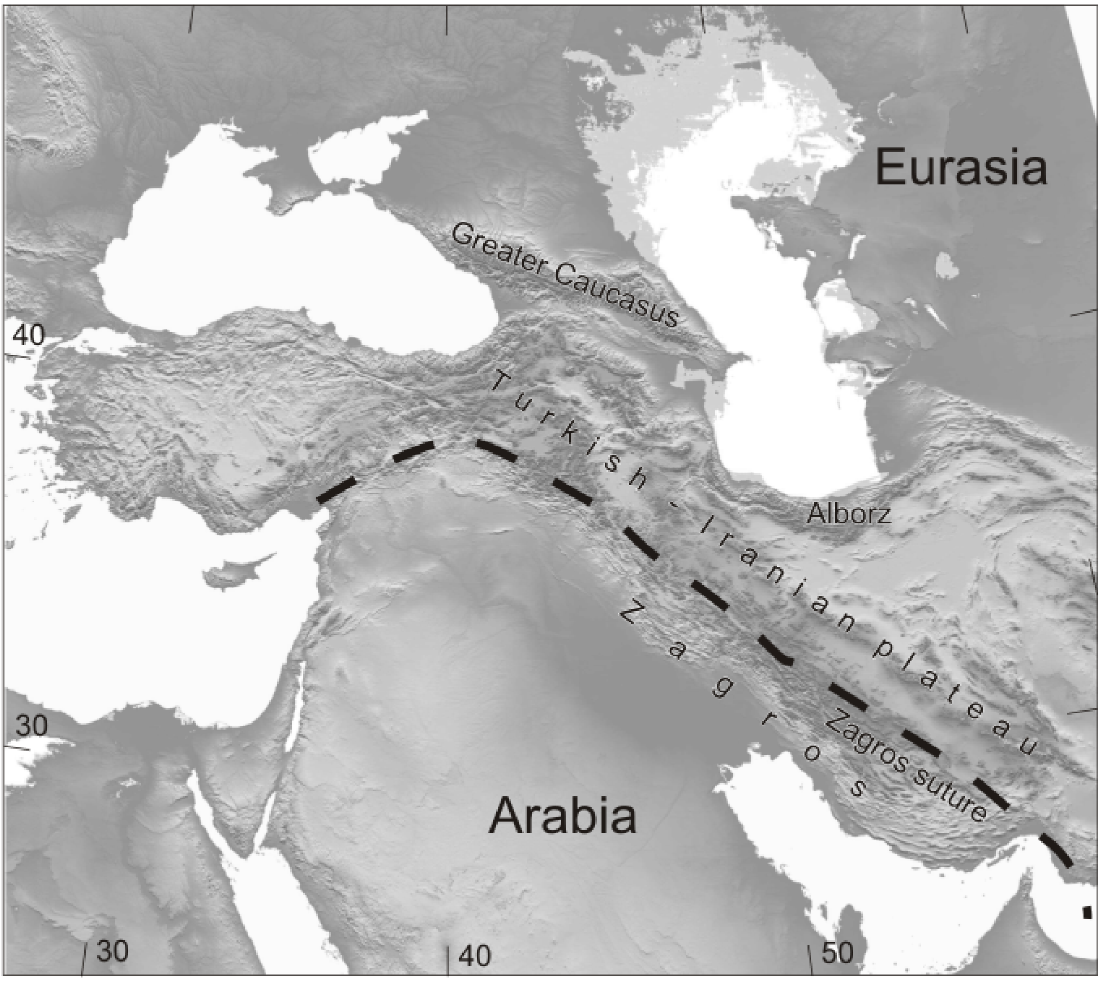

Figure 3.1: Arabia Eurasia collision - Location map of the Arabia-Eurasia collision zone. The dashed line shows the position of the suture between the overriding Eurasian plate in the north and the subducted Arabian plate in the south.

The Arabia-Eurasia collision zone (Fig 3.1) offers an area for the study of topography changes associated with collision and slab break-off [Agard *et al.*, 2011]. Collision occurred here after the closure of the Neo-Tethys ocean basin. Collision is still active in the region with GPS measurements putting the current north–south convergence rate at $\sim 2.5\,\mathrm{cm\,yr^{-1}}$ [Sella *et al.*, 2002]. The time of initial collision is still debated, but estimates vary between $\sim$ 65–5 Ma [Berberian & King, 1981; Philip *et al.*, 1989; McQuarrie *et al.*, 2003; Ghasemi & Talbot, 2006]. A common estimate is late Eocene $\sim$ 35 Ma [Vincent *et al.*, 2007; Allen & Armstrong, 2008; Ballato *et al.*, 2010; Mouthereau *et al.*, 2012; Agard *et al.*, 2005]) based on deformation on both sides of the suture at that time, and a shutdown of arc magmatism. In this study we will use the estimate of 35 Ma for the initial collision in this region.

Local slab break-off has been estimated to have occurred at 10 Ma [Ghasemi & Talbot, 2006; Omrani *et al.*, 2008] for the Arabia-Eurasia collision giving a delay time of $\sim$ 25 Myrs since initial collision. This estimate for the timing of slab break-off comes from observations of collisional magmatism [Omrani *et al.*, 2008] which is used as an indicator of slab break-off. In that study, collisional magmatism is proposed to be produced by slab break-off due to the descent of the slab into the mantle drawing hot material into the mantle wedge region. There is also evidence from mantle tomography that slab break-off has occurred at the Arabia-Eurasia collision zone [Lei & Zhao, 2007], which shows low velocity regions where the slab would be expected. These low velocity regions can be interpreted as areas where the slab is no longer present and has been replaced by hot mantle material. Neo-Tethys opened in the Permian [Şengör *et al.*, 2008] making the subducted oceanic plate entering the subduction zone just before collision approximately 200 Myrs old. This old oceanic crust will have a thick lithosphere and high strength, so slab break-off would be expected to take longer than for young weak slabs. These properties support the case for using the upper estimate for the delay time between collision and break-off, of around 25 Myrs, as shown in numerical modelling studies [Andrews & Billen, 2009; van Hunen & Allen, 2011].

The current and past topography of the Arabia-Eurasia collision zone shows some interesting features that may allow further understanding of the dynamics of the transition from a subduction zone to a collision zone. Much of central Iran, north of the Zagros suture and within the present Turkish-Iranian plateau (Fig 3.1) also has the advantage of being relatively unaffected by compressional deformation for approximately 10–15 million years after initial collision [Ballato *et al.*, 2010; Mouthereau *et al.*, 2012].

Instead, the region underwent marine carbonate-dominated sedimentation, without major fault control [Morley *et al.*, 2009]. This history means that possible dynamic mantle effects on topography are expressed without an overprint of crustal shortening and thickening. This in turn will allow direct comparison of modelled dynamic topography with topography inferred from the sedimentary record in the region.

3.2 Methodology

The numerical modelling is done with a finite element geodynamical code, Citcom [Moresi & Gurnis, 1996; Zhong *et al.*, 2000; van Hunen & Allen, 2011]. Citcom uses a cartesian grid, assumes incompressible flow and makes the Boussinesq approximation. Non-dimensional governing equations are as follows [van Hunen & Allen, 2011]:

$$\nabla \cdot \mathbf{u} = 0 \tag{3.1}$$

$$-\nabla P + \nabla \cdot (\eta(\nabla \mathbf{u} + \nabla \mathbf{u}^T)) + (RaT + RbC)e_z = 0 \tag{3.2}$$

$$\frac{\partial T}{\partial t} + \mathbf{u} \cdot \nabla T = \nabla^2 T \tag{3.3}$$

$$\frac{\partial C}{\partial t} + \mathbf{u} \cdot \nabla C = 0 \tag{3.4}$$

where symbols are defined in Table 3.1 and mantle temperature $T_\mathrm{m} = 1350\,^\circ\mathrm{C}$ (mantle temperature).

The code used solves for conservation of mass, momentum, energy and composition [van Hunen & Allen, 2011], using quadrilateral finite elements with bi-linear velocity and constant pressure.

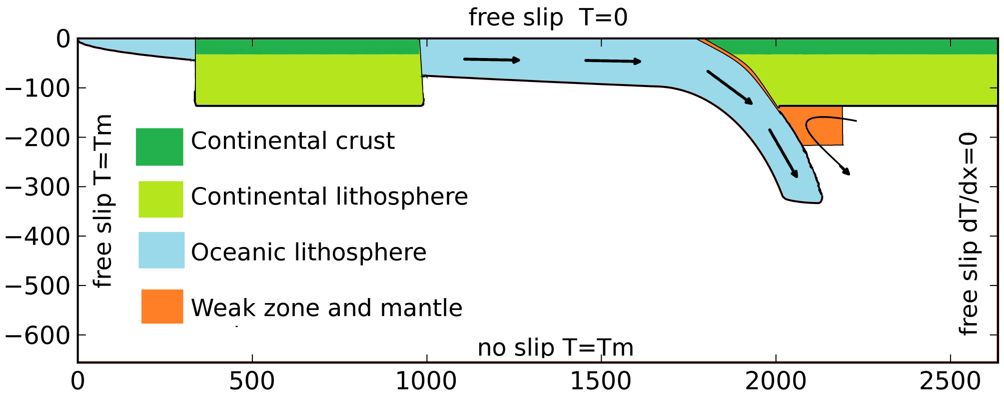

Figure 3.2: Initial model setup - The initial model setup shows the overriding plate made up of continental lithosphere and the subducting plate with a continental block embedded in oceanic lithosphere. Subduction is initiated by a pre-existing oceanic slab in a partially subducted position. Subduction is facilitated by a weak zone that decouples the subducting and overriding plates.

3.2.1 Model setup

The models in this study simulate the closure of a small oceanic basin leading to continental collision and subsequent slab detachment. The initial model setup is shown in Fig. 3.2. The modelling domain is 660 km by 2640 km giving a 1:4 aspect ratio. The grid is refined in the top 200 km and between 1700 km and 2200 km in the horizontal. This gives a grid resolution, over the collision zone, of 4 km by 5 km, in the x and z directions, respectively. Boundary conditions for the model are free slip on the top and sides with no slip on the base. The no-slip boundary condition at the base of the model is designed to simulate the interaction of a slab with a higher viscosity layer such as that proposed for the phase change at 660 km. The thermal boundary conditions are 0 °C at the surface and mantle temperature (1350 °C) at the bottom and left edge. The right edge has a zero heat flux boundary condition. Subduction is initiated by a hanging slab and facilitated by a zone of weak material between the subducting plate and the overriding plate (Fig 3.2; Appendix 8.2.1). This numerical 13.2 km wide weak zone is maintained in the same shape throughout the model run and kept at a constant mantle viscosity (1×10^{20} Pa·s) to allow permanent decoupling of the two plates. The coupling of the two plates in a real subduction zone is likely to change over time. As the coupling evolution during continental collision is not well known, we have chosen to keep the weak zone constant over time. The model also contains a 100 km deep, 200 km wide mantle wedge that is also held constantly at mantle viscosity (1×10^{20} Pa· s), thereby mimicking a weak, hydrated area above the subducting slab. These two features allow decoupling of the subducting and overriding plates without the complexities of slab dehydration and wedge hydration. A weak mid-ocean ridge (MOR) at the left edge of the model serves to decouple the plate from the left boundary to allow the subducting plate to move freely.

The model setup initially has a 60 Myrs old oceanic lithosphere partially subducted under a continental overriding plate with a zero age mid-ocean ridge at the left edge. The initial thermal structure of the oceanic lithosphere is calculated using the half-space cooling model. This plate age is representing generally “old” oceanic lithosphere, since beyond 70 Myrs there is little change in plate thickness and “apparent thermal age” [Ritzwoller *et al.*, 2004; van Hunen *et al.*, 2005]. The subducting plate has a 700 km long 40 km thick continental crustal block embedded in it. The overriding plate also has a 40 km thick continental crust and is fixed to the right edge of the model. The thermal structure of the continental regions is set as a linear geotherm from 0 °C at the surface to mantle temperature at 150 km depth. The age distribution of the oceanic lithosphere surrounding the continental block is linearly increasing with distance from the MOR, and does not reflect any rifting events that might have isolated the continental block. This simplification does not significantly affect the presented modelling results.

Compositional variation (crust versus mantle material) is advected using particle tracers [Di Giuseppe *et al.*, 2008]. The continental crust in the model resists subduction due to its compositional buoyancy. Oceanic crustal buoyancy is ignored in the models, as the transformation of basalt to eclogite occurs at 30–40 km, which would remove most compositional buoyancy [Cloos, 1993], making the buoyancy of the subducted oceanic lithosphere an almost purely thermal effect.

3.2.2 Rheology

The strength of the material in our model is governed by temperature and stress dependent rheology. Four different deformation mechanisms are used (diffusion creep, dislocation creep, a stress limiting rheology, and a model maximum viscosity). For both diffusion creep and dislocation creep the viscosity is described by

$$\eta = A\dot{\varepsilon}^{\frac{n-1}{n}} \exp\left(\frac{E^*}{nRT_{\mathrm{abs}}}\right) \tag{3.5}$$

Rheological pre-exponents of 10^{20} and 6.5×10^6 and rheological power law exponents of 1 and 3.5 are used for diffusion creep and dislocation creep, respectively [Karato & Wu, 1993]. Adiabatic compression is ignored in the Boussinesq approximation which allows simplification of the model by using zero activation volume. Rocks have limited strength and yield under high-enough stresses, both close to the surface, as described by Byerlee's rule [Byerlee, 1978], and deeper using Peierl's creep [Guyot & Dorn, 1967; Kameyama *et al.*, 1999]). We impose the following stress limiting rheology to simulate both these mechanisms

$$\eta = \frac{\tau_y}{\dot{\varepsilon}} \quad \text{where} \quad \tau_y = \min(\tau_0 + \mu p_0, \tau_{\max}) \tag{3.6}$$

The effective viscosity for each element is simply defined as the minimum of the individual viscosity components. The same rheology is assumed for both crustal and mantle material. For a further description of rheology see van Hunen & Allen [2011].

3.2.3 Model Topography calculation

Model topography is calculated with and without an "elastic filter" to illustrate the effect of an elastic strength. The unfiltered topography is purely the subaerial isostatic response from the normal stress (q_0) at the top free-slip surface. For this case (without any elastic strength) the topography is calculated by assuming that the surface is in direct isostatic equilibrium and the normal stresses generated by the model are balanced by a column of crustal material. The height needed for this column at each nodal point in the model gives a first order estimate of the topography.

Although this does give an estimate of the topography due to both dynamic forces and the isostatic buoyancy of the material, it does not account for any elastic properties of the overriding plate. To account for the lateral elastic strength of the lithosphere, the normal stress is filtered using the flexure equation

$$D\frac{d^4w}{dx^4} + \Delta\rho g w = q_0(x) \quad \text{where} \quad D = \frac{ET_e^3}{12\,(1-\nu^2)} \tag{3.7}$$

and symbols are defined in Table 3.1 for an elastic material [Turcotte & Schubert, 2002].

Equation 3.7 is solved using a finite difference technique. The boundary conditions used in this are (1)the left edge of the model is at -2.7 km to simulate the depth of the mid ocean ridge; (2) the right edge is at its expected isostatic height having corrected its height by the same amount required for boundary condition 1; (3) there is no change in topography gradient at either boundary, e.g. the second differential of topography with respect to distance is zero. These boundary conditions mean that we treat the whole model domain as one continuous elastic plate. An effective elastic thickness (*Te*) of 30 km was chosen as representative for the region based on elastic thickness estimates for the whole of Africa and the Middle East [Pérez-Gussinyé *et al.*, 2009]. We have also produced model results with 20 km, 40 km and 50 km elastic thicknesses (Appendix 8.2.2). Results for the pre-collisional back-arc basin depth are comparable to those produced by He [2012] for a visco-elastic numerical model of the mantle wedge and overriding plate. Instead of assuming two decoupled plates, we have chosen to use one elastic plate for the whole model: the topography of interest postdates initial collision, such that the two collided plates are assumed to behave mechanically as one. Although this is not likely to offer the best solution during on-going subduction, the coupling between the two plates will be complex and vary over time. Therefore, we choose to not add extra complexity to the model by trying to estimate the change in plate coupling over time.

This secondary calculation of elastic deformation offers an alternative to the use of a model with fully free surface and viscoelastic rheology. Models with a full free surface are computationally expensive [Schmeling *et al.*, 2008] though do simulate true elastic deformation. Although the elasticity in our models has to be calculated as a secondary process we would argue that we still resolve the important topographic features.

Symbol	Definition	Value and units
Non-dimensional Stokes equations Parameters		
T	Temperature	[°C]
$\mathbf{u}$	Velocity	$[\mathrm{m\,s^{-1}}]$
R_a	Thermal Rayleigh number	$4.4 \ \times 10^{6}$
R_b	Compositional Rayleigh number	$1.7 \ \times 10^{7}$
P	Deviatoric pressure	[Pa]
$\hat{e_z}$	Vertical unit vector	[–]
t	Time	[s]
C	Composition	[–]
T_{m}	Mantle temperature	1350 [°C]
C_P	Heat Capacity (constant pressure)	$1250\ [\mathrm{Jkg^{-1}\,K^{-1}}]$
α	Thermal expansivity	$3.5 \times 10^{-5}\ [\mathrm{K^{-1}}]$
κ	Thermal diffusivity	$1 \times 10^{-6}\ [\mathrm{m^2\,s^{-1}}]$
Rheological Parameters		
A	Rheological pre-exponent	10^{20} (df), 6.5×10^{6} (ds) $[\mathrm{Pa}^{-n}\,\mathrm{s}^{-1}]$
E^{*}	Activation energy	$360\ [\mathrm{kJ\,mol^{-1}}]$
n	Rheological power law exponent	1 (df), 3.5 (ds)
p_0	Lithostatic Pressure	[Pa]
R	Gas constant	$8.3\ [\mathrm{J\,mol^{-1}}]$
$\dot{\varepsilon}$	Strain rate	$[\mathrm{s^{-1}}]$
η	Viscosity	[Pa·s]
η_0	Reference Viscosity	10^{20} [Pa·s]
μ	Friction coefficient	0.1
τ_y	Yield stress	[MPa]
τ_0	Surface Yield stress	10 [MPa]
τ_{max}	Maximum Yield stress	400 [MPa]
Elastic equations Parameters		
E	Young's modulus	7×10^{10} [Pa]
D	Flexural rigidity	$[\mathrm{Pa{\cdot}m^3}]$
T_{e}	Elastic thickness	30 000 [m]
ν	Poisson's ratio	0.25 [–]
w	Deflection of the elastic beam (topography)	[m]
q_0	Normal stress	[Pa]
$\Delta\rho$	Density contrast between mantle and crust	$600\ [\mathrm{kg\,m^{-3}}]$
dx	Model Discretisation in x-direction	[m]
g	Acceleration due to gravity	$9.81\ [\mathrm{ms^{-2}}]$

Table 3.1: Notation and symbol definitions.

3.3 Results

This section describes how model dynamics are reflected in the surface topography and how these topographic features evolve over time.

As subduction slows down after the onset of collision [Molnar & Stock, 2009], the subducted slab steepens before finally slab break-off occurs. Fig. 3.3 shows four stages of the collision process, the resulting viscosity profile and the topographic expression. The two continental regions in the model are associated with relatively high elevation (Fig.3.3A), created by the buoyancy of the continental blocks. The movement of the continental block imbedded in the subducting plate can be tracked in the three further time slices in Fig. 3.3 from the position of crustal material. Other prominent topography features are the subduction trench and fore arc bulge, at 1700 km and 1600 km, respectively, from the mid ocean ridge at left edge of the model.

The features that are of particular of interest here are those that are on the overriding plate. This is because this area, in a collision setting, is most likely to preserve evidence of topography changes. The other reason to focus on the overriding plate is that convection in the mantle wedge is proposed to be responsible for dynamic topography. The results for this region of the model show a depression on the overriding plate at 300 km from the trench both before and after initial continental collision, but not after break-off. Before collision this feature is dynamically produced by flow in the mantle wedge [Husson, 2006]. This feature is purely dynamic since the model contains no mechanism for slab roll-back and associated spreading and thinning of the overriding crust. At 7 Myrs (Fig. 3.3B), this collisional dynamic basin (CDB) has deepened during the start of collision. At 10 Myrs (Fig 3.3C) it has become shallower again, until it has almost disappeared by the time slab break-off occurs at 17 Myrs (Fig 3.3D). The viscosity plots also show evidence of the basin in the weakening of the overriding plate at the position of this dynamic basin. This weakening is due to the stress imposed on the plate, caused by mantle wedge material being drawn away from the base of the plate. This stress causes weakening due to the stress and temperature dependent rheology.

Post-collisional uplift also occurs on the overriding plate between the trench and CDB. At 7 Myrs and 10 Myrs, this uplift is restricted to the region close to the trench where subduction of buoyant continental material is taking place. The uplift predicted

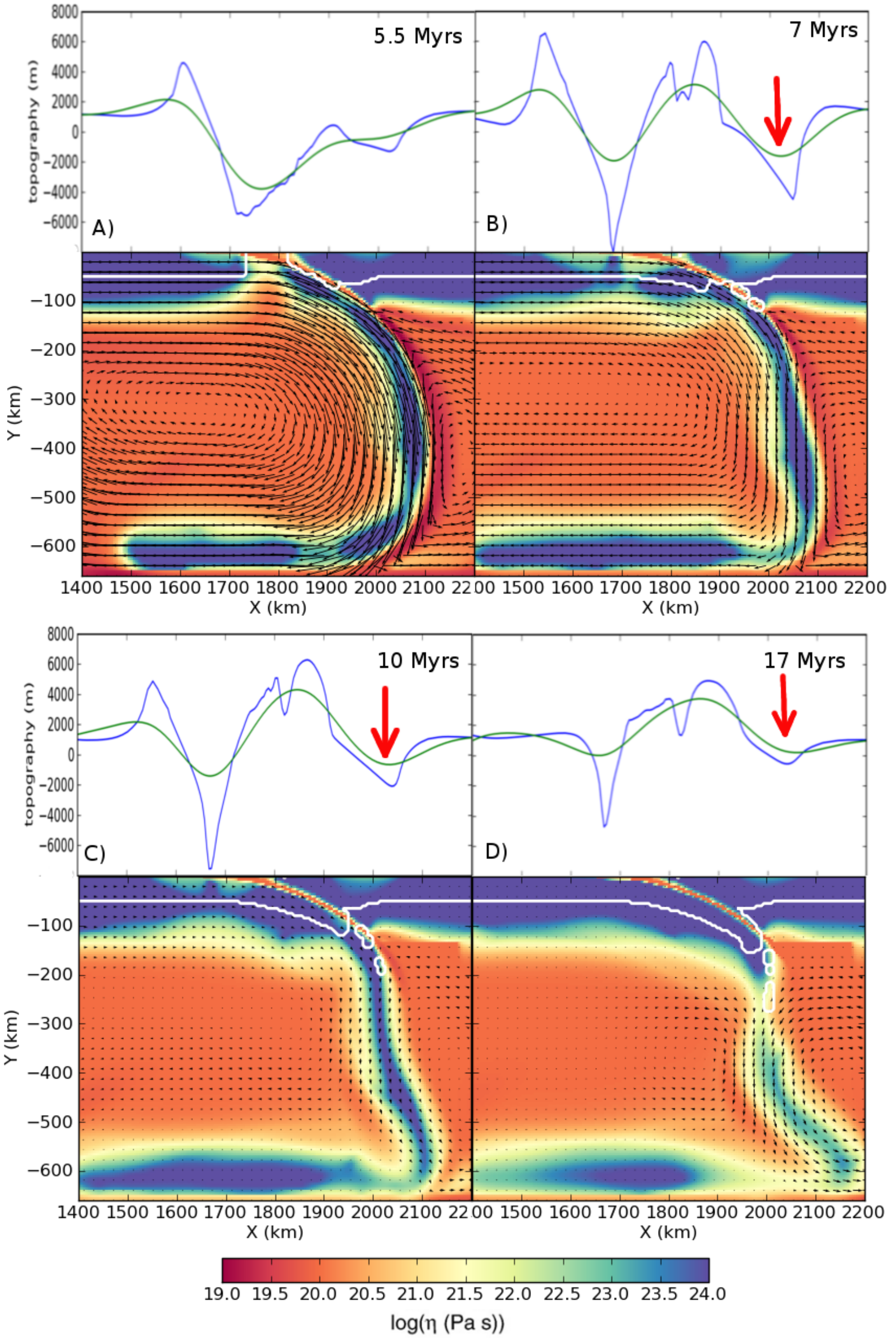

Figure 3.3: Evolution of Collision - Evolution of the continental collision process **(A)** before collision **(B)** at initial collision **(C)** during ongoing collision and **(D)** during slab break-off. Colour plots show the viscosity structure of the slab; white contour indicates the position of crustal material in the model, and arrows in the plot show the velocity field. Thick red arrows mark the position of the collisional dynamic basin (CDB). Line plots show topography generated by the model: blue shows the results without elastic effects, and green shows the effect of an elastically strong lithosphere with an effective elastic thickness (T_e) 30 km.

in this area should be considered a maximum, since we do not model any imbrication mechanisms. This means that initially large quantities of buoyant continental material are subducted, whereas we might expect some of this material to be removed during the subduction process. This uplift also coincides with the expected position of the arc (from the subduction angle) at 100 km behind the trench and 200 km in front of the CDB.

After slab break-off at 17 Myrs the uplift moves further into the overriding plate. This pattern of topography change is further displayed in Fig. 3.4 by a topography-time map. This topography presented is elastically filtered with an effective elastic thickness (T_e) of 30 km. This filtered topography is the same as that shown in green in Fig. 3.3. The elastic filter has the effect of removing a lot of the short wavelength variation in these topographic features, and reduces the overall amplitude of the signal. Topography time plots are useful as they show which topographic features are persistent for a significant time. They also allow easy linking of the dynamics of the model to topographic changes.

Fig. 3.4A contains three highlighted areas of particular interest and also shows the subduction velocity over time. The subduction velocity during this initial onset of subduction varies over a large range. This is caused by the initial large slab pull and lack of interaction with the 660 km discontinuity [Quinquis *et al.*, 2011]. This initial high velocity should not affect the results, as subduction has slowed to a more geologically realistic rate by the time collision occurs. Region 1 shows a basin on the overriding plate, approximately 300 km back from the trench, that is present between initial collision and break-off. We will refer to this post collisional basin as a collisional mantle dynamic basin (CDB). This region is due to slab steepening as it does not correlate with subduction velocity, unlike the back arc basin feature (below Region 1 Fig. 3.4A) in the same position during on-going subduction (Fig. 3.4A and D).

The effect of slab steepening can be more clearly observed by comparison between Fig.3.3 panels A (5.5 Myrs), B (7 Myrs) and C (10 Myrs). These show how the slab, defined by the region of high viscosity, steepens during collision. The topography profiles for these time slices show an increase in depth of the CDB. The steepening slab causes a deepening of the basin because it draws material away from the overriding plate causing the surface to sink. This hypothesis is further supported by the velocity fields for the three time slices in Fig. 3.3. At 7 Myrs the velocity field under the

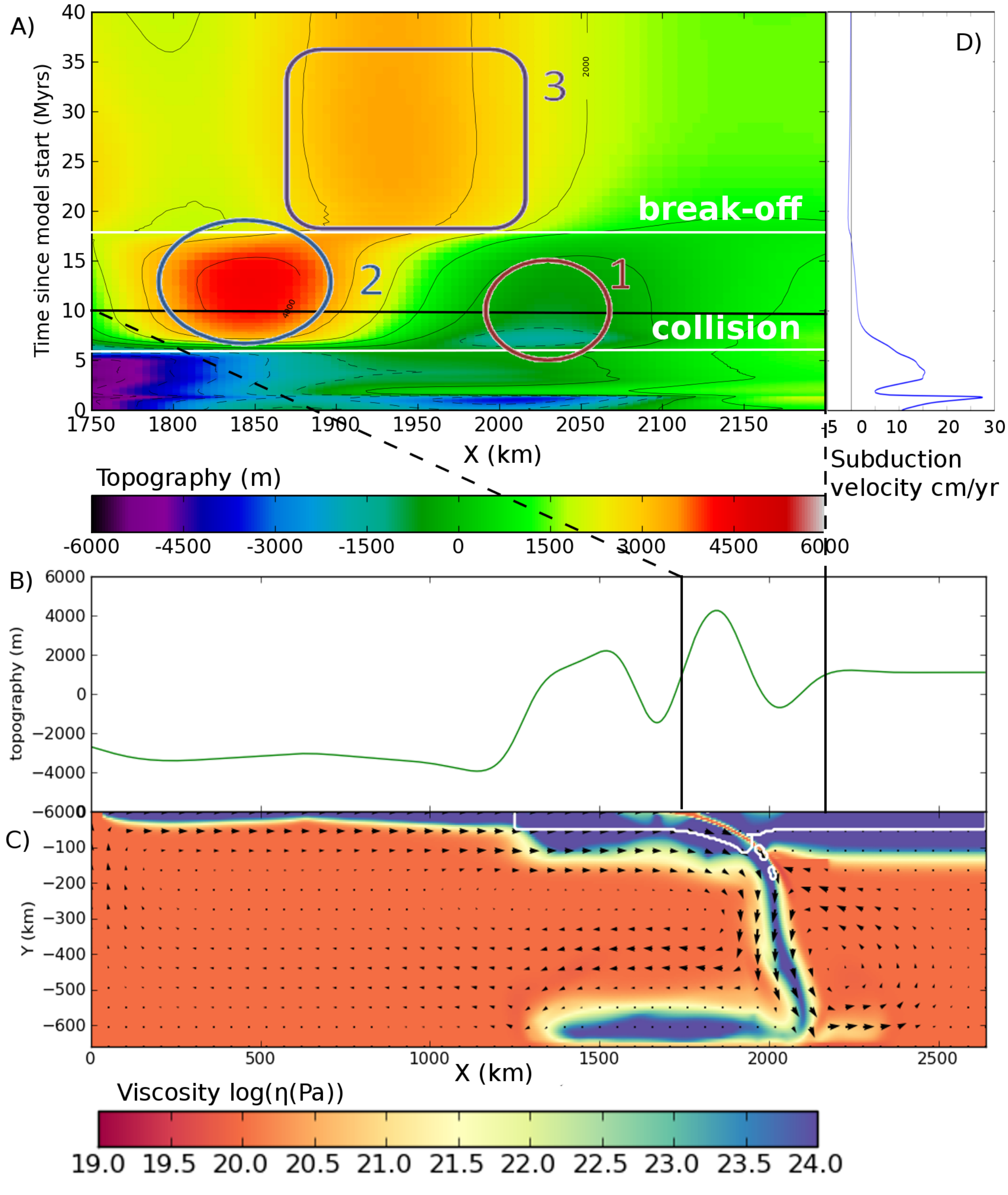

Figure 3.4: Topography time map - **(A)** Topography time map [Faccenda *et al.*, 2009; Duretz *et al.*, 2011b] showing a section of the overriding plate with the trench at the left edge of the figure. The topography shown in colour with time on the Y axis and distance from the MOR on the X axis. Regions 1 & 2 show the post collisional basin and uplift respectively. Region 3 show the broad scale uplift produced after slab break-off. **(B)** The topography at 10 Myrs during the collisional stage **(C)** The corresponding viscosity distribution in the model. **(D)** The subduction velocity throughout model time.

CDB region has steepened to almost vertical position compared to the velocity field for on-going subduction at 5.5 Myrs. At 10 Myrs the velocity field is also vertical but reduced in magnitude. This reduction in magnitude of the velocity field between 7 Myrs and 10 Myrs explains the reduction in size of the CDB. The combined effect of slab steepening over time is shown in Fig. 3.4A area 1.

Region 2 in Fig. 3.4A marks the initial uplift after collision. This is due to the partial subduction of the continental block in the subducting plate. This creates a region with double continental buoyancy and hence of large uplift. Fig. 3.3 shows the continental material (white contour line) in the subducting plate thrust under the continental material on the overriding plate. This partial subduction of continental material creates areas close to the trench on the overriding plate with crustal thickness of up to 80 km. This large crustal thickness creates uplift of 3 km after elastic filtering which is potentially unrealistically high. This should be treated as a maximum uplift value due to the lack of an imbrication mechanism in the model.

Region 3 in Fig. 3.4A shows migration of the uplift further into the overriding plate after slab break-off. This migration of uplift is also clear from comparison of Fig. 3.3 panel C (10 Myrs) and D (17 Myrs). This change in uplift pattern in the short-term is caused by the redistribution of stress after slab detachment allowing the whole region to uplift. The removal of the slab also allows some continental material to be educted back up the subduction channel as well as being underplated on to the overriding plate. The effect of this on the overriding plate is a slightly increased crustal thickness in the region due to under plating which accounts for the long-term uplift seen.

To test the sensitivity of model results to various subduction model parameters, a number of model calculations with different initial setups were performed. For comparison of these models, the maximum depth of the post collision basin was recorded. Appendix 8.2.1 elaborates how different input parameters affected the collisional dynamic depth of the basin. It was found that neither the wedge width nor viscosity affected the ultimate depth of the post collision basin by a statistically significant amount. The depth of the mantle wedge and the weak zone viscosity were found to have an effect on the basin depth. This is because these start-up parameters affect the coupling between the two plates, which in turn affects the model dynamics. The model was also found to be sensitive to the elastic thickness (T_e) (explored further in Appendix 8.2.2) and surface yield strength. Although several model parameters potentially could affect the topography, the start-up conditions chosen in our preferred model gives geologically reasonable subduction velocities once the slab interacts with the 660 km discontinuity.

We have also tested the model at double the resolution presented here. The result from these models qualitatively show very little difference to the standard model. Quantitatively, the maximum depth of the CDB is positioned 16 km closer to the trench in the high resolution model compared to the standard resolution model. The CDB maximum depth, in the high resolution model, was also found to reduce by 16 % compared to the standard resolution model. This shows that the features identified in this study are numerically robust.

3.4 Discussion

The modelled topography evolution in this study shows a clear pattern of topography change through the processes of subduction, collision and slab break-off. Identification of these topography changes in collision zones on Earth provides insight into continental collision dynamics. A schematic overview diagram of the main features of the topography change is shown in Fig. 3.5.

To illustrate the applicability of the presented model results, we compare them to geological observations from the Arabia-Eurasia collision zone. The Turkish-Iranian plateau is typically 1.5–2 km above sea level at present. To achieve such high topography, isostatic theory suggests the need for a large crustal thickness [Turcotte & Schubert, 2002]. Part of the crustal thickening is caused by thrusting within the crust, but active thrusting seems limited to areas with elevations below 1250 m [Nissen *et al.*, 2010]. Wholesale underthrusting/subduction of the northern side of the Arabian plate beneath Eurasia has been imaged on deep seismic lines Paul *et al.* [2006], which is a plausible mechanism for generating overall crustal thickening, and hence isostatic uplift, in regions with elevation above the limit of seismogenic thrusting. Our modelling highlights the potential contribution to crustal thickening, and hence topography of such underthrusting (Fig. 3.4A). The spatial extent of the plateau in the model output is more localised to the overriding plate compared to the much broader uplift observed in Turkey and Iran (see region 3, Fig. 3.4A). This is because of the complete decoupling between the plates in our models after collision, whereas the coupling in a real

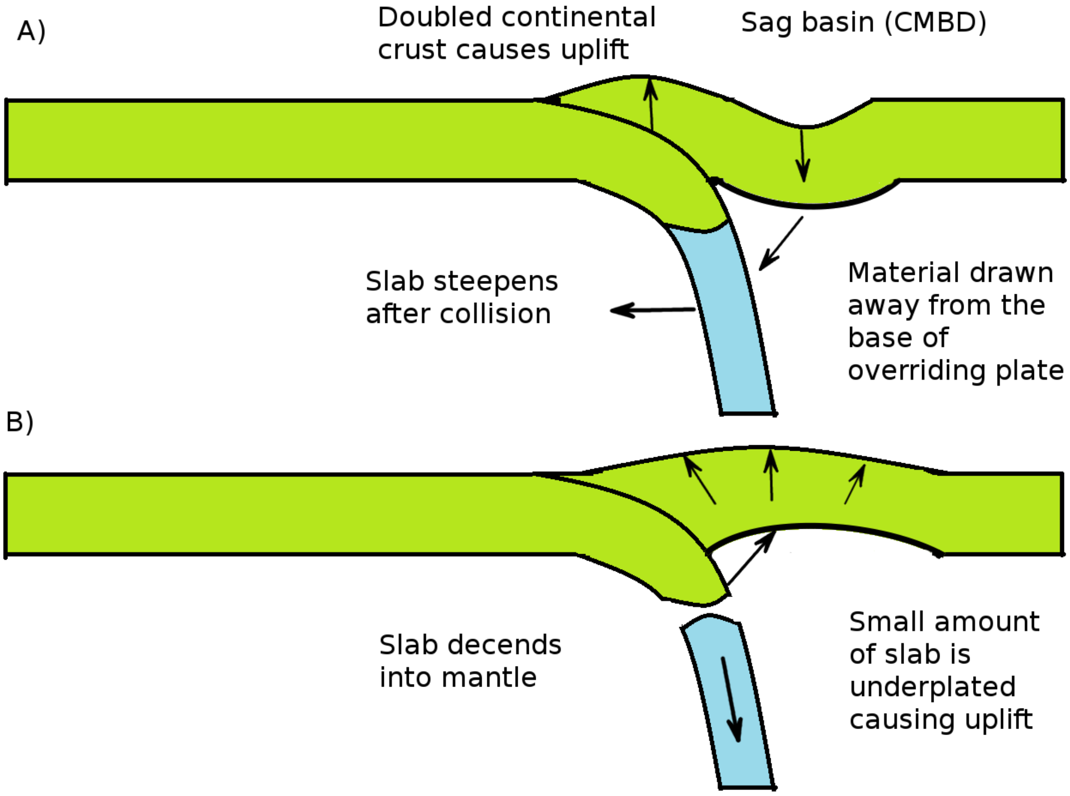

Figure 3.5: Topography evolution cartoon - Schematic diagram showing the topography evolution of the overriding plate from initial collision to slab break-off. **(A)** During initial collision uplift is generated close to the trench by under thrusting of continental material. Simultaneously, on the overriding plate a dynamic depression occurs due to slab steepening inducing flow that draws material away from the base of the overriding plate. **(B)** After slab break-off, the basin is replaced by uplift when the remains of the subducted continental block rise buoyantly under the overriding plate.

subduction zone is likely to change throughout the subduction process. The uplift predicted by the model is larger than the observed uplift in the region because of complete subduction of buoyant crustal material and the lack of imbrication to remove some of this material.

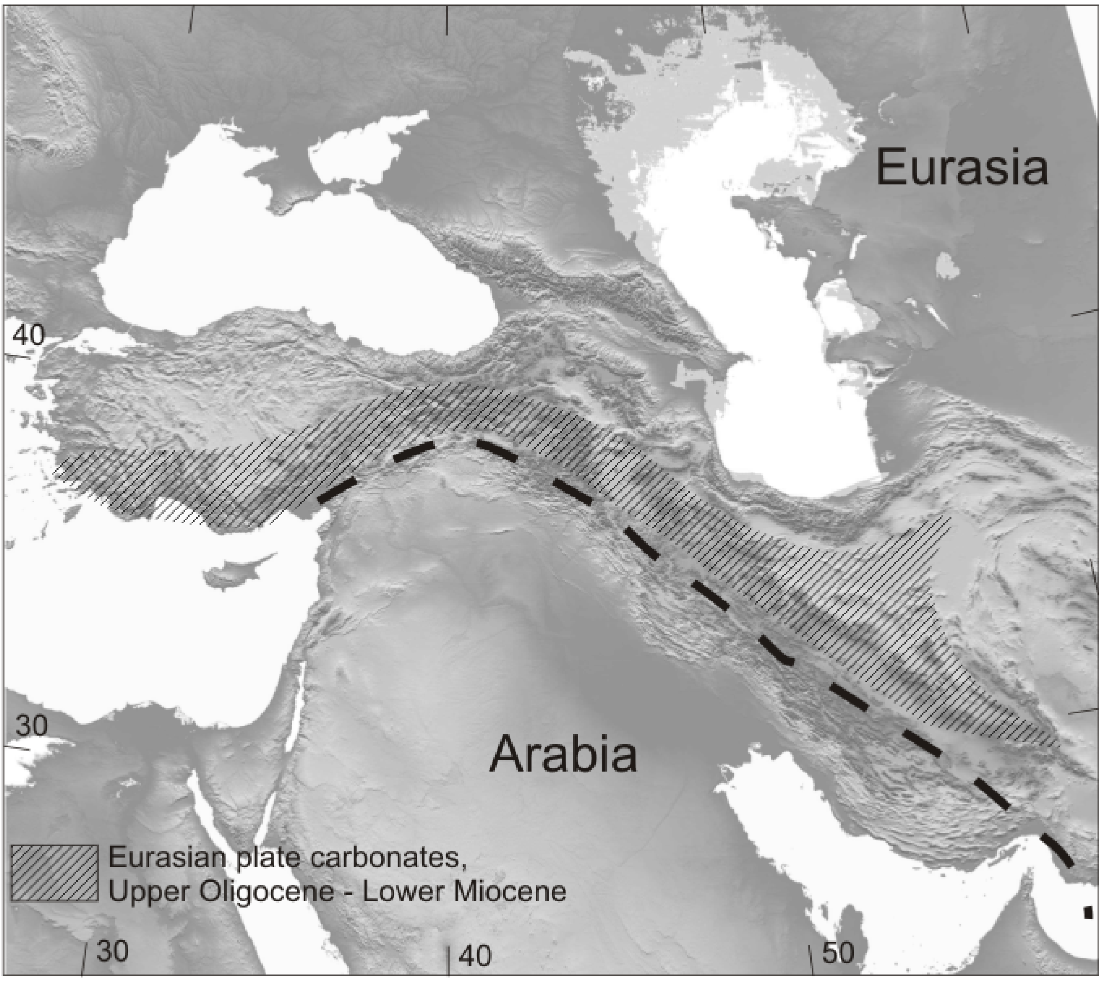

Figure 3.6: Extent of Limestone basin units - The extent of Upper Oligocene – Lower Miocene carbonate strata present on the overriding Eurasian plate in the Arabia-Eurasia collision zone. These carbonate deposits were laid down after initial collision. Compiled from National Iranian Oil Company [1977b,a, 1978]; Şenel [2002]; Reuter *et al.* [2007]; Morley *et al.* [2009].

A second topographic feature of the Arabia-Eurasia collision is related to a sequence of Upper Oligocene-Lower Miocene carbonate sedimentary rocks found on the overriding Eurasian plate, in modern day Iran and southern Turkey (Fig. 3.6, [Reuter *et al.*, 2007]. The unit is known in central Iran as the Qom Formation. The Qom Formation and its equivalents are typically 500–1000 m thick in central Iran [Gansser, 1955; Morley *et al.*, 2009], and lie sandwiched between terrestrial clastic strata of the Lower Red Formation and the Upper Red Formation. This relationship implies that the area on the overriding plate was above sea level during the Early Oligocene, then subsided below sea level during the Late Oligocene – Early Miocene, before returning to above sea level in the late Early Miocene (Burdigalian stage). These carbonate deposits also extend laterally along most of the collision zone, suggesting that they are intimately associated with the collision process. Importantly, the carbonates indicate there was little or no compressional deformation within or adjacent to a large portion in the overriding plate in the collision zone, for up to 15 Myr after initial collision, assuming that initial collision was at 35 Ma.

The carbonate deposits occupy a region 200-300 km from the suture zone and have a trench-perpendicular width of approximately 200–500 km (Fig. 3.6) (Morley et al., 2009). The geometry and timing of the carbonate basin in Iran and Turkey (Fig. 3.6) fits well with the identified collisional dynamic basin from the modelling results (Fig. 3.4A, Region 1). The CDB width in our model is around 300 km (Fig. 3.4), which fits well with the area over which carbonate sediments are found across Iran (Fig. 3.6).

The CDB is present in our modelled results for a period of 10 Myrs between collision and slab break-off. Such a pattern of topographic change fits well with the change in elevation needed to deposit the carbonate sediments that are currently found across Iran and southern Turkey. We therefore propose that slab steepening after collision (Fig. 3.3C) would have caused the subsidence necessary to deposit these carbonates in a CBD.

This pattern of topography change calculated from our models is similar to that produced in Duretz *et al.* [2011b], but the absolute topography range, we produced using the elastic filter, is closer to actual examples of subsidence or elevation observed in collision zones. The models also reproduce well the scale of the dynamic topography modelled and observed at subduction zones: Husson [2006] predicts a dynamic back arc basin of 1.5–2 km during on-going subduction similar to the models in this study before collision when subduction is at a normal rate of around 10 $\mathrm{cm\,yr^{-1}}$.

Another geographic area that offers possibility for observation of topography change produced during continental collision is the Italian Apennines. Here, slab detachment is proposed to have started around 30 Ma and a tear propagated north to south along Italy [Wortel & Spakman, 2000]. van der Meulen *et al.* [1999] observed a period of basin formation followed by uplift using the sedimentary record. Migrating depocentres were interpreted as evidence of a slab tear propagating north to south. Using modern estimates of the position of the suture in Italy, these depocentres seem to be mainly located on the overriding plate with the maximum observed depression around 100 km from the suture [Ascione *et al.*, 2012]. Tentatively, these observed depocentres could have been created by the same slab steepening mechanism discussed here, and be analogous to our modelled CDB. This comparison is complicated by large roll back rates [Carminati *et al.*, 1998; Jolivet *et al.*, 2009] for subduction adjacent to Italy. This roll back would put the overriding plate into extension thinning it and forming basins pre collision. However, dating of sediments from the basins van der Meulen *et al.* [1999] puts the time of deposition after initial collision, around the time of slab break-off, when the overriding plate would be expected to be in compression. This therefore does still fit with our model but could also be explained by delamination proposed for this region [Channell & Mareschai, 1989].

In our models there are a number of assumptions that will affect the modelled topography. One of the main assumptions is that the overriding plate does not shorten or thicken during subduction or collision. Substantial shortening and thickening obviously occur at collision zones, which must influence the overall topography. Our model does not incorporate these features, so our resultant topography does not include these effects. Therefore, although our study might not fully model the expected topography in some regions, it does allow us to understand the contribution of dynamic topography through time. This lack of crustal shortening and consequent crustal thickening is particularly relevant to the subduction of stretched and thinned continental material during the early stages of collision [Ballato *et al.*, 2010].

3.5 Conclusions

Our modelling work emphasises that changes in surface elevation form a useful tool to study the process of continental collision. Dynamic topography is expected in the form of a back-arc basin during ongoing subduction, whose depth is correlated to subduction speed. As collision starts, this basin deepens due to the steepening of the slab. Surface uplift is expected between this basin and the trench, caused by subduction of continental material. After slab detachment, the uplift migrates into the overriding plate, where the basin had previously been.

These modelling results fit well with the sedimentation record and topography on the overriding plate for the Arabia-Eurasia collision zone. Upper Oligocene – Lower Miocene carbonates deposited in between terrestrial clastics show that a basin around 300 km-wide contained a shallow sea during the Upper Oligocene – Early Miocene for a period of around 8 Myr [Reuter *et al.*, 2007]. Present-day high elevation of the region also fits with the expected evolution of uplift after slab break-off on the overriding plate, although there is also a contribution from internal shortening and thickening.

4

Along strike topography

Along strike topography variation and further investigation into topography forming collision dynamics.

Dynamic three-dimensional models of an asymmetric collision, demonstrate the lateral tearing of the subducted slab. The predicted topography change for an asymmetric collision and lateral slab tearing show that the three main overriding plate topographic features, previously described in Chapter 3, propagate along the subduction zone. These topographic features are the initial uplift associated with the subduction of continental material, the collisional dynamic basin (CDB) caused by slab steepening and the broad uplift after slab break-off. The first-order control on the along strike propagation rate of topographic features is the rate at which the collision progresses across the subduction zone. The use of three-dimensional asymmetric collision models allows separation of the collision, the deep slab response to initial collision, and slab break-off components. This result prompts further investigation into the exact mechanism that generates the dynamic elements of the observed topography change. Analysis of the model velocity field and strain rate together with topography illustrates that the onset of collision coupled with steepening in the upper portion of the slab is responsible for the formation of a collisional dynamic basin (CDB). The pattern of topography changes are compared to both the Carpathians and Apennines collision zones, and suggests that the modelled topographic response is a useful observable at collisions that provide, important constraints on collision zone dynamics.

4.1 Introduction

The topography at any point on the earth's surface can be described as a combination of isostasy, the lateral rigidity of tectonic plates [Watts, 2001], and any dynamic forces from the mantle acting on the overriding tectonic plate [Forte *et al.*, 2010]. These different mechanisms are evident in the unique topographic signature of subduction zones [Melosh & Raefsky, 1980; Hager, 1984; Gephart, 1994]. General subduction zone topography comprises a trench, flanked by a fore-arc bulge on the subducting plate side, and by elevated topography on the overriding plate. Further into the overriding plate some subduction systems also have a back-arc basin. These topographic features are potential examples of the different mechanisms of producing topography. The fore-arc bulge is a consequence of the subducting lithosphere stiffness [Nadirov *et al.*, 1997]. The elevated topography on the overriding plate is due to accretion of material (either tectonically or through juvenile magmatism) and back arc basins have been shown to be produced by the dynamic forces associated with trench retreat [Husson, 2006] as well as rifting of the overriding plate. Dynamic topography is the changes in height of the Earth's surface due to forces exerted on the plates by movement of material in the mantle and asthenosphere [Lithgow-Bertelloni & Silver, 1998]. These changes in topography are of particular interest as they offer a potential insight into mantle dynamics.

The topography at a collision zones is usually assumed, to first order, to be dominated by thrusting and crustal thickening. However there are a number of important events in the collision process that each affect the topography. The initial collision of continental material results in both the subduction of continental material and the accretion of material into an orogenic wedge. Slab break-off is proposed to occur once subduction is stopped, allowing the subducted slab to thermally neck and detach [Davies & von Blanckenburg, 1995]. Both these processes will potentially affect the observed topography due to the change in distribution of buoyant material and the forces exerted on the base of the lithosphere. The topography due to slab break-off [Gerya *et al.*, 2004; Andrews & Billen, 2009; Duretz *et al.*, 2011b], has been proposed to offer an insight into break-off dynamics.

Numerical modelling can help to offer an insight into the dynamics of continental collision and subsequent slab detachment as well as the associated topography changes.

Numerical models of slab break-off have shown how the slow down of subduction and detachment of the subducting slab change the flow of material in the asthenosphere under the subduction system [Buiter *et al.*, 2002; Gerya *et al.*, 2004; Duretz *et al.*, 2012; Le Voci *et al.*, 2013]. Further studies have demonstrated how different collisions can generate different deep dynamics [Ghazian & Buiter, 2013]. This change in flow will change the forces exerted on the base of the lithosphere and thereby affect the overriding topography. A small number of studies have looked at the dynamics of slab break-off for a full 3D collision zone [Yoshioka *et al.*, 1995; Burkett & Billen, 2010; van Hunen & Allen, 2011]. These numerical studies demonstrate that it is possible to form a lateral slab tear [van Hunen & Allen, 2011] as proposed by [Wortel & Spakman, 2000].

Along-strike changes in topography have been noted for a number of collision zones around the world. The Apennines are the mountain belt that run along the spine of Italy and formed during the final stages of the Calabrian slab subduction to the west. The Calabrian arc is shown to have rolled back to its present position over the last 35 Myrs [Jolivet & Faccenna, 2000]. The Appenine collision is associated with a series of wedge-top basins (fore-deep) which show an age progression from north to south (Fig. 4.1 [van der Meulen *et al.*, 1998; Ascione *et al.*, 2012]). These basins are attributed to the localisation of slab pull force at the hinge of a slab tear [van der Meulen *et al.*, 1999; Ascione *et al.*, 2012]. The slab under Italy is proposed to be in two sections; the northern slab is shown to be detached in tomographic images [Wortel & Spakman, 2000; Faccenna *et al.*, 2007; Faccenna & Becker, 2010]. The southern section of the slab is thought to be partially detached, but subduction still continues at the Calabrian arc [Faccenna *et al.*, 2011]. The Carpathian-Pannonian system also shows evidence of wedge-top (fore-deep) basins. These basins show a decrease in age clockwise around the subduction system (Fig. 4.1B [Meulenkamp *et al.*, 1996]). This progression is again thought to be the surface manifestation of slab break-off that started in the west and propagated around the collision zone [Wortel & Spakman, 2000].

The use of a three-dimensional (3D) model will allow the inclusion of some processes that are not present in a two-dimensional (2D) models. One of these is the effect on topography of toroidal flow (around-slab flow) [Becker & Faccenna, 2011]. The 3D simulation will also allow us to investigate the topography change with the propagation of a slab tear [van Hunen & Allen, 2011]. Topography observations such as along-strike migrating depressions [van der Meulen *et al.*, 1998] could be simulated with a 3D model.

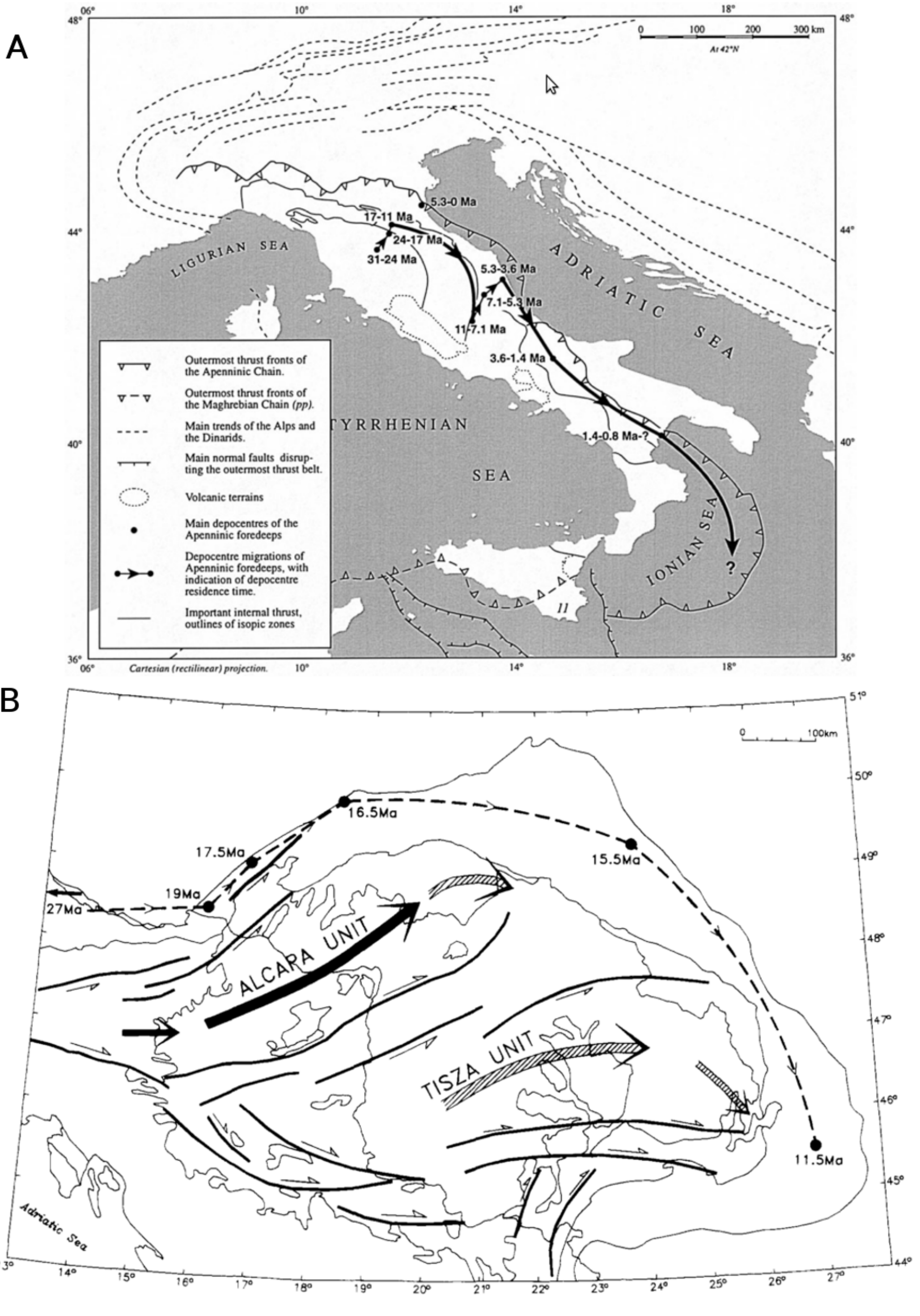

Figure 4.1: Lateral movement of foredeep basins - Summary figures showing progression of foredeep basins along the Apennine collision in Italy [van der Meulen *et al.*, 1998] (top). Progression of foredeep basins around the Carpathian collision system [Meulenkamp *et al.*, 1996] (bottom). Both figures show the age progression of basins along their respective subduction / collision systems.

Understanding the topography produced from propagating slab tear may allow us to further understand areas such as the complex tectonic situation in the Mediterranean [Faccenna & Becker, 2010] or South east Asia [Hayes, 1980; Hall, 2002; Spakman & Hall, 2010].

This study builds on previous studies of topography change at collision zones due to slab break-off [Duretz *et al.*, 2011b; Bottrill *et al.*, 2012] by investigating along strike[Wortel & Spakman, 2000], temporal changes to topography. We use 3D numerical models simulating the closure of an oceanic basin with an asymmetric incoming continental block. We compare both the dynamics and calculated topography with 2-D topography calculations from Chapter 3. We compare results with observed collision zones topography including the Carpathians and Apennines.

4.2 Methodology

We use the finite element code Citcom model described in Chapter 2). The model setup is shown in Fig. 4.2. The 3D model has an aspect ratio of 4:4:1 (in x:y:z direction). The overriding plate is fixed to the left edge of the model, occupies the whole model width in the y-direction and contains a 40 km thick continental crust with a 150-km thick lithosphere.

The central portion of the subducting plate is bounded by two transform faults that serve to decouple the central section of the plate from the oceanic plates either side. The transform faults are 20 km wide and held at the model reference viscosity $eta = 1 \times 10^{20}$ Pa·s. As in the 2D models (Chapter 3), subduction is facilitated by a numerical weak zone between the subducting and overriding plate. We also include a weak mantle wedge under the overriding plate to simulate the presence of a hydrated mantle wedge. Both the weak zone and mantle wedge are kept at the model reference viscosity throughout the model. Subduction is initiated by partial subduction of the front portion of the oceanic plate to provide an initial slab pull force.

The subducting plate includes a continental block, with a 40-km thick continental crust and 150-km thermal thickness of the lithosphere. The front edge of the continental block in the model is at an oblique angle with respect to the collision zone. This creates a diachronous collision where the point of collision propagates through time along the subduction zone. I investigate three different-shaped continental blocks, which create different rates of collision propagation, along the subduction zone. The initial starting conditions for these three models are shown in Fig. 4.3. I refer to these models as I,II and III where the angle between the collision zone and the front edge of the continental block is 6°, 22° and 45° respectively. The laterally propagating 3D collision model has an additional advantage over the previous 2D model in that it separates out the initial collision of the whole continental block from the onset of continental subduction at different points along the subduction zone. This allows further analysis of the timing and collision dynamics that produce the topographic features described in Chapter 3.

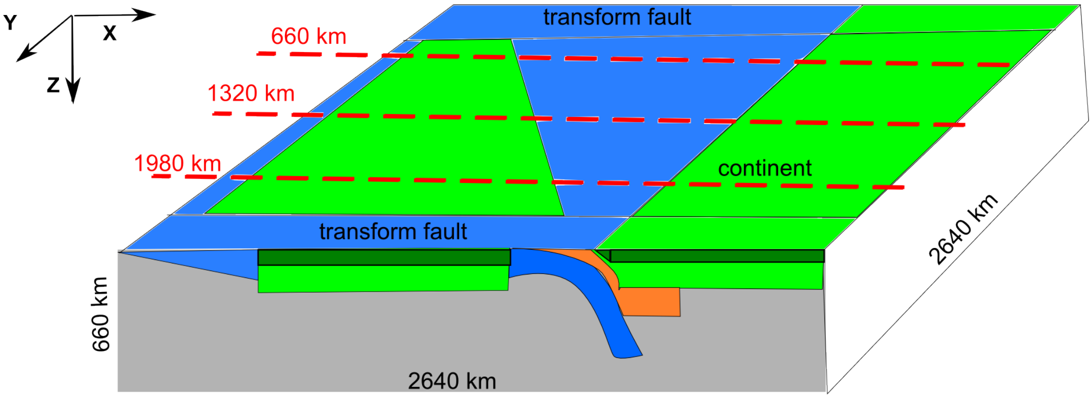

Figure 4.2: 3D model setup - 3D model set-up showing the position of the continental material (green) and oceanic material (blue) as well as the numerical weak zone (orange). The continental lithosphere is represented by light green with the darker green representing continental crustal material (not drawn to scale). Two transform faults bound the subducting plate continental block and facilitate subduction. The red dotted lines show the position of the slices presented in Section 4.3 Fig. 4-7.

The boundary conditions for this 3D model are free slip on all boundaries except the base which is no slip. The thermal boundary conditions are mantle temperature at the base and left side (as drawn in Fig. 4.2), 0°C at the surface and a zero heat flux condition on all other boundaries. The model uses the same temperature and stress-dependent rheology described in Chapter 2 and [van Hunen & Allen, 2011; Bottrill *et al.*, 2012].

The weak zone, between the plates and mantle wedge are as described in Chapter 2. The weak zone is defined by a section of a circle and is 20 km wide (trench perpendicular). In these 3D models the weak zone extends the full width of the model in the y-direction.This ensures that subduction can occur all along the subduction zone.

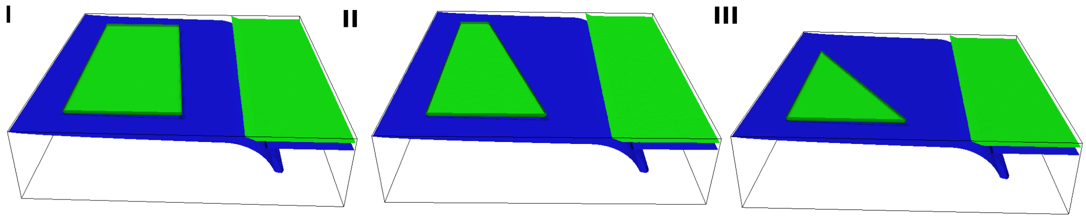

Figure 4.3: Three 3D models investigated - Three initial model setups used each with a continental block that makes a different angle with respect to the subduction zone. Model I makes an angle of 6°, model II makes an angle 22° and model III makes an angle 45° with respect to the subduction zone.

With these models we want to explore the lateral along trench changes in topography produced at subduction-collision zones. Previous work [van Hunen & Allen, 2011] has shown that blocking of a subduction zone at one end produces a lateral tearing of the subducted slab. These models will allow investigation into if this lateral tearing generates a specific topographic response.

To further investigate the mechanism responsible for the production of topographic features on the overriding plate, we examine the 2D model presented in Chapter 3. From this model we present the velocity field for the overriding plate to examine how material moves in response to the subduction and subsequent collision processes. The velocities in the overriding plate are extremely small in comparison to the velocities in other parts of the subduction system. Therefore, to display the velocities for the overriding plate, the velocities in other areas of the model are muted and the vector arrows representing the velocity field are scaled up compared to the regular plots to make them visible. We also present the strain-rate ellipsoid for the overriding plate. This allows us to examine the possible deformation expected in the overriding plate during subduction collision and slab break-off.

4.3 Results

I first present the dynamics of a diachronous collision model II where the incoming continental block is at 22° to the subduction zone. We then compare these results to the models with I and III to investigate the effect of different along-strike collision propagation rates. The collision dynamics of a diachronous collision, are shown as 3D iso-temperature plots (Fig. 4.4) that show the position of all cold lithosphere and crustal material. I also present topography and viscosity plots at three slices through the model perpendicular to the subduction zone (Fig. 4.5).

4.3.1 Along strike propagation of collision topography

Fig. 4.4 shows the dynamics associated with an asymmetric collision. Subduction velocity is trench perpendicular before collision Fig. 4.4A. As the promontory of the continental block first collides, the velocity of the subducting plate develops a rotation component due to decrease in the rate of subduction in the areas of initial collision (Fig. 4.4B & C). Fig. 4.4E shows how the initial tear in the slab forms closer to the side of the model where collision initially occurs. The slab then necks in both directions with the slab being completely detached 25 Myrs after the initial collision of the leading corner of the continental block. The tear propagates across the subducting slab at ∼40 cm/yr. The point of collision, defined as a position along the subduction system where continental material first starts to subduct, progresses across the 1980 km width of the continental block in ∼14 Myrs, giving an along strike speed of ∼14 cm/yr (Fig. 4.7D). The rate at which collision progresses across the subduction zone is determined by the geometry of the subducting plate's continental block and so models I & II have different rates of collision.

Fig. 4.5 shows viscosity cross sections through model II at y= 660 km, y= 1320 km and y=1980 km with the corresponding surface topography without elastic filtering. The panels show how the topography evolution is similar to that observed in Chapter 3. This consists of a fore-arc bulge, subduction trench and back arc basin during the subduction phase. During the collision and continental subduction phase, there is a deepening of the basin on the overriding plate (CDB) situated at ∼300km from the trench and uplift between the basin and trench. After slab detachment there is wide spread uplift on both the overriding and subducting plate because the remains of the subducted continental material rise buoyantly. The three different cross sections show different timings for the production of the described features since collision occurs at different times along the collision zone. This difference in onset timing for topographic features is of interest for two reasons; it shows that topographic features propagate

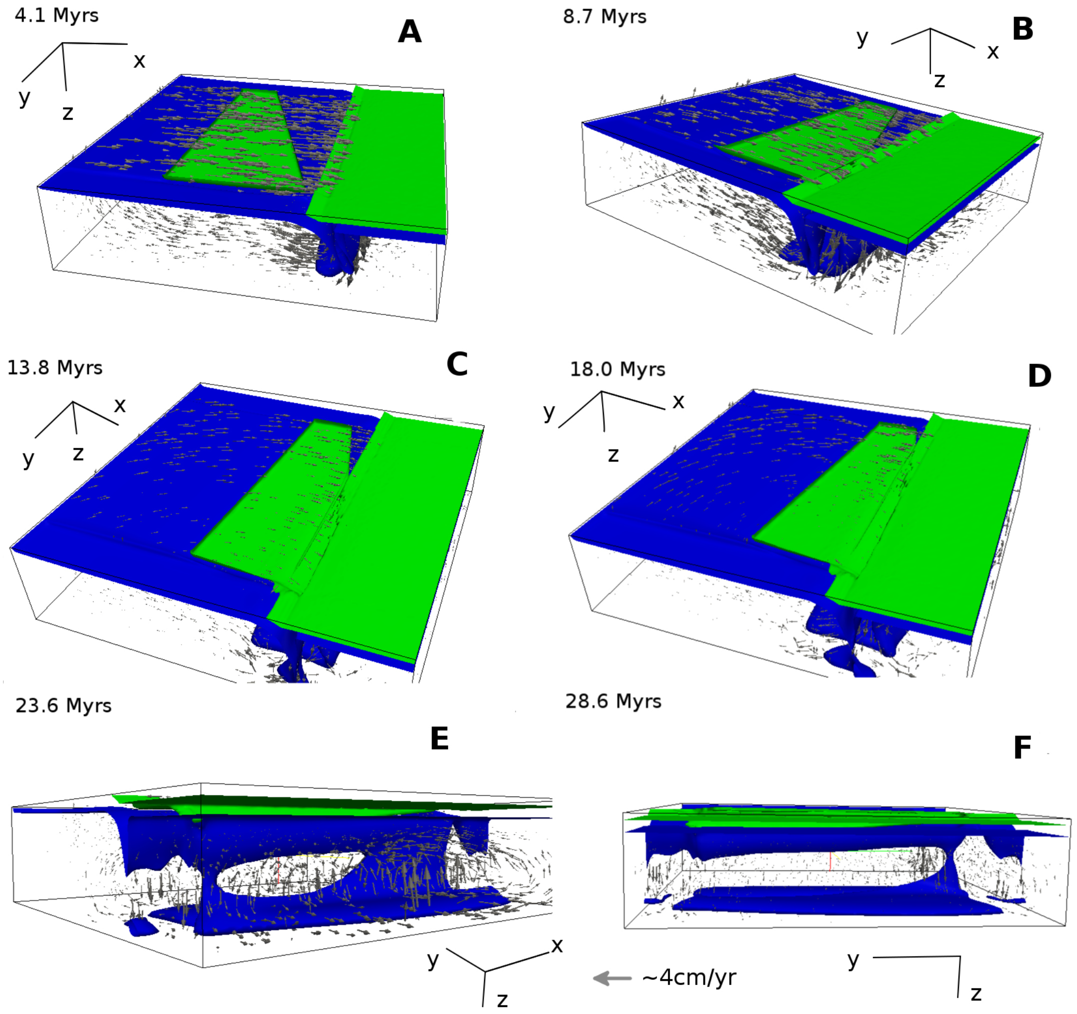

Figure 4.4: Diachronous model dynamics - Model dynamics shown by a blue iso-temperature surface at 1155°C. Green areas show the position of the continental material as defined by the tracers. The velocity field for the model is also shown by the vector arrows. The times shown represents the time since the start of the model. The model is rotated in subsequent slices to show first the collision from above A-D and then the slab break-off E & F. This shows how the subducting plate rotates as it collides B-D and starts to break off in the area of initial collision E.

along the subduction system and it also allows linking of the dynamics at different points along the subduction system to the topography formed. The propagation of topographic features along the subduction zone is also shown in Fig. 4.6.

The slices through the model in Fig. 4.5 show that the deep slab dynamics are controlled by the initial collision of the promontory of the continental block at 7-8 Myrs. This can be seen in Fig. 4.5 at 8.68 & 13.79 Myrs, where the deeper part of the slab has steepened up all across the collision zone when initial collision has occurred. Fig. 4.5 21.45 - 28.56 Myrs show how the uplift on the overriding plate and the deepening of the basin on the overriding plate (CDB) occurs only in each slice when continental subduction is occurring. The wholesale uplift is only present in each slice after slab detachment has occurred.

The three topography-time maps (Fig. 4.6) for the three sections through model II show similar patterns of topographic change along each section. There is a delay in collision time between the section (y = 1980 km) closest to the initial collision and the section that collides last (y = 660 km). These maps also show how the post-collisional uplift is greater for the slice through the area of initial collision due to subduction of greater amounts of continental crust. The section in the centre of the model shows the deepest and longest lived collisional dynamic basin which occurs on the overriding plate 300 km from the trench.

To further investigate the relationship between the collision, the post collisional basin and slab break-off we calculate the trench-parallel location of the deepest part of the basin on the overriding plate along with the lateral position of initial collision and slab break-off (Fig. 4.7D). This illustrates that with the progression of the initial collision along the trench, the basin location shows a similar progression. Fig. 4.7 does show that initial collision at a given location along the subduction zone precedes the basin formation by 2-3 Myrs and that the collision progresses along the trench marginally quicker than the location of the post-collisional basin (CDB). This is due to a slowing of subduction after the initial collision of the continental block promontory. Slab break-off propagates along the collision system rapidly at a rate of 40 cm/yr. The subducted slab starts to neck and tear 12 Myr after initial collision of the leading promontory of the continental block. This plot suggests that the timing and positioning of the overriding plate's post collision basin is directly related to the onset of the subduction of continental material at that point along the subduction zone.

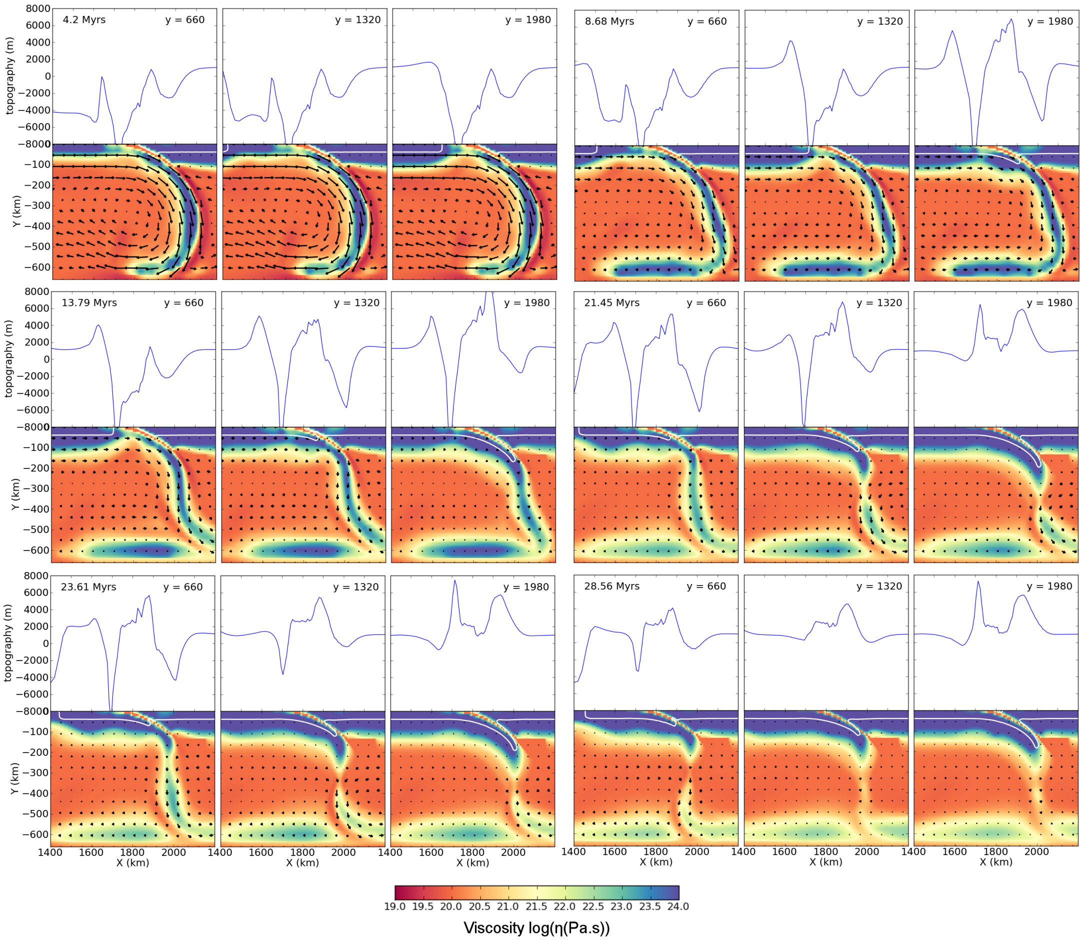

Figure 4.5: Section through diachronous collision - This figure contains 6 panels that represent different times during the subduction and collision process. Each of the panels contain three viscosity and topography (without elastic filtering) plots for the three slices through model II. Slices are at 660 km (left) 1320 km (centre) and 1980 km (right) from the far side of the model. Continental material is shown by white contour, the velocity field is shown by the vector arrows the colour scale shows the viscosity.

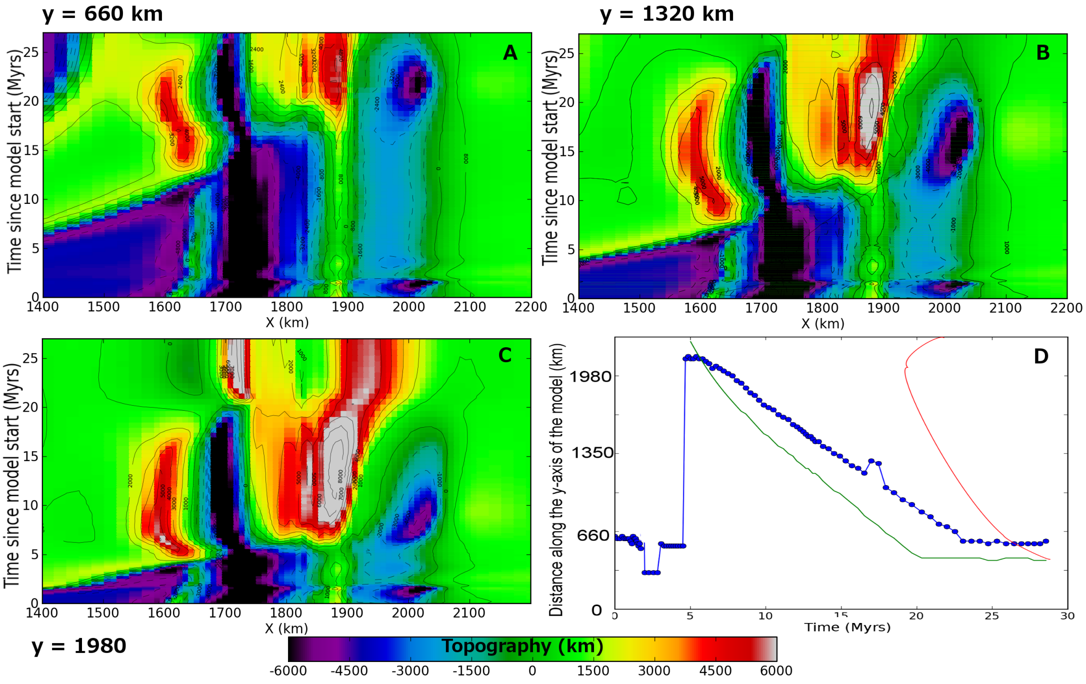

Figure 4.6: Topography time maps model II - A-C) Topography time maps for the 3 section across model II. The x-axis shows the distance along the section with the trench positioned at 1700 km. The y-axis represents the time since the model started. The colour scale shows the topography over the collision zone. D) shows the position over time of collision events along the subduction zone (y-axis). The blue line shows the position of the CDB (collisional dynamic basin), defined as the deepest point on the overriding plate. The green line shows the position of the initial collision defined as the point along the subduction zone where continental crust from the overriding plate is first contacts continental crust from the subducting plate. The red line shows the position of Slab break-off.

For other models with different collision rates we observe a similar pattern of topography production. In the model I, collision occurs almost simultaneously everywhere along the trench due to the small angle between the front of the continental block and subduction zone (Fig. 4.8). This model therefore shows little variation in the timing of the topographic features as well as the magnitude of the topography generated for the 3 slices through the model(Fig. 4.8A-C). This model shows again a lag time between initial collision and the production of overriding plate basin (CDB), with the CDB propagating along the subduction zone marginally slower than the collision. For this model the initial collision progresses across the subduction zone fast at almost $\sim$1 m/yr. The CDB also progresses quickly across central section of the subduction zone but shows slower progression towards the ends of the collision zone. Slab break-off in this model has a 12 Myr delay between in initial collision and break-off like in model II. Break-off also progresses across the subduction rapidly at $\sim$1 m/y a similar rate to initial collision.

Model III shows the slowest propagation of topographic features along the subduction system due to the large angle between the front of the subducting plate's continental block and the subduction zone (Fig. 4.9). This gives a much slower rate for the propagation of initial collision along the subduction zone of 9 cm/yr. The CDB for this model still propagate along the subduction zone but even slower than the initial collision. In contrast slab break-off still progresses rapidly along the subduction zone. The delay time between initial collision and break-off is also larger at 17 Myrs. This longer delay time can be attributed to the continuation of rapid subduction further along the subduction system that prevents the slab from remaining stationary and heating up to break-off.

All three diachronous collision models demonstrate that the rate at which the initial continental collision propagates along the subduction zone is directly related to the rate at which the CDB on the overriding plate propagates along the subduction zone. In contrast slab break-off propagates along the subduction zone much more rapidly for all three collision models. These observation of propagation rate of various collision features and the observation that the initial collision, of the of the continental block's leading promontory, cause the deeper part of the slab, to steepen up all along the subduction system. We can conclude that the CDB (overriding plate basin) is created due

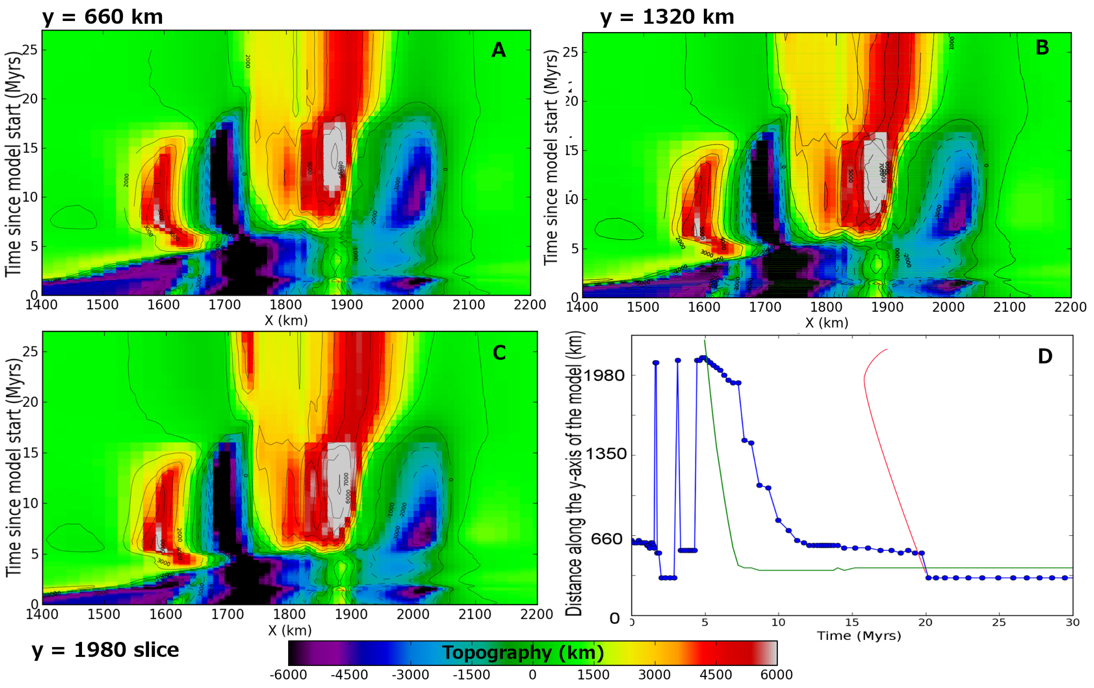

Figure 4.7: Topography time maps model I - A-C) Topography time maps for the 3 section across model II. The x-axis shows the distance along the section with the trench positioned at 1700 km. The y-axis represents the time since the model started. The colour scale shows the topography over the collision zone. D) shows the position over time of collision events along the subduction zone (y-axis). The blue line shows the position of the CDB (collisional dynamic basin), defined as the deepest point on the overriding plate. The green line shows the position of the initial collision defined as the point along the subduction zone where continental crust from the overriding plate is first contacts continental crust from the subducting plate. The red line shows the position of Slab break-off.

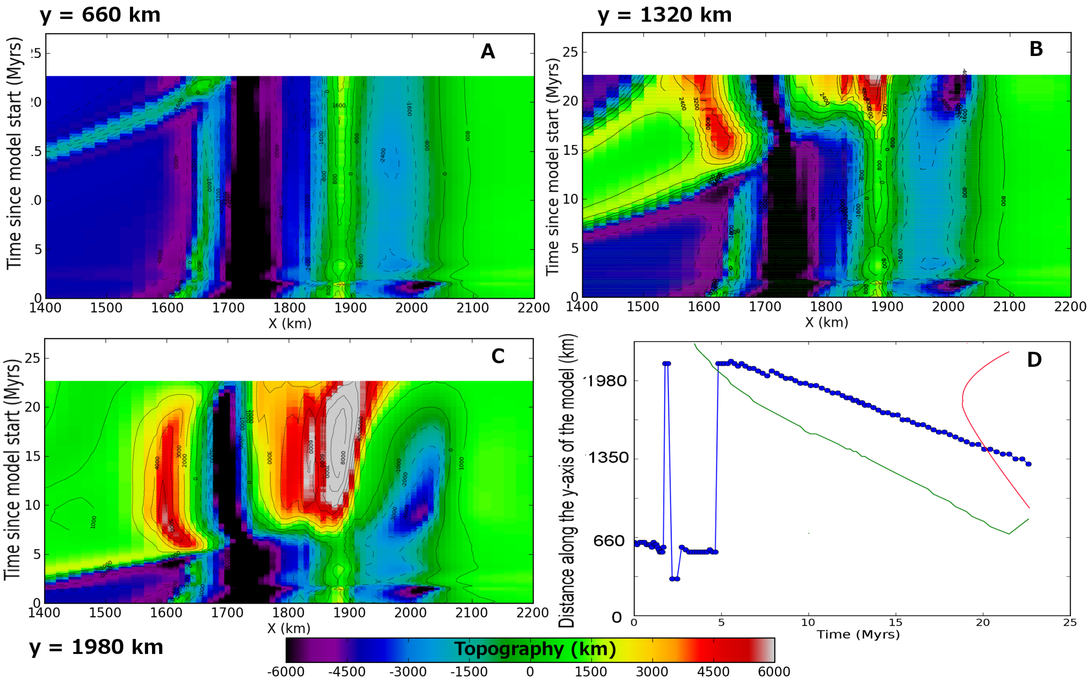

Figure 4.8: Topography time maps model III - A-C) Topography time maps for the 3 section across model II. The x-axis show the distance along the section with the trench positioned at 1700 km. The y-axis represents the time since the model started. The colour scale shows the topography over the collision zone. D) shows the position over time of collision events along the subduction zone (y-axis). The blue line shows the position of the CDB (collisional dynamic basin), defined as the deepest point on the overriding plate. The green line shows the position of the initial collision defined as the point along the subduction zone where continental crust from the overriding plate is first contacts continental crust from the subducting plate. The red line shows the position of Slab break-off.

to the subduction of buoyant continental crust. The subduction of buoyant continental material causes a steepening of the upper portion of the subducted slab and plate interface. This steepening of the upper slab appears to produce the CDB by pulling material away from the base of the overriding plate.

4.3.2 Dynamics of topography formation

To further investigate the dynamics associated with the overriding plate topography, magnified velocity plots for the overriding plate were produced (Fig. 4.9). These show changes in the movement of material in the overriding plate during the change from subduction to collision. Here I present the amplified velocity field from the overriding plate for our 2D subduction model as used in Chapter 3. We will refer to this model a model IV. The 2D model is used as it has a higher model resolution over the collision zone. It should be noted that the velocities presented in these plots are extremely small, typically 2 orders of magnitude smaller than the subduction velocity for the mode. The velocity vectors for the subducting plate and asthenosphere are not plotted since these are much larger, and would completely obscure the velocity field in the overriding plate.

Fig. 4.9A shows the small scale flow in the overriding plate during initial subduction. This plot just shows the over riding crust (white contour), lithosphere and small portion of the subducting plate. Once the slab has contacted the 660 km discontinuity, the velocity in the overriding plate is horizontal towards the trench (Fig. 4.9B). This velocity would be consistent with the subduction zone rolling back during on-going subduction.

As collision begins, the velocity field in the overriding plate (Fig. 4.9C) shows a very small-magnitude flow in the overriding plate. This flow shows that material close to the surface and the front of the overriding plate moves away from the subduction interface and material directly above the mantle wedge moving down. This velocity field illustrates how the forces on the front of the subducting plate cause the upper portion of the slab and the subduction interface to attempt to steepen. This steepening of the upper portion of the subducting plate is responsible for the production of the collisional dynamic basin (CDB).

Once break-off has occurred (Fig. 4.9D) the velocity in the overriding plate is again horizontal but now away from the trench. This could be consistent with the retreat of

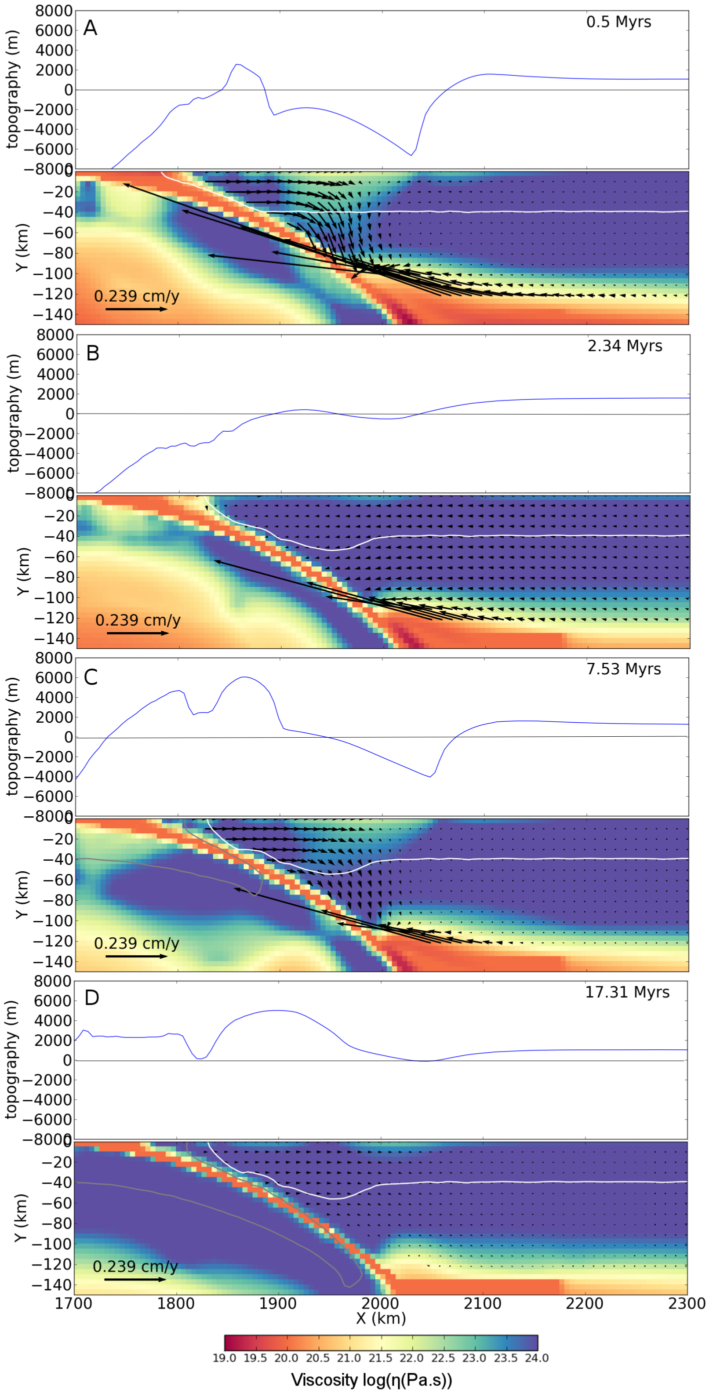

Figure 4.9: Small scale flow in the overriding plate - Magnified velocity field for the overriding plate at 4 time steps for model IV. The velocities in the subducting plate and asthenosphere have been muted out as they are many orders of magnitude greater than the velocities shown here. (A) Represents the initial subduction, (B) Normal subduction once the slab has contacted 660 km discontinuity, (C) Collision and (D) Post slab break-off. The top plots show the topography of the region as calculated from the normal surface stresses. The bottom plots show the viscosity as the colour scheme and the white contour shows the position of continental crust. The vector arrows show the velocity field for the overriding plate.

the subduction zone during on-going continental subduction and collision. Interestingly Fig. 4.9A shows that when subduction is first initiated in the model and the slab is descending into the mantle, a similar flow develops in the overriding plate as seen during collision. This shows that, during the slab's initial decent into the mantle, the slab and subduction interface are trying to steepen up, similar to the situation during collision. This explains the extra depth of the back-arc basin, in the model, during the initial descent of the slab into the mantle.

The strainrate tensor is also plotted, for model IV, to show how these small scale flows in the overriding plate affect the local strain (Fig. 4.10). This may explain deformation that might be expected in the frontal section of the overriding plate (both fore-arc and back-arc). Fig.4.10A shows that during normal subduction, once the slab has reached the 660 km discontinuity and after slab detachment the overriding plate experiences lower strain rates than during collision. The strain rate tensor for the overriding plate shows how, during the initial phase of subduction and during collision, the front of the overriding plate is in vertical extension. The extensional strain rates observed here are located under the region where the post-collisional basin forms and are consistent with the attempted steepening of the upper portion of the slab and the subduction interface. This result indicates that deformation in the front portion of the overriding plate would be expected during the initial phases of collision. We may also expect deformation directly after the initiation of subduction, though our model starts with a defined slab dip so our model may not capture fully complexities of the initial phases of subduction.

The results presented here demonstrate that an asymmetric collision generates similar topography to that presented in Chapter 3. There were three main topographic features identified, in Chapter 3, as forming post-initial collision (CDB collisional dynamic basin, post collisional uplift and broad scale uplift after slab break-off) and these are shown to propagate along the subduction zone for a diachronous collision. The post-collisional uplift is generated by the subduction of continental material and the added buoyancy from this additional crust. Uplift therefore propagates along the subduction zone at the same rate as the collision. The broad scale uplift, observed after slab break-off, is generated by the subducted crust rising buoyantly under the overriding plate. This uplift propagates along the subduction zone at the rate of slab detachment as the removal of the slab allows the subducted crust to rise buoyantly. The post-collisional

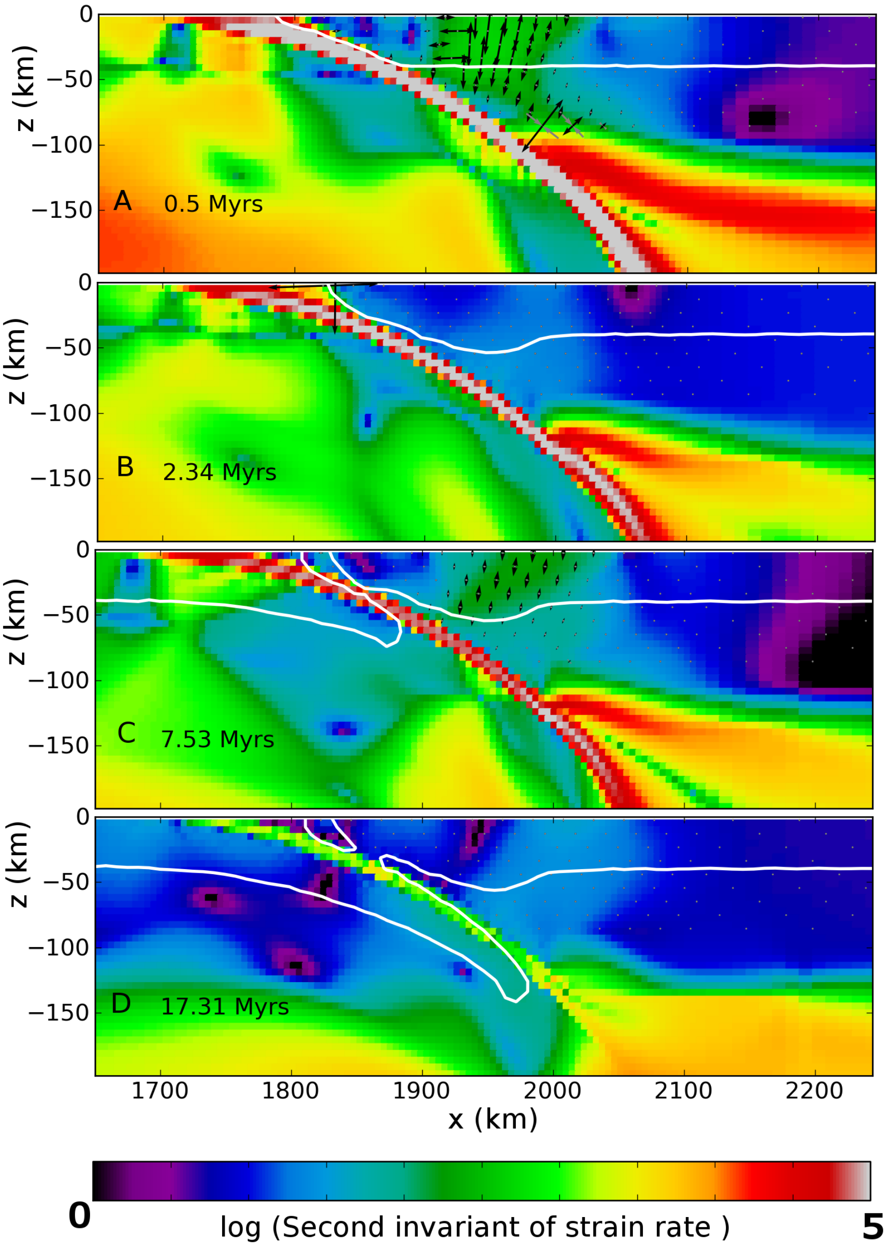

Figure 4.10: Strain tensor for the overriding plate - Second invariant of strain rate is represented by the colour scale (non-dimensional units) and the strain rate tensor by vector arrows (black arrows show extension and grey show compression). The white contour shows the position of continental crustal material. As in Fig. 4.9 the high strains in the subducting plate and mantle wedge are muted out so as not to obscure the signal from the overriding plate.

dynamic basin (CDB) is produced by a steepening of the upper portion of the slab and the subduction interface during the initial collision. Basin-forming processes therefore also travel along the subduction zone at the same rate as collision. Figs. 4.7,4.8 & 4.9 do show the basin propagating marginally slower than the collision, which is due to the slow down in subduction as collision takes place at one end of the subduction system. Both models demonstrate that the subduction of buoyant continental crust is required to cause steepening of the upper part of the subducting slab and form the CDB. As collision progresses further along the collision zone, more of the subduction zone the time between the first crust entering the subduction zone and it getting to the required depth increases, explaining the apparent differences in propagation speed for the collision and CDB.

These results show how movement of material can generate short-lived dynamic topographic features such as the CDB but also long-lived isostatically compensated features where movement of crustal material generates the topography. The models also demonstrate how changes in subduction dynamics can affect the shape of the subduction interface and the deformation in the overriding plate.

4.4 Discussion

The results presented here expand on the topography predictions from Chapter 3. In Chapter 3 we identified three main topographic features that were associated with different stages of the collision and slab detachment process. These features are the initial uplift generated by the subduction of continental crust, the collisional dynamic basin produced by slab steepening and the broad scale uplift produced after slab break-off. Here we show that for an asymmetric collision all of these features propagate along the subduction-collision zone but at different rates depending on the mechanism generating the topography. The uplift generated after slab break-off is seen to progress rapidly across the subduction zone with approximately the same rate as the slab tear propagates. In contrast, the CDB tracks along the subduction zone at a distance of ~300 km from the trench at the rate of initial collision propagating along the subduction zone.

Slab break-off has been proposed to generate overriding plate basins that propagate along the subduction system [van der Meulen *et al.*, 1998]. The Apennines, along the

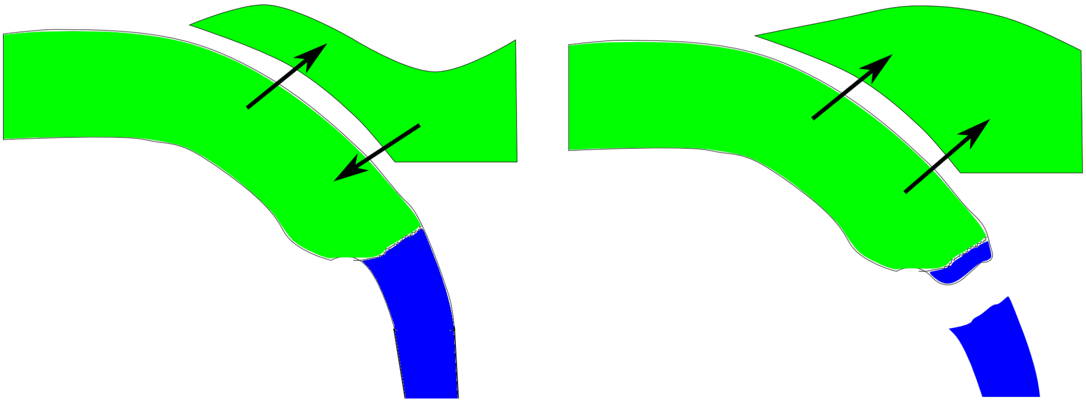

Figure 4.11: Schematic cartoon of the topography-forming mechanisms. - A) As subduction slows down the subduction interface and upper part of the subducting plate steepens up. This opens a basin on the overriding plate. B) Once slab break-off has occurred, the partially subducted continental material in the subducting plate rises buoyantly under the overriding plate, thereby producing uplift.

spine of Italy, has a series of Pliocene-Quaternary basins that are proposed to be formed on top of the Apennine orogenic wedge [van der Meulen *et al.*, 1998; Ascione *et al.*, 2012]. These basins have been shown to have progressing subsidence ages towards the SE, with ages of 31 Ma in the north to 0.8 Ma in the south [van der Meulen *et al.*, 1998] (Fig. 4.1A). The basins have been proposed to be the surface manifestation of a propagating slab tear along the Apennine system [van der Meulen *et al.*, 1999; Faccenna *et al.*, 2001], where the slab pull force is concentrated at the tear hinge creating a depression in the subducting plate and overlying plate. The collision and break-off dynamics are complicated for this region. Firstly, the subduction zone that presently forms the Apennines (Fig. 4.1A rolled back rapidly towards the east to its current position [Capitanio & Goes, 2006; Jolivet *et al.*, 2009], thinning the overriding plate and forming the Tyrrhenian basins off western Italy. There is also not a full continent-continent collision in the Apennines as the subducting plate is thought to be a predominately thinned continental margin Manatschal & Bernoulli [1999] with the Calabrian slab subducting west under Italy and the Hellenic slab subducting east under the Balkans [Jolivet & Faccenna, 2000].

These wedge-top, foredeep basins seem unconnected to the post-collisional basins in our models as the general theory for their formation places them in the orogenic wedge (material accreted between the subducting and overriding plate during subduction of continental material) [Doglioni, 1993]. However, for some subduction zones the accretionary wedge may be >200 km wide (trench perpendicular) [Lin *et al.*, 2009]. Our model does not erode or accrete material so there is no real accetionary wedge, but the front portion of the overriding plate can be assumed to represent previously accreted material. For Italy the basins are situated around 100 - 150km into the hinterland from the deformation front that defines the suture between the two plates [Ascione *et al.*, 2012], whereas the CDB for our results in Chapter 3 is 300 km from the trench. However, we have also found that the collisional dynamic basin moves closer to the subduction suture with decreasing overriding lithosphere thickness (Appendix 8.3), so with the known low lithosphere thicknesses for the Mediterranean the basins that are present along the length of Italy could be recording the time of collision between mainland Italy and the Adria micro plate subduction slow-down and subduction interface steepening [Faccenna *et al.*, 2001]. This may indicate that basins on the overriding plate previously assumed to be slab break-off related could actually show the time of collision with later whole scale uplift being a better indicator of slab break-off.

Post-collisional basins that propagate along the collision zone have also been suggested for the Carpathian-Pannonian collision [Meulenkamp *et al.*, 1996]. Here a “depocentre” migrated east along the subduction zone at 7-45 cm/yr (Fig. 4.1B). It is again proposed that this topographic depression is created by the lateral tearing off of the subducted slab. Here the slab break-off proposed to have started at the western end of the collision zone at 27 Ma and propagated clockwise round the subduction zone reaching the eastern end by 11.5 Ma [Meulenkamp *et al.*, 1996]. The overriding plate contains the Pannonian Basin formation which stretches between 0-400 km into the overriding plate from the trench [Bada *et al.*, 1999; Matenco & Radivojević, 2012]. The Carpathian region is now uplifted with an average elevation of 1000 m. Slab break-off is thought to have happened between 27 - 11.5 Ma. These observations could also fit with the results from our model that the basin formed during the initial collision and then broad scale uplift happens after slab break-off.

The increase in strain rate in the front portion of the overriding plate during the start of collision could also explain post-collisional magmatism found at a number of collision zones [Keskin, 2003; Allen *et al.*, 2013]. This increase in strain rate would weaken the overriding plate and potentially provide a pathway for melt formed at a later stage in the collision to migrate upwards. Tentatively the vertical extensional strain may even allow for the possibility of decompression melting at lithospheric depths. This could fit with the generation of post collisional calc-alkaline type magmatism as documented in Tibet [Frank *et al.*, 1999], the intra-Carpathian region [Seghedi *et al.*, 1998] and Dabie Orogen in China [Zhao *et al.*, 2007]. Slab steepening has been previously proposed to create weakening in the overriding plate and produce the subsidence observed for the Carpathians [Bertotti *et al.*, 1998], although the formation of a lithospheric drip beneath the basin due thickening of the lithosphere has also been proposed as a subsidence mechanism [Houseman & Gemmer, 2007].

Our results demonstrate the possibility to create topographic features that propagate along a subduction system. However, they also highlight the challenge in differentiating between topographic features produced by the collision of continental material and those produced by slab break-off. Here we show that the collision process and associated steepening of the upper portion of the slab and subduction interface produce a basin on the overriding plate (Fig. 4.11). Subsequent slab break-off produce broader scale uplift due to the partially subducted continental material buoyantly rising under the overriding plate. For an asymmetric collision, the basins develop laterally parallel to the subduction zone at the same rate as collision, whereas the later uplift propagates at the (different) rate of slab break-off. These results show that the complex nature of the subduction interface has a large influence on topography. Our results offer an alternative explanation for the observed basins that propagate around the collision zones in both the Apeninines and the Carpathians which have previously been attributed to purely slab break-off. The rates of basin prorogations from the Appenines and Carpathians of 7-45 cm/yr compare favourable with the propagation rates from Models I & II of 6.6 - 26 cm/yr. The models also demonstrate a region of high strain in the front portion of the overriding plate during initial collision. This high strain region may assist in the eruption of post-collisional magmatism.

5

Eduction of UHPM terrains

Factors affecting the Eduction of UHPM terrains: comparison with the Western

Eduction is a proposed mechanism for the exhumation high / ultra-high pressure terranes. This mechanism refers to a complete reversal of the plate motion once the subducted oceanic slab has broken off. Here we use a 2D numerical model of the closure of an oceanic basin to investigate the effects that several physical parameters of the subduction / collision system have on its ability to educt HP/UHP material. To that end, we use a series of material markers placed in the front of the subducting plate's continental block from which we reconstruct synthetic P-T paths. To investigate the applicability of our results, we compare our model results to the high / ultra-high HP/UHP pressure terranes in the Western Gneiss Complex (WGC) in south west Norway.

Our results show that the dominant controls on the eduction process are the positive and negative buoyancy forces associated with the crustal and lithosphere thickness of the subducting plate. We also develop a simple relationship between the physical parameters that define the subduction system and the peak pressure and temperatures that would be expected in educted crustal material. From this relationship we show that a range of different possible subduction systems can transport material to the peak depths estimated for the WGC, but most never reach the required peak temperatures. This observation is of interest as it indicates that a further mechanism may be required to fully explain the peak P-T conditions experienced by the WGC. A possible mechanism involves plate rotation and diachronous collision, and is explored in the Chapter 6.

5.1 Introduction

Ultra-high pressure metamorphic (UHPM) rocks are present in most Phanerozoic collision zones but their emplacement and structure vary greatly. Globally there are over 20 UHPM exposures mostly in Phanerozoic continental orogenic belts [Liou *et al.*, 2004; Warren, 2013]. Some of these sites show multiple episodes of UHPM exhumation over 10 million years. The size of these terranes also vary from >30,000 km^2 giant UHP terranes in Norway [Little *et al.*, 2011] and China [Li & Gerya, 2009] to small kilometre sized bodies found in mélanges such as the European Alps [Federico *et al.*, 2007]. A lot of these bodies are made up of quartzofeldspathic gneiss with some mafic rock (eclogite) or ultramafic rock (garnet-bearing peridotite) included in them [Massonne, 2003; Coleman Robert, 2005]. UHPM rocks can also contain diamonds indicating they have experienced pressures of greater than 3 GPa [Kennedy & Kennedy, 1976]. Some of the larger units also include evidence of protoliths involving sediments and volcanic rift units, which can be interpreted as evidence of the exhumation of a previous passive margin. Most UHPM terranes record a history of high pressures, of >3 GPa or greater, indicating that the material has been to a depth of over 90 km. However most UHP metamorphic material have experienced relatively low temperatures (800°C) compared to ambient mantle temperatures. This history suggests that exhumation of these rocks occurs relatively quickly, before they can fully thermally equilibrate to the expected lithospheric temperature at that depth. However, some show temperatures as high as 1200°C such as Kokchetav Massif [Massonne, 2003] implying that the dynamics of exhumation vary between collision zones.

Subduction is the only known process capable of transporting crustal material to the depths required to form these UHPM rocks [Coleman Robert, 2005]. The subduction of oceanic crust and sediments is well documented in many arc settings around the world where crustal signatures can be recognised in arc lavas [Winter & Winters, 2001; Hacker *et al.*, 2005]. Continental crust is generally less dense than oceanic and so resists subduction. However slab pull from a dense oceanic slab is still capable of pulling this continental crust over 100 km deep down the subduction zone [Andrews & Billen, 2009; Duretz *et al.*, 2012]. Crust is required to be transported to depths of greater than 100km to explain the observed mineral assemblages found in HP/UHP terranes.

There are a number of different suggested mechanisms for the exhumation of UHPM terranes, all of which offer a good explanation for some of the UHPM terranes on earth. One proposed mechanism for the Western Gneiss in Norway is eduction, the reversal of the subduction process. This mechanism returns the subducted plate (crust and lithosphere) coherently to the surface [Andersen *et al.*, 1991]. The force balance for eduction is explored in Duretz *et al.* [2012] which shows that removal of the slab pull force, by slab break-off, can allow the subducted continental material to return back to the surface. This mechanism has advantages for explaining large areas of UHPM rock such as the Western Gneiss of Norway [Andersen *et al.*, 1991] as it allows a large section of crustal material that was previously subducted to be returned coherently to the surface. A criticism of this method is that some believe that the 3D nature of a subduction zone would not allow a reversal of subduction after break-off, due to continued subduction at other points along the arc, this is the focus of Chapter 6.

In this study we address how the physical parameters that affect the subduction and collision system influence the ability to educt UHPM material. P-T paths for material markers in the subducting plate's continental crust are used to compare our models to petrological estimates for the peak pressure and temperature conditions experienced by exhumed material from the Western Gneiss Complex in Southern Norway which formed during the Caledonian collision.

The Caledonian collision between the continental masses of Laurentia and Baltica occurred in the Silurian [Dewey & Strachan, 2003]. The Western Gneiss Complex (WGC) in south west Norway was formed during this collision, and proposed subsequent slab loss [Brueckner & Cuthbert, 2013]. This region is of special interest as it contains coesite and micro-diamonds, implying it has experienced pressures of 1.5 - 5 GPa and temperatures 550 - 900 °C [Chopin, 2003]. The WGC also forms one of the spatially most extensive high and ultra-high pressure terranes preserved on earth. The Western Gneiss Complex also shows prograding metamorphism from high or ultra-high pressures recorded in the west to material that has not been transported to depth in the east [Hacker *et al.*, 2010]. This prograding pattern of metamorphism has been interpreted as evidence that the whole region that makes up the WGC was transported to depth down the subduction system to the west and returned east to the surface as one coherent unit [Brueckner, 2006]. This observation supports the eduction mechanism for the exhumation of the WGC where exhumation happens due to reversal of the shear sense on the subduction system. Further field evidence that supports the eduction process include lineation data [Labrousse *et al.*, 2004] and the passive transport of nappes on top of the educting plate.

5.2 Methodology

In order to investigate the formation of UHP metamorphic terranes, numerical modelling was done with a finite element geodynamical code, Citcom [Moresi & Gurnis, 1996; Zhong *et al.*, 2000; van Hunen & Allen, 2011]. The model uses a Cartesian grid, assumes incompressible flow and makes the Boussinesq approximation. The code used solves for conservation of mass, momentum, energy and composition [van Hunen & Allen, 2011]. Non-dimensional governing equations are as follows:

$$\nabla \cdot \mathbf{u} = 0 \tag{5.1}$$

$$-\nabla P + \nabla \cdot (\eta(\nabla \mathbf{u} + \nabla \mathbf{u}^T)) + (RaT + RbC)e_z = 0 \tag{5.2}$$

$$\frac{\partial T}{\partial t} + \mathbf{u} \cdot \nabla T = \nabla^2 T \tag{5.3}$$

$$\frac{\partial C}{\partial t} + \mathbf{u} \cdot \nabla C = 0 \tag{5.4}$$

where symbols are defined in Table 5.1

The model simulates the closure of an oceanic basin leading to continental collision and subsequently slabs detachment. The initial model setup, for the default model, is shown in Fig. 5.1A. The model has an overriding continental plate on the right edge of the model containing a continental crust and thick lithosphere. The subducting plate is made of an oceanic lithosphere with a continental block made up of crust and

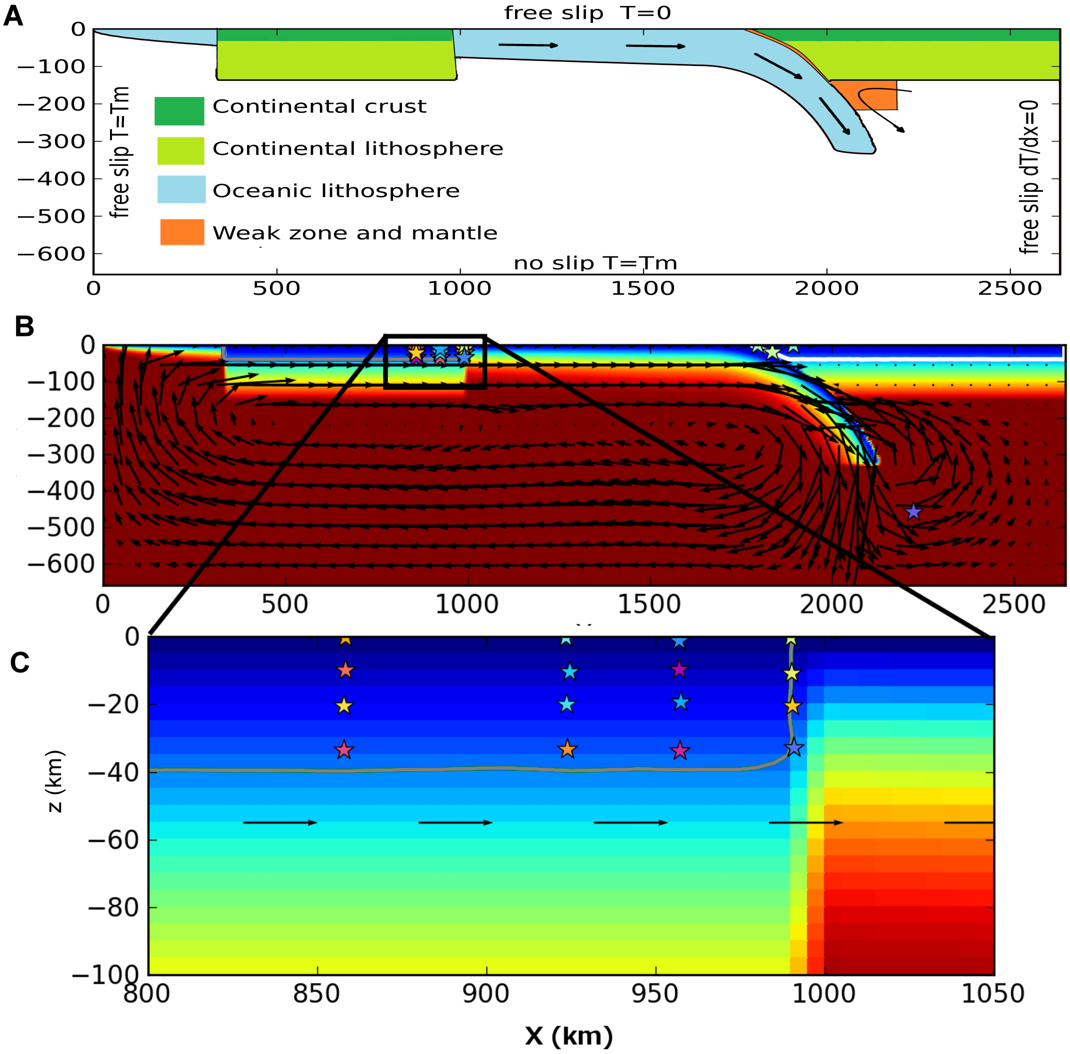

Figure 5.1: Reference model - A) shows a schematic model of the reference model. This shows the thickened lithosphere and crust in continental areas (green), the oceanic lithosphere in blue. B) shows the temperature distribution of the default model along with the initial position of the material markers that are followed to create PT paths. The white contour highlights continental crust on the overriding plate. The grey contour highlights continental material on the subducting plate. C) shows a zoom-in of the front portion of the subducting plate's continental block. The stars represent the material markers that are followed to create PT paths

lithosphere embedded in it. The modelling domain is 660 km by 2640 km giving a 1:4 aspect ratio. There is grid refinement in the top 200 km and between 1700 km and 2200 km in the horizontal. This gives a grid resolution, over the collision zone, of 4 km by 5 km, in the x and z directions respectively. The no slip boundary condition at the base of the model is designed to simulate the interaction of a slab with a higher viscosity layer such as that proposed for the phase change at 660 km [Ringwood, 1994]. All other boundaries have a free slip boundary condition. The thermal boundary conditions are 0°C at the surface and mantle temperature (1350°C) at the base and left boundary. The right boundary has a zero heat flux boundary condition. Subduction is initiated by a partially subducted slab and facilitated by a zone of weak material between the subducting plate and the overriding plate. This numerical weak zone (fully described in Chapter 2) is sustained throughout the model run and kept at constant viscosity (1×10^{20} Pa·s in the reference model) to allow permanent decoupling of the two plates. The reference model setup initially has a 60 Myrs old oceanic lithosphere partially subducted under a continental overriding plate and a zero age mid-ocean ridge at the left edge. The initial thermal structure of the oceanic lithosphere is calculated using the half space cooling model. The initial age of the oceanic lithosphere is set assuming a constant spreading rate for the model (3cm/yr for the reference model) from the left edge of the model. The thermal structure of the continental regions is set as a linear geotherm from 0°C at the surface to mantle temperature at 150 km depth.

Four different deformation mechanisms control the strength of material in the models. Diffusion creep and dislocation creep [Karato & Wu, 1993] describe the rheology of mantle material, a stress limiting rheology [Byerlee, 1978] weakens highly stressed material near the surface of the model. We also impose a model maximum viscosity for numerical stability. For a full description of rheology see [van Hunen & Allen, 2011; Bottrill *et al.*, 2012].

The subducting plate has a 700 km long 40 km thick (in the reference model) continental crustal block embedded in it. The overriding plate also has a 40 km thick continental crust and is fixed to the right edge of the model. The continental material is advected using particle tracers [Di Giuseppe *et al.*, 2008]. The continental plates in the model resist subduction due their compositional buoyancy of 600kg/m^2. Oceanic crustal buoyancy is ignored in the models, as the transformation of basalt to eclogite occurs at 30-40 km which would remove most additional compositional buoyancy [Cloos, 1993] making the buoyancy of the subducted and oceanic lithosphere a purely thermal effect. The lack of the transformation to denser phases such as eglogite also potentially has an influence on the buoyancy of continental material that is transported to depth.

Pressure temperature paths are reconstructed for a set of 16 material markers. Initially these markers are placed in the front portion of the overriding plate in a 4×4 grid with markers at 0 km, 10 km, 20 km, and 30 km depth and 0 km, 33 km, 66 km and 130 km from the front edge of the continental block Fig. 5.1C. The markers are advected with the model's velocity field and report their temperature and depth at every time step. Depths are converted into pressures by assuming that all pressure experienced is lithostatic with a lithostatic gradient of 33 MPa/km.

Here we investigate the sensitivity of the produced P-T paths to 6 different model start-up parameters. The parameters we investigate are: age (or thermal thickness) of the subducting oceanic lithosphere, crustal thickness of the subducting continental block, thermal thickness of the subducting continental lithosphere, radius of curvature of the subduction interface, viscosity of the weak decoupling layer that forms the subduction interface and the depth to the mantle wedge (i.e. the lithosphere thickness of the overriding plate). A visual representation of all the parameters investigated is shown in Fig. 5.2. To compare models we extract the peak pressure and temperature experienced by each followed material marker. These parameters are investigated to determine which subduction system can transport material to ultra-high pressure conditions.

For all of the parameters investigated in this study and the marker start position, we produces a simple linear relationship to peak pressure and temperature. All of these linear relationships can then be combined into one relationship that describes the peak pressure and temperature conditions for any model setup and material start condition. This relationship is then compared to the measured peak pressure and temperature condition from our simulations to check the fit of our new simple relationship. We also use the relationship and petrological peak pressure and temperature estimates from the Western Gneiss to offer some insight into the type of subduction system capable of exhuming an extensive UHPM terrane such as the WGC in Norway.

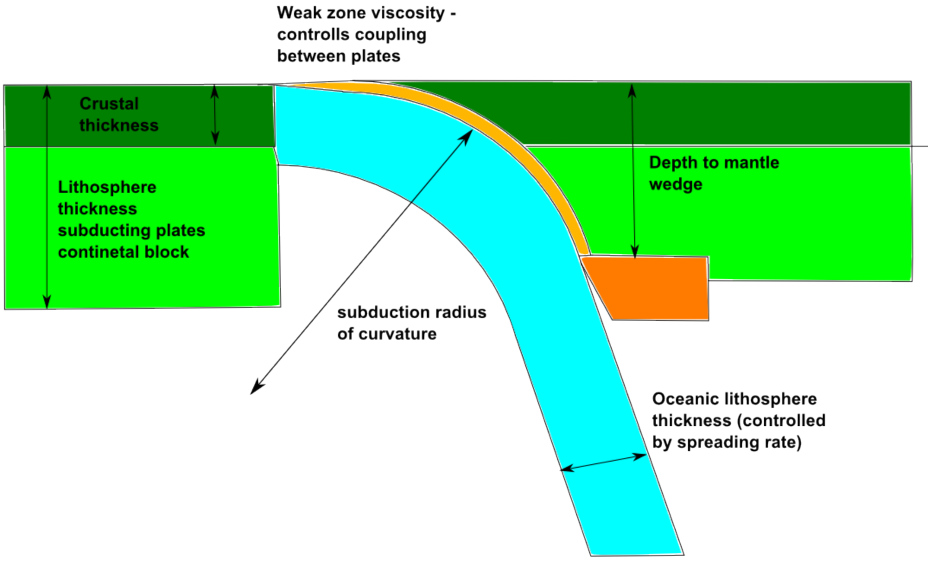

Figure 5.2: Schematic diagram of the model - the six parameter investigated are shown pictorially. These are: age (or thermal thickness) of the subducting oceanic lithosphere, crustal thickness of the subducting continental block, thermal thickness of the subducting continental lithosphere, radius of curvature of the subduction interface, viscosity of the weak decoupling layer that forms the subduction interface and the depth to the mantle wedge (i.e. the lithosphere thickness of the overriding plate).

Symbol	**Definition**	**Value and units**
C	Compositional Parameter	[-]
C_P	Heat capacity (constant pressure)	1250 $[J.kg^{-1}.K^{-1}]$
e_z	Vertical unit vector	[-]
g	gravitational acceleration	9.81 $[ms^{-1}]$
h	Model dimension	660 [km]
P	Deviatoric pressure	[Pa]
Ra	Thermal Rayleigh number	4.4×10^6 [-]
Rb	Compositional Rayleigh number	1.7×10^7 [-]
δT	Temperature range	$0 - 1350$ [°C]
T	Temperature	[°C]
t	time	[s]
$\mathbf{u}$	Velocity	[m/s]
T_m	Mantle temperature	1350 [°C]
α	Thermal expansivity	3.5×10^{-5} [K^{-1}]
κ	Thermal diffusivity	1×10^{-6} [$\mathrm{m}^2\,\mathrm{s}^{-1}$]
η_0	Reference viscosity	10^{20} [Pa·s]
ρ	Density	$[kgm^{-3}]$

Table 5.1: Symbols and definitions used in the governing equations

5.3 Results

We first present the model dynamics and calculated P-T paths for our reference model. The reference model has identical start-up conditions to our preferred model in Chapter 3, [Bottrill *et al.*, 2012]. Then we investigate how six different model start-up parameters affect the peak pressure and temperature that crustal material reaches.

5.3.1 Reference model

Fig. 5.3 shows the viscosity field for the model with the material markers (stars) used to create P-T paths. This shows how the markers are initially arranged in a grid pattern in the front of the continental block. As continental material starts to enter the subduction zone, the markers that started at the surface in the subducting continental block are accreted onto the overriding plate and remain at the surface. The subduction velocity also reduces due to buoyant continental material entering the subduction zone. After ∼10 Myrs subduction stops and the slab starts to neck and break-off. At this point the deepest material markers have reached ∼150 km (4.95 GPa). After slab break-off, the subducted continental material moves back up towards the surface and return a number of the material markers to crustal levels. The exhumation velocity is much slower than the subduction velocity but material is still returned to crustal levels 20 Myrs after it reached peak depth. This model demonstrates exhumation by eduction, the wholesale return of subducted material to the surface. Next, we investigate the physical parameters that are most likely to affect the P-T paths travelled by subducted material.

P-T paths for all markers in the subducting plate are shown in Fig. 5.4. All P-T paths are clockwise, i.e. pressure increases during descent before temperature does. The markers that started at the front of the continental block achieve higher temperatures and depths than markers that started further into the continental block, with markers at the front getting down to 140 km and temperatures of 600°C. Markers also demonstrate better return towards the surface if they started further back from the front of the continental block and deeper below the surface. The markers that started at the surface are scraped off during the initial collision and remain at the surface.

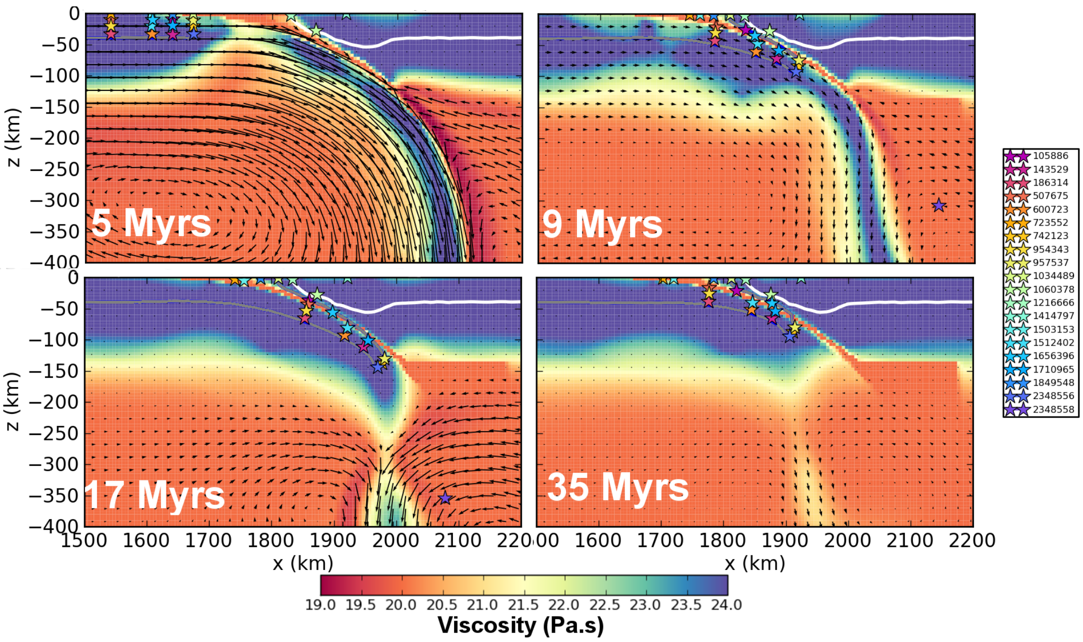

Figure 5.3: Subduction dynamics - Snapshots of the subduction zone just before collision, during continental subduction, subsequent slab break-off and eduction. The colour scheme shows viscosity, the white contour outlines crustal material that started in the overriding plate and the grey contour highlights material that started in the continental block of the subducting plate. The stars show the positions of material markers followed to create P-T paths.

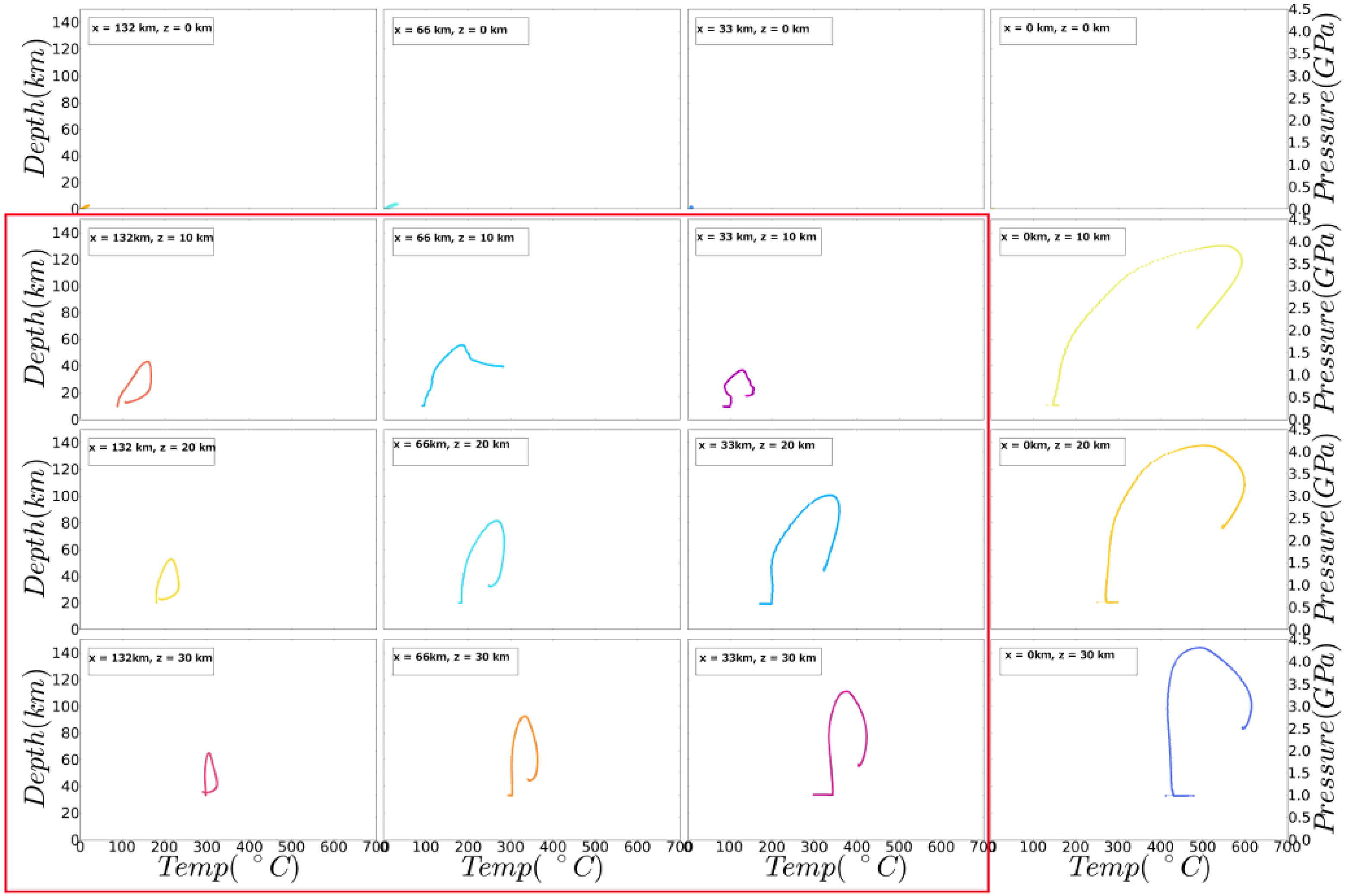

Figure 5.4: P-T paths for the reference model. - The markers are organised in their initial x-z configuration in the front of the subducting continental block, e.g. the PT paths on the top right of the figure is for a marker that started at the surface and at the front of the subducting plate's continental block. Markers are placed between 0, 10, 20, 30 km depth (z-axis) and 0, 30, 60, 120 km from the edge of the continental block. Fig. 5.1 provides more detail on the original positions of markers.

These P-T paths show that the initial position of markers inside the continental block has a large effect on the peak pressure and temperature conditions that the marker reaches. Chemical analyses of ultra-high pressure material can give estimates for the experienced peak pressure and temperature [Dobrzhinetskaya *et al.*, 2011b]. These numbers are useful as they define the apexes of a standard (clockwise) P-T path and so surmise the conditions a sample has experienced and hence which mineral phases might be present. We develop a simple relationship for the peak pressure and temperature conditions experienced with respect to the markers start position for the 9 markers in the red box in Fig. 5.4. We exclude the surface markers from our analysis as they are accreted on to the overriding plate during collision and so do not experience normal subduction or eduction. We also exclude the markers that start at the edge of the continental block at the transition from continental to oceanic plate. These markers' P-T histories include effects due to being at the boundary between continental and oceanic plate and also do not generally return to crustal levels.

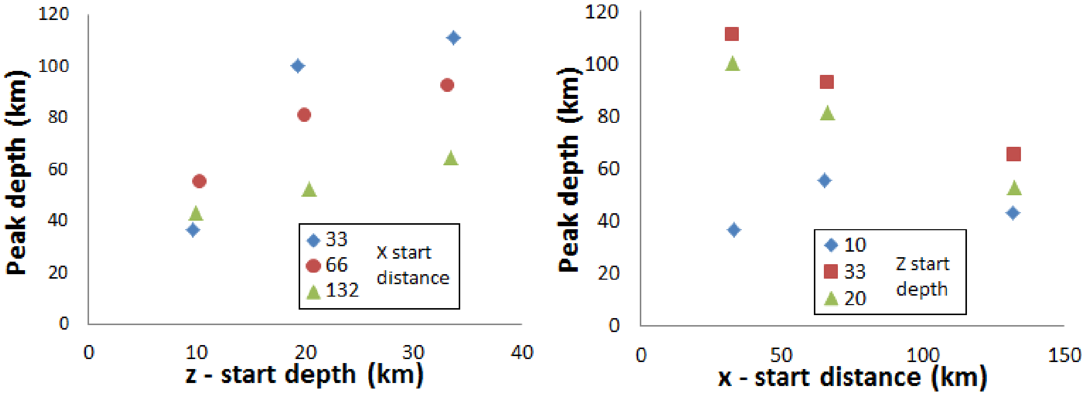

Figure 5.5: Peak depth in terms of markers initial position - Plots showing the relationship between the peak depth (pressure) and the markers start position in both depth and distance from the front of the continental block.

Fig. 5.5 shows that there is a roughly linear relationship between the start depth, start distance and the peak depth achieved by the markers. They also show how the gradient and intercept of this relationship is also dependant on the marker start position. The marker that started at 33 km back from the front of the continental block and 10 km deep does not seem to fit well with these trends which is because this marker is not being transported coherently with the subducting plate but instead being caught in the plate interface, similar to the fate of many of the markers that originally were at the surface. We choose to include this marker as it represents an important transition point in the subducting continental block from material being accreted to being subducted.

Due to the linear nature of these relationships we describe the relationship between the peak pressure and temperature conditions and the markers start position in the continental block, for our reference model, in the form:

$depth_{peak} = ax + bz + c$ $\qquad T_{peak} = dx + ez + f$

Where the coefficients a-f are determined using a Generalized Reduced Gradient Algorithm [Gabriele & Ragsdell, 1977] to reduce the mismatch between the peak pressure and temperature estimates from our simple relationship and those measured from our numerical models.

We find that the peak depth of any marker can be described by:

$$depth_{peak} = -0.43x + 1.24z + 82.84 \tag{5.5}$$

Where both the peak depth and start position of the marker are measured in km, the horizontal distance (x) is measured relative to the front of the continental block and the initial depth (z) is measured relative to the top of the model domain.

Comparison of this relationship to the peak depth measurements from our numerical models we calculate a coefficient of determination $R^2 = 0.96$. This shows that our description of peak depth in terms of marker start position fits well with the peak depths from our model.

Fig. 5.6 shows a similar relationship between temperatures and start position, as Fig. 5.5 does for depth (pressure). For temperature in terms of start position we find the following relationship:

$$T_{peak} = -0.60x + 7.22z + 175.4 \tag{5.6}$$

Comparison of this relationship to peak temperature measurements from our numerical model we calculate a coefficient of determination $R^2 = 0.83$, which shows that our simple relationship successfully predicted the changes in temperature due to the markers pre-collision position in the continental block.

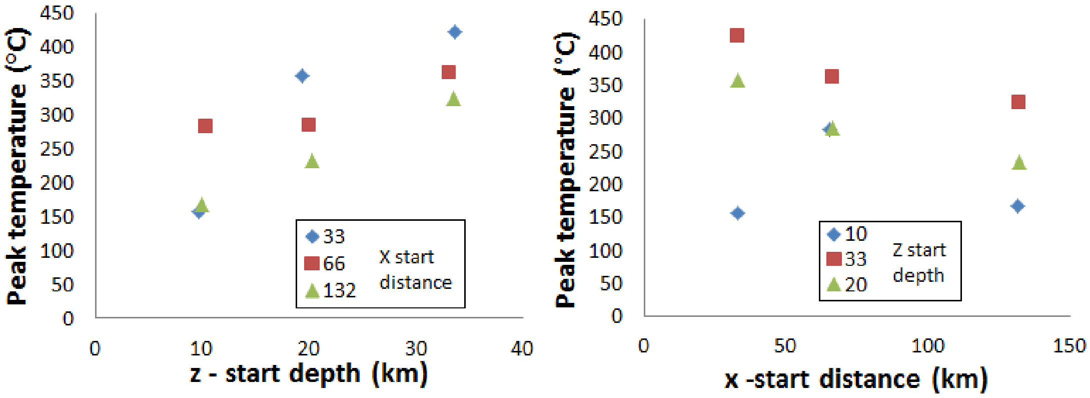

Figure 5.6: Peak temperature in terms of markers initial position - Plots showing the relationship between the peak temperature and the markers start position in both depth and distance from the front of the continental block.

These relationships show that for every 1 km closer to the front of the continental block a marker starts, it travels 0.4 km deeper and reaches a peak temperature 0.6 °C hotter. We also see that for every 1 km deeper in the continental block, the markers peak depth increases by 1.2 °C and peak temperature is reduced by 7.2 °C.

5.3.2 Sensitivity Study Peak pressure and temperature

Here we compare the peak depth and temperature achieved by markers, which started in the same position, for models with different starting conditions. This allows us to compare how different physical properties of a subduction zone influence the peak pressure and temperature that subducted crust experienced. We still only consider the 9 markers that were used for our analysis of our reference model. The P-T paths of the markers used are highlighted in Fig. 5.4 by the red box. The model start-up parameters that are investigated are listed in Table 5.2.

We also derive a simple linear relationship between each of the sensitivity parameters investigated and the peak depth (in km) and temperatures (in °C) achieved by markers. All of the relationships take the form:

$$depth_{peak} \propto (mx + nz + o) \times Q \tag{5.7}$$

$$T_{peak} \propto (qx + rz + s)) \times Q \tag{5.8}$$

Parameters investigated	Symbol	Reference model value	Range investigated	Units
Subducting oceanic plate age	*pl*	60	29 - 165	[Myrs]
Crustal thickness	*ct*	40	22 - 59	[km]
Continental lithosphere thickness	*lt*	150	52 - 198	[km]
Radius of subduction interface	*rs*	528	330 - 792	[km]
Viscosity of subduction interface	η_i	1×10^{20}	$0.5 - 6\times10^{20}$	[Pa·s]
Depth to mantle wedge overriding (lithosphere thickness)	*dmw*	132	0 - 132	[km]

Table 5.2: Symbols, definitions, range investigated and value used in default model

Where Q is the parameter under investigation.

This is done through a two-step linear regression where first a linear relation is sought for each marker to describe how the investigated parameter affects peak pressure and temperature for that marker. Then a linear regression is used to find a description of the gradient in terms of the markers start position. We choose to describe each of the relationships as linear so that they can be easily combined into one description for the peak pressure and temperature in terms of all the sensitivity parameters and the starting position of material in the subducting plates continental block.

5.3.2.1 Oceanic plate age

The first investigated parameter is the age (thickness) of the subducting oceanic plate, which defines the thermal thickness of the oceanic lithosphere. Thicker (older) oceanic slab is denser and so drags continental material deeper. This is shown by the increase in pressure and temperature conditions achieved by markers in models with thicker (older) subducting oceanic plates (Fig. 5.7).

The relationship between the subducting slab age and peak depth and temperature is approximately linear (Fig. 5.8). The gradient of this linear relationship is dependent on the starting position of the marker.

We derive an empirical relationship between the subducting slab age (yrs) and the peak depth (km).

$depth_{peak} \propto (3.23 \times 10^{-8} z + 1.56 \times 10^{-9}) \times pl$

This shows that for every million year increase in subducted plate age the markers are transported to between 0.0015 - 1 km deeper, depending on the depth at which the crustal material started.

Increasing subducting plate age also increases the peak temperatures reached by markers as the continental crust is subducted deeper and so exposed to hotter regions in the mantle. An older (thicker) subducting oceanic plate is stronger and denser, meaning continental crust is dragged deeper and slab break-off takes longer giving crust a greater amount of time to equilibrate to the temperature at depth. The peak temperature (°C) also shows a linear relationship to oceanic slab age (yrs) but with no dependence on the markers' initial position (Fig. 5.8). We again derive an empirical relationship:

$T_{peak} \propto 2.6355 \times 10^{-6} \times pl$

This shows that for every million year increase in subducting slab age the crustal material reaches a peak temperature 2.6°C greater. The increase in peak temperature, achieved by markers, with increasing subducting slab age is independent of the initial depth that the crustal material started at.

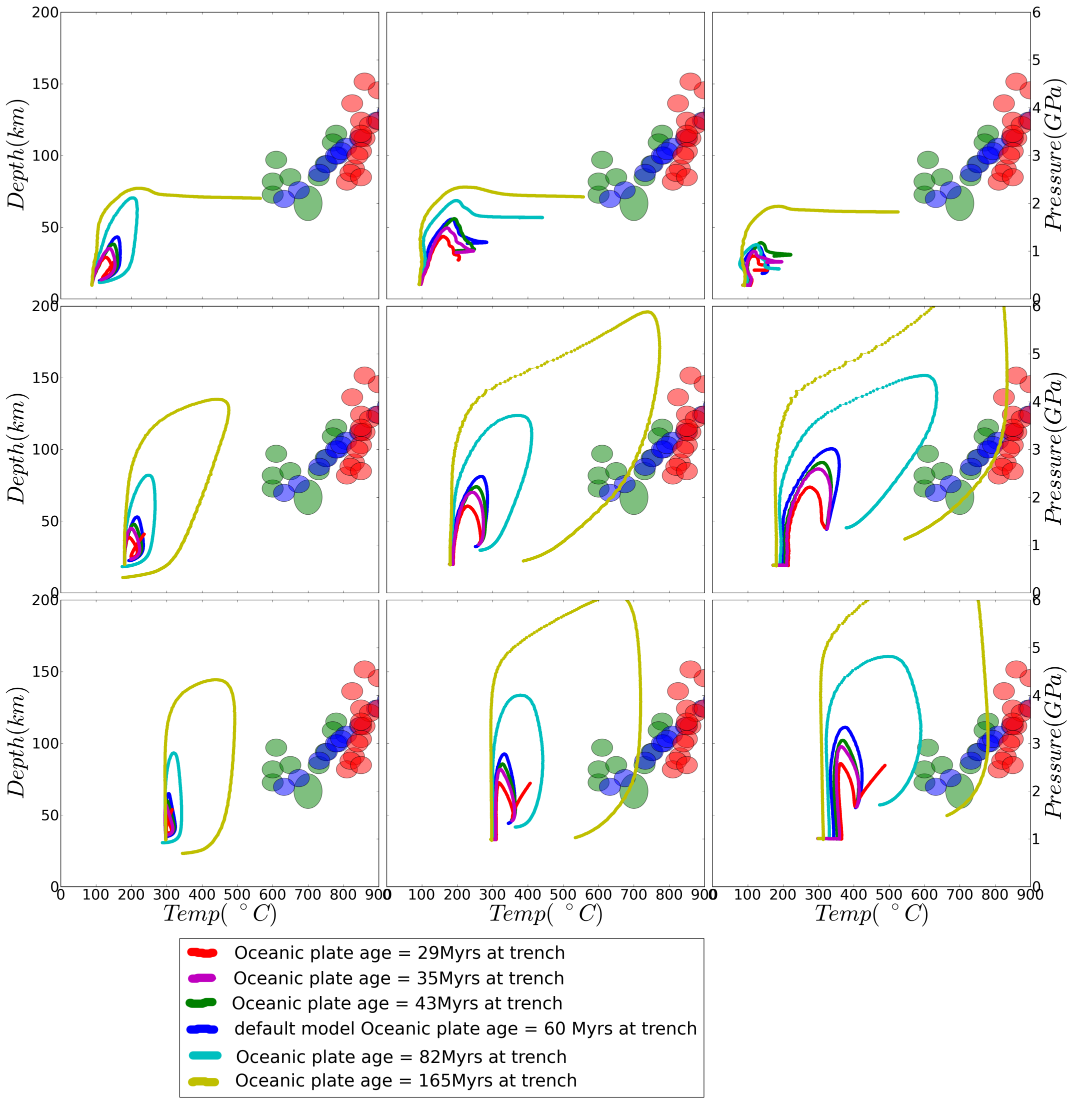

Figure 5.7: P-T paths for different subducting plate ages - Compilation of P-T paths for model calculations with different subducting oceanic plate ages between 29 Myrs to 165 Myrs. The position of the sub-plots represents the initial position of the markers in the front of the continental block. Markers started at 10, 20, 30 km depth and 33, 66 , 132 km from the front of the subducting plate. The age of the subducting lithosphere affects the slab pull force as older slabs are thicker and colder. Therefore we find that for models with older oceanic plates, markers follow a deeper and hotter P-T paths. Peak P-T estimates from the WGC are from Hacker *et al.* [2005]; Carswell *et al.* [2006]; Vrijmoed *et al.* [2006] and are plotted as red, green and blue circles respectively. These values are chosen to be representative of the range of peak P-T conditions experienced by exhumed sections of the Western Gneiss region. Data from Hacker *et al.* [2005] are from the Kli and Seve Nappes in the Trondelag-Jmtland region in the north of the WGC. Carswell *et al.* [2006] presents data from the islands of Fjortoft and Otroy in the north west of the WGC. Vrijmoed *et al.* [2006] shows data from the west coast of Norway on the north-western edge of the WGC.

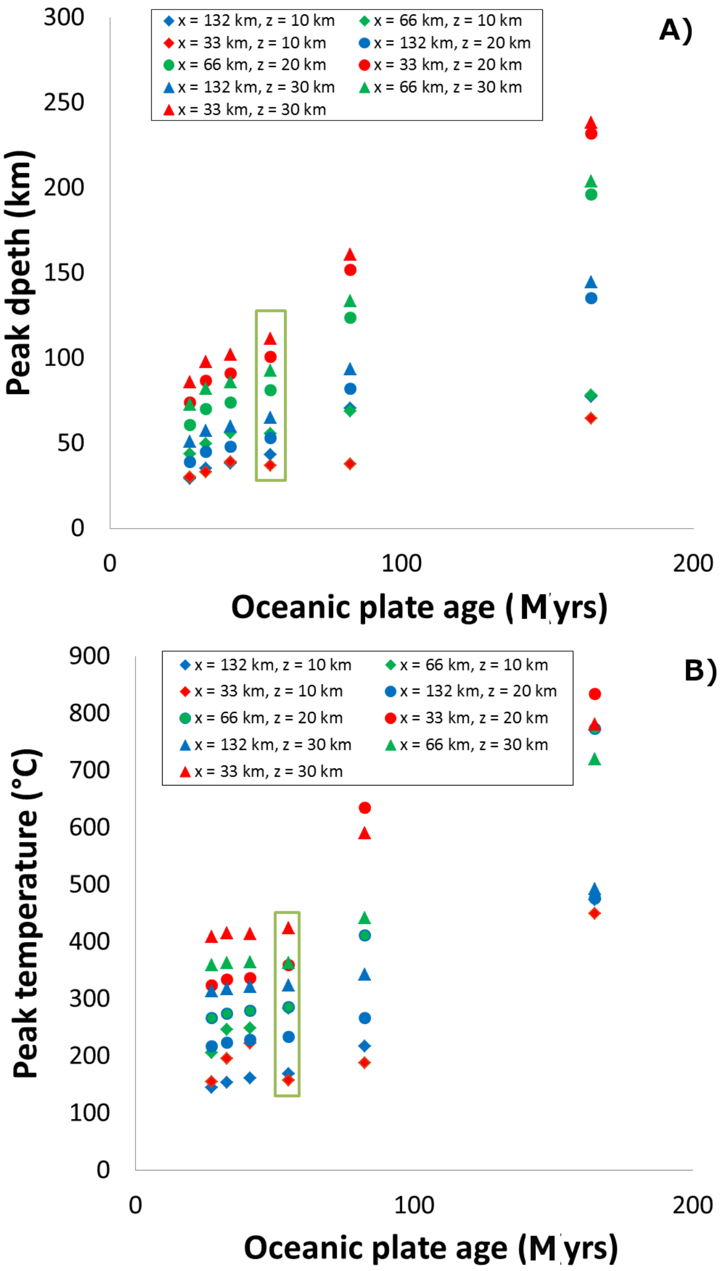

Figure 5.8: Peak depth and temperature with respect to subducting plate age - A) shows the relationship between peak marker depth and the age (thickness) of the subducting plate's lithosphere. B) shows the relationship between peak temperature reached by the markers and the age (thickness) of the subducting plate's lithosphere. The colour and shape of symbols in the plot represents the pre-collision position of markeres. Diamonds represent markers that started at 10 km depth, circles for 20 km depth, and triangle 30 km depth. Red symbols started at 33 km from the front of the continental block, green at 66 km, and blue at 132 km. The green box highlights the values from our reference model.

]

5.3.2.2 Crustal thickness

Crustal material provides the buoyancy responsible for continental material resisting subduction. Therefore as the thickness of crustal material is reduced, we see an increase in depth that markers are transported to, as expected from basic isostatic principles. However, for very thin crustal thicknesses subduction is not stopped and continued subduction of continental material occurs without a full continental 'collision' and subsequent slab break-off (Fig. 5.9).

We discard the model with 22 km thick crust, where subduction does not stop as the peak depths and pressures do not refer to material that educted back to the surface. For simplicity we describe the relationship between crustal thickness and peak depth achieved as linear. This approximation is used to allow all the relationships for all parameters used in this study to be easily combined to give an overall prediction of peak depth (km) and temperature (°C) in terms of initial model parameters.

$depth_{peak} \propto (0.011x - 0.036z - 7.1) \times ct$

This shows that crust experienced a decrease in peak depth reached, as crustal thickness increases. The relationship shows that a 1 km decrease in crustal thickness would result in a 7-8 km increase in the peak depth. This relationship shows a slight dependence on the start position of the marker, so markers that started deeper and closer to the front of the plate show a greater increase in depth with decreasing crustal thickness.

There is a similar linear trend in the relation of peak temperatures achieved and crustal thickness (km).

$T_{peak} \propto (0.032x - 0.170z - 19.90) \times ct$

Peak temperature also shows a decrease in the peak temperature achieved of 20-24°C with a 1 km increase in crustal thickness. Here again the markers that start deepest and nearest the front of the continental block experience the greatest increase in temperature.

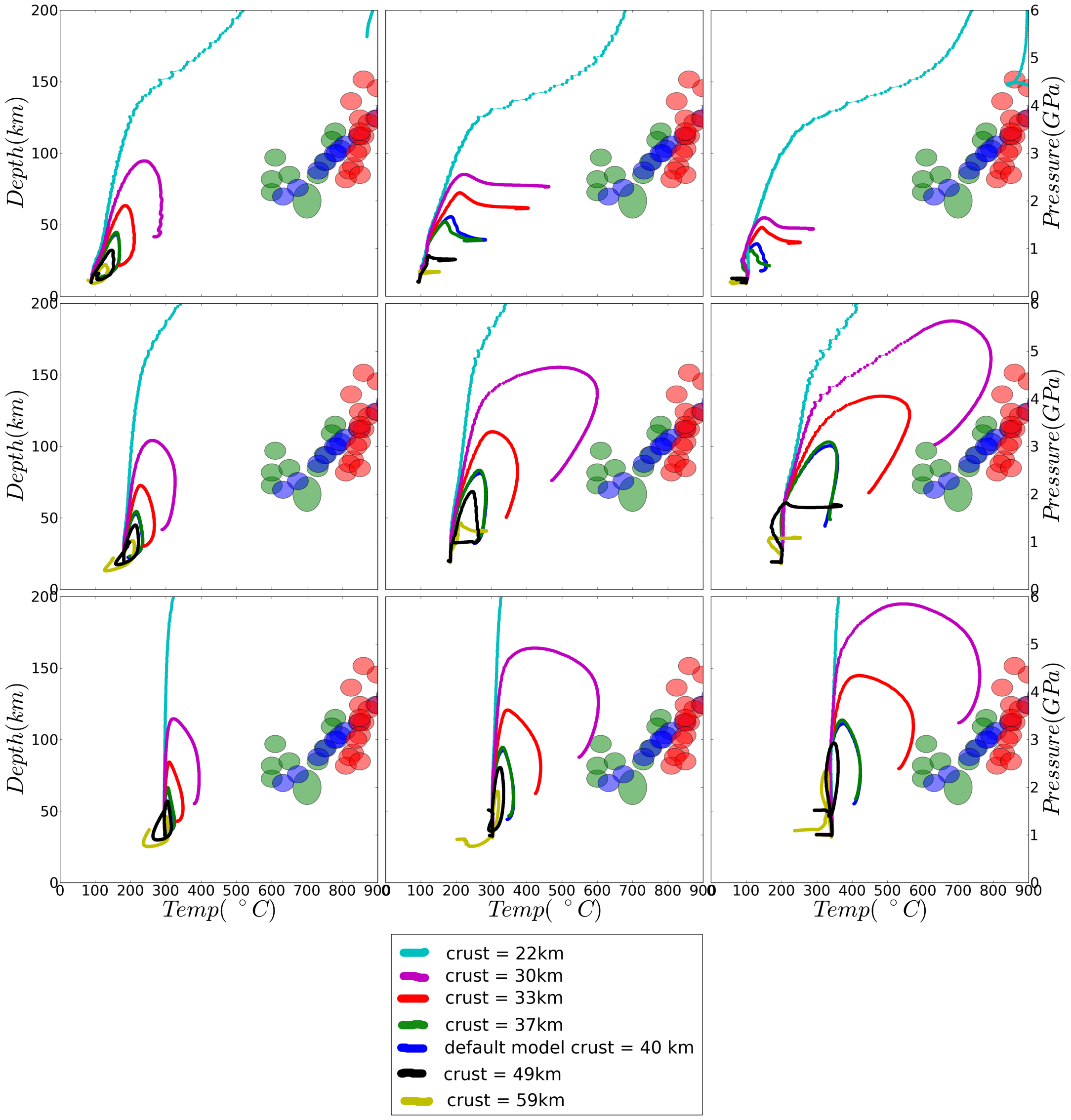

Figure 5.9: P-T paths for different crustal thickness's - Compilation of P-T paths for model calculations with different subducting plate continental crustal thicknesses. The position of the sub-plots represents the initial position of the markers in the front of the continental block. Markers started at 10, 20, 30 km depth and 33, 66 , 132 km from the front of the subducting plate. Continental crust provides the buoyancy that causes continental plates to resist subduction. We therefore find that with thinner crust markers follow deeper P-T paths. Peak P-T data is as described in Fig. 5.7.

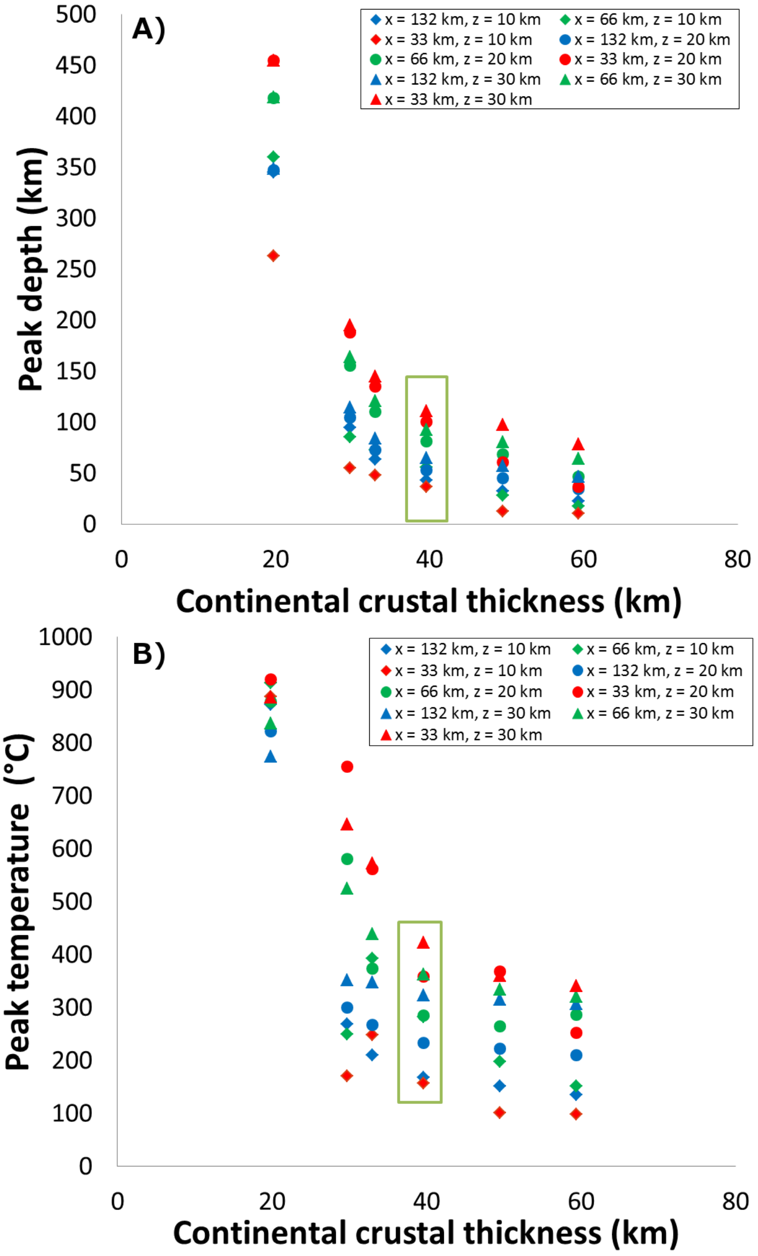

Figure 5.10: Peak depth and temperature with respect to continental crustal thickness - A) shows the relationship between peak depth achieved by the markers and the continental crustal thickness in the subducting plate. B) shows the relationship between peak temperature achieved by the markers and the continental crustal thickness in the subducting plate.

5.3.2.3 Continental lithosphere thickness

The presence of a thick continental lithosphere provides rheological strength of the subducting plate's continental block but also affects the initial thermal structure for the plate, which determines the markers start temperature. The added density from thickened lithosphere drags material deeper but also reduces the temperature a marker starts at. The P-T paths in Fig. 5.11 show how decreasing lithosphere thickness produces higher peak temperatures with slightly reduced peak depths.

For the two models with continental lithospheres thinner than 70 km, markers are not transported very deep (Fig. 5.11) and don't follow typical clockwise P-T paths. This is due to the plate being very weak and it rifting before getting to depth in the subduction zone. On the basis that this continental rifting is a different mechanism to eduction we exclude these models from our determined relationship.

Having excluded the models that don't demonstrate eduction we derive a linear empirical relationship between the peak depth (km) and the incoming continental lithosphere thickness (km).

$depth_{peak} \propto (-2.6 \times 10^{-5}x + 0.0021z + 0.078) \times lt$

This shows that for every 10 km increase in lithosphere thickness of the incoming plate, an extra 0.8 km of extra depth is reached by the markers. The small values for the coefficients of x and z in the relationship show that there is little dependence on the markers start position. The peak temperatures show a decrease in peak temperature (°C) with increasing lithosphere thickness (km):

$T_{peak} \propto (-0.00865x - 0.02783z + 0.4153) \times lt$

This inverse relationship is caused by the lower geothermal gradient in models with thicker continental lithospheres. There is however a smaller decrease in peak temperature with increasing lithosphere thickness for markers that started deeper.

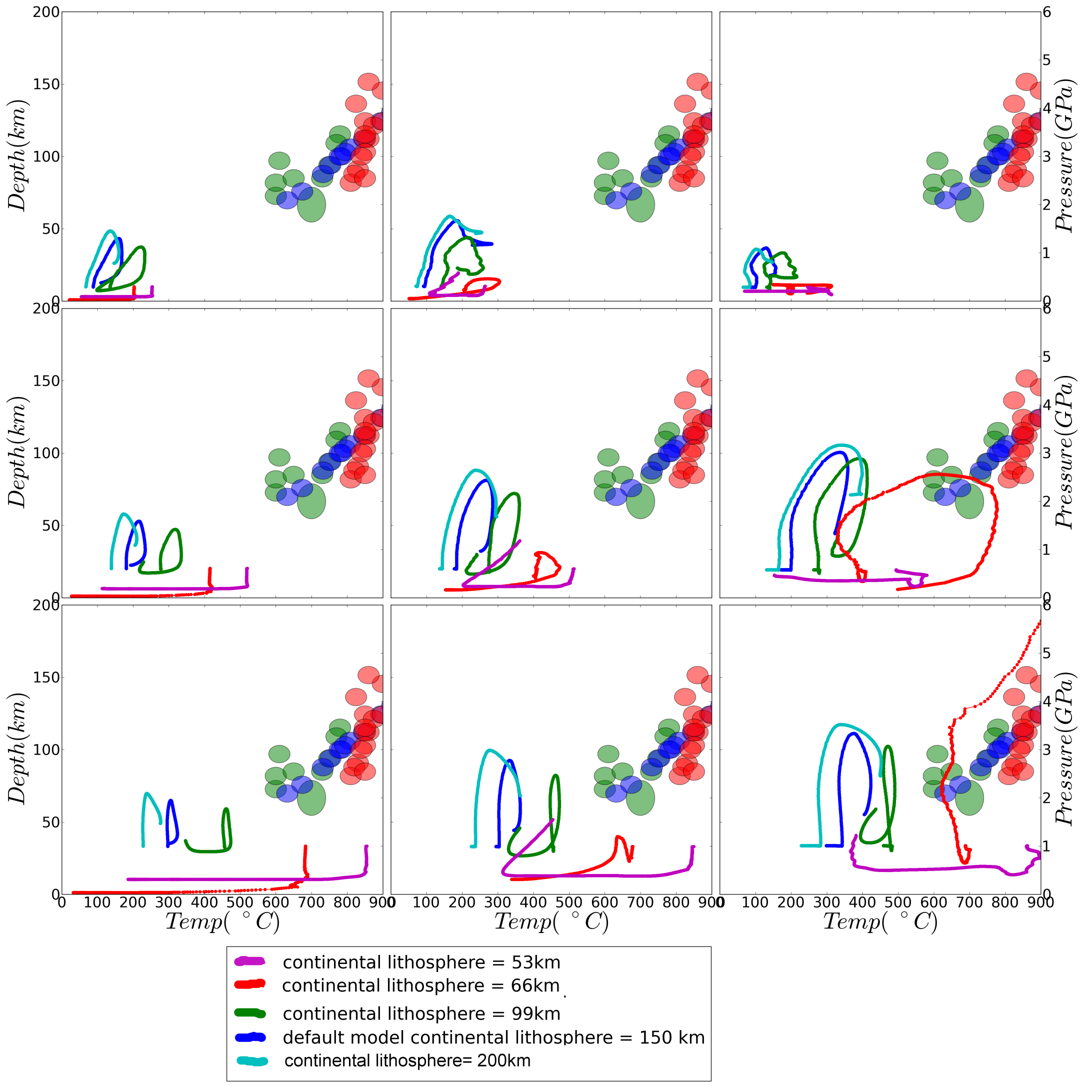

Figure 5.11: P-T paths for different continental lithosphere thickness - Compilation of P-T paths from models with different continental lithosphere thickness between 53 km and 200 km for subducting plate. The position of the sub-plots represents the initial position of the markers in the front of the continental block. Markers started at 10, 20, 30 km depth and 33, 66 , 132 km from the front of the subducting plate. The continental lithosphere provides both the strength for the continental plate but also defines its initial thermal structure. This means that models with thinner lithosphere have markers that follow P-T paths that start hotter. For very thin lithosphere markers stop following clockwise P-T paths due to the subducting plate being too weak to coherently subduct. Peak P-T data is as described in Fig. 5.7.

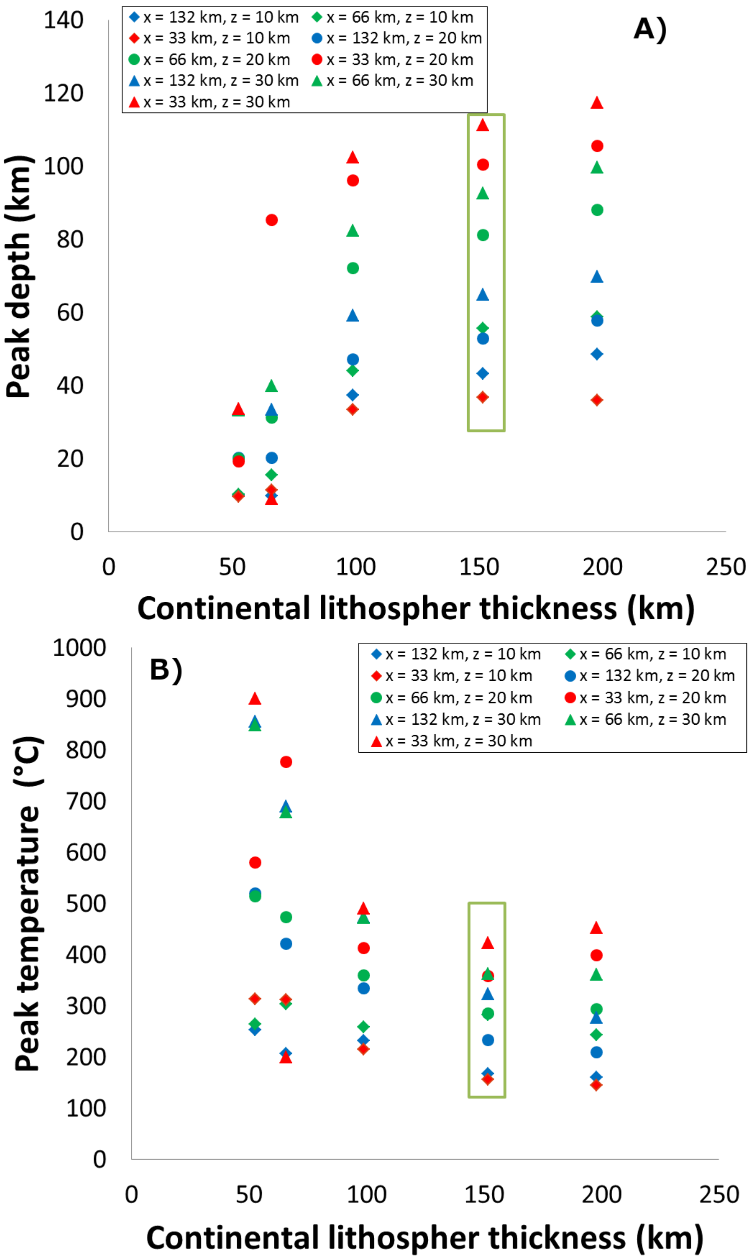

Figure 5.12: Peak depth and temperature with respect to continental lithosphere thickness - A) is shows the relationship between peak depth achieved by the markers and the continental lithosphere thickness. The right plot shows the relationship between peak temperature achieved by the markers and the continental lithosphere thickness subducting plate. The symbols used are as described in Fig. 5.8.

5.3.2.4 Radius of subduction interface

The radius of the subduction interface defines the steepness of the subduction zone with smaller radii representing steeper subduction zones at the lithosphere asthenosphere boundary (LAB) see Fig. 5.2. The P-T paths in Fig. 5.13 show that for makers furthest from the front of the continental block increasing subduction radius helps markers achieve higher peak pressures and temperatures. For markers closer to the edge of the continental block the relationship is more complex with both the largest and smallest radii investigated reaching the highest peak depth and temperature condition.

We again derive simple linear relationships between peak depth (km) and subduction radius (km) as well as peak temperature (°C) and subduction radius using Fig. 5.14.

$$depth_{peak} \propto (-2.6 \times 10^{-5}x + 0.0021z + 0.0078) \times rs$$

$$T_{peak} \propto (-0.0086x - 0.028z + 0.415) \times rs$$

These show that for a 100 km increase in subduction radius, peak depth reached by continental material increases by 2.5 km and peak temperatures would increase by 28 °C. This increase in depth and temperature with increasing subduction radius is due to it being energetically favourable to subduct material down a shallower subduction zone due to having to deform the subducting plate less.

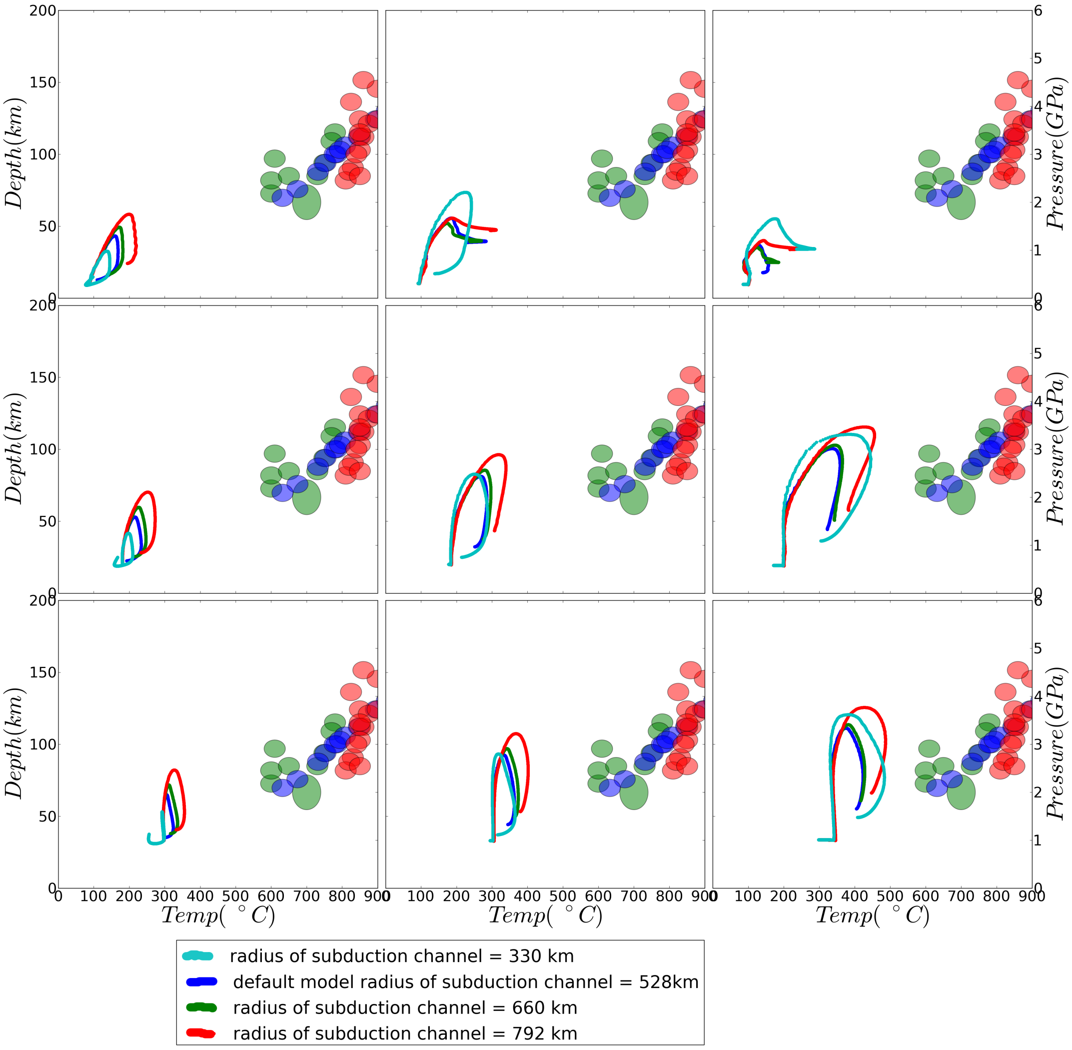

Figure 5.13: P-T paths for different subduction radii - Comparison of P-T paths for different subduction interface radii between 330 km and 792 km. The position of the sub-plots represents the initial position of the markers in the front of the continental block. Markers started at 10, 20, 30 km depth and 33, 66 , 132 km from the front of the subducting plate. The subduction interface radius describes the steepness of the plate interface with large radii giving shallower subduction angles. Peak P-T data is as described in Fig. 5.7.

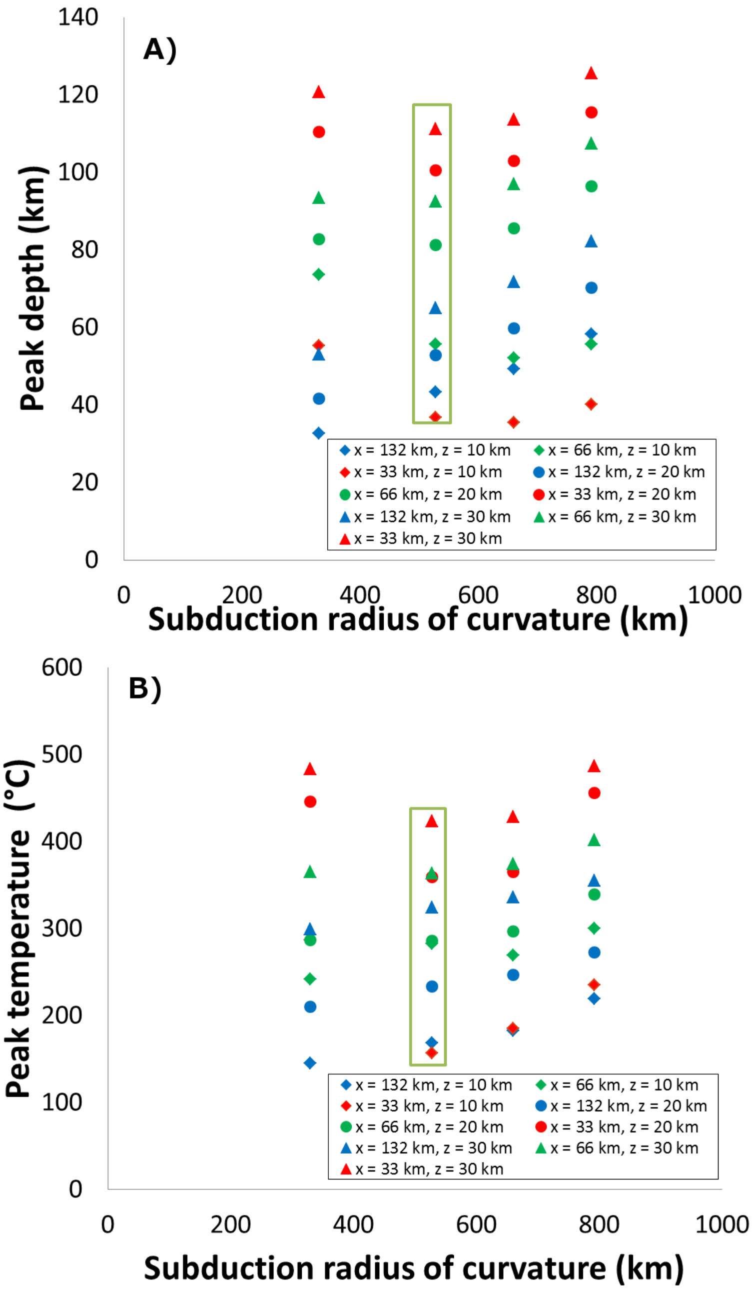

Figure 5.14: Peak depth and temperature with respect to subduction radius - A) shows the relationship between peak depth achieved by the markers and the subduction radius. B) shows the relationship between peak temperature achieved by the markers and the subduction radius. Symbols are as defined in Fig. 5.8.

5.3.2.5 Viscosity of subduction interface

In our model the interaction of the subducting and overriding plate is controlled by the inclusion of a zone of weak material that separates them. The viscosity of the subduction interface between the plates affects how quickly subduction progresses, with a stronger subduction interface making it harder for the plates to slide past each other. The speed at which subduction can progress is important as the longer material spends in the subduction zone the longer it has to equilibrate to temperatures at depth.

Fig. 5.16 shows that there is a slight increase in peak temperatures reached with increasing subduction interface viscosity (Pa·s). The peak depth (km) reach by material seems to be independent of the subduction interface viscosity (Fig. 5.15). Fig. 5.16 A) shows how the depth marker starts in the continental block affects the peak depths that are reached.

$$depth_{peak} \propto (0.0164x + 0.115z - 4.68) \times \frac{\eta i}{10^{20}}$$

$$T_{peak} \propto (0.0305x + 0.168z - 8.767 \times 10^{-5}) \times \frac{\eta i}{10^{20}}$$

With increasing subduction interface strength the peak depths reached by markers that were at 10 km pre-collision decreases implying that the top of the subducting plate is being sheared. The shearing of the front of the continental block is present in all models but the amount of shearing increases with greater subduction interface viscosity. Peak temperature shows an increase with increasing subduction interface viscosity for the markers that are at 20 & 30 km pre-collision depth. This is due to the whole subduction and eduction cycle taking longer and so giving crustal material longer to equilibrate to temperatures experienced at depth. The markers at 10 km are not transported as deep with increasing subduction interface viscosity so heat up less.

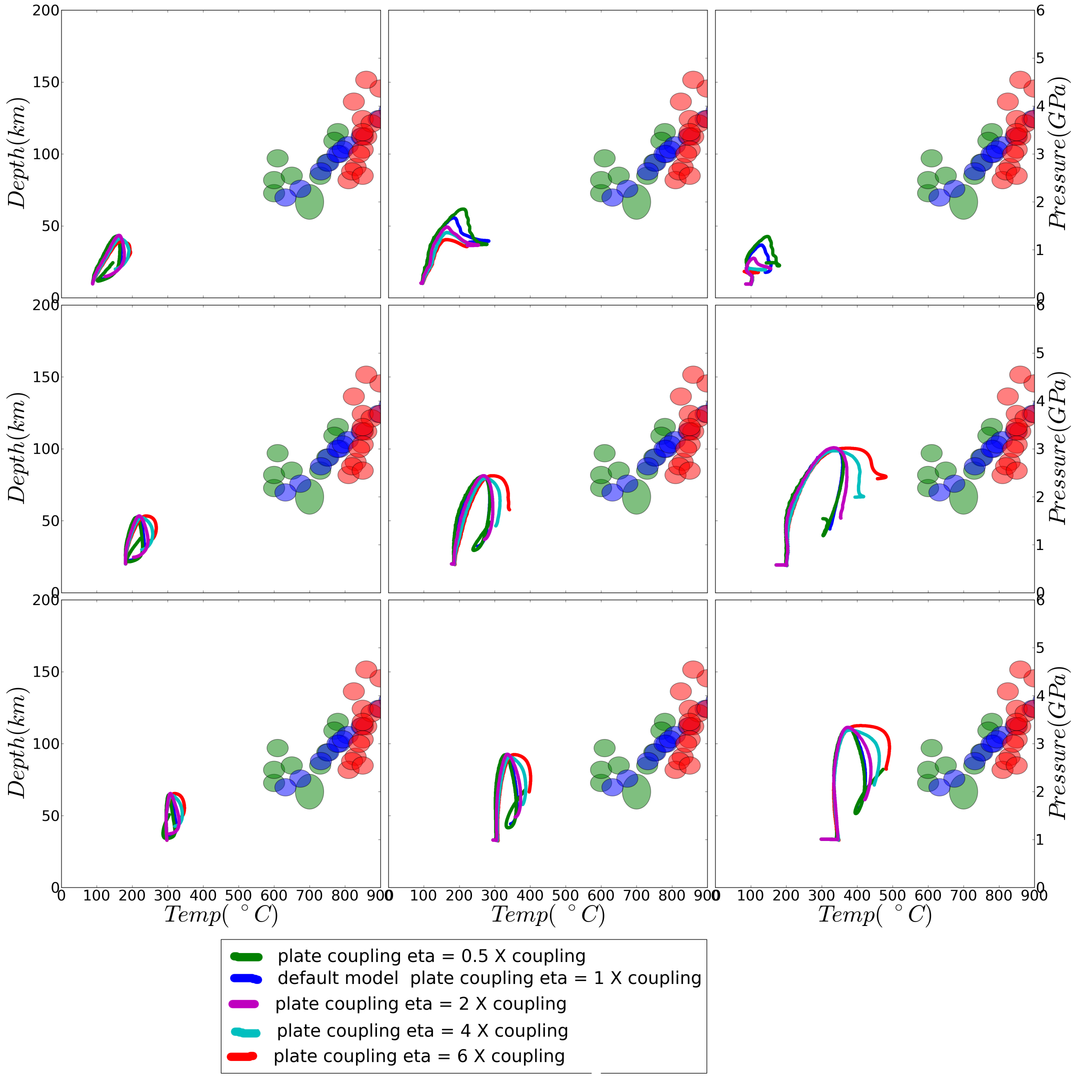

Figure 5.15: P-T paths for different subduction interface viscosities - Comparison of P-T paths from models with differing subduction interface viscosities between 0.5×10^{20} to 6×10 ^{20} Pa·s. The position of the sub-plots represents the initial position of the markers in the front of the continental block. Markers started at 10, 20, 30 km depth and 33, 66 , 132 km from the front of the subducting plate. The subduction interface in our models is defined as a zone of weak material. The relative strength of this material defines the coupling between the subducting and overriding plates. Peak P-T estimates are plotted for the western Gneiss as described in Fig. 5.7.

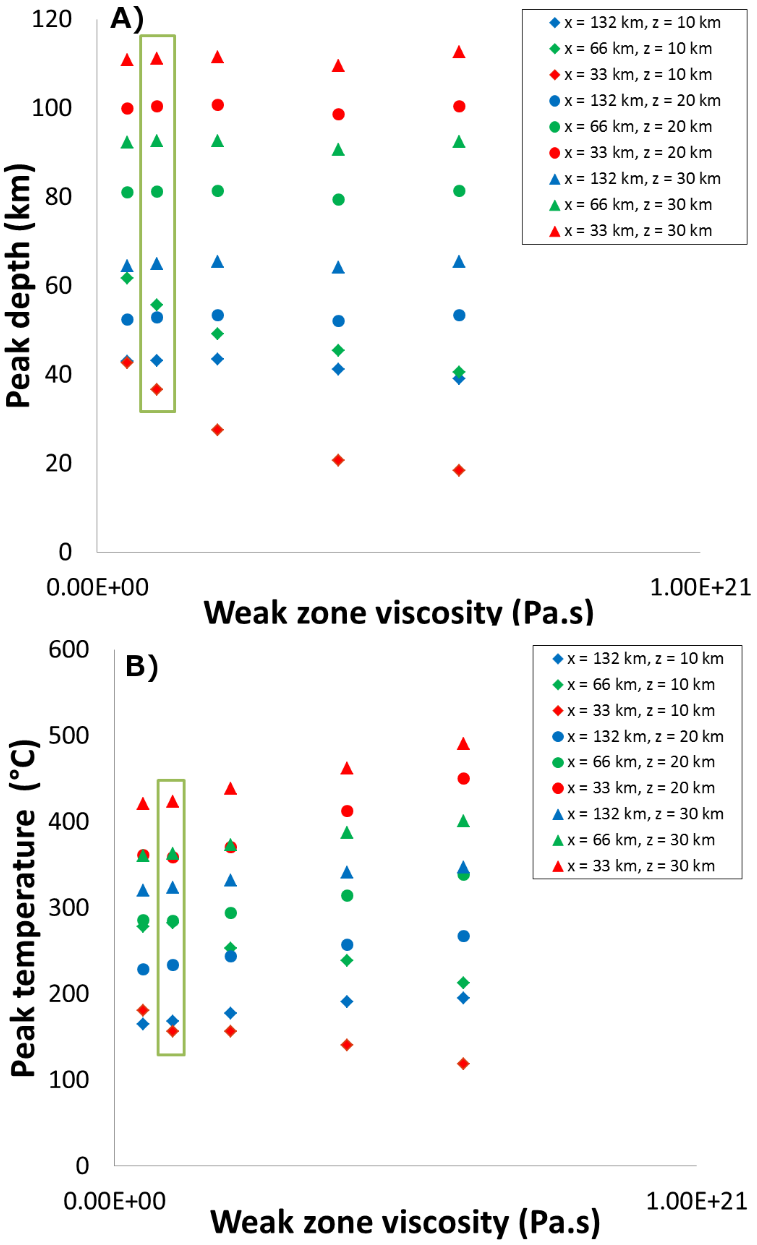

Figure 5.16: Peak depth and temperature with respect to subduction interface viscosity - A) shows the relationship between peak depth reached by markers and the subduction interface viscosity. The B) shows the relationship between peak temperature reached and the subduction interface viscosity. Symbols are as definedin Fig. 5.8.

5.3.2.6 Depth to mantle wedge overriding (lithosphere thickness)

The depth to the mantle wedge affects the thermal structure of the overriding plate but also its strength. The P-T paths in Fig. 5.17 show that for depths less that 66 km a clockwise P-T path is not followed by the majority of the markers. This is because the overriding plate becoming so weak that material can pass across the subduction interface and accrete directly onto the overriding plate. This seems to suggest the need for a strong overriding plate for eduction but our simple model set-up with fixed subduction interface precludes further investigation. Both peak depth and temperature show maximum values for the model with a 66km deep mantle wedge (Fig. 5.18).

We again derive simple relationships for the peak depth and temperature though to do this we exclude the models with a mantle wedge shallower than 66km because of the aforementioned complication:

$$depth_{peak} \propto (0.00152x - 0.0383z + 0.359) \times dmw$$

$$T_{peak} \propto (0.0197x - 0.139z - 0.1627) \times dmw$$

The depth relationships shows that an increase of 0.3-1 km in peak depth reached by markers is expected for every km reduction in the depth to the mantle wedge. The temperature relation shows an increase in the peak temperature of 4-0.1°C for ever km shallower the wedge is placed. Both these relationships show a dependence on the initial depth of the marker, with initially deep markers showing a decrease in peak depth and temperature with increasing depth to wedge, whereas shallower markers actually show an increase in peak depth and temperature with increasing depth to wedge.

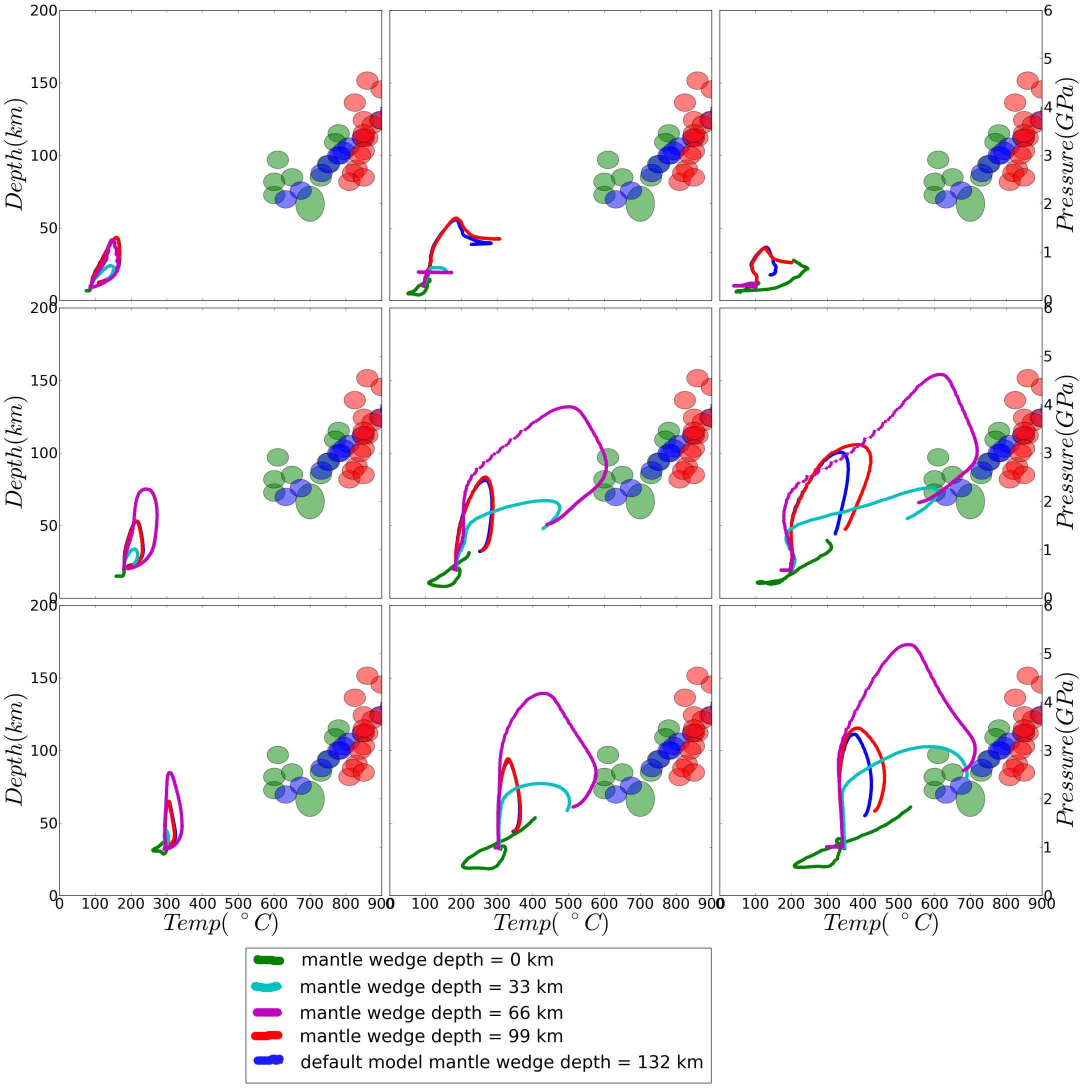

Figure 5.17: P-T paths for different depths to the mantle wedge - Comparison of P-T paths for models with differing depths of the weak mantle wedge (overriding lithosphere thickness). The position of the sub-plots represents the initial position of the markers in the front of the continental block. Markers started at 10, 20, 30 km depth and 33, 66 , 132 km from the front of the subducting plate. The depth to the mantle wedge (km) defines the thermal and mechanical structure of the overriding plate against which the markers in the continental block are subducted. Peak P-T estimates are plotted for the western are plotted as in Fig. 5.7.

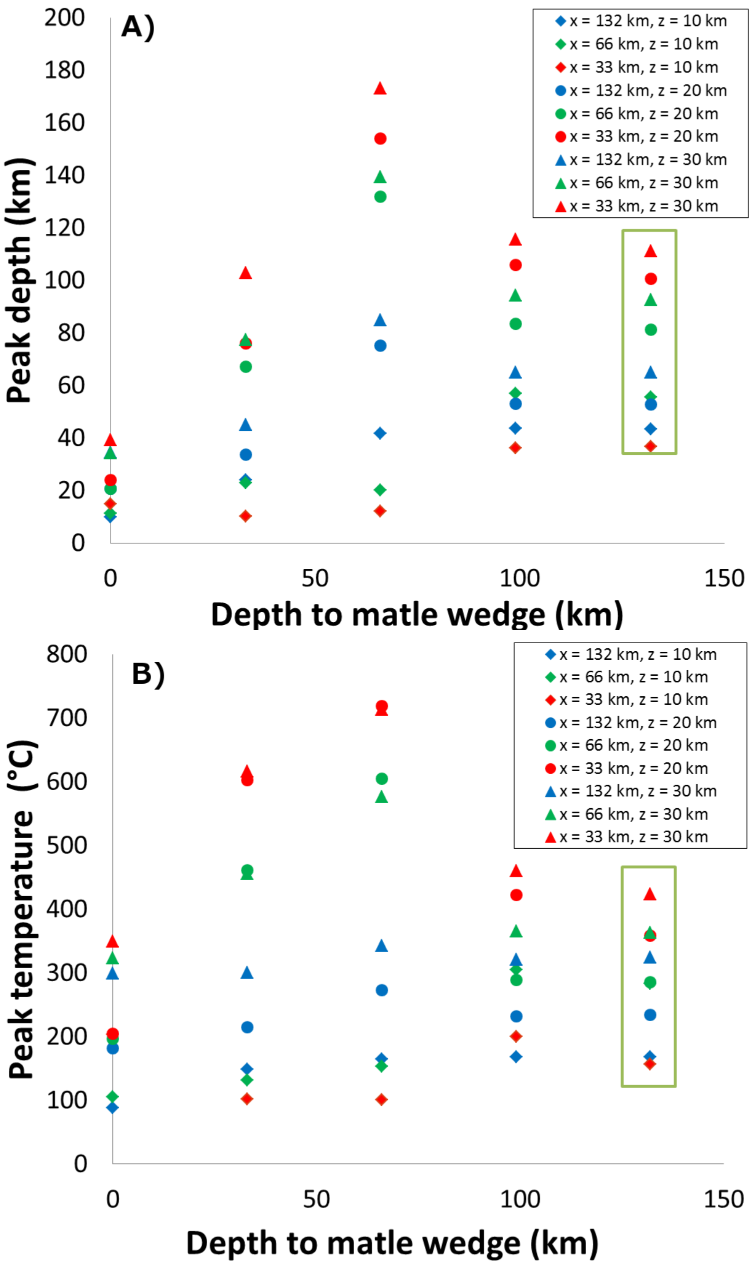

Figure 5.18: Peak depth and temperature with respect to the depth to the mantle wedge - A)shows the relationship between peak depth reached by the markers and the depth to the mantle wedge. B) shows the relationship between peak temperature reached and the depth to the mantle wedge. Symbols are as defined in Fig. 5.8.

5.3.3 Simple eduction relationships

These results demonstrate that the dominant controls on eduction are the buoyancy forces involved in the subduction and continental collision process. This is illustrated by the fact that the three parameters that have the greatest effect on the peak depth and temperatures achieved are the crustal thickness, thickness of the oceanic and continental lithosphere, all of which significantly affect the average slab density.

The six pairs of individual relationships derived above can be combined to give two relationships that describe the peak pressure or temperature expected for a given subduction system. As the relationships are all linear and independent, we can produce an overall description of the following form:

$$depth_{peak} = (ax + bz + c) + \sum_{i=1}^{nQ} (m_i x + n_i z + o_i) \times (Q_i - Q_{default}) \tag{5.9}$$

$$T_{peak} = (dx + ez + f) + \sum_{i=1}^{nQ} (q_i x + r_i z + s_i) \times (Q_i - Q_{default}) \tag{5.10}$$

where the values of a-f are those calculated at the end of section 5.3.1, Q_i is one of the parameters investigated (Table 5.2) and m,n,o and q,r,s are the corresponding coefficients calculated in 5.3.2.

We use these relationships to predict a value for peak pressure and temperature conditions experienced for all the markers from all the models that were used to create the relationship. We then compare the correlation between the predicted and measured values of peak pressure and temperature. This results in a coefficient of determination $R^2 = 0.58$ between the measured peak pressures and predicted one (Fig. 5.19). For temperature we get a coefficient of determination $R^2 = 0.76$ between measure and predicted values (Fig. 5.20). To further test the relationship we plot the peak pressure and temperatures for a range of models where more than one parameter has been varied (red points, Fig. 5.19 & 5.20). These points plot around the 1:1 line showing that our simple relationship is capable of predicting the peak pressure and temperatures that a marker will experience.

Overall this shows that our simple relationship allows parameterisation of the peak P-T conditions experienced by continental material in terms of the physical subduction set-up. This is useful as it allows a quick calculation of expected peak depths and

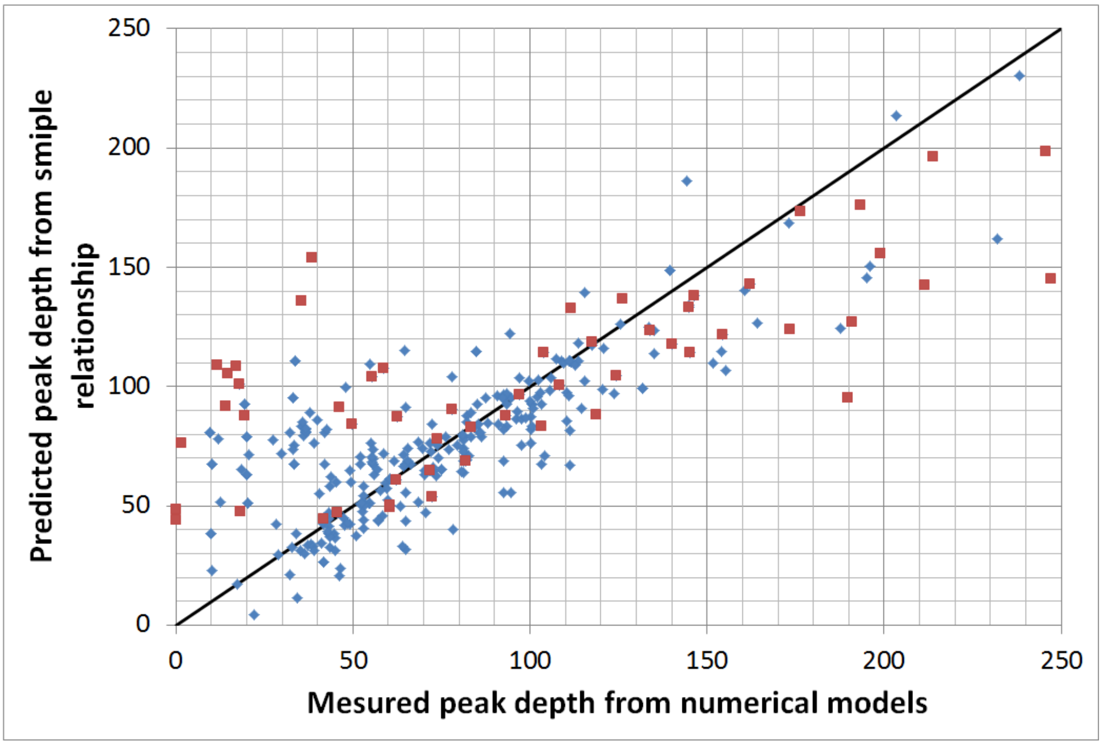

Figure 5.19: Analysis of peak depth predictions fit with model results - measure peak depth from our numerical models against predicted values from our simple relationship. The blue points are from models that were used to create the simple relationship. Red points are for models with multiple input parameters varied.

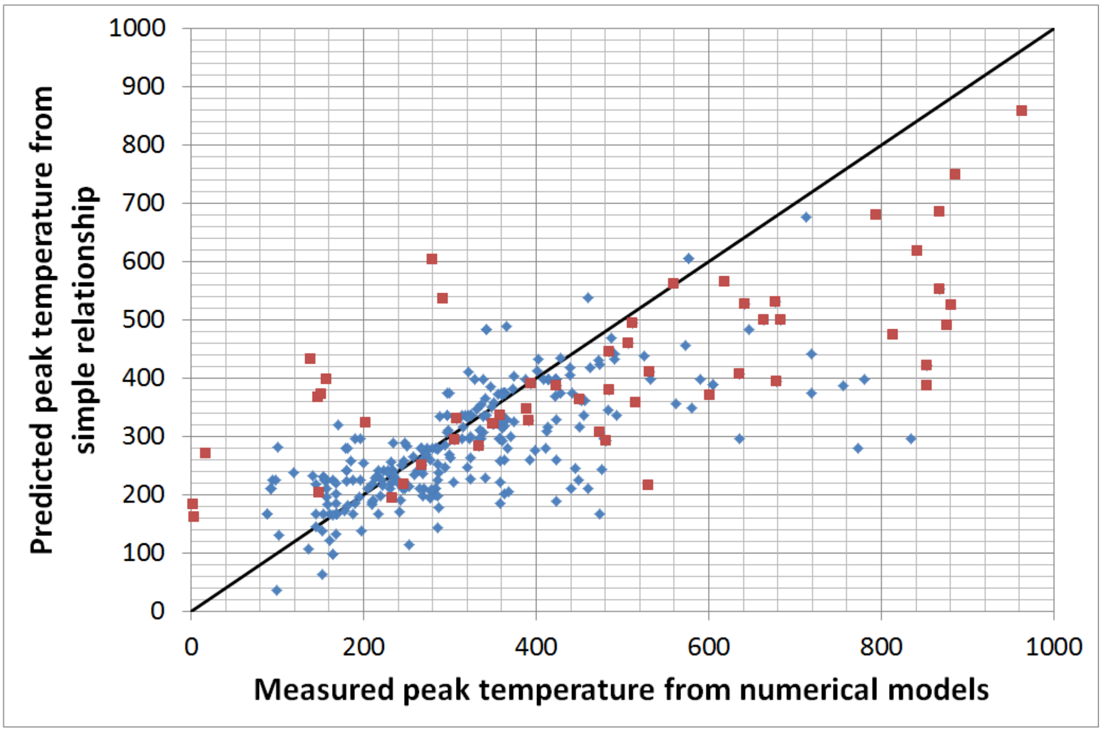

Figure 5.20: Analysis of peak temperature predictions fit with model results - measure peak temperature from our numerical models against predicted values from our simple relationship. The blue points are from models that were used to create the simple relationship. Red points are for models with multiple input parameters varied.

temperatures for educted material for any given collision zone. Conversely it also allows us to estimate the physical nature of a subduction system that educted material for which there are petrological P-T estimates.

5.4 Discussion

Our results firstly show that eduction can exhume material that has travelled a clockwise P-T path and experienced temperatures and pressures close to those predicted for the WGC. However there are a number of model parameters that control the peak pressure and temperature conditions achieved. Here we will discuss how we can use these results and data from the Western Gneiss Complex to categorise the type of subduction and collision system where UHP terranes can be formed by eduction.

The WGC shows a change in metamorphic grade from high pressure and temperatures near the coast to lower grade inland (Fig. 5.21) [Hacker *et al.*, 2010; Brueckner & Cuthbert, 2013]. This is interpreted as evidence that WGC is an exhumed terrane which entered the subduction zone and was subsequently returned to the surface as one coherent unit. Peak pressure and temperature maps for this region Hacker *et al.* [2010] show a change in peak pressure from NW to SE of ∼11 MPa/km. This compares favourably with our models that show a decrease in peak depth with distance from the front of the subducting plate of 0.43 km/km or 14 MPa/km as calculated in Section 5.3.1. Estimates of the spatial variation of temperature for the WGC from Hacker *et al.* [2010] give a temperature gradient of 3°C/km. This compares less favourably with our model where we predict only a 1.5-0.6°C/km temperature gradient (Fig. 5.6).

The depth within Baltica at which the material that now makes up the WGC was initially situated pre-collision, is harder to estimate. However it is thought that the protoliths of the HP-UHP WGC rocks are mainly Middle Proterozoic (∼ 1700 to 950 Ma) orthogneisses [Tucker *et al.*, 2004]. These rocks are thought to have made up the metamorphic basement of Baltica and so pre-collision were located in the lower crust [Tucker *et al.*, 2004]. Our models show that crustal material that was positioned close to the surface pre-collision is readily accreted onto the overriding plate and does not subduct and subsequently educt. This fits with the observation that the protolith of the WGC was lower crustal material. We also find that markers that started deeper achieve higher pressure and temperature conditions that fit with the mapping of the

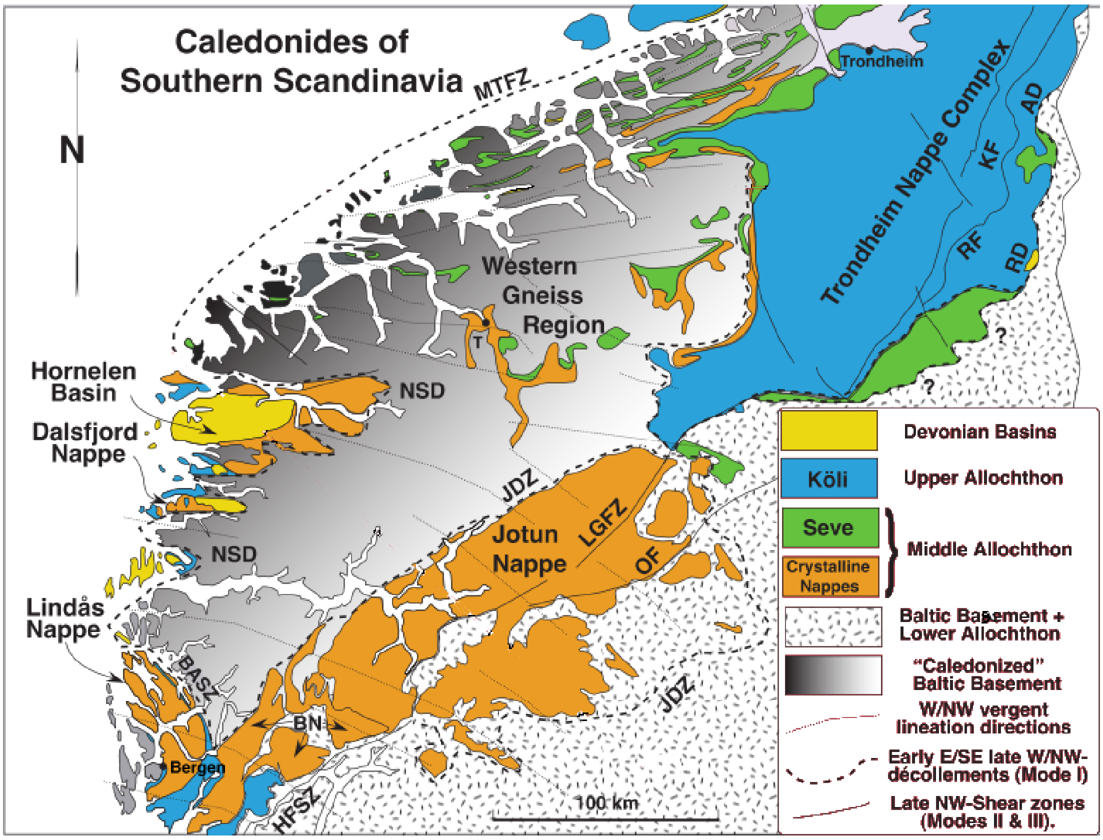

Figure 5.21: Map of major structure and tectonic units in the western Gneiss - Reproduced from Brueckner & Cuthbert [2013]. The grey shading shows the variation in metamorphic grade in the Baltic Basement. It also shows the two large Nappe structures (orange and blue) that are proposed to have formed in the accretionary prism and then ridden on top of Baltica as it educted. Thick dashed lines are approximate positions of and possible relationships between major, top-W mode I detachments developed during the exhumation of the Western Gneiss Region (ÅD - Åre detachment; BASZ - Bergen Arcs shear zone; JDZ - Jotunheimen detachment zone [aka basal Jotun thrust]; MTFZ - Møre Trondelag fracture zone; NSD - Nordfjord-Sogn detachment zone [includes the Sandane shear zone]; RD - Røranger detachment). Thin NE and NW-trending continuous lines are approximate positions of selected later, high-angle, ductile/brittle extensional faults (HSZ - Hardangerfjord shear zone; LGFZ - Laerdal-Gjende fault zone; OF - Olestøl fault; KF - Kopperå fault; Røranger fault). Thin dotted ENE to SW trending lines represent shear sense trajectories during the exhumation of the Western Gneiss Complex (generalized from [Fossen, 1993, 2010; Hacker *et al.*, 2010]. Most shear senses are top to the W/SW imprinted on an earlier top to E/SE thrust fabric.

highest pressure material being found in glacially eroded fjords on the west coast of Norway. This has been interpreted as evidence for higher grade material situated below the current surface exposure of the Western Gneiss [Vrijmoed *et al.*, 2006]. The relationships found in Section 5.3.1 for the peak temperature and depth with respect to the pre-collisional start position, show that both peak depth and temperature are strongly influenced by the crustal materials pre-collisional position in the subducting plate's continental block.

Investigating the model set up parameters that affect the peak pressures and temperatures, the dominant parameters were found to be the crustal and lithosphere thickness (both oceanic and continental). Our results demonstrate that, in order to transport crustal material to the depths experienced by the WGC, the oceanic lithosphere needs to be dense, and hence old and thick. For models with very thin oceanic lithosphere we see that slab break-off occurs rapidly after the onset of continental subduction. This prevents material reaching UHP depth, but also from heating up significantly, since it is held at depth for less time. The need for old oceanic lithosphere fits with the published plate reconstructions [Torsvik *et al.*, 1996, 2012; Cocks & Torsvik, 2002] for the collision of Laurentia and Baltica, where the Iapetus ocean that separated Laurentia and Baltica is >1000 km wide at 500 Ma (around the start of closure).

The thickness of the continental crust in the subducting plate also has a strong influence on the depth and temperature that crustal material reaches. For the continental lithosphere thickness in our reference model, a crustal thickness <25 km fails to stop subduction, although this value will also be dependent on the continental lithosphere thickness. However we also find that thick crust increases the buoyant resistance to subduction and so crustal material doesn't get as deep. From this we can infer that the crust on the Baltica margin must have been relatively thick (30-40 km), especially considering that some crustal material is likely to have been accreted into an accretionary prism, that is suggested to have been passively transported during eduction and presently form the bounding nappe structures [Carswell *et al.*, 2003; Brueckner & Cuthbert, 2013]. We would estimate the crustal thickness for Baltica to have been in the range of 30-40 km as this provides sufficient buoyancy to stop subduction but not so much that crustal material never reaches sufficient depths. The eduction mechanism also requires strong crustal material, including a strong lower crust to prevent accretion of crustal material at the trench [Ghazian & Buiter, 2013].

The continental lithosphere thickness also has an influence over the peak P-T conditions crustal material experiences. Reducing the continental lithosphere thickness has the effect of 1) reducing the negative buoyancy that will drag the continental material into the mantle but 2) also increasing the initial temperature of crustal material 3) reducing the strength of the plate. Our results show that the markers' initial temperatures (set by the lithosphere thickness) dominates over any additional heating material experiences by material transported to greater depths due to increased negative buoyancy with increased lithosphere thickness. Our results also demonstrate that eduction is not possible with very thin continental lithosphere due to the plate being so weak that break-up of the continental block occurs before continental subduction. This is a problem for our models since to achieve the published temperature estimates for the WGC the lithosphere has to be made too thin to support eduction due to the continental plate being too weak. This result suggest that for the WGC to form via eduction Baltica must have had a thick mechanically strong lithosphere. However to fit with the peak temperature estimates for the WGC, crustal material may have been held at depth longer than in our model or exposed to an additional heat source during its ascent to the surface.

Both these results demonstrate that for eduction to happen the buoyancy provided by continental crust needs to be higher that the negative buoyancy provided by the lithosphere. In other words subduction of continental material happens when the subducting plate's excess density is positive and eduction occurs when the plates excess density becomes negative due to the loss of the slab pull force. Our models contain a simplified density structure for the continental crust and lithosphere but to recreate successful subduction and eduction our excess density values can be assumed to be approximately correct for Earth's collision zones.

The depth to the mantle wedge (overriding lithosphere thickness) controls the thermal structure of the subduction zone so a shallower mantle wedge heats up subducted crustal material more. However, a shallower depth to the mantle wedge in our models also weakens the front portion of the overriding plate and so promotes accretion of material across the subduction interface on to the overriding plate. Therefore, to be able to successfully subduct crustal material to depth and then educt it, a strong overriding plate is required. The WGC was formed when Baltica collided with and partially subducted under Laurentia at around 430-410 Ma. At that time, Laurentia was probably already an old, cold, and therefore strong plate, since it contained the Archean craton that presently forms the centre of the North American plate.

Both the radius of the subduction interface and its viscosity have a minor effect on the peak P-T values that crustal material reaches. It is therefore difficult to gain any insight into potential values for these parameters for the exhumation of the WGC. It is likely that the plate interface in the Laurentia-Baltica collision was weak and remained weak throughout the collision to assist the eduction process. Our previous work on topography Chapter 3 & 4 [Bottrill *et al.*, 2012] indicates that the angle of the subduction interface may well change through the collision process. However the subduction angle remaining shallow would likely assist eduction due to being energetically favourable as less bending of the subducted slab is required during eduction.

Using our simple relationship between physical parameters of the subduction system and the peak temperature and pressure conditions that can be reached, we can now attempt to find the best-fitting model for the WGC region. This model is very similar to the reference model, but with 100 km continental lithosphere in the subducting plate and a 30 km thick crust (Fig. 5.22).

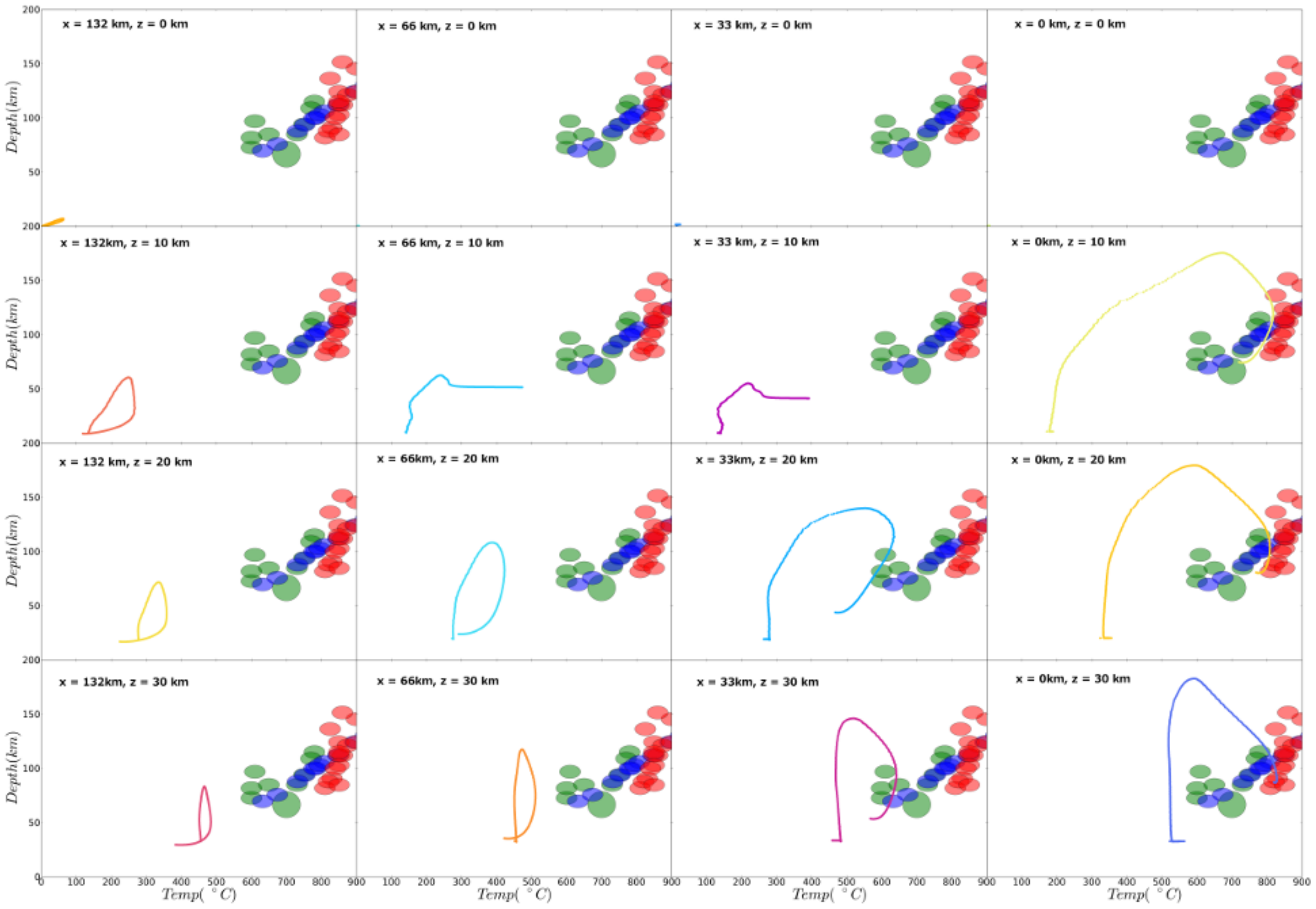

Figure 5.22: P-t paths for best fit model - Model has 30 km thick crust and 100 km thick lithosphere for the subducting plate's continental block. P-T paths for the 16 markers that started in the front portion of the subducting plate's continental block. The P-T paths positioning in the figure represent the markers initial position in the continental block with markers starting at 0, 33, 66, 132 km from the edge of the continental block and 0, 10, 20, 30km depth. Peak P-T estimates from the WGC are as described in Fig. 5.7.

Fig. 5.22 demonstrates that although the majority of the markers in our optimised model achieve the petrological pressure estimates for the WGC only a few manage to achieve the peak temperature estimates. Our simple relationships indicate that these higher temperatures could be obtained by further reducing the lithosphere thickness for both the continental regions in the subducting and overriding plate. However models run with a thinner subducting continental lithosphere rift before slab break-off occurs and models with a shallow mantle wedge accrete the majority of markers into the overriding plate before they are subducted. We can therefore conclude that to successfully educt HP/UHP back to crustal levels the subduction system needs to satisfy three conditions:

1. The competing buoyancy forces from the low density crust and dense lithosphere need to be such that crust is subducted to sufficient pressure before slab break-off but rises buoyantly once the slab has detached.
2. Both the subducting and overriding plate need to be sufficiently strong so as to remain coherent throughout both the subduction and eduction phases.
3. The subduction interface needs to remain sufficiently weak after collision to assist the eduction phase.

The ability of our preferred model to successfully reproduce the peak pressure conditions of UHP metamorphic material from the WGC indicates that the buoyancy forces responsible for continental subduction, slab break-off and eduction might be similar to those operating during the collision between Laurentia and Baltica. However the failure of our crustal material to reach the petrological estimates for temperature indicates that our simple model does not fully reproduce the dynamics of the subduction eduction event that the WGC experienced. We argue that this extra temperature is not due to the thermal structure of the subduction system, since such higher geothermal gradient would likely weaken the plate beyond the point where eduction is still possible. Instead we suggest that the higher peak temperatures are due to a pausing of crustal material at depth for longer than in our models. This could be achieved by older oceanic lithosphere which would take longer to break off, but would also pull the crust deeper. However more likely for the WGC is that continued subduction to further along the trench stalls material at depth, and allows it to further heat up. The effect of continued subduction further along the collision system is investigated in the following Chapter 6.

6

Plate rotation and exhumation

Plate rotation during continental collision and its relationship with the exhumation of UHP metamorphic terranes: application to the Norwegian Caledonides.[1]

Lateral variation and asynchronous onset of collision during the convergence of continents can significantly affect the burial and exhumation of subducted continental crust. Here, we use 3D numerical models for continental collision to discuss how deep burial and exhumation of high and ultrahigh pressure metamorphic (HP/UHP) rocks are enhanced by diachronous collision and the resulting rotation of the colliding plates. Rotation during collision locally favours eduction, the inversion of the subduction, and may explain the discontinuous distribution of ultra-high pressure (UHP) terranes along collision zones. For example the terminal (Scandian) collision of Baltica and Laurentia, which formed the Scandinavian Caledonides, resulted in the exhumation of only one large HP/UHP terrane, the Western Gneiss Complex (WGC), near the southern end of the collision zone. Rotation of the subducting Baltica plate during collision may provide an explanation for this distribution. We explore this hypothesis by comparing orthogonal and diachronous collision models and conclude that a diachronous collision can transport continental material up to 60 km deeper, and heat material up to 300°C hotter, than an orthogonal collision. Our diachronous collision model predicts that subducted continental margin material returns to the surface only in the region where collision initiated.

The diachronous collision model is consistent with petrological and geochonological observations from the Western Gneiss Complex and makes predictions for the general evolution of the Scandinavian Caledonides. We propose the collision between Laurentia and Baltica started at the southern end of the collisional zone, and propagated northward. This asymmetric geometry resulted in the counter clockwise rotation of Baltica with respect to Laurentia, consistent with paleomagnetic data from other studies. Our model may have applications to other orogens with regional UHP terranes, such as the Dabie Shan and Papua New Guinea cases, where block rotation during exhumation has also been recorded.

---

[1] This chapter is slightly modified from the publication Bottrill, A.D., van Hunen, J., Cuthbert, S.J., Brueckner, H.K. & Allen, M.B. (2014). Plate rotation during continental collision and its relationship with the exhumation of uhp metamorphic terranes: Application to the norwegian caledonides. *Geochemistry, Geophysics, Geosystems*, doi:10.1002/2014GC005253. All the numerical experiments produced for the manuscript were done by A. D Bottrill who would like to acknowledge the useful discussions, training, support and extensive knowledge of the Western Gneiss Complex provided by his co-authors.

6.1 Introduction

The study of high pressure/ultra-high pressure (HP/UHP) metamorphic rocks is important as these rocks offer an insight into lithospheric conditions as well as providing useful constraints on the continental collision process [Dobrzhinetskaya *et al.*, 2011a; Warren, 2013]. Exhumed HP/UHP rocks are present in most Phanerozoic collision zones [Dobrzhinetskaya *et al.*, 2011b] and probably resulted from the subduction of one continental margin beneath another, but their exhumation mechanisms and resultant structures vary. A number of different mechanisms have been proposed for the return of HP/UHP rocks to the surface, ranging from whole scale return of the subducted plate to exhumation of small supracrustal slivers [Kylander-Clark *et al.*, 2012]. Numerical modelling work by Burov *et al.* [2001] shows how return flows generated in the subduction channel can return subducted continental crust to the surface. Others have shown how exhumation can occur when the buoyancy of subducted continental crust exceeds the shear traction exerted on it by its underlying lithosphere [Warren *et al.*, 2008b], resulting in its return toward the surface as a coherent slab. Furthermore, eduction has been proposed [Dixon & Farrar, 1980; Andersen *et al.*, 1991] where the subduction trajectory is completely reversed, bringing the whole plate (crust and lithosphere) back to the surface. The need for different exhumation mechanisms is a reflection on the variety in size and structure of UHP terranes [Kylander-Clark *et al.*, 2012]. This study focuses on eduction as a mechanism for returning HP/UHP metamorphic terranes to the surface (we follow the convention that UHP rocks are those that have equilibrated at pressures above the minimum stability of coesite; some such rocks are known to have formed at pressures well into the P-T stability field of diamond see [Dobrzhinetskaya *et al.*, 2011a]). The force balance for the reversal of plate motion is explored by Duretz *et al.* [2012] who show that slab break-off removes the slab pull force allowing the partially subducted buoyant continental plate to return back up along the original subduction trajectory. This bulk movement of the partially subducted continental block and its underlying mantle lithosphere back along the original subduction path reverses the shear sense on the upper subduction interface and has the potential of exhuming large quantities of continental material in one coherent section. This mechanism is favoured for large terranes as it explains both the size and structural coherence of exhumed crustal material. An example of a large HP/UHP terranes is the Norwegian

Western Gneiss Complex (WGC) in the southern Scandinavian Caledonides, [Andersen *et al.*, 1991; Teyssier, 2011; Brueckner & Cuthbert, 2013].

The Western Gneiss Complex (WGC) is one of the largest exposed HP/UHP terranes currently preserved on earth. It formed during the terminal Caledonian collision between the continents Laurentia and Baltica. This collision, known as the Scandian Orogeny, occurred in the Silurian [Dewey & Strachan, 2003]. The collision dynamics are complicated by the earlier collisions of a number of continental and island arc fragments [Brueckner & van Roermund, 2004] but paleomagnetic evidence suggests the final collision started in the south then closed progressively towards the north [Torsvik *et al.*, 2012]. The WGC is considered to represent the continental margin of Baltica that underwent deep but transient subduction beneath Laurentia during collision, followed by wholesale exhumation [Hacker *et al.*, 2005; Hacker, 2007; Brueckner & Cuthbert, 2013]. A map of the major tectono/stratigrapic units and structures is provided in Appendix (Figure 5.21) adapted from Brueckner & Cuthbert [2013].

The metamorphism recorded in the WGC shows a progression in metamorphic grade, from ultra-high pressures recorded in the northwest to weakly metamorphosed in the southeast [Hacker *et al.*, 2010]. The pressures experienced by the westernmost portion of this terrane are thought to have been particularly high as some lithologies contain coesite [Smith, 1984; Wain, 1997; Cuthbert *et al.*, 2000; Terry *et al.*, 2000; Walsh & Hacker, 2004; Butler *et al.*, 2013] and micro-diamonds [Dobrzhinetskaya *et al.*, 1995; van Roermund *et al.*, 2002; Vrijmoed *et al.*, 2006], which are consistent with thermobarometric estimates of pressure temperature (P-T) conditions of up to 5 GPa and 900 °C [Cuthbert *et al.*, 2000; Terry *et al.*, 2000; Carswell *et al.*, 2006; Vrijmoed *et al.*, 2006] and indicate subduction of continental crust to depths of as much as 165 km. This progression in metamorphic grade has been interpreted as evidence that Baltica was subducted northwestward (present coordinates) beneath Laurentia [Krogh, 1977; Griffin *et al.*, 1985; Hacker *et al.*, 2010], metamorphosed under HP/UHP conditions, and then returned, as the WGC, to the surface as one quasi-coherent unit [Andersen *et al.*, 1991; Wilks & Cuthbert, 1994; Brueckner, 2006; Warren *et al.*, 2008a]. The timing of collision and continental subduction in the southern Norwegian Caledonides is constrained by the development of a clastic fill in a foredeep basin during Ludlow to Pridoli times, from 427-419Ma [Davies *et al.*, 2005], by early eclogite development in the associated Linds Nappe at ∼430 Ma [Glodny *et al.*, 2008], and by the older ages obtained from UHP eclogites and garnet pyroxenites in the WGC at around 434-425 Ma [Kylander-Clark *et al.*, 2007; Spengler *et al.*, 2009], which probably document subduction after initial collision. Collision is unlikely to have initiated earlier than 434.0 ± 3.9 Ma, the age of a pre- or syn-collisional granite intruded into an ophiolite/arc unit in the Upper Allochthon [Hacker *et al.*, 2003]. WGC eclogite mineral ages continue to range down to about 400 Ma, with a few as young as 370 Ma, indicating that parts of the WGC remained at mantle depths until at least that time [Kylander-Clark *et al.*, 2009]. A review of the age patterns in the WGC as well as evidence for the reversal of shear sense between the allochthons and the WGC suggests the transition from subduction to eduction occurred at ∼405 Ma [Brueckner & Cuthbert [2013] and references therein].

The WGC outcrops within a very large tectonic window and is separated by a major shear zone from two overlying thrust-nappe complexes, the Jotun nappe complex of the Middle Allochthon and the Trondheim nappe complex of the Upper Allochthon, which outcrop to the east and southeast of the WGC, respectively, and which have further equivalents in the western coastal region (Figure 5.21) [Hacker *et al.*, 2005; Andersen & Austrheim, 2008; Milnes & Corfu, 2008; Gee *et al.*, 2010]. These allochthons comprise the Scandian orogenic wedge created during the early phases of Caledonian (Scandian) Laurentia-Baltica collision. Brueckner & Cuthbert [2013] have recently argued that this orogenic wedge was ruptured during the reversal of shear sense between the WGC and the allochthons, and the Jotun and Trondheim Nappe Complexes were then further transported piggy-back on top of the educting WGC to their current position. This deformation of the wedge was argued to have also resulted in the formation of the Devonian intra-montane basins that lie along the west coast of southern Norway. As noted above, motion reversal in the subduction channel and the initiation of eduction is thought to have happened at about 405Ma [Brueckner & Cuthbert, 2013] after which the WGC cooled to Ar^{40}-Ar^{39} closure temperatures of white mica by 397-380 Ma [Walsh *et al.*, 2013]. The youngest Ar-Ar ages are broadly coincident with depositional ages in the intra-montane basins [Wilks & Cuthbert, 1994]. Final exhumation of the WGC is not well constrained as no detritus from it is recognisable in the intra-montane basins [Cuthbert *et al.*, 1983], but the most deeply subducted material now at outcrop had reached normal mid-crustal depths by about 380 Ma, giving a total interval of ∼50 Ma from collision to the approximate end of eduction.

Ar-Ar cooling ages for the WGC are 20 Myr older in the southeast portion of its outcrop area than in the northwest [Walsh *et al.*, 2013] suggesting again that exhumation occurred progressively from southeast to northwest, which is consistent with eduction towards the south-east. The process of whole-lithosphere eduction as an exhumation mechanism for the WGC remains controversial; for example exhumation as a giant flake or nappe up to 14 km thick has been proposed [Carswell *et al.*, 2003], but to date no convincing basal thrust to accommodate transport of such a large mass has been discovered. The presence of basement-involved eclogite-bearing allochthons such as the Lindås nappe [Glodny *et al.*, 2008] and the upper basement unit in the Trollheimen-Moldefjord region [Robinson, 1995] undoubtedly indicate that the Baltica margin underwent at least superficial imbrication during the early stages of its subduction, hence some crustal flakes or nappes may have exhumed by extrusion along the subduction channel. However, this cannot explain the exhumation of the remaining, much larger, structurally underlying mass of the HP WGC. Hence, in the absence of convincing evidence for a basal thrust zone, we prefer a mechanism involving wholesale withdrawal (eduction) of the Baltica margin from the subduction channel while still attached to the rest of the Baltic craton as well as the underlying lithosphere.

Exhumation by eduction relies on a change in the force acting on the subducting continental margin. One way to achieve this is the breaking off of the dense oceanic slab to allow the buoyant continental block to exhume. Slab break-off has been proposed as one of the final stages of continental collision [Davies & von Blanckenburg, 1995], and imaged with tomography for a number of collision zones [Nolet, 2009], as well as being inferred from earthquake gaps [Roecker, 1982]. Slab break-off may also be regarded as the trigger for exhumation as a result of the release of “slab pull”. Slab-breakoff probably occurs by lateral tearing along the subducted slab [Yoshioka *et al.*, 1995; Wortel & Spakman, 2000; van Hunen & Allen, 2011,chapter 4] and is suggested to be responsible for topographic depressions that propagate along collision zones [van der Meulen *et al.*, 1998; Sperner *et al.*, 2001]. Slab tearing has been shown to start where collision first occurred [van Hunen & Allen, 2011]. The force balance for the continental collision and slab break-off [Duretz *et al.*, 2012] is influenced by the buoyancy of the partially subducted continental plate which will cause return of subducted material once the slab pull force has been removed. If the subducted continental material remains strong and coherent, this return will take the form of wholesale plate eduction. Far field forces that act on the subduction system also need to be considered as they could assist in the eduction process [Fossen, 2010; Brueckner & Cuthbert, 2013]. Considering the likelihood of the propagation of break-off along the collision zone, we expect there would also be variation in timing and amount of material exhumation along the collision zone. The exact nature of the Iapetus subduction system and slab detachment between Laurentia and Baltica is still debated [Andreasson *et al.*, 2003; Fossen, 2010] though the majority of evidence suggests a westward subduction of Baltica under Laurentia.

Here we examine numerically the exhumation of HP/UHP rocks after collision, subduction and slab break-off, and investigate the differences in exhumation patterns produced by diachronous versus orthogonal collisions. We present two 3D dynamic numerical models of the closure of an oceanic basin; a first where collision occurs all along the collision zone at the same time (orthogonal collision), and a second where collision initiates at one end and propagates along the collision system (diachronous collision). These models are then compared to pressure, temperature and time (P-T-t) estimates from the WGC.

6.2 Methodology

To assess the role of an oblique collision and associated plate rotation on the exhumation of UHP terranes we developed 3D numerical flow models of continental collision and slab break-off. Synthetic pressure-temperature-time (P-T-t) paths are calculated so that they can be compared to field observations. The numerical model uses a Cartesian, incompressible-flow version of the finite element geodynamical code Citcom [Moresi & Gurnis, 1996; Zhong *et al.*, 2000; van Hunen & Allen, 2011]. In the model setup, we adopt the Boussinesq approximations. Conservation of mass, momentum, energy and composition is applied using the following non-dimensional governing equations

$$\nabla \cdot \mathbf{u} = 0 \tag{6.1}$$

$$-\nabla P + \nabla \cdot (\eta(\nabla \mathbf{u} + \nabla \mathbf{u}^T)) + (RaT + RbC)e_z = 0 \tag{6.2}$$

$$\frac{\partial T}{\partial t} + \mathbf{u} \cdot \nabla T = \nabla^2 T \tag{6.3}$$

$$\frac{\partial C}{\partial t} + \mathbf{u} \cdot \nabla C = 0 \tag{6.4}$$

where $\mathbf{u}$ is the velocity, P is the deviatoric pressure, η the viscosity, Ra the thermal Rayleigh number, Rb the compositional Rayleigh number, e_z the vertical unit vector, C a material parameter that distinguishes crust from mantle material, T the temperature and t is time.

In this setup, flow of material is driven by combined thermal and compositional buoyancy. The continental material is advected, in accordance with equation 6.4, using particle tracers [Di Giuseppe *et al.*, 2008]. These tracers are also used as passive markers to monitor the P-T-t path of individual pieces of the continental plate that enter the subduction zone.

The models in this study simulate the closure of an oceanic basin leading to continental collision, partial subduction of continental material, slab detachment and subsequent exhumation. The two initial model setups investigated are shown in Fig. 6.1. We present the model rotated, compared to previous models, so that subduction runs right to left. This aids comparison of the model with the Laurentia-Baltica collision where subduction was east to west. The computational domain is 660 km by 2640 km by 2640 km giving a 4:4:1 aspect ratio in x,y,z, where the x-direction is perpendicular to the collision zone, and the y-direction is parallel to the collision zone, and the z-direction is downwards. The models use a non-deformable Cartesian grid with a high resolution region in the top 200 km and between x = 1700 km and x = 2200 km over the collision zone. This gives a grid resolution, over the collision zone, of 10 km by 20 km by 10 km in the x,y,z directions respectively (see Appendix Fig. 8.9 and 8.10 for a representative cross section through the grid and results of a resolution test, respectively).

Flow boundary conditions for the model are free-slip on the top and sides and no-slip on the base. These boundary conditions do not allow any flow through the model boundaries. This means that all forces that drive subduction, such as slab pull, are generated internally in the model. The no-slip boundary condition at the base of the model is designed to simulate the interaction of a slab with a higher viscosity lower mantle. The thermal boundary conditions are 0°C at the surface and a mantle temperature of 1350°C at the base of the model domain and x = 0 boundary. Keeping

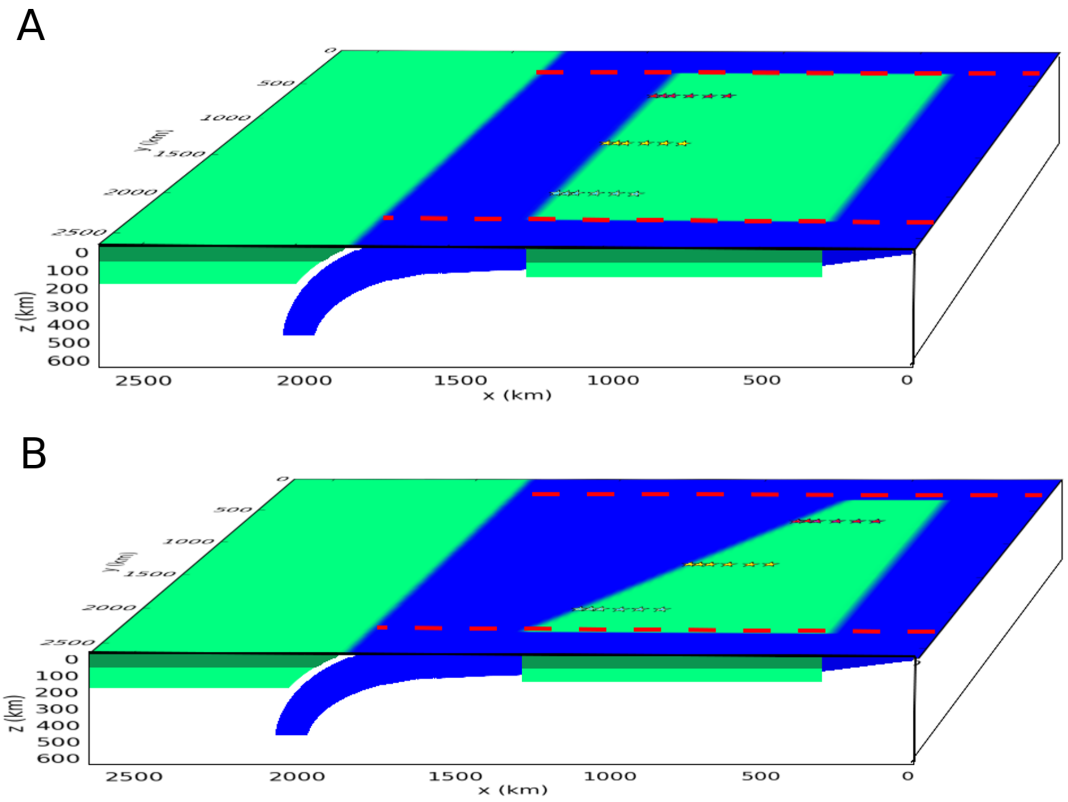

Figure 6.1: Schematic 3D model setup for the collision models. - Models have a computational domain size of 2640 km by 2640 km by 660 km. Both models have a 20 km weak zone and 100 km × 66 km mantle wedge that decouple the two plates. Two transform faults (red dashed lines) cut the subducting plate and decouple it from the model boundaries. The models differ in the shape of the continental block embedded in the subducting plate: A) has a rectangular continental block and will be referred to as the orthogonal collision model. B) has a trapezoid shaped continental block and shall be referred to as the diachronous collision model. Each of the 3 sets of 6 stars represents a family of material markers placed at y = 660, 1320 and 1980 km. Each family contains 24 markers placed in a 6×4 grid in the x-z plane. An example of the position of the markers for one family in x and z directions is shown in Figure 6.2.

the x = 0 boundary at mantle temperature simulates a mid ocean ridge. The other three sides have a zero heat flux boundary condition.

Subduction is initiated by an oceanic slab, hanging down to 400 km depth, sinking into the mantle and facilitated by a 20 km wide zone of weak material between the subducting plate and the overriding plate, as well as a 100 km high and 66 km wide weak mantle wedge. The weak zones are sustained throughout the model calculations and kept at a relatively low viscosity (10^{20} Pa·s) to allow permanent decoupling of the two plates. The model set-up initially has a 60 Myr old oceanic lithosphere subducting to the left under a continental overriding plate. In the y-direction (trench parallel) the 1980 km slab is bounded at y = 330 and 2310 by two 20 km-wide weak zones (viscosity 10^{20} Pa·s) that serve as transform faults (Fig. 6.1). The initial thermal structure (Fig. 6.2) of the oceanic lithosphere is calculated using the half space cooling model, which converts a lithosphere age to a thickness. There is a linear increase in oceanic plate age from 0 Myr at the right edge to 60 Myr at the trench. A thicker, lower density continental block is embedded in the subducting plate with a linear geotherm from 0°C at the surface to mantle temperature of 1350°C at 100 km depth. The thermal structure of the still thicker overriding continental plate is set as a linear geotherm from 0°C at the surface to mantle temperature at 150 km. The thicker lithosphere of the overriding plate is designed to simulate the collision of a smaller continent with a larger cratonic continent.

The 40-km-thick continental crust in the model resists subduction due its compositional buoyancy of 600 kg/m^3. Oceanic crustal buoyancy is ignored in the models, as the assumed transformation of basalt to eclogite of oceanic crust would remove any initial compositional buoyancy [Cloos, 1993]. The transformation to denser rock types such as eclogite within the continental crust would also have an influence on the buoyancy of continental material that is transported to depth. Large HP/UHP terranes such as in the WGC in Norway do indeed contain dense eclogitic rocks but generally eclogite makes up a low percentage of the total rock [Cuthbert *et al.*, 2000]. The limited evidence available from felsic rocks that have escaped the pervasive retrogressive metamorphic overprint indicates that transformation of the dominant granitoid orthogneisses to dense UHP mineral assemblages was very limited [Carswell *et al.*, 2003]. Therefore, for buoyancy purposes, we ignore the complexity of possible phase changes in the continental crust, and assume that, on average, the material that currently makes up terranes such as the WGC lack sufficient dense lithologies to substantially influence the average crustal density.

To investigate possible reasons for differences in the exhumation processes along the collision zone such as those proposed by Fossen [2010] and [Zhang *et al.*, 2009], we compare two end-member models, one with a rectangular shaped continental block (Fig. 6.1A) and the other with a trapezoid shaped continental block (Fig. 6.1B). The rectangular continental block is 1000 km long along both the transform faults, and thus represents an orthogonal collision. The trapezoid shaped continental block is 500 km long along the y =330 km transform fault and 1000 km long along the y =2310 km transform fault. This geometry was chosen as it generates a diachronous collision that propagates along the full length (1980 km) of the subduction zone in ∼20 Myr. The diachronous collision also creates a rotation of the subducting plate, thereby assisting eduction at one end of the subduction zone. The continental block extends over the full 1980 km width between the two transform faults in both models. The overriding plate does not move in the reference frame of the model, extends over the full model width in the y-direction and has a 40 km thick continental crust and a lithosphere that extends down to 150 km.

The strength of the material in our model is governed by temperature and stress-dependent rheology. Four different deformation mechanisms are used: 1), diffusion creep, 2), dislocation creep [Karato & Wu, 1993], 3), a stress limiting rheology [Byerlee, 1978], which weakens material near the surface when under high stresses, and 4) a model maximum viscosity for numerical stability. A more detailed description of the applied rheology is presented in van Hunen & Allen [2011], Bottrill *et al.* [2012] and Chapter 2.

Three families of material markers are placed in the frontal portion of the subducting continental block at y = 660 km (red stars), y = 1320 km (yellow stars) and y = 1980 km (blue stars), and are followed to calculate P-T-t paths (Fig. 6.1 and 6.2). The 1320 km marker-set is in the centre of the continental block whereas the 660-km and 1980-km marker-sets are 330 km inwards from the two edges of the continental block. Each family contains 24 material markers that are placed in a 6×4 grid in the x-z plane with markers at depths of 0, 10, 20, 30 km and at distances of 0, 30, 60, 120, 180, 240 km from the front of the continental block (Fig. 6.2B). When calculating the P-T-t path for the marker, we add an additional vertical thermal gradient $\frac{dT}{dz} = 0.5°\text{C/km}$

to account for adiabatic heating. We define the y = 0 edge of the model as the north edge and the y = 2640 km as the south edge.

Maximum horizontal eduction distances are calculated for each family of markers. Only the markers furthest from the front of the continental block (i.e. 240 km from the front) are used as they only just reach the subduction zone and so have almost no vertical component to their motion. The maximum eduction distance is defined as the maximum horizontal return distance, as measured along the x-axis of the model.

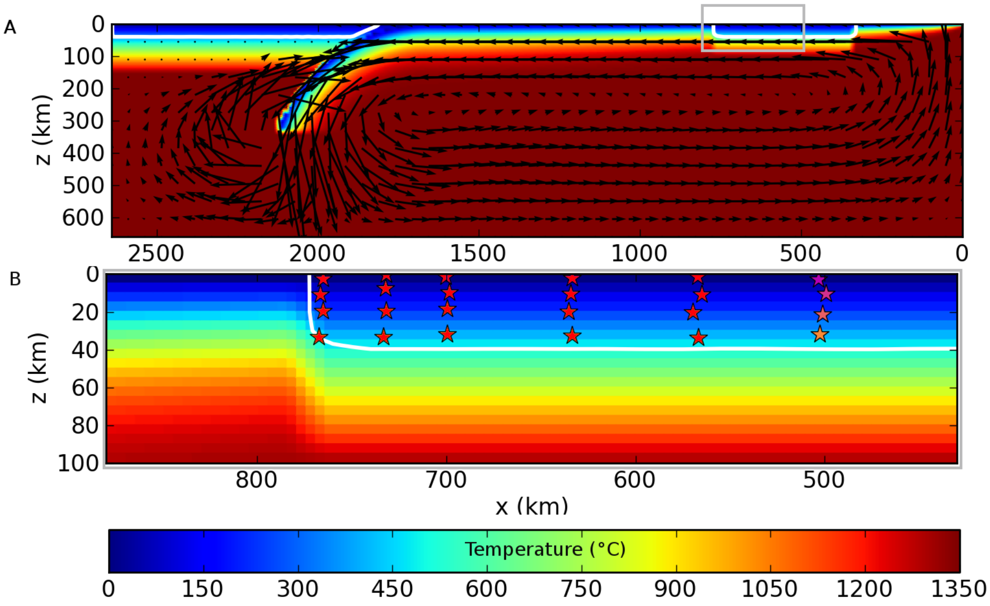

Figure 6.2: Thermal structure of model - A) Initial temperature distribution and velocity vectors at t=0. B) Zoom-in of grey rectangle in A showing the initial positions of one family of markers within the continental crust of the subducting plate. White contour lines outline the continental crust. Markers are initially placed at depths of 0 km, 10 km, 20 km and 30 km, and at distances of 0 km, 30 km, 60 km, 120 km, 180 km and 240 km from the front of the continental block. The model is rotated compared to previously presented models to allow easy comparison with the Laurentia-Baltica collision.

6.3 Results

We first present the dynamics, exhumation patterns and pressure temperature time (P-T-t) paths for the orthogonal collision model, which we then compare with results from the diachronous collision model. For simplicity we only present results for one family of material markers in each model (the middle family at y = 1320 km for the orthogonal collision and the family at y = 1980 km for the diachronous collision). Full results for all material markers for both models are presented in the Appendix 8.4.2.

6.3.1 Orthogonal Collision

The dynamics of an orthogonal collision mode are presented for y =1320 km in cross section (left side) and for all three families of markers in plan view (right-hand side) in Fig. 6.3. The model shows a slowing of the subduction velocity (represented by the lengths of the velocity arrows in Fig. 6.3E,F) after collision, when continental material starts to be subducted. At t = 20 Myr, slab break-off detaches the dense oceanic lithosphere from the buoyant continental block, and changes the average buoyancy of the subducted plate. The partially subducted continental plate therefore returns back towards the surface along the original subduction path (reversed arrows in Fig. 6.3G). This velocity reversal is shown within the slices through the modelling domain (Fig. 6.3C,D) by the movement of the material markers back up the along their original subduction path after slab break-off.

The material markers indicate the movement of the continental crust during collision, subduction, and exhumation. Some of the surface markers are accreted onto the base of the overriding plate during the continental subduction. However, the deeper markers, positioned initially at 10-30 km, are transported to depth along with the front portion of the continental plate. After slab break-off, these markers move backwards, out of the subduction zone, together with the rest of the subducted lithosphere. Fig. 6.3A-D shows that, after eduction, markers that started furthest from the trench are still orientated in the same grid pattern as they started in. The markers in the front portion of the plate experience some reorganisation but generally the continental plate was coherently subducted and then educted as shown by the white contour that outlines the crustal material. The orthogonal model has a horizontal eduction distance of 156 km along the whole length of the collision zone.

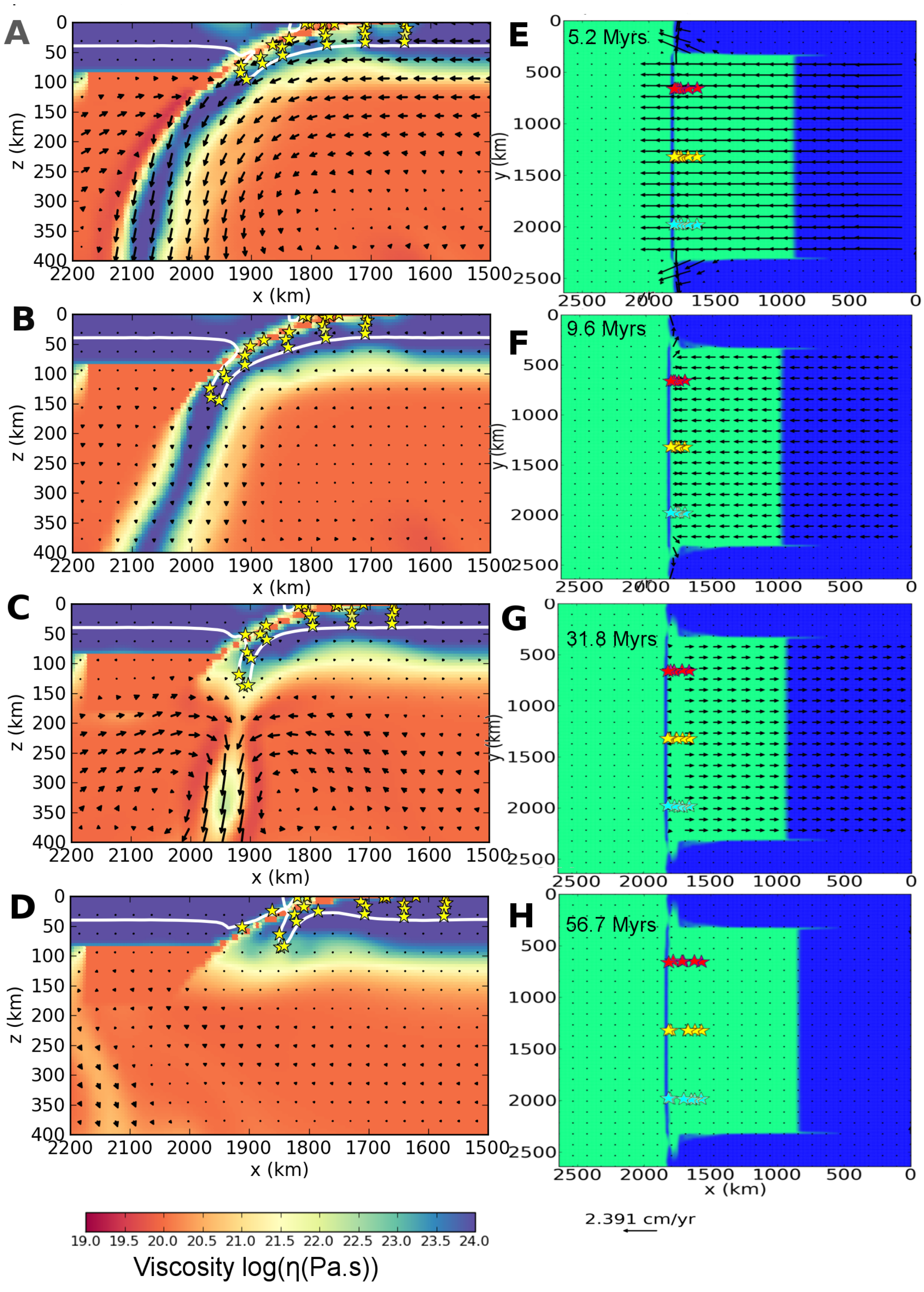

Figure 6.3: Orthogonal collision model dynamics - A-D) Time slices through the centre of the orthogonal collision model, with time increasing from A to D. Colour scheme shows viscosity variations, the white contour highlights crustal material and stars show the positions of followed material markers. E-H) Time snapshots of surface velocity (green = continental material, blue = oceanic material). The stars represent surface markers. Time increases from E to H.

P-T-t paths are presented in Fig. 6.4 for the material markers from the family of markers that started in the centre of the model domain (yellow stars at y =1320 km in Figs. 6.1 and 6.3) and were initially positioned between depths of 10-30 km and at distances 0-120 km from the front of the subducting continental block. P-T paths for all markers from all three families are presented in the Appendix 8.4.2. Similarly positioned markers from the two other families show almost identical P-T-t paths (Appendix Fig. 8.11-8.15), suggesting that a similar quantity and type of exhumed material is produced along the entire collision zone.

A number of the markers reach pressures and temperatures consistent with the production of HP/UHPM material ($>$ 2.7 GPa and $>$ 600°C) [Chopin, 1984]. The markers at the front of the continental block enter the subduction zone first and reach depths of $>$ 150 km (~4.5 GPa) and temperatures 800°C. Even markers that started 120 km from the front of the continental block reach depths of 50 km (~1.5 GPa) and temperatures of 200-400°C. A number of these rearward markers also return successfully to normal crustal levels. Some of the markers in the front of the continental block do not return completely to crustal levels, probably for two reasons: 1) limited exhumation of the whole subducted plate, and 2), markers initially placed at 0 to 10 km depth partly accrete to the overriding plate during exhumation (Fig. 6.3). At all depths there is a gradient in the peak pressures and temperatures achieved by markers (Fig. 6.4), e.g. markers that are in the leading edge of the plate and enter the subduction zone first achieve much higher peak pressures and temperatures than markers further back from the front. The plate educts coherently, therefore the pressure and temperature gradients defined by all markers are preserved in the educted material.

The P-T-t paths show that all the markers reach their peak pressure after ~20 Myr with an average initial burial rate of ~1-2cm/yr followed by a slower phase of burial of ~0.5 cm/yr until the markers reach peak pressure (Fig. 6.4). Exhumation rates are initially ~0.5 cm/yr but slow down even further as the material nears the surface. All the markers that successfully return to crustal depths do so within 40 Myrs after their peak pressure and temperature was reached.

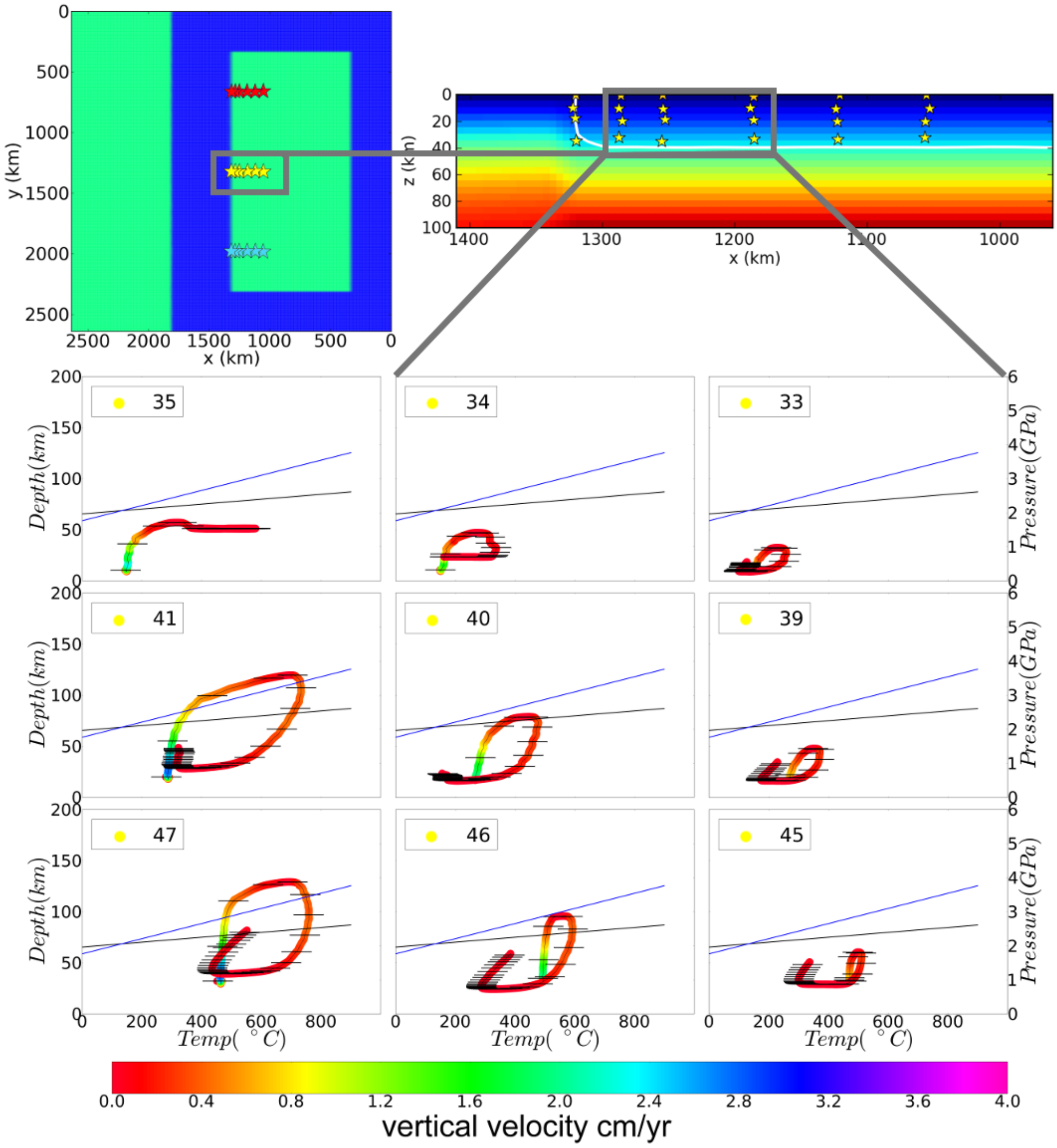

Figure 6.4: Orthogonal collision model P-T-t paths - P-T-t (pressure temperature time) paths for material markers that started in the centre of the orthogonal collision model and were placed, from top to bottom, at 10, 20, 30 km depth and, from left to right at 30, 60, 120 km form the front of the subducting continental block. The shown configuration of P-T-t paths represents the grid in which the markers were originally arranged at the start of the model. The number in the top left of the plot is the markers unique number. The colours of each P-T-t path show the vertical velocity of the material markers. The distances between the black horizontal bars across the paths represent a time period of 5 Myr. The the diamond-graphite (blue line)[Kennedy & Kennedy, 1976] and coesite-quartz (black line) [Bohlen & Boettcher, 1982] are also shown. The total calculation was run for approximately ∼ 150 Myrs.

6.3.2 Diachronous Collision

The large-scale dynamics of a diachronous collision model are illustrated in Fig. 6.5. The plate velocities are initially trench-perpendicular during oceanic plate subduction. Initial collision is in the south (Fig. 6.5E) as a result of the promontory at the southern end of the incoming plate. Collision grades into continental subduction as this promontory slides beneath the overriding plate, and, consequently, subduction velocity reduces in the region of collision. In the meantime collision and subduction continue to the north further along the collision zone, reaching the northern edge of the plate 18 Myr after initial collision (Fig. 6.5F). The decrease in velocity at the point of initial collision causes a counter-clockwise rotation of the subducting plate with the pole of rotation starting below or to the south of the point of initial collision (i.e. outside our modelling domain at $y > 2640$km), but then moves northward along the subduction zone as the point of collision progresses along the subduction zone (Fig. 6.5E, F, G).

Slab break-off in this model starts at 22 Myr, under the region of the subduction zone that first experienced continental collision. A tear is created in the subducted oceanic slab at its contact with the continental leading edge (Appendix 8.4.5), which then propagates northward along the collisional zone until the full width of the oceanic slab (1980 km) detaches at 31 Myr. The break-off results in a reversal in subduction velocity, starting in the area of initial collision in the south at 22 Myr (while subduction continues further along the subduction zone) and moving northward until the entire oceanic slab is detached at 31 Myr (Fig. 6.5G).

The surface markers in each family are accreted onto the upper plate during continental subduction, as they are in the orthogonal collisional model. The deeper markers positioned initially at 10-30 km, however, are transported down along with the front portion of the continental plate (Fig. 6.5). The southernmost markers experience the greatest amount of both burial and eduction compared to the other families of marker further along the collision zone (Appendix Fig. 8.16 - 8.18). The continental plate subducts and exhumes coherently in the diachronous collision model (Fig. 6.5 A-D). A comparison of Fig. 6.5 A-D to Fig. 6.3 A-D also shows that, in the area of initial collision, the diachronous collision model transports crustal material deeper (maximum depth of crustal material 220 km) than the orthogonal collision (maximum depth of crustal material 170 km).

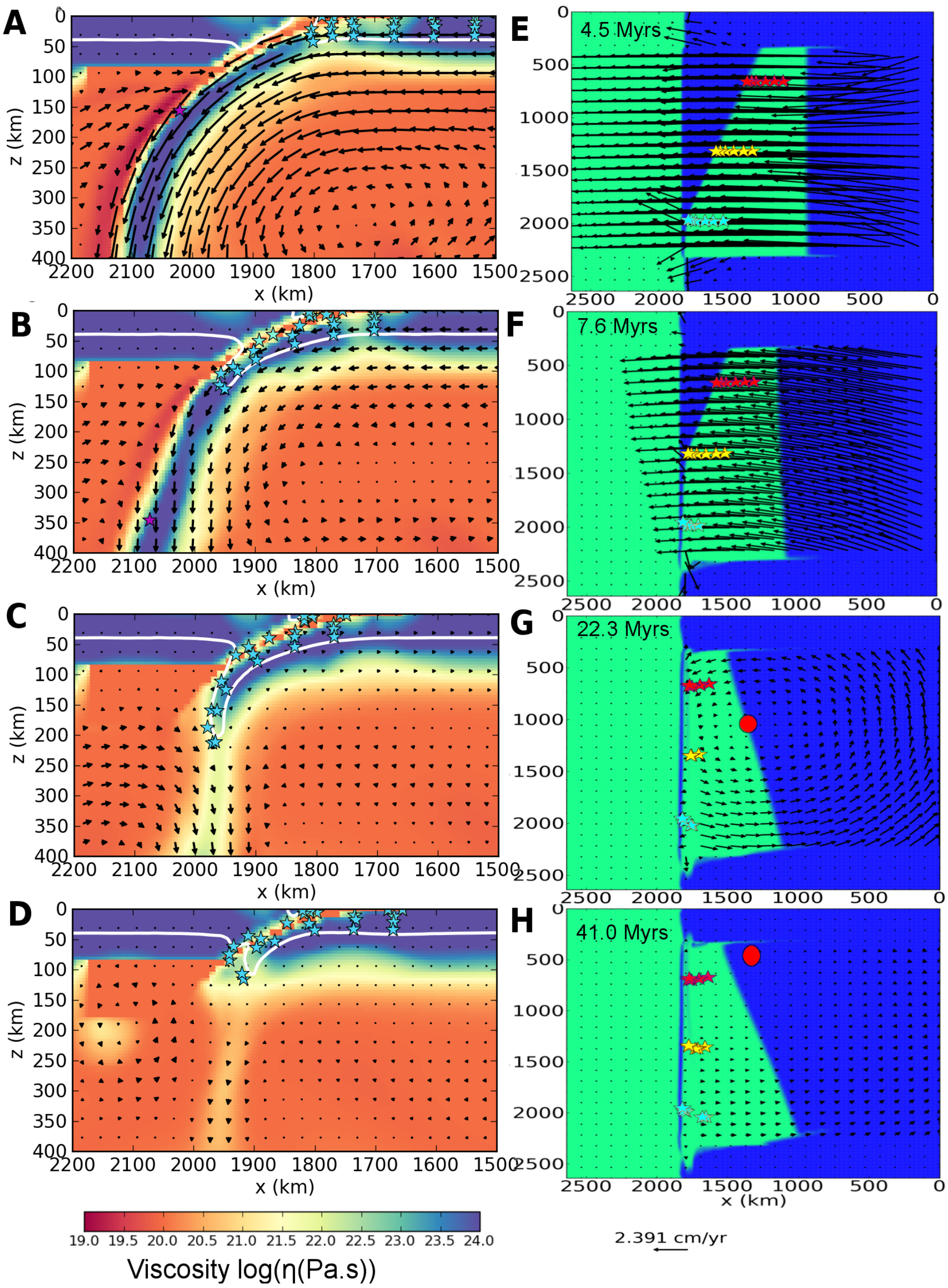

Figure 6.5: Diachronous collision model dynamics - A-D) Time slices through the diachronous collision model at y = 1980 km. These show how the markers are transported to depth during the initial collision and returned to the surface after slab break-off. E-H) Time snapshots of surface velocity. See Fig. 6.3 for details. Red dot shows the position of the rotational pole.

The diachronous model also has the largest horizontal eduction distance of 174 km where collision was initiated, at the southern end of the collisional zone. Horizontal eduction distances decrease northward to 70 km in the centre of the collision zone, and no eduction is recorded at all at the northern end of the collisional zone.

P-T-t paths for diachronous collision are presented in Fig. 6.6 for the markers that start at 10-30 km depth and are from the family of markers positioned in the southern promontory of the subducting continental block (y =1980 km). These markers lie at 0-120 km from the front of the continental block. P-T paths for all three marker families are presented in the Appendix (Fig. 8.16 8.18), which show that there are large along-trench variations in P-T paths, and that exhumation is much more likely in the region of initial collision than at the later, more northern, continental collision sites.

Markers closest to the front edge of the continental block reach depths of 200-250 km and temperatures of $> 900°C$, though they only return to ∼60 km below the surface (Fig. 6.6). However, a number of the markers that start further back from the edge of the continental block do return to crustal levels. For example, markers that start 30 km from the front of the continental block reach depths of 170 km (5 GPa) and temperatures of 850°C before returning to crustal levels (Fig. 6.6). Even markers that start 120 km from the front of the continental block reach depths of 60 - 100 km and temperatures of 300 - 600°C (Fig. 6.6). The difference in peak P-T conditions experienced by markers at the front edge of the plate and those further back from the edge produces a progressive metamorphic pattern towards the trench after the material is ultimately educted back to crustal depths.

The modelled P-T-t paths show that all the southernmost markers reach their peak pressure after ∼15 Myr with average burial rates that start at ∼1.5-3 cm/yr and then decline to a slower burial rate of 1-0.5cm/yr until the markers reach their peak pressure (Fig. 6.6). Exhumation rates are initially 0.5-1 cm/yr but slow down as the material nears the surface. All the markers that successfully return to crustal depths do so within 40 Myr after peak pressure and temperature were reached.

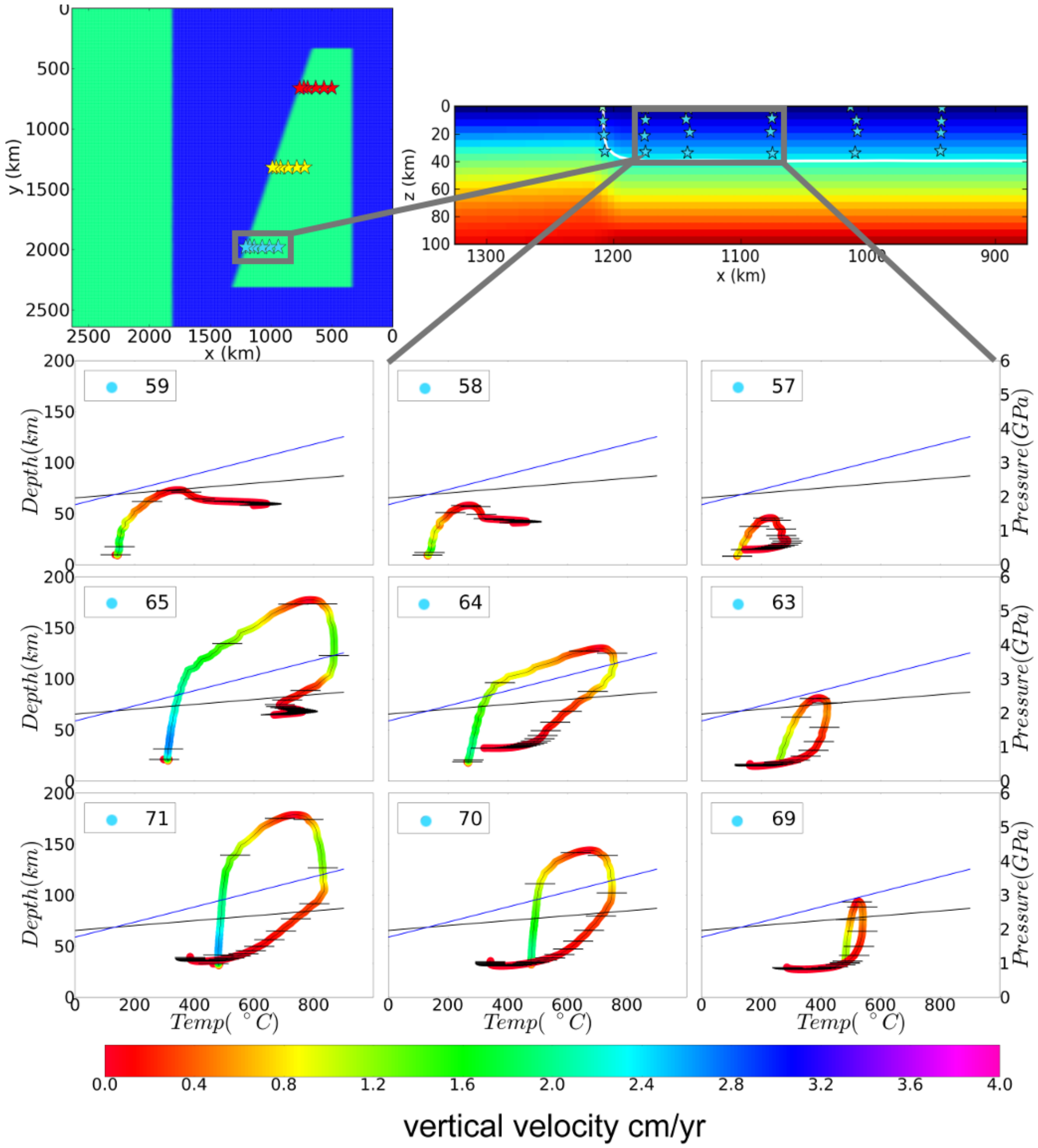

Figure 6.6: Diachronous collision model P-T-t paths - P-T-t (pressure- temperature-time) paths for material markers for diachronous collision that started at the southern promontory (y =1980 km) and were placed, from top to bottom, at 10, 20, 30 km depth and, from left to right, at 0, 30, 60, 120 km from the front of the subducting plates continental block. The colour of each P-T-t paths shows the vertical velocity of the material markers; the distances between the horizontal bars across the paths represent a passage of 5 Myr between bars. The the diamond-graphite (blue line)[Kennedy & Kennedy, 1976] and coesite-quartz (black line) [Bohlen & Boettcher, 1982] are also shown. The total calculation was run for approximately ∼ 150 Myrs

6.4 Discussion

The P-T-t loops that generate maximum P-T conditions in both the orthogonal and diachronous collision model are compared with published pressure and temperature estimates based on the geothermobarometry of eclogite facies assemblages that recrystallized within the WGC during Scandian subduction and early exhumation (Fig. 6.7, data from [Carswell *et al.*, 2006; Vrijmoed *et al.*, 2006; Hacker *et al.*, 2010]). Some estimates from garnet peridotites are excluded because they may have formed while the peridotites were still in the mantle wedge, and not in the subducted continental crust.

It can be seen by inspection that the diachronous collisional model results in much higher P-T conditions (60 km deeper and 300°C hotter) than the orthogonal model and that the loop modelled for the most deeply subducted continental crust at the point of initial collision in the diachronous model successfully reaches the UHP stability fields of coesite and diamond. The loop also matches the pressure estimates from all of the P-T studies as well as the lower temperature estimates (600-800°C) from some of the studies. Some petrological temperature calculations are 50 to 100°C hotter than achieved by the loop, a difference not considered significant in view of the uncertainties in geothermobarometry (see discussions in [Cuthbert *et al.*, 2000; Krogh Ravna & Terry, 2004; Carswell *et al.*, 2006]).

The published estimates for P-T paths followed by the WGC [for example, Labrousse *et al.*, 2004] show skinny hairpin shapes indicating that the large increase in pressure experienced by the eclogites was accompanied by a relatively small temperature change ($<$ 200°C). Our modelled P-T paths have fatter loops than the petrological estimates. This difference could imply that the modelled initial crustal temperature may have been hotter, or perhaps there was significant heating during the initial continental subduction. The diachronous collision model tends to create skinnier hairpin P-T paths by generating faster subduction and eduction, relative to the orthogonal model, thereby allowing material less time to equilibrate to mantle temperatures before and during its return to the surface. This can be seen by comparing Figs. 6.4, 6.6 and 6.7 where the diachronous model shows slightly faster burial and exhumation rates. The degree to which a P-T loop is skinny or fat are likely to be related to the rate of subduction and exhumation. Very rapid rates for one or both of these processes should result in limited temperature increases as a result of the short time available for temperatures within the subducted slab to equilibrate with ambient mantle temperatures. The skinny loops in Labrousse *et al.* [2004] would imply relatively rapid subduction and eduction rates whereas the fatter loops generated by our models would allow for slower rates. Subduction rates are difficult to calculate, but exhumation rates have been estimated at 0.2 - 2.5 cm/yr [Carswell *et al.*, 2003; Root *et al.*, 2005]. These estimates, in turn, are strongly dependent on radiometric age determinations for the various steps in the subduction-exhumation process. The first dates generated from eclogites in the WGC gave ages from 440 to 400 Ma [Griffin & Brueckner, 1980], implying very slow subduction and/or exhumation. The older ages were challenged when more recent age determination gave more restricted ages closer to 400 Ma, implying the duration of subduction and exhumation was much shorter, on the order of 10 Myr [Carswell *et al.*, 2003; Root *et al.*, 2005]. However still more recent publications have verified some of the older ages [Spengler *et al.*, 2006] leading to revised subduction/eduction cycles lasting as long as 35 Myr [Kylander-Clark *et al.*, 2012]. Therefore, given the uncertainties in both P-T calculations and age determinations, we propose that the P-T-t loops given, particularly by the diachronous model, are broadly consistent with the P-T-t history of the WGC.

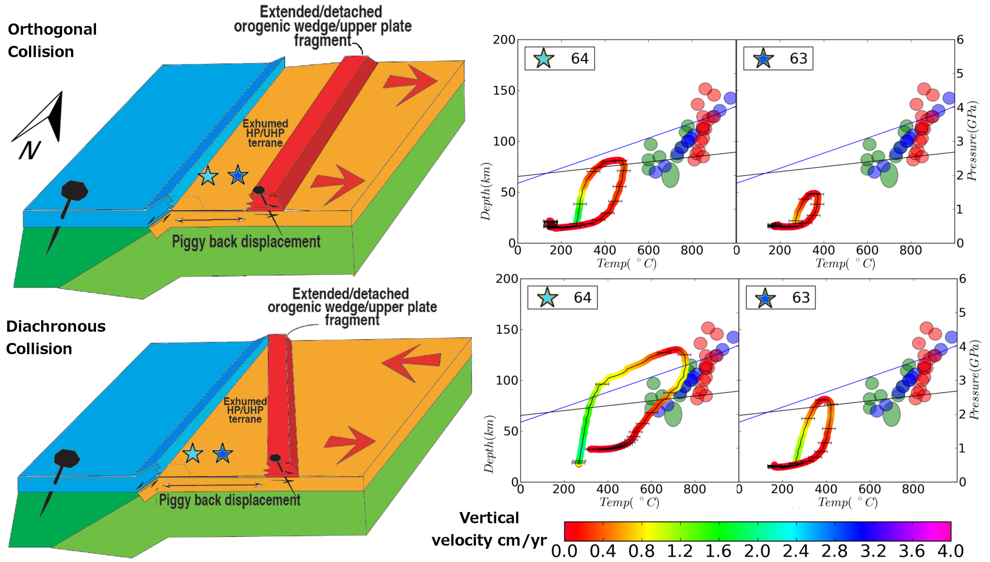

Figure 6.7: A schematic diagram of the exhumation dynamics - for both the orthogonal and diachronous collision models [after Brueckner & Cuthbert [2013]]. The orthogonal collision model (top) subducts and educts uniformly all along the subduction zone whereas the diachronous collision model, (bottom) generates the greatest eduction distance at the southern end of the collision zone. This greater eduction distance is capable of passively transporting overlying allochthons shown in red) much further towards the foreland (bottom left) than would happen during orthogonal collision (top left). The P-T-t paths for identical tracers (start position, 20 km depth and 130 km (marker 64) and 190 km (marker 63) from the front edge of the continental block) now both models are compared to petrological P-T estimates from the WGC, shown as ellipses [Hacker *et al.*, 2010](green); [Carswell *et al.*, 2006](red); [Vrijmoed *et al.*, 2006](blue). These values are chosen to represent the deepest level of subduction in different rigions of the WGC (see text for locations). We also show the diamond-graphite (blue line)[Kennedy & Kennedy, 1976] and coesite-quartz (black line) [Bohlen & Boettcher, 1982] stability fields. The P-T-t path for marker 64 shows that diachronous collision transports material 50 km deeper and to temperatures 300°C hotter than orthogonal collision and reaches the peak P-T data for the WGC whereas it doesnt in the orthogonal collision. The P-T-t path for marker 63 reaches the coesite transition during diachronous collision, but does not reach peak P-T conditions estimated for the WGC as it started 60 km further back from the front of the subducting plate and so was never subducted to the deepest levels of the WGC. This marker is analogous to the lower grade rock found in the interior of the WGC where eclogites were not generated.

The modelled P-T loops in Fig. 6.7 broadly coincide with the cloud of published peak P-T estimates for the WGC. The data in Fig. 6.7 came from a variety of locations, Hacker *et al.* [2010], (green ellipsis) data is a compilation of estimates from several areas of the WGC while Carswell *et al.* [2006] (red ellipses) present data from the islands of Fjørtoft and Otrøy in the most deeply subducted north west corner of the WGC. The Vrijmoed *et al.* [2006] data (blue ellipsis) are from a garnet peridotite on the west coast of Norway on the north-western edge of the WGC. This data represents the most deeply subducted material exhumed in the WGC. On the basis that the peak metamorphic paragenesis and mineral chemistry for a rock sample is frozen in at the pressure corresponding to the highest temperature in the P-T evolution it experienced [Spear *et al.*, 1984], the plotted P-T points in Fig. 6.7 should approximately correspond to the start of the return segment of their P-T-t paths. However, the conversion of a dry eclogite protolith (gabbro, granulite) to eclogite requires water to drive the reactions [Krabbendam *et al.*, 2000]. This water may come from outside the eclogite or be produced inside by a dehydration reaction [Konrad-Schmolke *et al.*, 2008], but neither of these processes necessarily takes place at the pressure associated with maximum temperature. Therefore it is possible that eclogite-facies assemblages can form during both prograde and retrograde metamorphism, as long as P-T conditions are in the eclogite-facies stability field. Given these considerations and the limitations inherent in present day available data we conclude again that the modelled P-T paths give a reasonable approximation of the likely conditions achieved by the WGC.

Material nearer the leading edge of the subducted continental block in both models achieves higher peak P-T conditions than material further back into the continental block. This variation fits with observations from the WGC, as the eclogites of the WGC show increasing metamorphic grade from southeast to northwest (i.e. towards the Laurentia-Baltica suture zone) [Hacker *et al.*, 2010; Brueckner & Cuthbert, 2013]. The protoliths of the HP/UHP WGC rocks are mainly Middle Proterozoic (∼1700 to 950 My) orthogneisses [Tucker *et al.*, 2004], and could well have been buried to mid-crustal depths under younger sequences by the time of Paleozoic continental collision of Laurentia and Baltica. HP/UHP material from both models return to depths between 10-30 km, and later erosion and/or extension is likely to bring this material closer the surface. Several studies [Carswell *et al.*, 2003; Labrousse *et al.*, 2004; Root *et al.*, 2005] propose that the WGC experienced a reduction in exhumation rate after an initial phase of more rapid exhumation, possibly driven by later tectonic events, such as extension [Fossen, 1993, 2010].

The two different collision modes obviously result in very different spatial distribution patterns for where a HP/UHP terrane will ultimately return to the surface. The orthogonal collision zone exhumes material uniformly along its entire length with an eduction distance of 156 km along its entire length whereas the diachronous collision model exhumes HP/UHP crustal material further (174 km) but only at one end of the collision zone, where the promontory that collided earliest was located. The Laurentia-Baltica collision only has one extensive Scandian (i.e. 430-390 Ma) HP/UHP terrane, the Western Gneiss Complex, near the southern end of the Scandinavian Caledonides. The diachronous collisional model was intentionally designed for initial collision to occur at the southern end of the collisional zone. This design is consistent with paleomagnetic plate motion reconstructions [Torsvik *et al.*, 1992; Cocks & Torsvik, 2002] that show how Baltica first collided with Laurentia at its southern tip and then collision migrated to the north. The plate reconstruction of Torsvik *et al.* [1992, 2012] also demonstrates that the south to north collision caused Baltica to rotate counter clockwise. Balticas pole of rotation can be calculated, from the reconstruction [Torsvik *et al.*, 2012], (Fig. 8.19 & 8.4.5) for 15 Myr prior to Baltica and Laurentia locking together (430 Ma, in the reconstruction). Balticas rotational pole moves north, roughly parallel to the collision zone, which is broadly consistent with the diachronous collisional model after initial collision of the continental promontory.

The amount of lateral exhumation predicted by both collision models provides additional support for the piggyback transport model of allochthons that rest tectonically on top of the WGC [Rice, 2005; Brueckner & Cuthbert, 2013]. Estimates for the lateral translations for some of these allochthons exceed 300 km [Törnebohm, 1896; Gee, 1975; Hossack & Cooper, 1986; Gale *et al.*, 1987]. Much of this displacement occurred by thrusting during the construction of the orogenic wedge associated with the initial collision of Baltica and Laurentia. However a significant amount of the additional displacement may have been the result of piggyback transport on top of the WGC as it exhumed towards the east/southeast. Two of these allochthons, the Jotun and Trondheim Nappe Complexes, are estimated to have been carried a minimum distance of 30-60 km to their current position by this piggyback mechanism [Brueckner & Cuthbert, 2013], but much larger distances of 215 to 320 km have also been proposed [Rice, 2005]. The lower estimates fit with both models, which show horizontal eduction distances for the WGC of 156 km for orthogonal collision and 179 km for diachronous collision. If the allochthons began passive transport immediately after the initiation of eduction, half of their total displacement could be accounted for by the piggyback mechanism. The larger estimates of Rice [2005], however, are not consistent with the model.

Neither model reproduces all of the structural features that are typical of the WGC. For example, the Møre-Trøndelag Fault Zone bounds the WGC to the north and is a large high-angle shear zone with major left lateral displacement [Fossen, 2010]. The rather simple visco-plastic rheology in the model calculations and the absence of imposed pre-existing faults, weak zones or other structures within the continental block precludes the formation of such structural features during the model runs. However, the Møre-Trøndelag Fault Zone (MTFZ) could still fit the proposed diachronous collision and rotation model by acting as a vertical decollement that accommodated some of the differential movement between the north and south of Baltica during its collision with Laurentia. The surface boundary condition in the model is a non-deformable free slip boundary, which prevents the generation of actual topography in the model. The effect of a free slip boundary compared to a deformable boundary or the use of a sticky air layer has been summarised by both Schmeling *et al.* [2008] and Crameri *et al.* [2012] for topography modelling. These studies conclude that although a true deformable surface is important, first order features are still reproduced with a simple non-deforming boundary. We therefore suggest that our models do capture the expected pattern of exhumed material and that a true free surface may actually assist in the eduction of material by providing less resistance to the bending of the subducted plate.

Finally, we briefly discuss the applicability of our results to other UHP terranes. In their recent review of ultrahigh-pressure tectonism Hacker & Gerya [2013] summarised six different mechanisms for the exhumation of UHP rocks, of which eduction and microplate rotation were noted as two separate cases, with the rider that "There are, to date, no published analogue or computational models of UHP exhumation by microplate rotation." Our study supplies that model, and furthermore suggests that the rotation and eduction processes may be linked, with rotation enhancing the degree of eduction, and favouring both the deepest burial and greatest exhumation of continental crust. We therefore suggest that our results have relevance to UHP terranes where eduction and/or rotation have previously been proposed, including the Dabie Shan of China [Wang *et al.*, 2003] and eastern Papua New Guinea [Webb *et al.*, 2008]. It may also explain the exhumation process in regions where combined plate rotations and eduction have not been proposed so far, such as the Dora Maira Massif of the Alps, where vertical axis rotations of the right age have been proposed [Ford *et al.*, 2006]. Additionally, our model may help explain why regional exposures of UHP rocks are rare in orogenic belts. If orthogonal collision produces lower degrees of burial, and, just as crucially, lower rates and amounts of exhumation, such collision zones will be less favourable sites for the generation and preservation of regional UHP terranes. We suggest that a future direction for research should be the evaluation of what amount, if any, of rotation and eduction is involved in the exhumation of each UHP region.

6.5 Conclusions

The diachronous collision and rotation of two colliding plates can assist in the eduction of material that has been transported to greater depths and experienced higher temperatures than would have been the case with an orthogonal collision. We also find that plate rotation exhumes material only in the area of initial collision, whereas an orthogonal collision exhumes material all along the subduction zone. Plate reconstructions for the Laurentia-Baltica collision suggest a diachronous collision mechanism and show a rotation of Baltica during its collision with Laurentia. Diachronous collision and the ensuing rotation of Baltica relative to Laurentia can explain the position of the WGC at the southern end of the Scandinavian Caledonides as the result of being the area of first collision. It also explains the extreme pressures and temperatures (4-5 GPa and 600-800°C) that generated eclogite in the most deeply subducted portions of the WGC since diachronous collision will drive crustal material deeper into the mantle than orthogonal collision, and makes it easier to exhume this deeply subducted material. Thus rotation of the colliding Baltica plate may be important in explaining the subduction and exhumation of the WGC and potentially may be important for other extensive HP/UHP terranes both in terms of their positioning and experienced P-T-t evolution.

7

Conclusions and perspectives

7.1 Thesis summary

The work completed for this thesis covers two main topics related to the dynamics of continental collision: the prediction of associated topography and any resulting exhumation of UHP terranes. The results are split into four major numerical modelling results chapters; a brief summary of each chapters results and conclusions is provided below.

Chapter 3 - explores the change in topography during subduction, collision and subsequent slab break-off. These results were obtained using 2D numerical models of the closure of a small oceanic basin and subsequent continental collision. Results show that during collision, slab steepening forms a short-lived dynamically driven basin on the overriding plate. The same collision results in uplift closer to the trench, which is produced by the isostatic forces associated with the subduction of buoyant continental material. After slab break-off, topography shows a widespread uplift produced by the rising of the partially subducted continental material under the overriding plate. We relate these topography predictions to observations from the Arabia-Eurasia collision and show that the limestone deposits of Qom Formation broadly relate to the syn-collisional basin found in our models. We also show that the current surface uplift of the region, not explained by crustal shortening and thickening, could be associated with slab break-off.

Chapter 4 - further investigates the mechanisms behind the generation of topography changes using 3D models to investigate both the along strike topography changes but also to temporally isolate surface effects of collision from the associated deep slab dynamics. We show how the previously identified post-collisional basin propagates along the collision zone at a similar rate to collision. This leads to the conclusion that the basin is formed by steepening of the upper portion of the subducting plate at the interface between the plates. Further results confirm that the front of the overriding plate is under a vertical tensional strain during the collision process. We discuss these results in relation to the propagating basin features observed along both the Apennine and Carpathian collision zones.

Chapter 5 - investigates the exhumation of HP/UHP terranes via the eduction mechanism. 2D models of continental collision are used to investigate how the physical structure of the subduction / collision zone affects the depth and temperature that crustal material can reach. P-T paths for crustal material are compared to petrological estimates of peak pressure and temperatures from the Western Gneiss Complex (WGC) in south-west Norway. Our results show that the main physical parameters that affect the pressures and temperatures experienced by crustal material are those that affect the buoyancy of the subducting plate, such as the lithosphere thickness of the oceanic and continental portion of the subducting plate and the crustal thickness. These results highlight the difficulty in producing a model that produces exhumed crustal material that has experienced both the temperature and pressure conditions that are proposed for the WGC. We also find that for the eduction process to operate successfully, a strong subducting and overriding plate are required.

Chapter 6 - builds on the results from the previous chapter, and investigates the difference in the pattern of exhumed material and the pressure and temperature conditions experienced by crustal material in an oblique and orthogonal collision. We use 3D models of the closure of an oceanic basin with different shapes of incoming continental blocks. We compare our results again to observation from the WGC and find that a diachronous collision better reproduces observation in terms of the spatial distribution of HP/UHP material and the achieved pressures and temperatures.

Taken together these results demonstrate how the use of numerical models and surface observation together can help us build a better understanding of how subduction and collision systems operate. The results demonstrate how the dynamics of a subduction and collision system can influence both changes in topography as well as the exhumation of material, and how we can use these observations to understand the dynamics of a system. Generally, these studies highlight the importance of buoyancy forces, both positive from continental crust and negative from subducting lithosphere, in shaping the Earth's surface. But, we also find that collision zones have a dynamic contribution to topography. The mechanical strength of the colliding plates is important for the surface expression of deep dynamics, as this controls both the wavelength of topography signals and influences the dynamics that form topography. The need for 3D treatment of subduction and collision is highlighted by our investigation of along-strike variation in both topography and exhumation generated by variations in initial collision timing along the subduction zone. Our results also highlight the important influence the plate interface has on the dynamics of subduction and collision, and hence the resultant surface expression. Understanding how these factors affects subduction dynamics is important in developing future numerical models of subduction and collision.

Numerical modelling results are compared to two major collision zones, the Cenozoic Arabia-Eurasia collision and the Palaeozoic Laurentia-Baltica collision. We find that our numerical models recreate the topography signature for the overriding plate for the Arabia-Eurasia collision. This area recorded the topographic events due to the formation of sedimentary basins on the overriding plate but we would suggest that the steepening of the subduction interface and associated topographic response presented here would be applicable to all world collision zones. We briefly discuss the possible application of our model to both the Apennine and Carpathian collision zone in Chapter 4 and show how this region also generated basins on the overriding plate and later experienced uplift. This topography evolution is also likely to apply to other world collision zones.

Using a 3D model we successfully simulate the exhumation of material that fits with the P-T-t conditions experienced by the WGC, the large exhumed terrane from the Laurentia-Baltica collision. However the eduction model tested here may also be applicable to the extensive UHP metamorphic terrane in the Dabi Shan China [Wang *et al.*, 2003], eastern Papua New Guinea [Webb *et al.*, 2008] some of the small UHP inclusion found at world collision zones and so future work should focus on determining what tectonic setting and collision zone structure favour different exhumation mechanisms.

7.2 Suggestions for future study

Future work that would extend this study should focus on three main areas of numerical model improvements: modification of the surface boundary conditions, the plate interface and compositional feedback to rheology.

The free slip boundary condition in all models used here is a simplification. This boundary condition reproduces the first order topographic features and dynamics [Quinquis *et al.*, 2011]. Improvements would probably be observed with a free surface however model resolution would also need to be increased to deal with adding this to the model. The current version of Citcom uses a purely Eulerian grid so is not suited to the implication of a true free surface without an adaptation to a semi-Lagrangian method or even full Lagrangian grid. Lagrangian grids allow the nodal points of the grid to move and hence the elements of grid to deform whereas Eulerian grids do not deform and so remain constant throughout the model run. A semi-Lagrangian method uses a Eulerian grid which obtains it's properties by interpolation to a system of free to move particles.

One method that could be used to approximate a free surface at the top of the model is the addition of a sticky air layer at the top of the model [Schmeling *et al.*, 2008]. This would comprise of a thin weak layer at the top of the model domain into which the plates can deform. This allows the generation of actual topography at the plate surface and allows the plate to exhibit features such as a fore-arc bulge associated with bending of the plate. The version of Citcom used in this study participated in the community bench-mark [Schmeling *et al.*, 2008] but results were found to be computationally very expensive to produce though potential improvements in numerical efficiency could be achieved by implementation of the methods used in Kaus *et al.* [2010].

The plate interface is another topic that might benefit from further methodological model refinement [Laigle *et al.*, 2004; Wada *et al.*, 2008; Jolivet *et al.*, 2009]. Here we use a simple, static, isoviscous weak zone between the two plates. This has the advantage of being able to easily control the coupling between the two plates but it is probably a simplification of the complex nature of the actual plate interface. We know that the plate interface deforms in different ways dependent on depth, with brittle deformation near the surface and ductile deformation at depth. Further work should investigate how this interface affects subduction and collision dynamics. The interface should also be free to deform and change shape dynamically in response to the subduction process. Future improvements to the model description of the subduction interface may also include the use of different highly non-linear rheologies to describe the plate interface. This would potentially better simulate weakening effects of hydrous minerals and sediments in the subduction interface.

Our current model uses a single rheological description for all material, this simplification is acceptable to a first order but experimental results show that continental crust and mantle material have different strengths. To address this issue different rheological descriptions are often applied to crust and mantle materials in numerical models [Buiter *et al.*, 2002; Gerya *et al.*, 2004; Arcay *et al.*, 2005]. Full compositionally dependent rheology could prove a substantial challenge in terms of storing the amount of compositional information required to calculate materials strength [Turcotte, 1987; Wang *et al.*, 2014]. Efforts have been made to link dynamic models with a calculation of composition to generate melt and residue compositions [Kaislaniemi *et al.*, 2014] though this would need to be combined with measured rheologies for different materials. Including these mechanisms may allow dynamic weakening of the plate interface as well as show how subducted material and, in particular, water affect the strength of the overriding plate. Our models have very little deformation of the overriding plate compared to the large scale deformation observed in subduction zones such as the Andes in south America or collision zones such as the Himilaya. This lack of deformation is advantageous for studying the dynamic effects on topography as signals are not over printed by crustal shortening and thickening. However future models should address whywhat causes overriding plate deformation and its role in subduction and collision. Some recent studies have started to investigate why some subduction systems build topography where others do not [Husson, 2012].

7.3 Developments in geodynamics

With the further affordability of 3D geodynamic models, the future studies of continental collision will utilise larger model domains [Davies *et al.*, 2011; Kronbichler *et al.*, 2012] and better model resolution, even for larger global models [e.g. REF Nakagawa & Tackley [2004]]. Adaptive meshing methods [Berger & Colella, 1989] have also allowed much larger models to be run relatively cheaply in terms of computation time. These increases in the possible size of models used will allow the inclusion of changes in slab pull force due to deep interactions of the slab with the phase transition boundaries in both the upper and lower mantle. The use of large 3D models to investigate along strike features of collision such as shown in Chapter 3 and 6 would also be improved by the use of large models. With increasing model sizes the use of spherical or partially spherical domains [Baumgardner, 1985; Zhong *et al.*, 2000] will become important to account for the spherical nature of the Earth.

Future models will likely also include surface processes such as erosion to be able to make more accurate comparisons between surface observations and model predictions [Chen *et al.*, 2013]. The inclusion of surface processes may be important to subduction modelling in order to accurately simulate trench sediment supplies that are thought to affect the nature of the plate interface [Wada *et al.*, 2008]. Models are also likely to use observations from mantle tomography [Becker & Faccenna, 2011], plate velocities [Gurnis *et al.*, 2012] to provide boundary and initial conditions for numerical simulation. This may lead to models that can be more easily compared directly with specific world collision zones. This comparison is always important as it provides validation to the modelling and grounds the model in geological and geophysical observations. This study demonstrates an important linking of surface observation to lithosphere and upper mantle dynamics on which future studies using more advanced models can build.

References

Agard, P., Omrani, J., Jolivet, L. & Mouthereau, F. (2005). Convergence history across Zagros (Iran): constraints from collisional and earlier deformation. *International Journal of Earth Sciences*, **94**, 401–419, doi:10.1007/s00531-005-0481-4.

Agard, P., Omrani, J., Jolivet, L., Whitechurch, H., Vrielynck, B., Spakman, W., Monie, P., Meyer, B. & Wortel, R. (2011). Zagros orogeny: a subduction-dominated process. *Geological Magazine*, **148**, 692–725, doi:10.1017/S001675681100046X.

Allen, M.B. & Armstrong, H.a. (2008). ArabiaEurasia collision and the forcing of mid-Cenozoic global cooling. *Palaeogeography, Palaeoclimatology, Palaeoecology*, **265**, 52–58, doi:10.1016/j.palaeo.2008.04.021.

Allen, M.B., Kheirkhah, M., Neill, I., Emami, M.H. & Mcleod, C.L. (2013). Generation of Arc and Within-plate Chemical Signatures in Collision Zone Magmatism: Quaternary Lavas from Kurdistan Province, Iran. *Journal of Petrology*, **54**, 887–911, doi:10.1093/petrology/egs090.

Andersen, T.B. & Austrheim, H. (2008). The Caledonian infrastructure in the fjord region of western Norway: With special emphasis on formation and exhumation of high- and ultrahigh-pressure rocks, late- to post-orogenic tectonic processes and basin formation,. In *33rd International Geological Congress*, 1–88., Oslo, Norway.

Andersen, T.B., Jamtveit, B.r., Dewey, J.F. & Swensson, E. (1991). Subduction and eduction of continental crust: major mechanisms during continent-continent collision and orogenic extensional collapse, a model based on the south Norwegian Caledonides. *Terra Nova*, **3**, 303–310, doi:10.1111/j.1365-3121.1991.tb00148.x.

Anderson, D.L. (2007). The eclogite engine: Chemical geodynamics as a galileo thermometer. *SPECIAL PAPERS-GEOLOGICAL SOCIETY OF AMERICA*, **430**, 47.

Andreasson, P.G., Gee, D.G., Whitehouse, M.J. & Schoberg, H. (2003). Subduction-flip during Iapetus Ocean closure and Baltica-Laurentia collision, Scandinavian Caledonides. *Terra Nova*, **15**, 362–369, doi:10.1046/j.1365-3121.2003.00486.x.

Andrews, E.R. & Billen, M.I. (2009). Rheologic controls on the dynamics of slab detachment. *Tectonophysics*, **464**, 60–69, doi:10.1016/j.tecto.2007.09.004.

Arcay, D., Tric, E. & Doin, M. (2005). Numerical simulations of subduction zones Effect of slab dehydration on the mantle wedge dynamics. *Physics of The Earth and Planetary Interiors*, **149**, 133–153, doi:10.1016/j.pepi.2004.08.020.

Ascione, A., Ciarcia, S., Di Donato, V., Mazzoli, S. & Vitale, S. (2012). The Pliocene-Quaternary wedge-top basins of southern Italy: an expression of propagating lateral slab tear beneath the Apennines. *Basin Research*, **24**, 456–474, doi:10.1111/j.1365-2117.2011.00534.x.

Bada, G., Horvath, F., Gerner, P. & Fejes, I. (1999). Review of the present day geodynamics of the Pannonian basin progress and problems. *Journal of Geodynamics*, **27**.

Ballato, P., Uba, C.E., Landgraf, A., Strecker, M.R., Sudo, M., Stockli, D.F., Friedrich, A. & Tabatabaei, S.H. (2010). Arabia-Eurasia continental collision: Insights from late Tertiary foreland-basin evolution in the Alborz Mountains, northern Iran. *Geological Society of America Bulletin*, **123**, 106–131, doi:10.1130/B30091.1.

Barazangi, M. & Isacks, B.L. (1976). Spatial distribution of earthquakes and subduction of the Nazca plate beneath South America. *Geology*, **4 11**, p. 686–692.

BARAZANGI, M., ISACKS, B.L., OLIVER, J., DUBOIS, J. & PASCAL, G. (1973). Descent of lithosphere beneath New Hebrides, Tonga-Fiji and New Zealand: evidence for detached slabs. *Nature*, **242**, 98–101.

BAUMANN, C., GERYA, T.V. & CONNOLLY, J.A.D. (2010). Numerical modelling of spontaneous slab breakoff dynamics during continental collision. *Geological Society, London, Special Publications*, **332**, 99–114, doi:10.1144/SP332.7.

BAUMGARDNER, J.R. (1985). Three-dimensional treatment of convective flow in the earth's mantle. *Journal of Statistical Physics*, **39**, 501–511, doi:10.1007/BF01008348.

BECKER, T.W. & FACCENNA, C. (2011). Mantle conveyor beneath the Tethyan collisional belt. *Earth and Planetary Science Letters*, **310**, 453–461, doi:10.1016/j.epsl.2011.08.021.

BERBERIAN, M. & KING, G.C.P. (1981). Towards a paleogeography and tectonic evolution of Iran. *Canadian Journal of Earth Sciences*, **18**, 210–265, doi:10.1139/e81-019.

BERGER, M. & COLELLA, P. (1989). Local adaptive mesh refinement for shock hydrodynamics. *Journal of Computational Physics*, **82**, 64–84, doi:10.1016/0021-9991(89)90035-1.

BERTOTTI, G., PICOTTI, V. & CLOETINGH, S. (1998). Lithospheric weakening during retroforeland basin formation: Tectonic evolution of the central South Alpine foredeep. *Tectonics*, **17**, 131–142, doi:10.1029/97TC02066.

BILLEN, M.I. & GURNIS, M. (2001). A low viscosity wedge in subduction zones. *Earth and Planetary Science Letters*, **193**, 227–236, doi:10.1016/S0012-821X(01)00482-4.

BIRD, P. (1978). Initiation of intracontinental subduction in the Himalaya. *Journal of Geophysical Research*, **83**, 4975, doi:10.1029/JB083iB10p04975.

BOHLEN, S.R. & BOETTCHER, A.L. (1982). Coesite Transformation ' of Other Components. *Journal of Geophysical Research*, **87**, 7073–7078.

BOTTRILL, A.D., VAN HUNEN, J. & ALLEN, M.B. (2012). Insight into collision zone dynamics from topography: numerical modelling results and observations. *Solid Earth*, **3**, 387–399, doi:10.5194/se-3-387-2012.

Bottrill, A.D., van Hunen, J., Cuthbert, S.J., Brueckner, H.K. & Allen, M.B. (2014). Plate rotation during continental collision and its relationship with the exhumation of uhp metamorphic terranes: Application to the norwegian caledonides. *Geochemistry, Geophysics, Geosystems*, doi:10.1002/2014GC005253.

Brueckner, H.K. (2006). Dunk, Dunkless and Re-dunk Tectonics: A Model for Metamorphism, Lack of Metamorphism, and Repeated Metamorphism of HP/UHP Terranes. *International Geology Review*, **48**, 978–995, doi:10.2747/0020-6814.48.11.978.

Brueckner, H.K. & Cuthbert, S.J. (2013). Extension , disruption , and translation of an orogenic wedge by exhumation of large ultrahigh-pressure ter- ranes : Examples from the Norwegian Caledonides. *Lithosphere*, 1–13, doi:10.1130/L256.1.

Brueckner, H.K. & van Roermund, H.L.M. (2004). Dunk tectonics: A multiple subduction/eduction model for the evolution of the Scandinavian Caledonides. *Tectonics*, **23**, 1–20, doi:10.1029/2003TC001502.

Brun, J.P. & Faccenna, C. (2008). Exhumation of high-pressure rocks driven by slab rollback. *Earth and Planetary Science Letters*, **272**, 1–7, doi:10.1016/j.epsl.2008.02.038.

Buiter, S.J., Govers, R. & Wortel, M. (2002). Two-dimensional simulations of surface deformation caused by slab detachment. *Tectonophysics*, **354**, 195–210, doi:10.1016/S0040-1951(02)00336-0.

Burke, K., Steinberger, B., Torsvik, T.H. & Smethurst, M.a. (2008). Plume Generation Zones at the margins of Large Low Shear Velocity Provinces on the coremantle boundary. *Earth and Planetary Science Letters*, **265**, 49–60, doi:10.1016/j.epsl.2007.09.042.

Burkett, E.R. & Billen, M.I. (2010). Three-dimensionality of slab detachment due to ridge-trench collision: Laterally simultaneous boudinage versus tear propagation. *Geochemistry Geophysics Geosystems*, **11**, doi:10.1029/2010GC003286.

Burov, E., Jolivet, L., Le Pourhiet, L. & Poliakov, A. (2001). A thermomechanical model of exhumation of high pressure (HP) and ultra-high pressure (UHP) metamorphic rocks in Alpine-type collision belts. *Tectonophysics*, **342**, 113–136, doi:10.1016/S0040-1951(01)00158-5.

Burov, E.B. & Watts, A. (2006). The long-term strength of continental lithosphere: "jelly sandwich" or "crème brûlée"? *GSA today*, **5173**, 4–10, doi:10.1126/science.1125771.

Butler, J.P., Jamieson, R.A., Steenkamp, H.M. & Robinson, P. (2013). Discovery of coesite-eclogite from the Nordøyane UHP domain, Western Gneiss Region, Norway: field relations, metamorphic history, and tectonic significance. *Journal of Metamorphic Geology*, **31**, 147–163, doi:10.1111/jmg.12004.

Byerlee, J. (1978). Friction of rocks. *Pure and Applied Geophysics*, **116**, 615–626.

Capitanio, F.a. & Goes, S. (2006). Mesozoic spreading kinematics: consequences for Cenozoic Central and Western Mediterranean subduction. *Geophysical Journal International*, **165**, 804–816, doi:10.1111/j.1365-246X.2006.02892.x.

Carminati, E., Wortel, M., Spakman, W. & Sabadini, R. (1998). The role of slab detachment processes in the opening of the westerncentral Mediterranean basins: some geological and geophysical evidence. *Earth and Planetary Science Letters*, **160**, 651–665, doi:10.1016/S0012-821X(98)00118-6.

Carswell, D.A., Brueckner, H.K., Cuthbert, S.J., Mehta, K. & O'Brien, P.J. (2003). The timing of stabilisation and the exhumation rate for ultra-high pressure rocks in the Western Gneiss Region of Norway. *Journal of Metamorphic Geology*, **21**, 601–612, doi:10.1046/j.1525-1314.2003.00467.x.

Carswell, D.A., van Roermund, H.L. & de Vries, D.F. (2006). Scandian ultrahigh-pressure metamorphism of proterozoic basement rocks on Fjørtoft and Otrøy, Western Gneiss Region, Norway. *International Geology Review*, **48**, 957–977, doi:10.2747/0020-6814.48.11.957.

Cathles, L.M. (1975). *The Viscosity of the Earth's Mantle.*. Princeton Univ. Press, Princeton N.J.

Channell, J.E.T. & Mareschai, J.C. (1989). Delamination and asymmetric lithospheric thickening in the development of the Tyrrhenian Rift The evolution of the western Mediterranean. *Geological Society Special Publication*, 285–302, doi:10.1144/GSL.SP.1989.045.01.16.

CHEN, L., GERYA, T., ZHANG, Z., ZHU, G., DURETZ, T. & JACOBY, W.R. (2013). Numerical modeling of eastern Tibetan-type margin: Influences of surface processes, lithospheric structure and crustal rheology. *Gondwana Research*, **24**, 1091–1107, doi:10.1016/j.gr.2013.01.003.

CHOPIN, C. (1984). Coesite and pure pyrope in high-grade blueschists of the western Alps: a first record and some consequences. *Contributions to Mineralogy and Petrology*, **86**, 107–118.

CHOPIN, C. (2003). Ultrahigh-pressure metamorphism: tracing continental crust into the mantle. *Earth and Planetary Science Letters*, **212**, 1–14, doi:10.1016/S0012-821X(03)00261-9.

CHRISTENSEN, U. (1995). Effects of Phase Transitions on Mantle Convection. *Earth-Science Reviews*, 65–87.

ČÍŽKOVÁ, H., VAN HUNEN, J., VAN DEN BERG, A.P. & VLAAR, N.J. (2002). The influence of rheological weakening and yield stress on the interaction of slabs with the 670 km discontinuity. *Earth and Planetary Science Letters*, **199**, 447–457, doi:10.1016/S0012-821X(02)00586-1.

CLOOS, M. (1993). Lithospheric buoyancy and collisional orogenesis: Subduction of oceanic plateaus, continental margins, island arcs, spreading ridges, and seamounts. *Geological Society of America Bulletin*, **105**, 715, doi:10.1130/0016-7606.

CLOOS, M. & SHREVE, R.L. (1988). Subduction-channel model of prism accretion, melange formation, sediment subduction, and subduction erosion at convergent plate margins: 1. background and description. *Pure and Applied Geophysics*, **128**, 455–500.

COCKS, L.R.M. & TORSVIK, T.H. (2002). Earth geography from 500 to 400 million years ago : a faunal and palaeomagnetic review. *Journal of the Geological Society*, **159**, 631–644, doi:10.1144/0016-764901-118.

COLEMAN ROBERT, X.W., ed. (2005). *Ultrahigh pressure metamorphism*. Cambridge University Press, Cambridge, UK, 2nd edn.

Condie, K.C. (1998). Episodic continental growth and supercontinents: a mantle avalanche connection? *Earth and Planetary Science Letters*, **163**, 97–108.

Conrad, C.P. & Hager, B.H. (1999). Effects of plate bending and fault strength at subduction zones on plate dynamics. *Journal of Geophysical Research*, **104**, 17551, doi:10.1029/1999JB900149.

Crameri, F., Schmeling, H., Golabek, G.J., Duretz, T., Orendt, R., Buiter, S.J.H., May, D.a., Kaus, B.J.P., Gerya, T.V. & Tackley, P.J. (2012). A comparison of numerical surface topography calculations in geodynamic modelling: an evaluation of the sticky air method. *Geophysical Journal International*, **189**, 38–54, doi:10.1111/j.1365-246X.2012.05388.x.

Cuthbert, S., Carswell, D., Krogh-Ravna, E. & Wain, A. (2000). Eclogites and eclogites in the Western Gneiss Region, Norwegian Caledonides. *Lithos*, **52**, 165–195, doi:10.1016/S0024-4937(99)00090-0.

Cuthbert, S.J., Harvey, M.A. & Carswell, D.A. (1983). A tectonic model for the metamorphic evolution of the Basal Gneiss Complex, Western South Norway. *Journal of Metamorphic Geology*, **1**, 63–90, doi:10.1111/j.1525-1314.1983.tb00265.x.

Davidson, J., Reed, W. & Davis, P. (2002). *Exploring Earth*. Pearson Education Ltd, New Jersy, 2nd edn.

Davies, D. & Davies, J. (2009). Thermally-driven mantle plumes reconcile multiple hot-spot observations. *Earth and Planetary Science Letters*, **278**, 50–54, doi:10.1016/j.epsl.2008.11.027.

Davies, D.R., Wilson, C.R. & Kramer, S.C. (2011). Fluidity: A fully unstructured anisotropic adaptive mesh computational modeling framework for geodynamics. *Geochemistry, Geophysics, Geosystems*, **12**, doi:10.1029/2011GC003551.

Davies, J.H. & Davies, D.R. (2010). Earth's surface heat flux. *Solid Earth*, **1**, 5–24, doi:10.5194/se-1-5-2010.

Davies, J.H. & von Blanckenburg, F. (1995). Slab breakoff: a model of lithosphere detachment and its test in the magmatism and deformation of collisional orogens.

Earth and Planetary Science Letters, **129**, 85–102, doi:10.1016/0012-821X(94)00237-S.

Davies, N.S., Turner, P. & Sansom, I.J. (2005). A revised stratigraphy for the Ringerike Group (Upper Silurian , Oslo Region). *Norwegen Journal of Geology*, **85**, 193–202.

De Franco, R., Govers, R. & Wortel, R. (2008). Dynamics of continental collision: influence of the plate contact. *Geophysical Journal International*, **174**, 1101–1120, doi:10.1111/j.1365-246X.2008.03857.x.

Deschamps, F., Godard, M., Guillot, S. & Hattori, K. (2013). Geochemistry of subduction zone serpentinites: A review. *Lithos*, **178**, 96–127, doi:10.1016/j.lithos.2013.05.019.

Dewey, J. & Strachan, R. (2003). Changing Silurian-Devonian relative plate motion in the Caledonides: sinistral transpression to sinistral transtension. *Journal of the Geological Society*, **160**, 219–229, doi:10.1144/0016-764902-085.

Di Giuseppe, E., van Hunen, J., Funiciello, F., Faccenna, C. & Giardini, D. (2008). Slab stiffness control of trench motion: Insights from numerical models. *Geochemistry Geophysics Geosystems*, **9**, 1–19, doi:10.1029/2007GC001776.

Dixon, J.M. & Farrar, E. (1980). Ridge subduction, eduction,and the Neogene Tectonics of southwestern North America. *Tectonophysics*, **67**, 81–99, doi:10.1016/0040-1951(80)90166-3.

Dobrzhinetskaya, L., Faryad, S. & Cuthbert, S.J. (2011a). Frontiers of ultrahigh pressure metamorphism: View from field and laboratory. In *Ultrahigh-Pressure Metamorphism: 25 Years After The Discovery Of Coesite and Diamond.*, Elsevier Insights Series, London.

Dobrzhinetskaya, L., Faryad, S.-W., ., Wallis, .S. & Cuthbert, S. (2011b). *Ultrahigh-Pressure Metamorphism: 25 Years After The Discovery Of Coesite and Diamond.*. Elsevier Insights Series, London.

Dobrzhinetskaya, L.F., Eide, E.A., Larsen, R.B., Sturt, B.A., Trø nnes, R.G., Smith, C., Taylor, W.R. & Posukhova, T.V. (1995). Microdiamond in high-grade metamorphic rocks of the Western Gneiss region , Norway. *Geology*, **23**, 597–600, doi:10.1130/0091-7613.

Doglioni, C. (1993). Some remarks on the origin of foredeeps. *Tectonophysics*, **228**, 1–20, doi:10.1016/0040-1951(93)90211-2.

Duretz, T., Gerya, T.V. & May, D.A. (2011a). Numerical modelling of spontaneous slab breakoff and subsequent topographic response. *Tectonophysics*, **502**, 244–256, doi:10.1016/j.tecto.2010.05.024.

Duretz, T., Kaus, B., Schulmann, K., Gapais, D. & Kermarrec, J.J. (2011b). Indentation as an extrusion mechanism of lower crustal rocks: Insight from analogue and numerical modelling, application to the Eastern Bohemian Massif. *Lithos*, **124**, 158–168, doi:10.1016/j.lithos.2010.10.013.

Duretz, T., Gerya, T.V., Kaus, B.J.P. & Andersen, T.B. (2012). Thermomechanical modeling of slab eduction. *Journal of Geophysical Research*, **117**, B08411, doi:10.1029/2012JB009137.

England, P.C. & Katz, R.F. (2010). Melting above the anhydrous solidus controls the location of volcanic arcs. *Nature*, **467**, 700–3, doi:10.1038/nature09417.

Erickson, J. (1996). *Marine Geology: Undersea Landforms and Life Forms*. Changing earth, Facts On File, Incorporated.

Ernst, W. (2009). Archean plate tectonics, rise of Proterozoic supercontinentality and onset of regional, episodic stagnant-lid behavior. *Gondwana Research*, **15**, 243–253.

Faccenda, M., Minelli, G. & Gerya, T.V. (2009). Coupled and decoupled regimes of continental collision: Numerical modeling. *Earth and Planetary Science Letters*, **278**, 337–349, doi:10.1016/j.epsl.2008.12.021.

Faccenna, C. & Becker, T.W. (2010). Shaping mobile belts by small-scale convection. *Nature*, **465**, 602–5, doi:10.1038/nature09064.

Faccenna, C., Becker, T.W., Lucente, F.P., Jolivet, L. & Rossetti, F. (2001). History of subduction and back-arc extension in the Central Mediterranean. *Geophysical Journal International*, **145**, 809–820, doi:10.1046/j.0956-540x.2001.01435.x.

Faccenna, C., Funiciello, F., Civetta, L., DAntonio, M., Moroni, M. & Piromallo, C. (2007). Slab disruption, mantle circulation, and the opening of the Tyrrhenian basins. *Cenozoic Volcanism in the Mediterranean Area*, 153–169.

Faccenna, C., Molin, P., Orecchio, B., Olivetti, V., Bellier, O., Funiciello, F., Minelli, L., Piromallo, C. & Billi, a. (2011). Topography of the Calabria subduction zone (southern Italy): Clues for the origin of Mt. Etna. *Tectonics*, **30**, 1–20, doi:10.1029/2010TC002694.

Federico, L., Crispini, L., Scambelluri, M. & Capponi, G. (2007). Ophiolite mélange zone records exhumation in a fossil subduction channel. *Geology*, **35**, 499, doi:10.1130/G23190A.1.

Ford, M., Duchene, S., Gasquet, D. & Vanderhaeghe, O. (2006). Two-phase orogenic convergence in the external and internal SW Alps. *Journal of the Geological Society*, **163**, 815–826, doi:10.1144/0016-76492005-034.

Forsyth, D. & Uyeda, S. (1975). On the Relative Importance of the Driving Forces of Plate Motion. *Geophysical Journal International*, **43**, 163–200, doi:10.1111/j.1365-246X.1975.tb00631.x.

Forte, A., Moucha, R., Simmons, N., Grand, S. & Mitrovica, J. (2010). Deep-mantle contributions to the surface dynamics of the North American continent. *Tectonophysics*, **481**, 3–15.

Forte, A.M. & Mitrovica, J.X. (1996). New inferences of mantle viscosity from joint inversion of long-wavelength mantle convection and post-glacial rebound data. *Geophysical Research Letters*, **23**, 1147–1150, doi:10.1029/96GL00964.

Fossen, H. (1993). The role of extensional tectonics in the Caledonides of south Norway. *Journal of Structural Geology*, **15**, 1379–1380, doi:10.1007/1-4020-4495-X$_7$4.

Fossen, H. (2010). Extensional tectonics in the North Atlantic Caledonides: a regional view. *Geological Society, London, Special Publications*, **335**, 767–793, doi:10.1144/SP335.31.

Fowler, C. (2005). *The Solid Earth: An Introduction to Global Geophysics*. Cambridge University Press.

Frank, W., Miller, C., Schuster, R., Klo, U., Purtscheller, F., Klotzli, U., Frank, W. & Purtscheller, F. (1999). Post-Collisional Potassic and Ultrapotassic Magmatism in SW Tibet: Geochemical and Sr-Nd-Pb-O Isotopic Constraints for Mantle Source Characteristics and Petrogenesis. *Journal of Petrology*, **40**, 1399–1424, doi:10.1093/petroj/40.9.1399.

Fukao, Y., Widiyantoro, S. & Obayashi, M. (2001). Stagnant slabs in the upper and lower mantle transition region. *Reviews of Geophysics*, **39**, 291, doi:10.1029/1999RG000068.

Fukao, Y., Obayashi, M. & Nakakuki, T. (2009). Stagnant slab: a review. *Annual Review of Earth and Planetary Sciences*, **37**, 19–46.

Gabriele, G. & Ragsdell, K. (1977). The generalized reduced gradient method: A reliable tool for optimal design. *Journal of Engineering for Industry*, **99**, 394–400.

Gale, R., Rice, A., Roberts, D., Townsend, C. & Welbon, A. (1987). Restoration of the Baltoscandian Caledonian margin from balanced cross sections: The problem of excess continental crust:. *Transactions of the Royal Society of Edinburgh: Earth Sciences*, **78**, 197–217.

Gansser, A. (1955). Geological note on NW Iran:. *Iran Oil Company Geological Report*, **98**, 76.

Gee, D.G. (1975). A tectonic model for the central part of the Scandinavian Caledonides. *American Journal of Science*, **275**, 468–515.

Gee, D.G., Juhlin, C., Pascal, C. & Robinson, P. (2010). Collisional Orogeny in the Scandinavian Caledonides (COSC). *GFF*, **132**, 29–44, doi:10.1080/11035891003759188.

Gephart, J.W. (1994). Topography and subduction geometry in the central Andes: Clues to the mechanics of a noncollisional orogen. *Journal of Geophysical Research*, **99**, 12279–12288, doi:10.1029/94JB00129.

Gerya, T.V. & Stöckhert, B. (2005). Two-dimensional numerical modeling of tectonic and metamorphic histories at active continental margins. *International Journal of Earth Sciences*, **95**, 250–274, doi:10.1007/s00531-005-0035-9.

Gerya, T.V. & Yuen, D.a. (2003). RayleighTaylor instabilities from hydration and melting propel cold plumes at subduction zones. *Earth and Planetary Science Letters*, **212**, 47–62, doi:10.1016/S0012-821X(03)00265-6.

Gerya, T.V., Yuen, D.a. & Maresch, W.V. (2004). Thermomechanical modelling of slab detachment. *Earth and Planetary Science Letters*, **226**, 101–116, doi:10.1016/j.epsl.2004.07.022.

Ghasemi, a. & Talbot, C. (2006). A new tectonic scenario for the SanandajSirjan Zone (Iran). *Journal of Asian Earth Sciences*, **26**, 683–693, doi:10.1016/j.jseaes.2005.01.003.

Ghazian, R.K. & Buiter, S.J.H. (2013). A numerical investigation of continental collision styles. *Geophysical Journal International*, **193**, 1133–1152, doi:10.1093/gji/ggt068.

Glodny, J., Kühn, A. & Austrheim, H. (2008). Geochronology of fluid-induced eclogite and amphibolite facies metamorphic reactions in a subductioncollision system, Bergen Arcs, Norway. *Contributions to Mineralogy and Petrology*, **156**, 27–48, doi:10.1007/s00410-007-0272-y.

Gordon, S., Little, T., Hacker, B., Bowring, S., Korchinski, M., Baldwin, S. & A., K.C. (2012). Multi-stage exhumation of young UHPHP rocks: Timescales of melt crystallization in the D'Entrecasteaux Islands, southeastern Papua New Guinea. *Earth and Planetary Science Letters*, **351**, 237–246, doi:10.1016/j.epsl.2012.07.014.

Griffin, W., Austrheim, G., Brastad, K., Brynhi, I., Krill, A., Krogh, J., Mork, J., Qvale, M. & Torudbakken, B. (1985). *High pressure metamorphism in the Scandinavian Caledonides*. Wiley, New York, New York.

Griffin, W.L. & Brueckner, H.K. (1980). Caledonian SmNd ages and a crustal origin for Norwegian eclogites. *Nature*, **285**, 319–321, doi:10.1038/285319a0.

Gurnis, M., Turner, M., Zahirovic, S., DiCaprio, L., Spasojevic, S., Müller, R., Boyden, J., Seton, M., Manea, V.C. & Bower, D.J. (2012). Plate tectonic reconstructions with continuously closing plates. *Computers & Geosciences*, **38**, 35–42, doi:10.1016/j.cageo.2011.04.014.

Guyot, P. & Dorn, J.E. (1967). A Critical Review of the Peierls Mechanism. *Canadian Journal of Physics*, **45**, 983–1016, doi:10.1139/p67-073.

Hacker, B.R. (2007). Ascent of the ultrahigh-pressure Western Gneiss Region , Norway. *Geological Society of America Special Papers*, **2419**, 171–184, doi:10.1130/2006.2419(09).

Hacker, B.R. & Gerya, T.V. (2013). Paradigms, new and old, for ultrahigh-pressure tectonism. *Tectonophysics*, **603**, 79–88, doi:10.1016/j.tecto.2013.05.026.

Hacker, B.R., Andersen, T.B., Root, D.B., Mehl, L., Mattinson, J.M. & Wooden, J.L. (2003). Exhumation of high-pressure rocks beneath the Solund Basin, Western Gneiss Region of Norway. *Journal of Metamorphic Geology*, **21**, 613–629, doi:10.1046/j.1525-1314.2003.00468.x.

Hacker, B.R., Luffi, P., Lutkov, V., Minaev, V., Ratschbacher, L., Plank, T., Ducea, M., Patiño Douce, A., McWilliams, M. & Metcalf, J. (2005). Near-Ultrahigh Pressure Processing of Continental Crust: Miocene Crustal Xenoliths from the Pamir. *Journal of Petrology*, **46**, 1661–1687, doi:10.1093/petrology/egi030.

Hacker, B.R., Andersen, T.B., Johnston, S., Kylander-Clark, A.R., Peterman, E.M., Walsh, E.O. & Young, D. (2010). High-temperature deformation during continental-margin subduction & exhumation: The ultrahigh-pressure Western Gneiss Region of Norway. *Tectonophysics*, **480**, 149–171, doi:10.1016/j.tecto.2009.08.012.

Hager, B.H. (1984). Subducted slabs and the geoid: Constraints on mantle rheology and flow. *Journal of Geophysical Research*, **89**, 6003, doi:10.1029/JB089iB07p06003.

HALL, R. (2002). Cenozoic geological and plate tectonic evolution of se asia and the sw pacific: computer-based reconstructions, model and animations. *Journal of Asian Earth Sciences*, **20**, 353–431, doi:10.1016/S1367-9120(01)00069-4.

HAWKESWORTH, C.J. & KEMP, A.I.S. (2006). Evolution of the continental crust. *Nature*, **443**, 811–7, doi:10.1038/nature05191.

HAYES, D.E. (1980). *The Tectonic and Geologic Evolution of Southeast Asian Seas and Islands*, vol. 23 of *Geophysical Monograph Series*. American Geophysical Union, Washington, D. C.

HE, L. (2012). Influence of lithosphere-asthenosphere interaction on the overriding lithosphere in a subduction zone: Numerical modeling. *Geochemistry Geophysics Geosystems*, **13**, 1–13, doi:10.1029/2011GC003909.

HEURET, A., LALLEMAND, S., FUNICIELLO, F., PIROMALLO, C. & FACCENNA, C. (2011). Physical characteristics of subduction interface type seismogenic zones revisited. *Geochemistry, Geophysics, Geosystems*, **12**, Q01004, doi:10.1029/2010GC003230.

HIRTH, G. & KOHLSTEDT, D.L. (1996). Water in the oceanic upper mantle: implications for rheology, melt extraction and the evolution of the lithosphere. *Earth and Planetary Science Letters*, **144**, 93–108, doi:10.1016/0012-821X(96)00154-9.

HOLMES, A. (1931). Radioactivity and Earth Movements. *Geological Soc, Glasgow*, **18**, 559–606.

HOSSACK, J. & COOPER, M. (1986). Collision tectonics in the Scandinavian Caledonides. In M. Coward & A. Ries, eds., *Collision tectonics: Geological Society of London Special Publication*, 287–304.

HOUSEMAN, G.A. & GEMMER, L. (2007). Intra-orogenic extension driven by gravitational instability: Carpathian-Pannonian orogeny. *Geology*, **35**, 1135, doi:10.1130/G23993A.1.

HUGHES, T.J.R. (2012). *The Finite Element Method: Linear Static and Dynamic Finite Element Analysis (Google eBook)*. Courier Dover Publications.

Husson, L. (2006). Dynamic topography above retreating subduction zones. *Geology*, **34**, 741, doi:10.1130/G22436.1.

Husson, L. (2012). Trench migration and upper plate strain over a convecting mantle. *Physics of the Earth and Planetary Interiors*, **212-213**, 32–43, doi:10.1016/j.pepi.2012.09.006.

Husson, L., Brun, J.P., Yamato, P. & Faccenna, C. (2009). Episodic slab rollback fosters exhumation of HP-UHP rocks. *Geophysical Journal International*, **179**, 1292–1300, doi:10.1111/j.1365-246X.2009.04372.x.

Husson, L., Guillaume, B., Funiciello, F., Faccenna, C. & Royden, L.H. (2012). Unraveling topography around subduction zones from laboratory models. *Tectonophysics*, **526-529**, 5–15, doi:10.1016/j.tecto.2011.09.001.

Hutko, A.R., Lay, T., Garnero, E.J. & Revenaugh, J. (2006). Seismic detection of folded, subducted lithosphere at the core-mantle boundary. *Nature*, **441**, 333–6, doi:10.1038/nature04757.

Iwamori, H. (1998). Transportation of {H2O} and melting in subduction zones. *Earth and Planetary Science Letters*, **160**, 65 – 80, doi:10.1016/S0012-821X(98)00080-6.

Jarrard, R.D. (1986). Relations among subduction parameters. *Reviews of Geophysics*, **24**, 217, doi:10.1029/RG024i002p00217.

Jaupart, C., Labrosse, S. & Mareschal, J. (2007). Temperatures, heat and energy in the mantle of the Earth. In G. Schubert, ed., *Treatise on Geophysics*, chap. 7, 253–303, Amsterdam: Elsevier.

Jolivet, L. & Faccenna, C. (2000). Mediterranean extension and the Africa-Eurasia collision. *Tectonics*, **19**, 1095–1106.

Jolivet, L., Faccenna, C. & Piromallo, C. (2009). From mantle to crust: Stretching the Mediterranean. *Earth and Planetary Science Letters*, **285**, 198–209, doi:10.1016/j.epsl.2009.06.017.

Kaislaniemi, L., van Hunen, J., Allen, M.B. & Neill, I. (2014). Sublithospheric small-scale convection–A mechanism for collision zone magmatism. *Geology*, doi:10.1130/G35193.1.

KAMEYAMA, M., YUEN, D.A. & KARATO, S.I. (1999). Thermal-mechanical effects of low-temperature plasticity (the Peierls mechanism) on the deformation of a viscoelastic shear zone. *Earth and Planetary Science Letters*, **168**, 159–172, doi:10.1016/S0012-821X(99)00040-0.

KARATO, S.I. & WU, P. (1993). Rheology of the upper mantle: a synthesis. *Science*, **260**, 771–8, doi:10.1126/science.260.5109.771.

KAUS, B.J., MÜHLHAUS, H. & MAY, D.A. (2010). A stabilization algorithm for geodynamic numerical simulations with a free surface. *Physics of the Earth and Planetary Interiors*, **181**, 12–20, doi:10.1016/j.pepi.2010.04.007.

KENNEDY, C.S. & KENNEDY, G.C. (1976). The Equilibrium Boundary Between Graphite and Diamond. *Journal of Geophysical Research*, **81**, 2467–2470.

KESKIN, M. (2003). Magma generation by slab steepening and breakoff beneath a subduction-accretion complex: An alternative model for collision-related volcanism in Eastern Anatolia, Turkey. *Geophysical Research Letters*, **30**, 8046, doi:10.1029/2003GL018019.

KONRAD-SCHMOLKE, M., O'BRIEN, P.J., DE CAPITANI, C. & CARSWELL, D.A. (2008). Garnet growth at high- and ultra-high pressure conditions and the effect of element fractionation on mineral modes and composition. *Lithos*, **103**, 309–332, doi:10.1016/j.lithos.2007.10.007.

KORENAGA, J. (2013). Initiation and Evolution of Plate Tectonics on Earth: Theories and Observations. *Annual Review of Earth and Planetary Sciences*, **41**, 117–151, doi:10.1146/annurev-earth-050212-124208.

KRABBENDAM, M., WAIN, A. & ANDERSEN, T.B. (2000). Pre-Caledonian granulite and gabbro enclaves in the Western Gneiss Region, Norway: indications of incomplete transition at high pressure. *Geological Magazine*, **137**, 235–255, doi:10.1017/S0016756800004015.

KROGH, E.J. (1977). Evidence of Precambrian continentcontinent collision in Western Norway. *Nature*, **267**, 17–19, doi:10.1038/267017a0.

Krogh Ravna, E.J. & Terry, M.P. (2004). Geothermobarometry of UHP and HP eclogites and schists - an evaluation of equilibria among garnet-clinopyroxene-kyanite-phengite-coesite/quartz. *Journal of Metamorphic Geology*, **22**, 579–592, doi:10.1111/j.1525-1314.2004.00534.x.

Kronbichler, M., Heister, T. & Bangerth, W. (2012). High accuracy mantle convection simulation through modern numerical methods. *Geophysical Journal International*, **191**, 12–29, doi:10.1111/j.1365-246X.2012.05609.x.

Kylander-Clark, a., Hacker, B.R., Johnson, C., Beard, B., Mahlen, N. & Lapen, T. (2007). Coupled Lu-Hf and Sm-Nd geochronology constrains prograde and exhumation histories of high- and ultrahigh-pressure eclogites from western Norway. *Chemical Geology*, **242**, 137–154, doi:10.1016/j.chemgeo.2007.03.006.

Kylander-Clark, A.R., Hacker, B.R. & Mattinson, C.G. (2012). Size and exhumation rate of ultrahigh-pressure terranes linked to orogenic stage. *Earth and Planetary Science Letters*, **321-322**, 115–120, doi:10.1016/j.epsl.2011.12.036.

Kylander-Clark, A.R.C., Hacker, B.R., Johnson, C.M., Beard, B.L. & Mahlen, N.J. (2009). Slow subduction of a thick ultrahigh-pressure terrane. *Tectonics*, **28**, 1944–9194, doi:10.1029/2007TC002251.

Labrousse, L., Jolivet, L., Andersen, T.B., Agard, P., Hébert, R., Maluski, H. & Schärer, U. (2004). Pressure-temperature-time deformation history of the exhumation of ultra-high pressure rocks in the Western Gneiss Region , Norway. *Geological Society of America Special Papers*, **380**, 155–183.

Laigle, M., Sachpazi, M. & Hirn, A. (2004). Variation of seismic coupling with slab detachment and upper plate structure along the western Hellenic subduction zone. *Tectonophysics*, **391**, 85–95, doi:10.1016/j.tecto.2004.07.009.

Lallemand, S., Heuret, A. & Boutelier, D. (2005). On the relationships between slab dip, back-arc stress, upper plate absolute motion, and crustal nature in subduction zones. *Geochemistry, Geophysics, Geosystems*, **6**, Q09006, doi:10.1029/2005GC000917.

Lambeck, K., Smither, C. & Johnston, P. (1998). Sea-level change , glacial rebound and mantle viscosity for northern Europe. *Geophysical Journal International*, **134**, 102–144, doi:0.1046/j.1365-246x.1998.00541.x.

Le Voci, G., Davies, D.R., Goes, S., Kramer, S.C. & Wilson, C.R. (2013). A systematic 2-D Investigation into the mantle wedge's transient flow regime and thermal structure: Complexities arising from a hydrated rheology and thermal buoyancy. *Geochemistry, Geophysics, Geosystems*, **15**, 28, doi:10.1002/2013GC005022.

Lei, J. & Zhao, D. (2007). Teleseismic evidence for a break-off subducting slab under Eastern Turkey. *Earth and Planetary Science Letters*, **257**, 14–28, doi:DOI: 10.1016/j.epsl.2007.02.011.

Li, C., van der Hilst, R.D., Engdahl, E.R. & Burdick, S. (2008). A new global model for P wave speed variations in Earth's mantle. *Geochemistry, Geophysics, Geosystems*, **9**, Q05018, doi:10.1029/2007GC001806.

Li, Z. & Gerya, T.V. (2009). Polyphase formation and exhumation of high- to ultrahigh-pressure rocks in continental subduction zone: Numerical modeling and application to the Sulu ultrahigh-pressure terrane in eastern China. *Journal of Geophysical Research*, **114**, 1–27, doi:10.1029/2008JB005935.

Lin, A.T., Yao, B., Hsu, S.K., Liu, C.S. & Huang, C.Y. (2009). Tectonic features of the incipient arc-continent collision zone of Taiwan: Implications for seismicity. *Tectonophysics*, **479**, 28–42, doi:10.1016/j.tecto.2008.11.004.

Liou, J.G., Tsujimori, T., Zhang, R.Y., Katayama, I. & Maruyama, S. (2004). Global UHP Metamorphism and Continental Subduction/Collision: The Himalayan Model. *International Geology Review*, **46**, 1–27, doi:10.2747/0020-6814.46.1.1.

Lithgow-Bertelloni, C. & Silver, P.G. (1998). Dynamic topography, plate driving forces and the African superswell. *Nature*, **395**, 345–348, doi:10.1038/26212.

Little, T., Hacker, B.R., Gordon, S., Baldwin, S., Fitzgerald, P., Ellis, S. & Korchinski, M. (2011). Diapiric exhumation of Earth's youngest (UHP) eclogites in the gneiss domes of the D'Entrecasteaux Islands, Papua New Guinea. *Tectonophysics*, **510**, 39–68, doi:10.1016/j.tecto.2011.06.006.

MAGGI, A., JACKSON, J., MCKENZIE, D. & PRIESTLEY, K. (2000). Earthquake focal depths, effective elastic thickness, and the strength of the continental lithosphere. *Geology*, **28**, 495, doi:10.1130/0091-7613(2000)28¡495:EFDEET¿2.0.CO;2.

MANATSCHAL, G. & BERNOULLI, D. (1999). Architecture and tectonic evolution of nonvolcanic margins: Present-day Galicia and ancient Adria. *Tectonics*, **18**, 1099–1119, doi:10.1029/1999TC900041.

MARTIN, H. & MOYEN, J.F. (2002). Secular changes in tonalite-trondhjemite-granodiorite composition as markers of the progressive cooling of earth. *Geology*, **30**, 319–322, doi:10.1130/0091-7613(2002)0302.0.CO;2.

MASSONNE, H.J. (2003). A comparison of the evolution of diamondiferous quartz-rich rocks from the Saxonian Erzgebirge and the Kokchetav Massif: are so-called diamondiferous gneisses magmatic rocks? *Earth and Planetary Science Letters*, **216**, 347–364, doi:10.1016/S0012-821X(03)00512-0.

MASTERS, G., LASKE, G., BOLTON, H. & DZIEWONSKI, A. (2000). *Earth's Deep Interior: Mineral Physics and Tomography From the Atomic to the Global Scale*, vol. 117 of *Geophysical Monograph Series*. American Geophysical Union, Washington, D. C.

MATENCO, L. & RADIVOJEVIĆ, D. (2012). On the formation and evolution of the Pannonian Basin: Constraints derived from the structure of the junction area between the Carpathians and Dinarides. *Tectonics*, **31**, n/a–n/a, doi:10.1029/2012TC003206.

MCKENZIE, D. & FAIRHEAD, D. (1997). Estimates of the effective elastic thickness of the continental lithosphere from Bouguer and free air gravity anomalies. *Journal of Geophysical Research*, **102**, 27523, doi:10.1029/97JB02481.

MCKENZIE, D. & PRIESTLEY, K. (2008). The influence of lithospheric thickness variations on continental evolution. *Lithos*, **102**, 1–11, doi:10.1016/j.lithos.2007.05.005.

MCKENZIE, D.P. (1969). Speculations on the Consequences and Causes of Plate Motions. *Geophysical Journal of the Royal Astronomical Society*, 1–32, doi:10.1111/j.1365-246X.1969.tb00259.x.

McQuarrie, N., Stock, J.M., Verdel, C. & Wernicke, B.P. (2003). Cenozoic evolution of Neotethys and implications for the causes of plate motions. *Geophysical Research Letters*, **30**, doi:10.1029/2003GL017992.

Melosh, H.J. & Raefsky, A. (1980). The dynamical origin of subduction zone topography. *Geophysical Journal of the Royal Astronomical Society*, **60**, 333–354, doi:10.1111/j.1365-246X.1980.tb04812.x.

Meulenkamp, J., Ková, M., Cicha, I. & Kovac, M. (1996). On Late Oligocene to Pliocene depocentre migrations and the evolution of the Carpathian-Pannonian system. *Tectonophysics*, **266**, 301–317, doi:10.1016/S0040-1951(96)00195-3.

Milnes, A. & Corfu, F. (2008). Structural geology and tectonic evolution of the Sognefjord transect, Caledonian orogen, southern Norway,. In *33rd International Geological Congress, Oslo, Norway*, 1–94.

Molnar, P. & Stock, J.M. (2009). Slowing of India's convergence with Eurasia since 20 Ma and its implications for Tibetan mantle dynamics. *Tectonics*, **28**, 1–11, doi:10.1029/2008TC002271.

Moresi, L. & Gurnis, M. (1996). Constraints on the lateral strength of slabs from three-dimensional dynamic flow models. *Earth and Planetary Science Letters*, **138**, 15–28, doi:10.1016/0012-821X(95)00221-W.

Moresi, L. & Solomatov, V.S. (1995). Numerical investigation of 2D convection with extremely large viscosity variations. *Physics of Fluids*, **7**, 2154, doi:10.1063/1.868465.

Morley, C.K., Kongwung, B., Julapour, A.A., Abdolghafourian, M., Hajian, M., Waples, D., Warren, J., Otterdoom, H., Srisuriyon, K. & Kazemi, H. (2009). Structural development of a major late Cenozoic basin and transpressional belt in central Iran: The Central Basin in the Qom-Saveh area. *Geosphere*, **5**, 325–362, doi:10.1130/GES00223.1.

Mouthereau, F., Lacombe, O. & Vergés, J. (2012). Building the Zagros collisional orogen: Timing, strain distribution and the dynamics of Arabia/Eurasia plate convergence. *Tectonophysics*, **532-535**, 27–60, doi:10.1016/j.tecto.2012.01.022.

NADIROV, R., BAGIROV, E., TAGIYEV, M. & LERCHE, I. (1997). Flexural plate subsidence, sedimentation rates, and structural development of the super-deep South Caspian Basin. *Marine and Petroleum Geology*, **14**, 383–400, doi:10.1016/S0264-8172(96)00054-2.

NAKAGAWA, T. & TACKLEY, P.J. (2004). Thermo-chemical structure in the mantle arising from a three-component convective system and implications for geochemistry. *Physics of the Earth and Planetary Interiors*, **146**, 125–138, doi:10.1016/j.pepi.2003.05.006.

NATIONAL IRANIAN OIL COMPANY (1977a). Geological Map of Iran Sheet 1 North-west Iran, scale 1:1,000,000. Tech. rep., National Iranian Oil Company, Tehran.

NATIONAL IRANIAN OIL COMPANY (1977b). Geological Map of Iran Sheet 5 South-Central Iran, scale 1:1,000,000. Tech. rep., National Iranian Oil Company, Tehran.

NATIONAL IRANIAN OIL COMPANY (1978). Geological Map of Iran Sheet 5 Sheet 1 North-west, scale 1:1,000,000. Tech. rep., National Iranian Oil Company, Tehran.

NISSEN, E., YAMINI-FARD, F., TATAR, M., GHOLAMZADEH, A., BERGMAN, E., ELLIOTT, J., JACKSON, J. & PARSONS, B. (2010). The vertical separation of mainshock rupture and microseismicity at Qeshm island in the Zagros fold-and-thrust belt, Iran. *Earth and Planetary Science Letters*, **296**, 181–194, doi:10.1016/j.epsl.2010.04.049.

NOLET, G. (2009). Slabs Do Not Go Gently. *Science*, **324**, 1152–1153, doi:10.1126/science.1174664.

OBAYASHI, M., YOSHIMITSU, J. & FUKAO, Y. (2009). Tearing of stagnant slab. *Science*, **324**, 1173.

OMRANI, J., AGARD, P., WHITECHURCH, H., BENOIT, M., PROUTEAU, G. & JOLIVET, L. (2008). Arc-magmatism and subduction history beneath the Zagros Mountains, Iran: A new report of adakites and geodynamic consequences. *Lithos*, **106**, 380–398, doi:10.1016/j.lithos.2008.09.008.

PAUL, A., KAVIANI, A., HATZFELD, D., VERGNE, J. & MOKHTARI, M. (2006). Seismological evidence for crustal-scale thrusting in the Zagros mountain belt (Iran). *Geophysical Journal International*, **166**, 227–237, doi:10.1111/j.1365-246X.2006.02920.x.

Pérez-Gussinyé, M., Metois, M., Fernández, M., Vergés, J., Fullea, J. & Lowry, A. (2009). Effective elastic thickness of Africa and its relationship to other proxies for lithospheric structure and surface tectonics. *Earth and Planetary Science Letters*, **287**, 152–167, doi:10.1016/j.epsl.2009.08.004.

Philip, H., Cisternas, A., Gvishiani, A. & Gorshkov, A. (1989). The Caucasus: an actual example of the initial stages of continental collision. *Tectonophysics*, **161**, 1–21, doi:10.1016/0040-1951(89)90297-7.

Pidwirny, M. (1999). *Fundamentals of Physical Geography*.

Quinquis, M.E., Buiter, S.J. & Ellis, S. (2011). The role of boundary conditions in numerical models of subduction zone dynamics. *Tectonophysics*, **497**, 57–70, doi:10.1016/j.tecto.2010.11.001.

Ramsey, M., J.G. Huber (1984). *The Techniques of Modern Structural Geology: Strain Analyses*. Academic Press.

Ranalli, G. (1995). *Rheology of the Earth*. Chapman & Hall, London.

Regard, V., Faccenna, C., Bellier, O. & Martinod, J. (2008). Laboratory experiments of slab break-off and slab dip reversal: insight into the Alpine Oligocene reorganization. *Terra Nova*, **20**, 267–273, doi:10.1111/j.1365-3121.2008.00815.x.

Reuter, M., Piller, W.E., Harzhauser, M., Mandic, O., Berning, B., Rögl, F., Kroh, A., Aubry, M.P., Wielandt-Schuster, U. & Hamedani, A. (2007). The Oligo-/Miocene Qom Formation (Iran): evidence for an early Burdigalian restriction of the Tethyan Seaway and closure of its Iranian gateways. *International Journal of Earth Sciences*, **98**, 627–650, doi:10.1007/s00531-007-0269-9.

Ricard, Y. & Wuming, B. (1991). Inferring the viscosity and the 3-D density structure of the mantle from geoid, topography and plate velocities. *Geophysical Journal International*, **105**, 561–571, doi:10.1111/j.1365-246X.1991.tb00796.x.

RICE, A.H.N. (2005). Quantifying the Exhumation of UHP-Rocks in the Western Gneiss Region , S . W . Norway : a Branch-line Balanced Cross- section Model. *Austrain Journal of Earth Sciences*, **98**, 2–21.

RING, U. & GLODNY, J. (2010). No need for lithospheric extension for exhuming (U)HP rocks by normal faulting. *Journal of the Geological Society*, **167**, 225–228, doi:10.1144/0016-76492009-134.

RINGWOOD, A. (1994). Role of the transition zone and 660 km discontinuity in mantle dynamics. *Physics of the Earth and Planetary Interiors*, **86**, 5–24, doi:10.1016/0031-9201(94)05058-9.

RITZWOLLER, M.H., SHAPIRO, N.M. & ZHONG, S.J. (2004). Cooling history of the Pacific lithosphere. *Earth and Planetary Science Letters*, **226**, 69–84, doi:10.1016/j.epsl.2004.07.032.

ROBINSON, P. (1995). Extension of Trollheimen tectono-stratigraphic sequence in deep synclines near Molde and Brattvåg, Western Gneiss Region, southern Norway. *Norsk Geologisk Tidsskrift*, **75**, 181–198.

ROECKER, S. (1982). Velocity structure of the Pamir-Hindu Kush region: Possible evidence of subducted crust. *Journal of Geophysical Research*, **87**, 945–959, doi:10.1029/JB087iB02p00945.

ROOT, D.B., HACKER, B.R., GANS, P.B., DUCEA, M.N., EIDE, E.A. & MOSENFELDER, J.L. (2005). Discrete ultrahigh-pressure domains in the Western Gneiss Region, Norway: implications for formation and exhumation. *Journal of Metamorphic Geology*, **23**, 45–61, doi:10.1111/j.1525-1314.2005.00561.x.

ROURE, F. (2008). Foreland and Hinterland basins: what controls their evolution? *Swiss Journal of Geosciences*, **101**, 5–29, doi:10.1007/s00015-008-1285-x.

RUDNICK, R.L. (1995). Making continental crust. *Nature*, **378**, 572–577, doi:10.1038/378571a0.

SCHMELING, H., BABEYKO, A.Y., ENNS, A., FACCENNA, C., FUNICIELLO, F., GERYA, T.V., GOLABEK, G., GRIGULL, S., KAUS, B., MORRA, G., SCHMALHOLZ, S. & VAN HUNEN, J. (2008). A benchmark comparison of spontaneous subduction modelsTowards a free surface. *Physics of the Earth and Planetary Interiors*, **171**, 198–223, doi:10.1016/j.pepi.2008.06.028.

Seghedi, I., Balintoni, I. & Szakács, A. (1998). Interplay of tectonics and neogene post-collisional magmatism in the intracarpathian region. *Lithos*, **45**, 483–497, doi:10.1016/S0024-4937(98)00046-2.

Sella, G.F., Dixon, T.H. & Mao, A. (2002). REVEL: A model for Recent plate velocities from space geodesy. *Journal of Geophysical Research*, **107**, 2–30, doi:10.1029/2000JB000033.

Şenel, M. (2002). Geological map of Turkey, scale 1:500,000. Tech. rep., General Directorate of Mineral Research and Exploration, Ankara.

Şengör, A.C., Özeren, M.S., Keskin, M., Saknç, M., Özbakr, A.D. & Kayan, I. (2008). Eastern Turkish high plateau as a small Turkic-type orogen: Implications for post-collisional crust-forming processes in Turkic-type orogens. *Earth-Science Reviews*, **90**, 1–48, doi:10.1016/j.earscirev.2008.05.002.

Shephard, G.E., Müller, R.D., Liu, L. & Gurnis, M. (2010). Miocene drainage reversal of the Amazon River driven by platemantle interaction. *Nature Geoscience*, **3**, 870–875, doi:10.1038/ngeo1017.

Smith, D.C. (1984). Coesite in clinopyroxene in the Caledonides and its implications for geodynamics. *Nature*, **310**, 641–644, doi:10.1038/310641a0.

Spakman, W. & Hall, R. (2010). Surface deformation and slabmantle interaction during Banda arc subduction rollback. *Nature Geoscience*, **3**, 562–566, doi:10.1038/ngeo917.

Spasojevic, S., Gurnis, M. & Sutherland, R. (2010). Mantle upwellings above slab graveyards linked to the global geoid lows. *Nature Geoscience*, **3**, 435–438, doi:10.1038/ngeo855.

Spear, F.S., Selverstone, J., Hickmott, D., Crowley, P. & Hodges, K.V. (1984). P-T paths from garnet zoning: A new technique for deciphering tectonic processes in crystalline terranes. *Geology*, **12**, 87–90, doi:10.1130/0091-7613(1984)12.

SPENGLER, D., VAN ROERMUND, H.L.M., DRURY, M.R., OTTOLINI, L., MASON, P.R.D. & DAVIES, G.R. (2006). Deep origin and hot melting of an Archaean orogenic peridotite massif in Norway. *Nature*, **440**, 913–7, doi:10.1038/nature04644.

SPENGLER, D., BRUECKNER, H.K., VAN ROERMUND, H.L., DRURY, M.R. & MASON, P.R. (2009). Long-lived, cold burial of Baltica to 200 km depth. *Earth and Planetary Science Letters*, **281**, 27–35, doi:10.1016/j.epsl.2009.02.001.

SPERNER, B., LORENZ, F., BONJER, K., HETTEL, S., MÜLLER, R.D., WENZEL, F. & MU, B. (2001). Slab break-off abrupt cut or gradual detachment ? New insights from the Vrancea Region (SE Carpathians , Romania). *Terra Nova*, **13**, 172–179, doi:10.1046/j.1365-3121.2001.00335.x.

STEIN, C.A. & STEIN, S. (1992). A model for the global variation in oceanic depth and heat flow with lithospheric age. *Nature*, **359**, 123–129, doi:10.1038/359123a0.

SYRACUSE, E.M. & ABERS, G.A. (2006). Global compilation of variations in slab depth beneath arc volcanoes and implications. *Geochemistry Geophysics Geosystems*, **7**, doi:10.1029/2005GC001045.

TAN, E., GURNIS, M. & HAN, L. (2002). Slabs in the lower mantle and their modulation of plume formation. *Geochemistry, Geophysics, Geosystems*, **3**, 1–24, doi:10.1029/2001GC000238.

TERRY, M.P., ROBINSON, P., RAVNA, E.J.K., ERRY, M.I.P.T., OBINSON, P.E.R. & AVNA, E.R.J.K.R.R. (2000). Kyanite eclogite thermobarometry and evidence for thrusting of UHP over HP metamorphic rocks , Nordøyane , Western Gneiss Region , Norway. *American Mineralogist*, **85**, 1637–1650.

TEYSSIER, C. (2011). Exhumation of deep orogenic crust. *Lithosphere*, **3**, 439–443, doi:10.1130/RF.L002.1.

TOKSÖZ, M., JOHNSTON, D. & TIMUR, A. (1979). Attenuation of seismic waves in dry and saturated rocks: I. laboratory measurements. *Geophysics*, **44**, 681–690, doi:10.1190/1.1440969.

TÖRNEBOHM, A.E. (1896). Grunddragen af det Centrala Skan- dinavians Bergbyggnad. *Svenska Vetenskap- sakademiens Handlingar*, **2**, 1–210.

Torsvik, T., Smethurst, M., Meert, J., Vandervoo, R., Mckerrow, W., Brasier, M., Sturt, B. & Walderhaug, H. (1996). Continental break-up and collision in the Neoproterozoic and Palaeozoic A tale of Baltica and Laurentia. *Earth-Science Reviews*, **40**, 229–258, doi:10.1016/0012-8252(96)00008-6.

Torsvik, T.H., Smethurst, M.a., Van der Voo, R., Trench, A., Abrahamsen, N. & Halvorsen, E. (1992). Baltica. A synopsis of vendian-permian palaeomagnetic data and their palaeotectonic implications. *Earth-Science Reviews*, **33**, 133–152, doi:10.1016/0012-8252(92)90023-M.

Torsvik, T.H., Van der Voo, R., Preeden, U., Mac Niocaill, C., Steinberger, B., Doubrovine, P.V., van Hinsbergen, D.J., Domeier, M., Gaina, C., Tohver, E., Meert, J.G., McCausland, P.J. & Cocks, L.R.M. (2012). Phanerozoic polar wander, palaeogeography and dynamics. *Earth-Science Reviews*, **114**, 325–368, doi:10.1016/j.earscirev.2012.06.007.

Tucker, R.D., Robinson, P., Solli, A., Gee, D.G., Thorsnes, T., Krogh, T.E., Nordgulen, O.y. & Bickford, M.E. (2004). Thrusting and Extension in the Scandian Hinterland, Norway: new U-Pb Ages and Tectonostratigraphic Evidence. *American Journal of Science JUNE*, **304**, 477–532, doi:10.2475/ajs.304.6.477.

Turcotte, D. (1987). *Composition, Structure and Dynamics of the LithosphereAsthenosphere System*, vol. 16 of *Geodynamics Series*. American Geophysical Union, Washington, D. C.

Turcotte, D. & Schubert, G. (2002). *Geodynamics*. Cambridge University Press.

van der Meulen, M., Meulenkamp, J. & Wortel, R. (1998). Lateral shifts of Apenninic foredeep depocentres reflecting detachment of subducted lithosphere. *Earth and Planetary Science Letters*, **154**, 203–219, doi:10.1016/S0012-821X(97)00166-0.

van der Meulen, M., Kouwenhoven, T., van der Zwaan, G., Meulenkamp, J. & Wortel, M. (1999). Late Miocene uplift in the Romagnan Apennines and the detachment of subducted lithosphere. *Tectonophysics*, **315**, 319–335, doi:10.1016/S0040-1951(99)00282-6.

van Hunen, J. & Allen, M.B. (2011). Continental collision and slab break-off: A comparison of 3-D numerical models with observations. *Earth and Planetary Science Letters*, **302**, 27–37, doi:10.1016/j.epsl.2010.11.035.

van Hunen, J. & Moyen, J.F. (2012). Archean Subduction: Fact or Fiction? *Annual Review of Earth and Planetary Sciences*, **40**, 195–219, doi:10.1146/annurev-earth-042711-105255.

van Hunen, J., Zhong, S., Shapiro, N.M., Ritzwoller, M.H. & van Hunen, J. (2005). New evidence for dislocation creep from 3-D geodynamic modeling of the Pacific upper mantle structure. *Earth and Planetary Science Letters*, **238**, 146–155, doi:10.1016/j.epsl.2005.07.006.

van Hunen, J., van Keken, P.E., Hynes, A. & Davies, G.F. (2008). Tectonics of early Earth: Some geodynamic considerations. In K.C. Condie & V. Pease, eds., *When did Plate Tectonics begin on planet earth*, vol. 440 of *Geological Society of America Special Papers*, 157–171, GEOLOGICAL SOC AMER INC, BOULDER, CO, USA.

van Roermund, H.L., Carswell, D.A., Drury, M.R., Heijboer, T.C. & Roermund, H.L.M.V. (2002). Microdiamonds in a megacrystic garnet websterite pod from Bardane on the island of Fjortoft, western Norway: Evidence for diamond formation in mantle rocks during deep continental subduction. *Geology*, **30**, 957–1052, doi:10.1130/0091-7613(2002)030¡0959.

Vigil, J.F. (2013). A cross section illustrating the main types of plate boundaries.

Vincent, S.J., Morton, A.C., Carter, A., Gibbs, S. & Barabadze, T.G. (2007). Oligocene uplift of the Western Greater Caucasus: an effect of initial Arabia-Eurasia collision. *Terra Nova*, **19**, 160–166, doi:10.1111/j.1365-3121.2007.00731.x.

Vlaar, N. & Wortel, M. (1976). Lithospheric aging, instability and subduction. *Tectonophysics*, **32**, 331–351, doi:10.1016/0040-1951(76)90068-8.

Vogt, K., Gerya, T.V. & Castro, A. (2012). Crustal growth at active continental margins: Numerical modeling. *Physics of the Earth and Planetary Interiors*, **192-193**, 1–20, doi:10.1016/j.pepi.2011.12.003.

Vrijmoed, J.C., Van Roermund, H.L.M. & Davies, G.R. (2006). Evidence for diamond-grade ultra-high pressure metamorphism and fluid interaction in the Svartberget FeTi garnet peridotitewebsterite body, Western Gneiss Region, Norway. *Mineralogy and Petrology*, **88**, 381–405, doi:10.1007/s00710-006-0160-6.

Vrijmoed, J.C., Podladchikov, Y.Y., Andersen, T.B. & Hartz, E.H. (2009). An alternative model for ultra-high pressure in the Svartberget Fe-Ti garnet-peridotite, Western Gneiss Region, Norway. *European Journal of Mineralogy*, **21**, 1119–1133, doi:10.1127/0935-1221/2009/0021-1985.

Wada, I., Wang, K., He, J. & Hyndman, R.D. (2008). Weakening of the subduction interface and its effects on surface heat flow, slab dehydration, and mantle wedge serpentinization. *Journal of Geophysical Research*, **113**, B04402, doi:10.1029/2007JB005190.

Wain, A. (1997). New evidence for coesite in eclogite and gneisses : Defining an ultrahigh-pressure province in the Western Gneiss region of Norway. *Geology*, **25**, 927–930, doi:10.1130/0091-7613(1997)025¡0927.

Walsh, E.O. & Hacker, B.R. (2004). The fate of subducted continental margins: Two-stage exhumation of the high-pressure to ultrahigh-pressure Western Gneiss Region, Norway. *Journal of Metamorphic Geology*, **22**, 671–687, doi:10.1111/j.1525-1314.2004.00541.x.

Walsh, E.O., Hacker, B.R., Gans, P.B., Wong, M.S. & Andersen, T.B. (2013). Crustal exhumation of the Western Gneiss Region UHP terrane, Norway: 40Ar/39Ar thermochronology and fault-slip analysis. *Tectonophysics*, **608**, 1159–1179, doi:10.1016/j.tecto.2013.06.030.

Wang, E., Meng, Q., Burchfiel, B.C. & Zhang, G. (2003). Mesozoic large-scale lateral extrusion , rotation , and uplift of the Tongbai Dabie Shan belt in east China. *Geology*, **31**, 307–310, doi:10.1130/0091-7613(2003)031¡0307.

Wang, H., van Hunen, J., Pearson, D.G. & Allen, M.B. (2014). Craton stability and longevity: The roles of composition-dependent rheology and buoyancy. *Earth and Planetary Science Letters*, **391**, 224–233, doi:10.1016/j.epsl.2014.01.038.

Warren, C., Beaumont, C. & Jamieson, R. (2008a). Modelling tectonic styles and ultra-high pressure (UHP) rock exhumation during the transition from oceanic subduction to continental collision. *Earth and Planetary Science Letters*, **267**, 129–145, doi:10.1016/j.epsl.2007.11.025.

Warren, C.J. (2013). Exhumation of (ultra-)high-pressure terranes: concepts and mechanisms. *Solid Earth*, **4**, 75–92, doi:10.5194/se-4-75-2013.

Warren, C.J., Beaumont, C. & Jamieson, R.a. (2008b). Formation and exhumation of ultra-high-pressure rocks during continental collision: Role of detachment in the subduction channel. *Geochemistry, Geophysics, Geosystems*, **9**, 1–33, doi:10.1029/2007GC001839.

Watts, A. & Burov, E. (2003). Lithospheric strength and its relationship to the elastic and seismogenic layer thickness. *Earth and Planetary Science Letters*, **213**, 113–131, doi:10.1016/S0012-821X(03)00289-9.

Watts, A.B. (2001). *Isostasy and Flexure of the Lithosphere*. Cambridge University Press.

Watts, A.B., Bodine, J.H. & Ribe, N.M. (1980). Observations of flexure and the geological evolution of the Pacific Ocean basin. *Nature*, **283**, 532–537, doi:10.1038/283532a0.

Webb, L., Baldwin, S., Little, T. & Fitzgerald, P. (2008). Can microplate rotation drive subduction inversion. *Geology*, **36**, 823, doi:10.1130/G25134A.1.

Wegener, A. (1912). Die Herausbildung der Grossformen der Erdrinde (Kontinente und Ozeane), auf geophysikalischer Grundlage. *Petermanns Geographische Mitteilungen*, **63**, 185–195.

Wilks, W. & Cuthbert, S. (1994). The evolution of the Hornelen Basin detachment system, western Norway: Implications for the style of late orogenic extension in the southern Scandinavian Caledonides. *Tectonophysics*, **238**, 1–30, doi:10.1016/0040-1951(94)90047-7.

Williams, S.E., Müller, R.D. & Landgrebe, T.C.W. (2012). An open-source software environment for visualizing and refining plate tectonic reconstructions using high-resolution geological and geophysical data sets. *GSA today*, **22**, 4–9, doi:10.1130/GSATG139A.1.

Wilson, J.T. (1966). Did the Atlantic close and then re-open? *Nature*, **211**, 676–681, doi:10.1038/211676a0.

Wilson, M. (1993). Plate-moving mechanisms: constraints and controversies. *Journal of the Geological Society*, **150**, 923–926, doi:10.1144/gsjgs.150.5.0923.

Winter, J.D. & Winters, J.D. (2001). *An introduction to Igneous and Metamorphic Petrology*. Prentice Hall.

Woodhouse, J.H. & Dziewonski, A.M. (1984). Mapping the upper mantle: Three-dimensional modeling of earth structure by inversion of seismic waveforms. *Journal of Geophysical Research*, **89**, 5953, doi:10.1029/JB089iB07p05953.

Wortel, M. & Spakman, W. (2000). Subduction and slab Detachment in the Meditaranian-Carpathian region Region. *Science*, **290**, 1910–1917, doi:10.1126/science.290.5498.1910.

Wortel, R. & Spakman, W. (1992). Structure and dynamics of subducted lithosphere in the Mediterranean region. *Proceedings of the Koninklijke Nederlandse Akademie van Wetenschappen*, **95**, 325–347.

Yoshioka, S., Wortel, M.J.R. & Wortel, R. (1995). Three-dimensional numerical modeling of detachment of subducted lithosphere. *Journal of Geophysical Research*, **100**, 20223–20244, doi:10.1029/94JB01258.

Zhang, R., Liou, J. & Ernst, W. (2009). The DabieSulu continental collision zone: A comprehensive review. *Gondwana Research*, **16**, 1–26, doi:10.1016/j.gr.2009.03.008.

Zhao, Z.F., Zheng, Y.F., Wei, C.S. & Wu, Y.B. (2007). Post-collisional granitoids from the Dabie orogen in China: Zircon UPb age, element and O isotope evidence for recycling of subducted continental crust. *Lithos*, **93**, 248–272, doi:10.1016/j.lithos.2006.03.067.

Zhong, S. & Gurnis, M. (1994). Controls on trench topography from dynamic models of subducted slabs. *Journal of Geophysical Research*, **99**, 15683, doi:10.1029/94JB00809.

Zhong, S., Zuber, M.T., Moresi, L. & Gurnis, M. (2000). Role of temperature-dependent viscosity and surface plates in spherical shell models of mantle convection. *Journal of Geophysical Research*, **105**, 11063, doi:10.1029/2000JB900003.

8

Appendices

8.1 Chapter 2 appendix

8.1.1 Strain rate tensor

Finite Strain theory allows us to describe the strainrate ellipsoid in 2D in the following form [Ramsey, 1984].

$$\epsilon_{ij} = \begin{pmatrix} \dot{\epsilon}_{xx} & \dot{\epsilon}_{xz} \\ \dot{\epsilon}_{zx} & \dot{\epsilon}_{zz} \end{pmatrix} \tag{8.1}$$

where $\dot{\epsilon}_{xx} = 2\frac{\partial v_x}{\partial x}$, $\qquad \dot{\epsilon}_{zz} = 2\frac{\partial v_z}{\partial z}$, $\qquad \dot{\epsilon}_{xz} = \frac{\partial v_x}{\partial z} + \frac{\partial v_z}{\partial x}$

The second invariant of the strainrate tensor gives a magnitude of the strain experience in that region of the model and is calculated as:

$$E = (\frac{1}{2}(\dot{\epsilon}_{xx}^2 + \dot{\epsilon}_{xz}^2 + \dot{\epsilon}_{zx}^2 + \dot{\epsilon}_{zz}^2))^{\frac{1}{2}} \tag{8.2}$$

The strainrate is plotted by calculating the maximum axis of extension and compression and the angle that they make with the principal z-axis in the mode. The angle between the axis of most extension and the principal z-axis (θ) is calculated

$$\tan 2\theta = \frac{\dot{\epsilon}_{zz} - \dot{\epsilon}_{xx}}{2\dot{\epsilon}_{xz}} \tag{8.3}$$

The magnitude of compression and extension are calculated using

$$\dot{\epsilon}_{1,2} = \frac{\dot{\epsilon}_{xx} + \dot{\epsilon}_{zz}}{2} \pm \left(\frac{(\dot{\epsilon}_{xx} + \dot{\epsilon}_{zz})^2}{4} + \dot{\epsilon}_{xz}^2 \right) \tag{8.4}$$

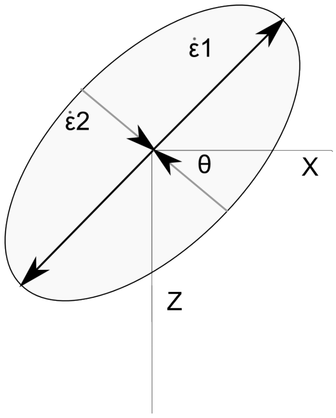

Figure 8.1: Diagram of strain tensor - with principal direction and angle markedϵ_1 and ϵ_2 represent the axis of compression and axis of extension

A graphical representation of the strainrate tensor is shown in Fig. 8.1.

The strainrate plotting was tested with a series of models that demonstrate simple and pure shear. The strainrate ellipsoid is well known for these cases and so provides a good test of the plotting. We first test the pure shear case 8.2. Where:

$\epsilon_{ij} = \begin{pmatrix} 0 & 0 \\ 0 & 2 \end{pmatrix}$ for extension and $\epsilon_{ij} = \begin{pmatrix} 0 & 0 \\ 0 & -2 \end{pmatrix}$ for compression.

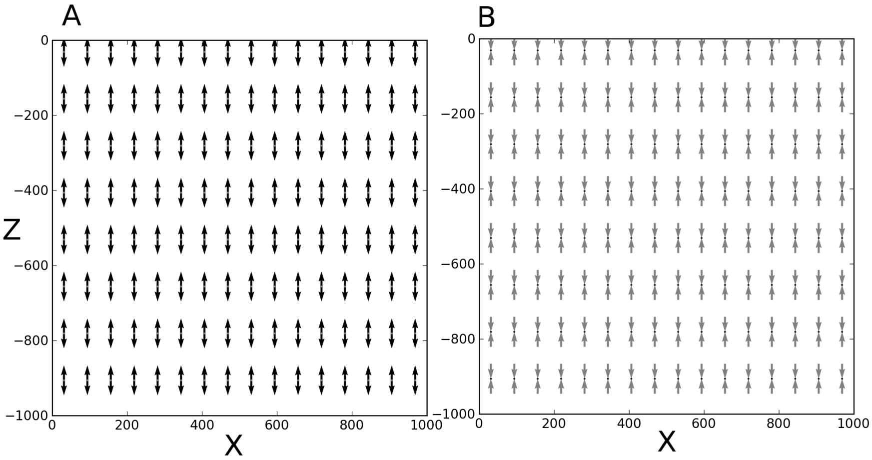

Figure 8.2: Pure shear extension and compression - Extension of the strain ellipsoid is plotted as black arrows compression is plotted as grey A) shows the strain ellipsoid for pure extension along the z-axis. Here we can see that the strain ellipsoid is just extended along the z axis B) shows the strain ellipsoid for pure compression along the z-axis. Here the stain ellipsoid is just compressed.

We can also represent the strainrate as the change in shape of a circle (in 2D). Here we show the pure shear cases plotted as ellipsoids.

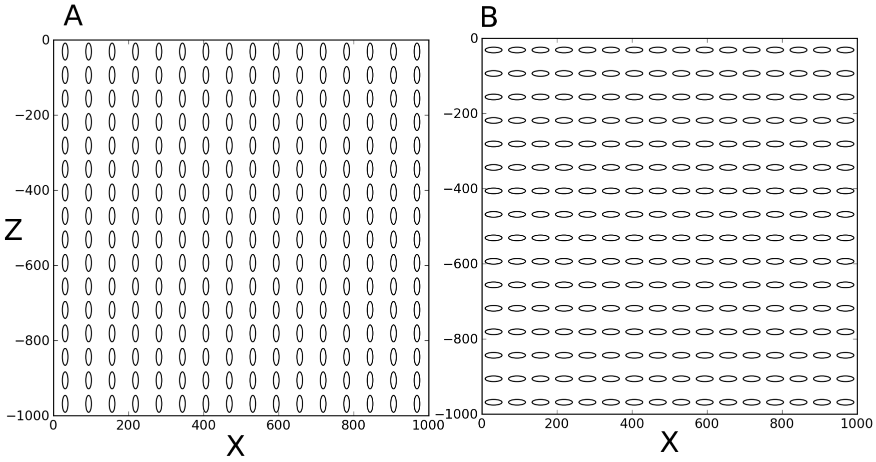

Figure 8.3: Pure shear extension and compression ellipses - A) how a circle would be deformed under a purely extensional strain field. B) how a circle would be deformed under a purely compressional strain field.

We further test the straintensor plotting on a Couette flow which simulates the simple shear situation. Where

$$\epsilon_{ij} = \begin{pmatrix} 0 & 1 \\ 1 & 0 \end{pmatrix}$$

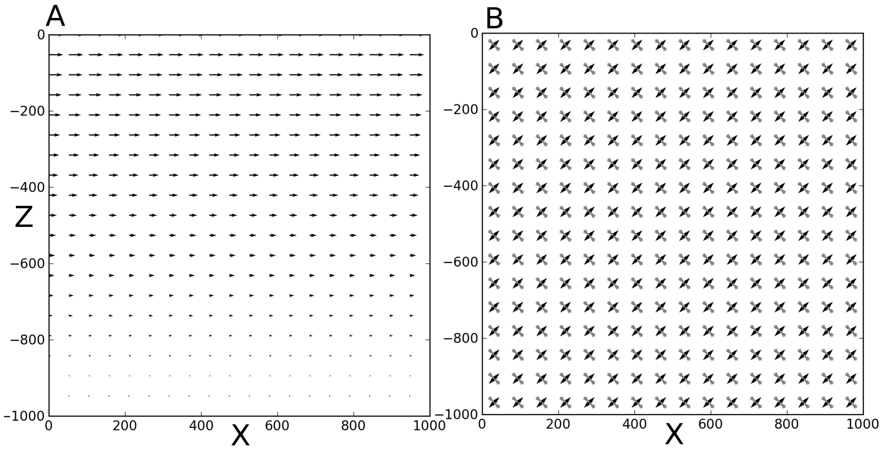

Figure 8.4: Strain rate tensor for Couette flow - A) shows the velocity field for a Couette flow with high horizontal velocities near the top of the model and zero horizontal velocities at the base of the model B) shows the strain tensor as calculated from the velocity field. The strain tensor shows equal extension and compression at an angle of 45° to the z-axis. This is the strainrate expected for the case of simple shear.

The correct representation of the strainrate field, for these simple cases, validates the ability to correctly plot the strainrate. For our full subduction models the 4 components of the strain tensor are calculated from the velocity field and then plotted over a colour plot of the second invariant of strainrate.

8.2 Chapter 3 appendix

8.2.1 Topography sensitivity testing

This Appendix discusses the sensitivity of modelling results to the choice of subduction model parameters. Fig. 8.5 illustrates a suite of model runs with different input parameters. For each model the maximum depth of the collisional dynamic basin was picked in time and space. Here we can see how each input parameter affects the depth of this depression. The value for our preferred model presented in this study is highlighted in red. All models share the initial set-up as described in the method section of this study, apart from the set-up condition under investigation.

In Fig 8.5A, we show how a reduction in surface yield strength reduces the depth of the basin. This is due to a smaller surface yield strength allowing material at the top boundary of the model to more easily deform. This has the effect of reducing the magnitude of all topography by lowering the normal stress placed on the boundary.

Fig. 8.5B shows how an increase in the weak zone viscosity slightly increases the depth of the basin. In our model the weak zone viscosity defines the coupling between the subducting and overriding plate. As the weak zone increases in viscosity this decreases subduction speeds but also holds the slab to the overriding plate with a greater force. This means that when steepening occurs it has more effect in models with a stronger weak zone. It should also be noted that for the higher weak zone viscosities the basin was formed much later in time and that subduction speeds were much slower.

In Fig. 8.5C, we show how the mantle wedge viscosity has little effect on the basin depth. This is due to the basin being due to slab steepening which creates a flow over a much larger area than just the mantle wedge. This means that even with a stronger or weaker mantle wedges the stress is still transmitted to the overriding plate, thereby creating the topography. In Fig. 8.5D we show how the width of the mantle wedge has little effect on the basin depth. This is for the same reason as the mantle wedge viscosity in that the flow responsible for the basin is much larger that the mantle wedge. The lack of sensitivity to the mantle wedge width also shows that the topography and in particular the CDB is not due to the placement of the mantle wedge. Which implies that our model set-up is not controlling our topography signal.

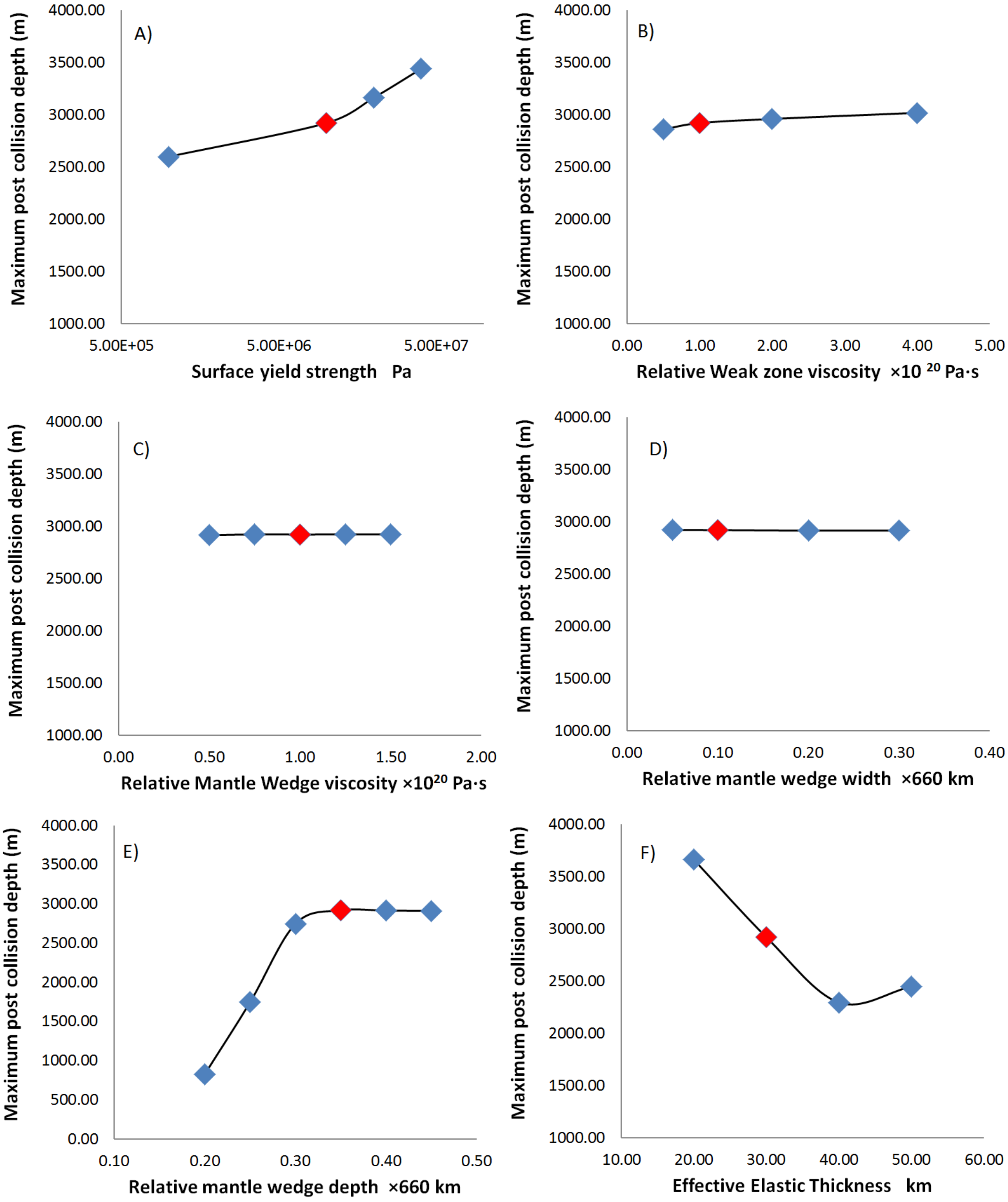

Figure 8.5: Topography sensitivity analysis - Graphs showing the sensitivity of the depth of the collisional dynamic basin (CDB) to six different model input parameters. The maximum basin depth on the overriding plate is picked in space and time between collision and break-off. Collision is defined as the point where the two continental blocks first make contact and break-off is defined as the point where subduction velocity is no longer positive. The comparison of how input parameters affect the basin depth gives us some measure on how different model set-ups interact with the results produced. The default value used in our preferred model is highlighted in red.

Fig. 8.5E shows how the depth of the weak mantle wedge affects the basin depth. Here, we can see that, as the wedge is made shallower from our preferred model, the basin becomes shallower. If made deeper than our preferred model, little effect is observed. This is due to the mantle wedge being placed below the lithosphere in our preferred model. If the wedge is placed shallower than this, it allows the slab to partially steepen before collision, so a smaller basin depth is created after collision. Placing the wedge deeper has little effect, since the material in this area is already weak due to being at mantle temperature.

Fig. 8.5F shows the effect of the chosen effective elastic thickness on the collisional dynamic basin depth. This shows that with larger effective elastic thickness, the depth of the basin is reduced. The choice of effective elastic thickness and its effects are further discussed in Appendix 8.2.2.

Overall, this Appendix demonstrates that the topography features are robust and not a product of the initial conditions. Although there are a number of initial set-ups that do affect the topography, the initial set-up chosen in our preferred model offers a geologically reasonable subduction and collision set-up. Our preferred model set-up is not specifically tuned to the Arabia-Eurasia collision, though it does offer a good model for comparison to this collision zone.

8.2.2 Elastic Thickness

The effective elastic thickness T_e of the lithosphere around the Arabia-Eurasia continental collision zone is relatively poorly defined given the uncertainty in plate thickness [McKenzie & Fairhead, 1997; Maggi *et al.*, 2000; Watts & Burov, 2003] and the uncertainty in the strength of the newly formed suture. The effect of increasing the effective elastic thickness can be seen in Fig. 8.6 were we show the topography time map from our preferred model with 20, 30, 40 and 50 km effective elastic thicknesses. This figure shows that greater elastic thickness gives topographic features a greater lateral extent as well as reducing their amplitude. Despite quantitative differences changing the elastic thickness produces, the discussed topographic features of this work are present over the full range of T_e values explored here. The exact T_e value representative of the collisional tectonics settings discussed here is not the focus of this study, though our results show the need to include elastic thickness to produce realistic topography estimate.

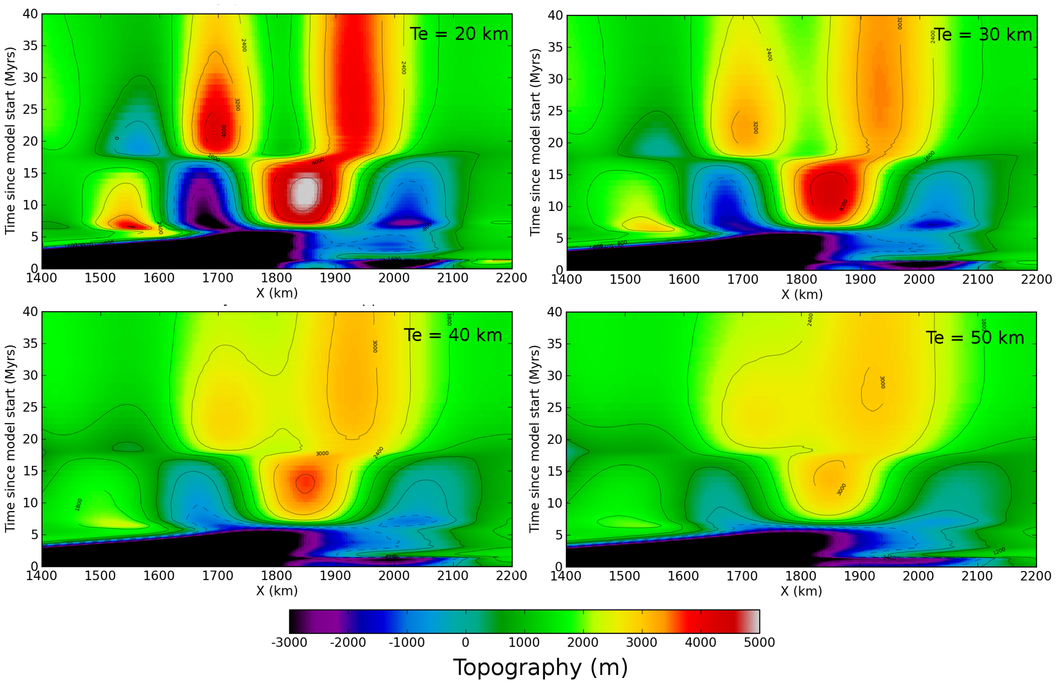

Figure 8.6: Effective elastic thickness effect on topography - Topography-time maps for our results with a 20 km, 30 km, 40 km and 50 km effective elastic thickness (T_e). The figure shows how with increasing effective elastic thickness the magnitude of topographic features are reduced while their spatial extent is increased. All the results shown in Chapter 3 $T_e = 30$ km is used.

8.3 Chapter 4 appendix

8.3.1 Thinned overriding lithosphere

The thickness of the overriding lithosphere is found to have an affect on the position that the CDB is formed on the overriding plate. Thinner overriding lithosphere thicknesses cause the CDB to form closer to the trench as shown in the Fig. 8.7.

Fig. 8.8 shows that the CDB moves towards the trench as the flow generated in the front of the overriding plate still goes from the front of the overriding plate to the top of the mantle wedge but with the mantle wedge higher it is also closer to the tench.

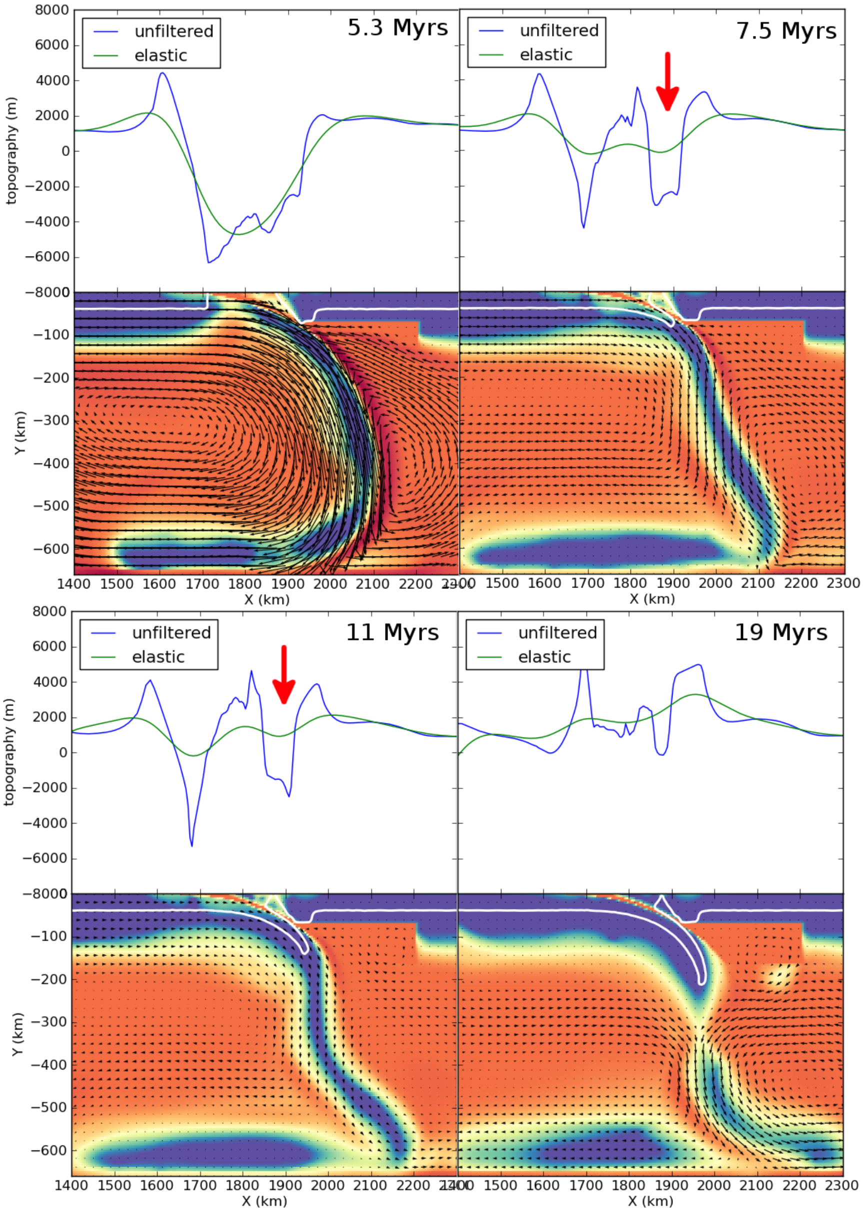

Figure 8.7: Collision Dynamics for thinned overriding plate - Here we present the collision dynamics and topography in the same way as Fig. 3.3 but for a model with only 60 km to the mantle wedge. Again the position of the CDB is highlighted by the red arrow. This shows how the CDB is formed closer to the trench for this model with a higher mantle wedge (thinner overriding lithosphere) that the model used in Chapter 3.

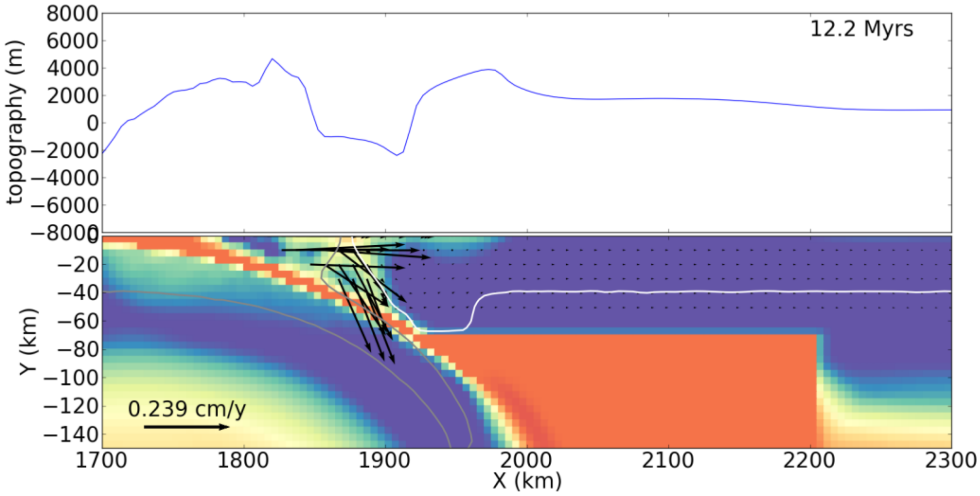

Figure 8.8: Affect of overriding plate thickness on topography - Velocity field and viscosity at 11 Myrs for a model identical to the model IV 4 but with only 60 km of overriding lithosphere to the mantle wedge. This time step is chosen as it is during continental subduction and shows the formation of the CDB. Here again we can see, as in Fig. 4.9 that the downward component of velocity in the overriding plate is still present even with a shallow mantle wedge. It also shows that the post collisional basin moves closer to the trench when the overriding plate is thinner.

8.4 Chapter 6 appendices

8.4.1 Mesh refinement and a resolution test.

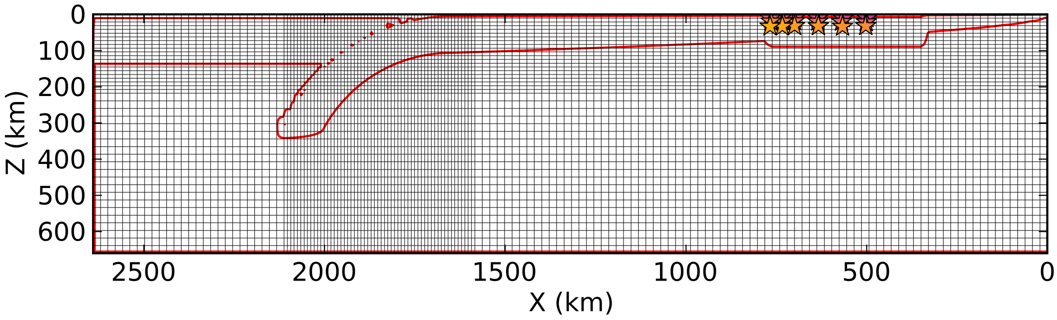

Figure 8.9: Numerical model grid - A section through the numerical grid used in the 3D model calculation the grid in the region of the collision zone is 10 km by 20 km by 10 km in the x,y,z directions respectively. The red contour shows the outline of the two plates. The model had approximately 9×10^5 nodes.

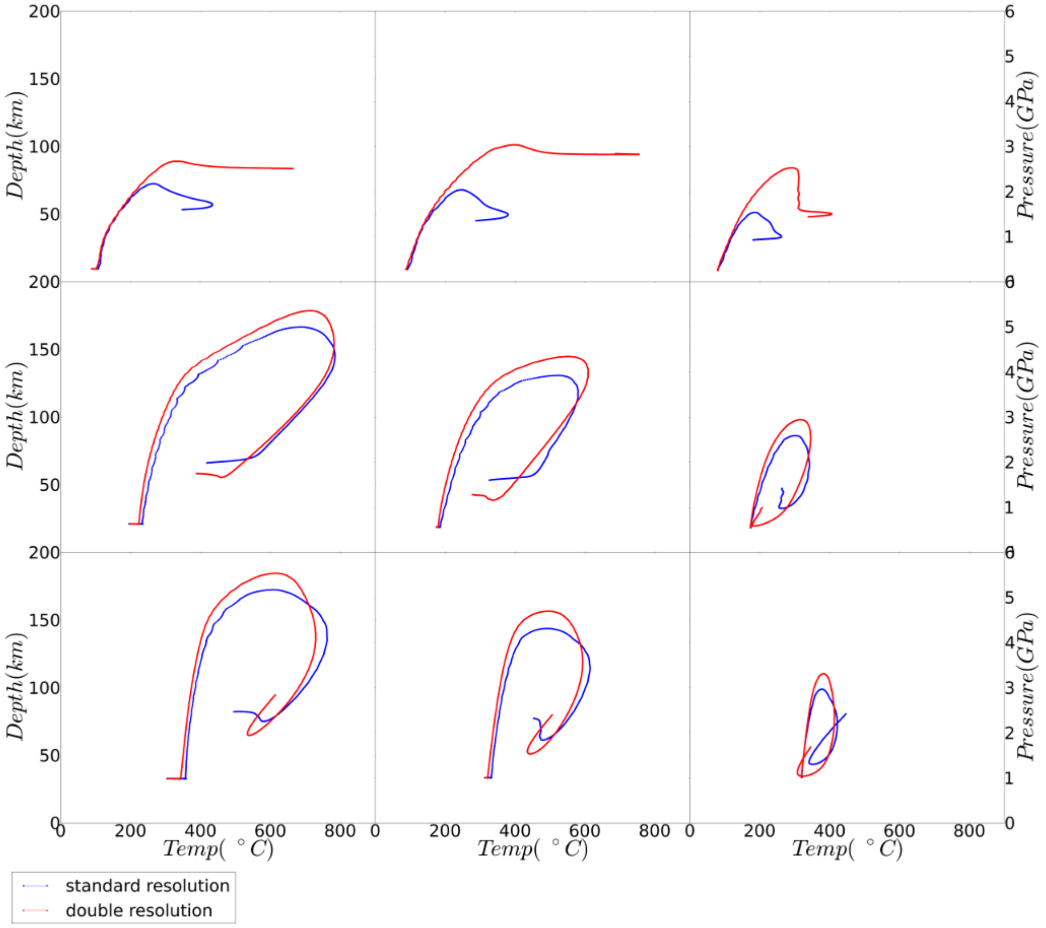

Figure 8.10: Resolution test - Comparison of the P-T paths travelled for the same tracer from the standard resolution model used in this study and a double resolution model. The standard model takes 36 hours to run on 64 cores the double resolution takes 7 days on 128 cores. The subplots in the figure represent the starting position of 9 markers from the center of the subducting continental block, that start at x = 33, 66 and 130 km from the front of the continental block and at depths of 10, 20 and 30 km.

8.4.2 The dynamics of both the orthogonal collision model and P-T paths for all markers used in the models.

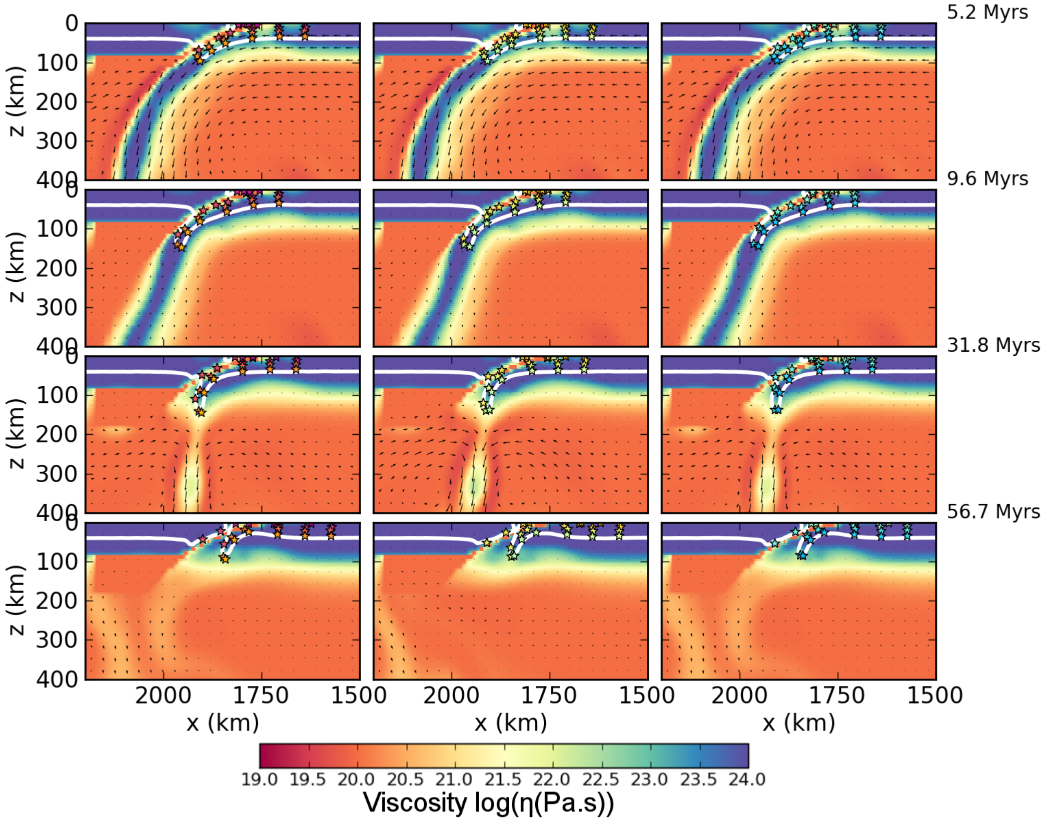

Figure 8.11: Vertical cross sections for the orthogonal collision model - perpendicular to the subduction trench through the orthogonal collision model. Colour scheme shows viscosity, white contour highlights crustal material and stars show the position of followed material markers. The first, second, and third column shows a slice at y=660, 1320, and 1980 km and contains the red, yellow and blue family of markers, respectively. Markers follow similar paths at the 3 different locations along the subduction zone.

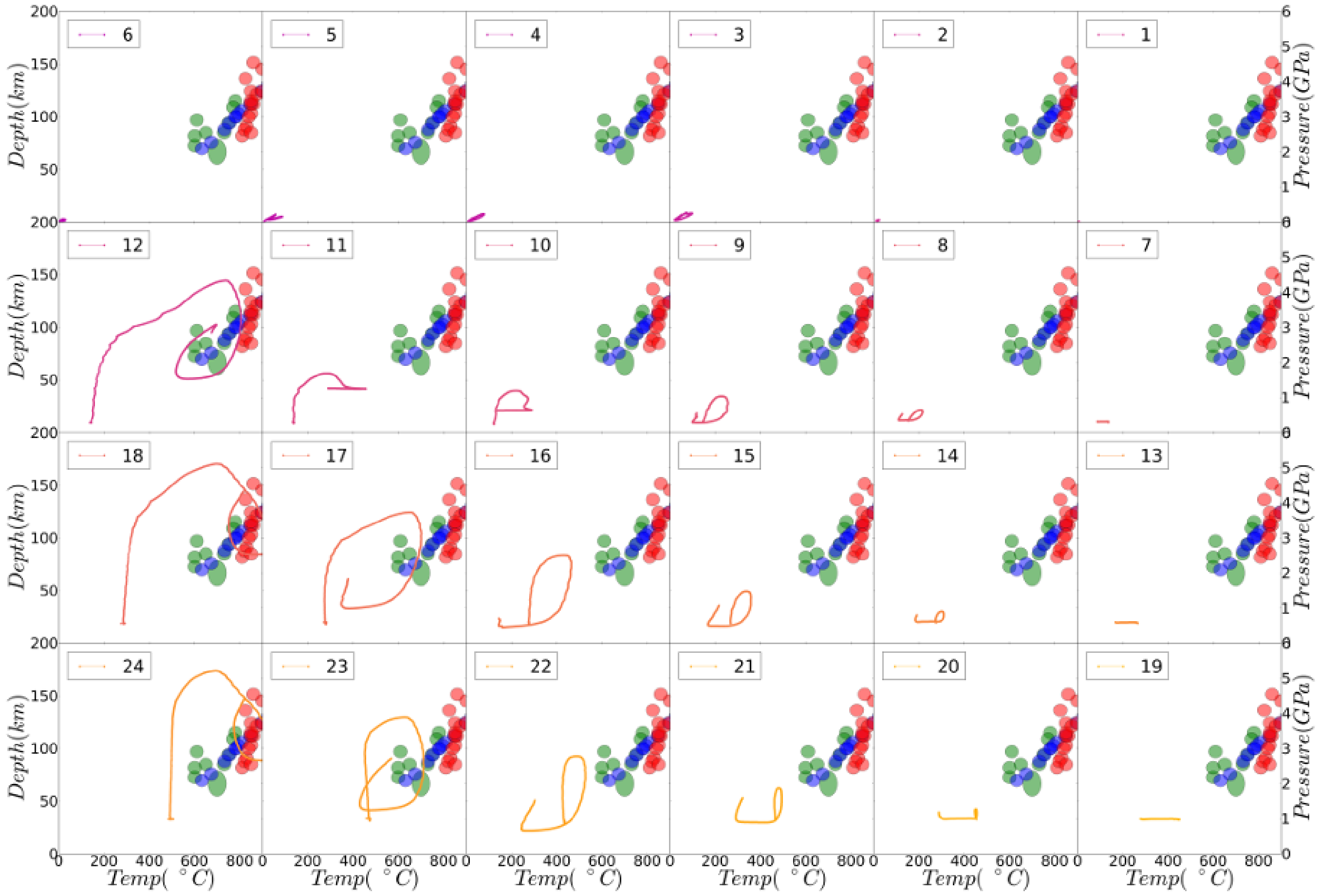

Figure 8.12: P-T paths for markers at y=660 km from the orthogonal collision model - The P-T paths are organised in the x-z orientation that the markers where originally positioned in, in the front of the subducting plates continental block e.g. the PT paths on the top left of the figure is for a tracer that started at the surface and at the front of the front of the subducting plates continental block. Markers are placed between 0-30 km depth (z-axis) and 0-240 km from the edge of the continental block. See Fig. 6.2 for more details on the start positions of the markers.

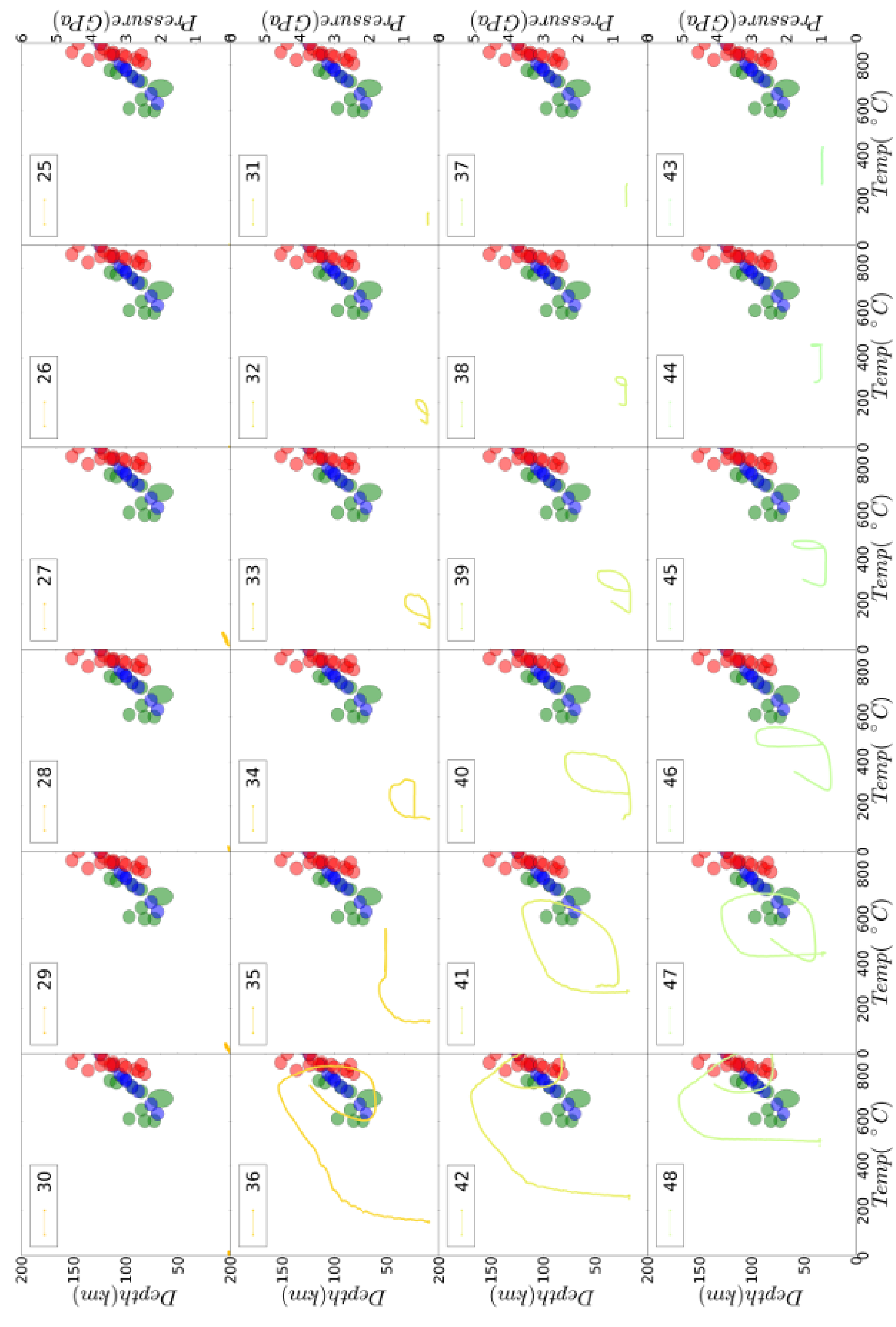

Figure 8.13: P-T paths for markers at y=1320 km from the orthogonal collision model - The P-T paths are organised in the x-z orientation that the markers where originally positioned in, in the front of the subducting plates continental block e.g. the PT paths on the top left of the figure is for a tracer that started at the surface and at the front of the front of the subducting plates continental block. Markers are placed between 0-30 km depth (*z*-axis) and 0-240 km from the edge of the continental block. See Fig. 6.2 for more details on the start positions of the markers.

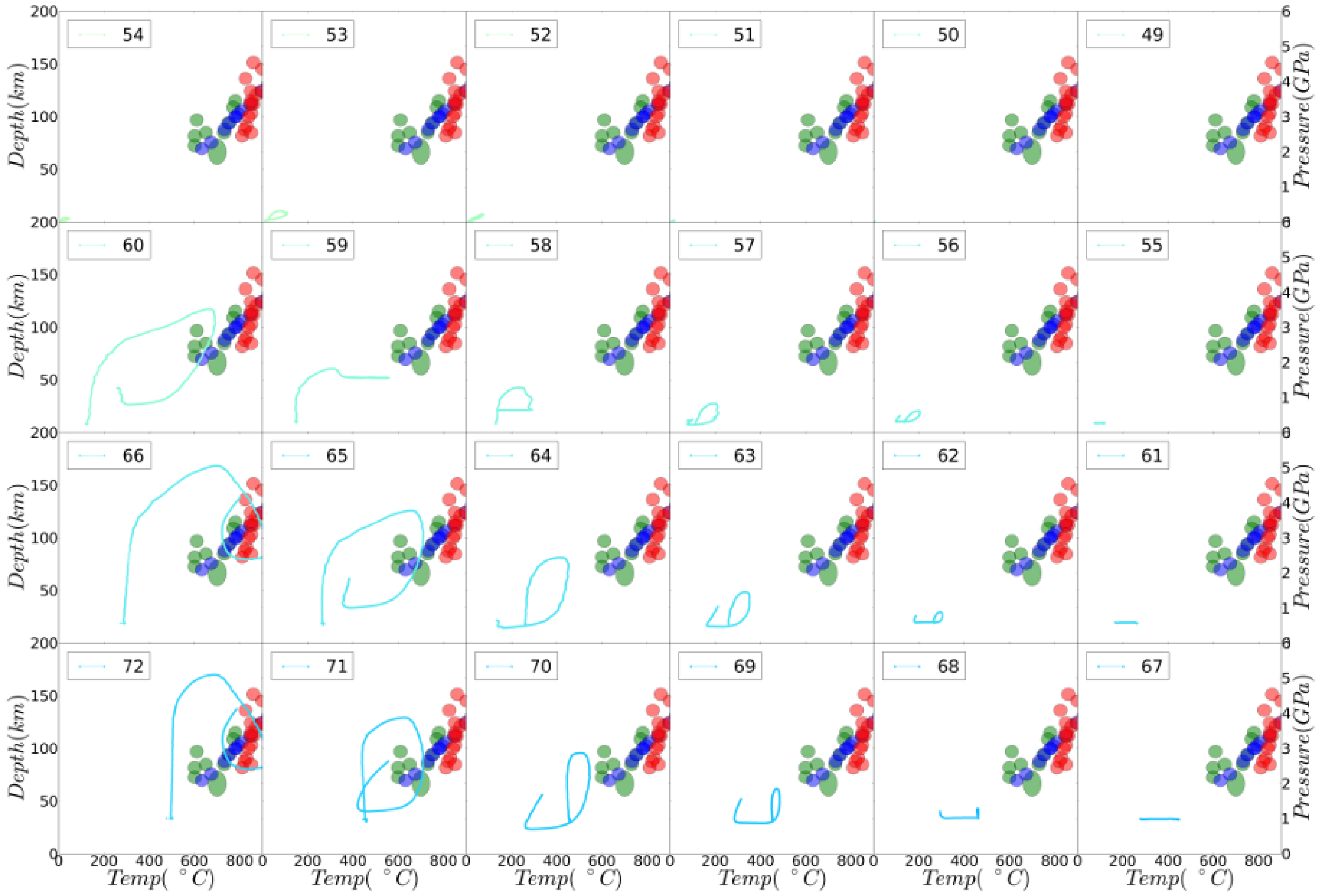

Figure 8.14: P-T paths for markers at y=1980 km from the orthogonal collision model - The P-T paths are organised in the x-z orientation that the markers where originally positioned in, in the front of the subducting plates continental block e.g. the PT paths on the top left of the figure is for a tracer that started at the surface and at the front of the front of the subducting plates continental block. Markers are placed between 0-30 km depth (z-axis) and 0-240km from the edge of the continental block. See Fig. 6.2 for more details on the start positions of the markers.

8.4.3 The dynamics of both the diachronous collision model and P-T paths for all markers used in the models.

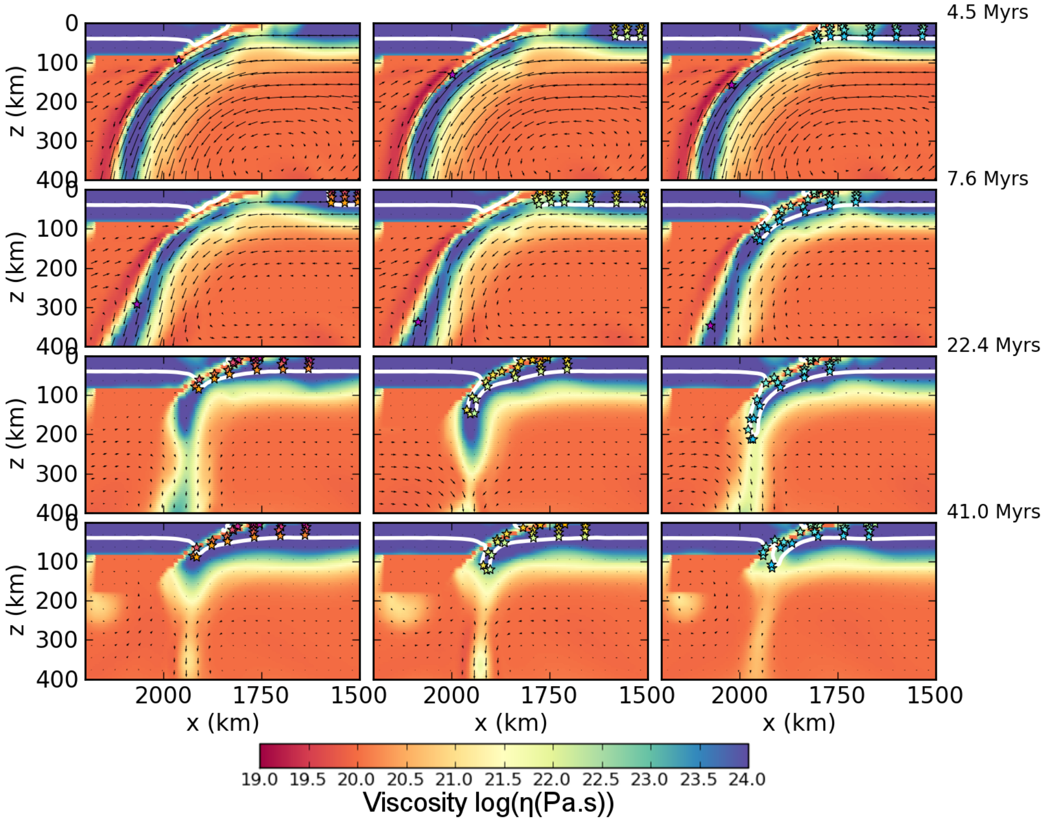

Figure 8.15: Vertical cross sections for diachronous collision model - perpendicular to the subduction trench through the diachronous collision model. Colour scheme shows viscosity, white contour highlights crustal material and stars show the position of followed material markers. The first, second, and third column shows a slice at y=660, 1320, and 1980 km and contains the red, yellow and blue family of markers, respectively. Markers follow similar paths at the 3 different locations along the subduction zone.

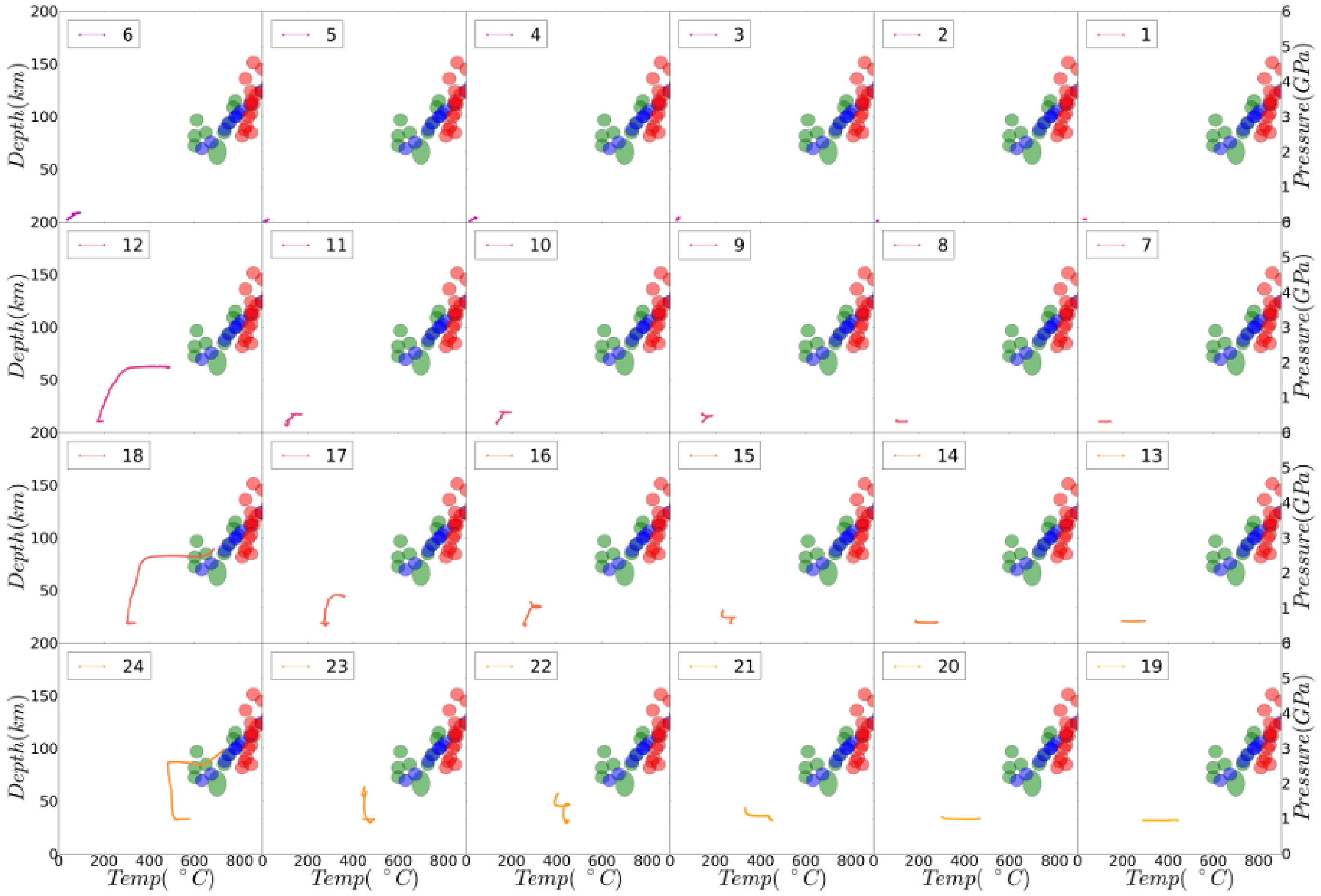

Figure 8.16: P-T paths for markers at y = 660 km from the diachronous collision model - The P-T paths are organised in the x-z orientation that the markers where originally positioned in, in the front of the subducting plates continental block e.g. the PT paths on the top left of the figure is for a tracer that started at the surface and at the front of the front of the subducting plates continental block. Markers are placed between 0-30 km depth (z-axis) and 0-240 km from the edge of the continental block. See Fig. 6.2 for more details on the start positions of the markers.

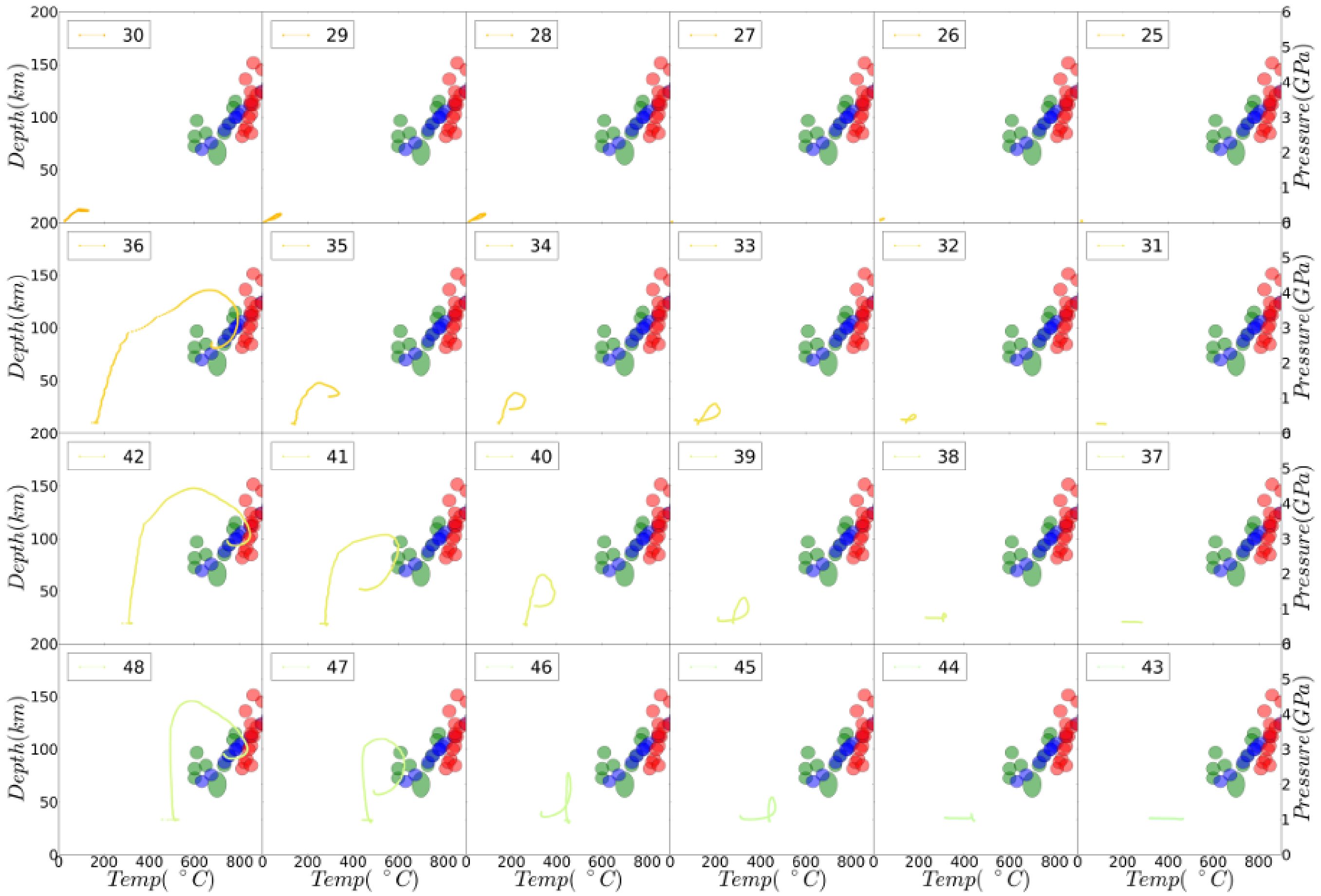

Figure 8.17: P-T paths for markers at y = 1320 km from the diachronous collision model - The P-T paths are organised in the x-z orientation that the markers where originally positioned in, in the front of the subducting plates continental block e.g. the PT paths on the top left of the figure is for a tracer that started at the surface and at the front of the front of the subducting plates continental block. Markers are placed between 0-30 km depth (z-axis) and 0-240km from the edge of the continental block. See Fig. 6.2 for more details on the start positions of the markers.

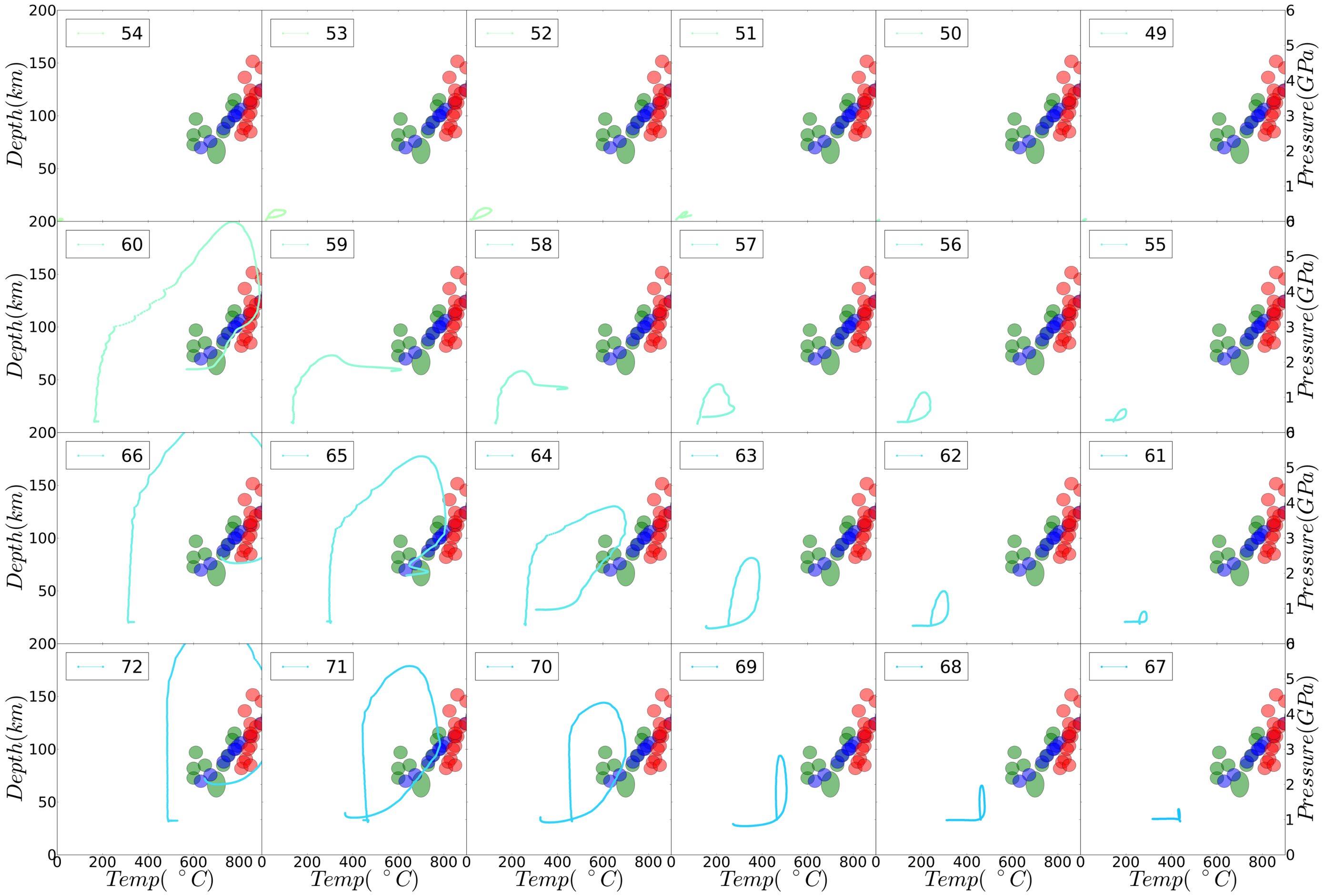

Figure 8.18: P-T paths for markers at y = 19800 km from the diachronous collision model - The P-T paths are organised in the x-z orientation that the markers where originally positioned in, in the front of the subducting plates continental block e.g. the PT paths on the top left of the figure is for a tracer that started at the surface and at the front of the front of the subducting plates continental block. Markers are placed between 0-30 km depth (z-axis) and 0-240 km from the edge of the continental block. See Fig. 6.2 for more details on the start positions of the marker.

8.4.4 Migration of the rotational pole of Baltica during its collision with Laurentia.

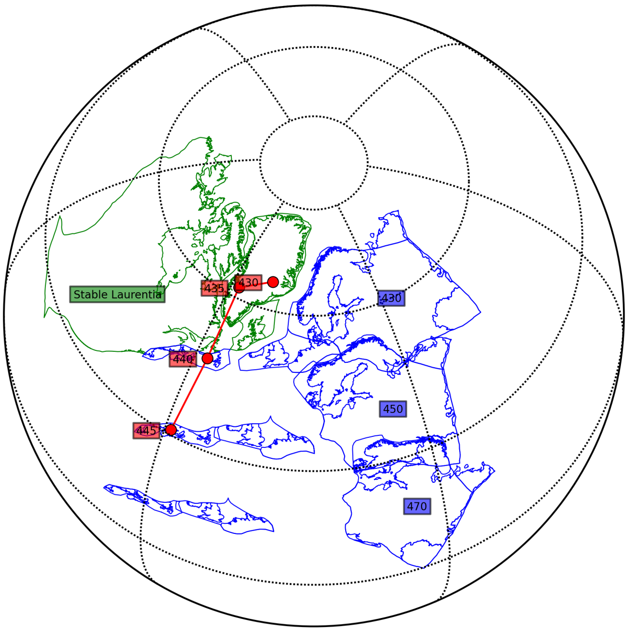

Figure 8.19: Plate reconstruction for the Laurentia Baltica collision - showing the motion of Baltica relative to a stable Laurentia between 470-430 Ma. The red path shows the associated rotational poles of Baltica between 445-430 Ma. The reconstruction shows how Baltica's rotates anti-clockwise during its collision with Laurentia. Balticas rotational pole propagates north roughly parallel to the position of the eventual suture between Laurentia and Baltica. This reconstruction shows that the rotation rate of Baltica increases around 435 Ma as the rotational pole continued to move north until 430 Ma. The paleomagnetic reconstructions are therefore broadly consistent (within the uncertainties in the locations of paleomagnetic poles) with the diachronous collisional model during initial continental subduction. Figure produced from data in Torsvik *et al.* [2012].

8.4.5 Animation

To supplement the static figures in Chapter 6 a few animations are provided:

`https://www.dur.ac.uk/a.d.bottrill/thesis.html`

These show the dynamics of the diachronous collision model and a plate reconstruction for the collision of Laurentia and Baltica.